

**Novel oxide nanoparticles and their polymer composites for  
visible light photocatalysis and adsorption applications**



**Thesis submitted in partial fulfillment**

**for the Award of Degree**

Doctor of Philosophy

by

**Somendra Singh**

**RAJIV GANDHI INSTITUTE OF PETROLEUM TECHNOLOGY**

**JAIS – 229304**

**Enrolment No.: PMS15001**

**2020**





**Rajiv Gandhi Institute of Petroleum Technology**  
**(An Institute of National Importance)**

**CERTIFICATE**

It is certified that the work contained in the thesis titled “**Novel oxide nanoparticles and their polymer composites for visible light photocatalysis and adsorption applications**” by **Somendra Singh** has been carried out under my supervision and that this work has not been submitted elsewhere for a degree.

It is further certified that the student has fulfilled all the requirements of Comprehensive, Candidacy, and SOTA.

**Dr. Amit Ranjan**  
**Supervisor**





**Rajiv Gandhi Institute of Petroleum Technology**  
**(An Institute of National Importance)**

**DECLARATION BY THE CANDIDATE**

I, **Somendra Singh**, certify that the work embodied in this thesis is my own bonafide work and carried out by me under the supervision of **Dr. Amit Ranjan** from August 2015 to August 2020 at Rajiv Gandhi Institute of Petroleum Technology, Jais, Amethi. The matter embodied in this thesis has not been submitted for the award of any other degree. I declare that I have faithfully acknowledged and given credits to the research workers wherever their works have been cited in my work in this thesis. I further declare that I have not willfully copied any other's work, paragraphs, text, data, results, etc. reported in journals, books, magazines, reports, dissertations, theses, etc. or available at websites and have not included them in this thesis and have not cited as my own work.

**Date:**

**Somendra Singh**

**Place:**





**Rajiv Gandhi Institute of Petroleum Technology**  
**(An Institute of National Importance)**

**CERTIFICATE BY THE SUPERVISOR**

It is certified that the declaration made by the student is correct to the best of my knowledge.

**Dr. Amit Ranjan**  
**Supervisor & Head of Department**





**Rajiv Gandhi Institute of Petroleum Technology**  
**(An Institute of National Importance)**

**COPYRIGHT TRANSFER CERTIFICATE**

**Title of the Thesis:** Novel oxide nanoparticles and their polymer composites for visible light photocatalysis and adsorption applications

**Name of the Student:** Somendra Singh

**COPYRIGHT TRANSFER**

The undersigned hereby assigns to the Rajiv Gandhi Institute of Petroleum Technology Jais, Amethi, all rights under copyright that may exist in and for the above thesis submitted for the award of the “*Doctor of Philosophy*”.

**Date:**

**Place:**

**Somendra Singh**

**Note:** However, the author may reproduce or authorize others to reproduce material extracted verbatim from the thesis or derivative of the thesis for author's personal use provided that the source and the Institute's copyright notice are indicated.





**Rajiv Gandhi Institute of Petroleum Technology**  
**(An Institute of National Importance)**

**CERTIFICATE**

It is certified that the work contained in the thesis titled “**Novel oxide nanoparticles and their polymer composites for visible light photocatalysis and adsorption applications**” by Mr. Somendra Singh has been carried out under my supervision. It is also certified that she fulfilled the mandatory requirement of TWO quality publications arose out of her thesis work.

It is further certified that the two publications (copies enclosed) of the aforesaid Mr. Somendra Singh have been published in the Journals indexed by –

- (a) SCI
- (b) SCI Extended
- (c) SCOPUS
- (d) \*Non-indexed journals  
(Only in special cases)

(\*Please enclosed DPGC resolution in this regard)

**Dr. Amit Ranjan**  
**Supervisor & Head of Department**

**Dr. Milan Kumar**  
**Convener, DPGC**



*Dedicated to my teachers and parents*



## ACKNOWLEDGMENT

I am thankful to the God for his mercy, and making me passionate, by providing the opportunity to step into the excellent world of science. I have been supported by many people to whom I would like to express my deepest gratitude. First and foremost, I wish to express my deepest gratitude to my thesis supervisor **Dr. Amit Ranjan** to guide me well throughout the research work from the title's selection to writing the thesis. His immense knowledge, motivation, and patience have given me more power and spirit to excel in the research. Conducting the academic study regarding such a difficult topic couldn't be as simple as he made this for me. He is my mentor and the best advisor for my doctorate study beyond the imagination. After continuing research with him, I realized that he is not only a great researcher but also a great human being. He kept faith in me and gives freedom during my research work to explore my scientific ideas. The discussion with him always is like a silver lining for research work which always fulfills me with motivational vibes. I would like to acknowledge all the Materials Science Group's members Dr. Shama Perween, Somya Kedia, and Ruchika Sharma (Passout); and Yogendra Yadawa, Anil Verma (currently working) for their assistance, fruitful discussion, and mental support. Without them, this task was not easy.

Apart from my Supervisor, I won't forget to express the gratitude to RPEC members: Dr. Milan Kumar, Dr. Debashis Panda for giving encouragement and sharing insightful suggestions. They all have played a major role in polishing my research work and data presentation. Their endless guidance is hard to forget throughout my life.

I am thankful to the current director (RGIPT) Prof. A. S. K. Sinha as well as former directors for extending research facilities in Strength of Materials Science/Engineering Mechanics Laboratory, RGIPT, and providing institutional fellowship to me. I would also like to thank my fellow researchers and teaching as well as non-teaching staffs of RGIPT for their kind cooperation.

I am also pleased to say thanks to Dr. Debashis Panda, Dr. Umapasana Ojha, and Dr. Shivanjali Sharma from RGIPT, who made my access simpler to their lab research facilities. It wouldn't have been possible to conduct this research without their precious support. They all really mean a lot to me. I am grateful to Dr. Vivek Polshettiwar (TIFR, Mumbai) and his team for doing BET surface analysis. Further, I would like to express my thanks to Dr. Sri Sivakumar (IIT, Kanpur) and his team for DRS analysis. I am sincerely thankful to the great teachers Dr. Jitendra Kumar, Dr. Rajiv Gupta from MSP, IIT Kanpur; Dr. Yashowanta N. Mohapatra from Dept. of Physics, IITK, Dr. Tanmay Maiti from MSE, IIT Kanpur, who taught me the basic of Materials Science during my Ph.D. course work.

I am indeed indebted and own my gratitude to Dr. Ajay Kumar Garg (Ex. HOD Physics, NAS College, Meerut), Dr. Sunil Kumar Sharma (HOD Physics, NAS College, Meerut), and Dr. Ajay Kumar (Department of Chemistry, NAS College, Meerut) for enlightening me

about research. I am thankful for their educational and moral support during my Master's degree.

I would always remember my colleagues too, for the fun-time we spent together, sleepless nights that gave us the courage to complete tasks before deadlines and for stimulating the discussions. I would also like to thank my senior colleagues Dr. Shama Perween, Dr. Awanish Kumar Bajpeyi, Dr. Mrityunjay K Jha, Dr. Rewati Raman Ujjawal, Dr. Tripti Rai and Dr. Amit Kumar Ghosh for their unconditional love and boundless support. Words fall short in expressing my special gratitude to my friends Praveen, Belal, Vivek, Reena, Bijoy, Mukkaram Mirza, Vartika, Ankit, Ravi Saini and Yogendra for their support at a tough time during my Ph.D.

In the end, I am grateful to my parents, relatives, and friends who remember me in their prayers and wish for my ultimate success. I consider myself nothing without them. They gave me enough moral support, encouragement, and motivation to accomplish my personal goals. My five lifelines, Mother (Kamla Devi), Father (Mahodar Singh), Brothers (Satish Singh, Satendra Singh) and Sisters (Puja and Arti) have always supported me and ensured that I pay adequate attention to the studies and achieve my objective without any obstacle on the way.

All the information taken from various sources (books, journals, thesis, catalogues, and research papers, *etc.*) and their authors has been duly acknowledged.

**Somendra Singh**

## PREFACE

Metal oxides and their composites with polymers are extensively desirable for a wide range of applications including visible light photocatalysis and adsorption. The visible light photocatalysis and adsorption are crucial for wastewater treatment as the water is being polluted by any segment of the society. The photocatalytic degradation of the pollutants in the presence of the visible light is most desirable where the visible light can be directly harvested. Therefore, photocatalysts with high efficiency of pollutant degradation are always under investigation. Besides the photocatalysis, the adsorption is highly attractive for wastewater treatment (dye adsorption) due to its simplicity and high uptake value. Therefore, the adsorbents of high uptake value of pollutants are always welcome.

In my thesis work, I have explored novel metal oxides and their composites as (i) *visible light sensitized photocatalysts* and (ii) *adsorbent materials*, targeting the removal of hazardous chemicals from wastewater as a potential application. In particular, we have prepared zinc titanate ( $\text{ZnTiO}_3$ ) and bismuth ferrite ( $\text{Bi}_2\text{Fe}_4\text{O}_9$ ) and their composites with polyaniline to meet our goals. Besides this, the  $\text{ZnTiO}_3$  has been doped by nitrogen. These prepared materials have been found their potential application in the field of photocatalysis and adsorption. The thesis has been divided into two parts based on the materials applications in visible light photocatalysis and adsorption. A brief introduction of the thesis chapters is given.

**Chapter 1:** A brief introduction of the thesis work has been presented in this chapter.

**Chapter 2:** In this chapter a short introduction of the characterization tools is presented. These characterization techniques are used in the data collection for the current research work. We have also written the raw materials used in research work.

**Chapter 3:** This chapter describes the formation of electrospun zinc titanate ( $\text{ZnTiO}_3$ ) *nanorods* and their application in the *visible light* photocatalytic degradation of the phenol. The fabrication of the nanorods has been achieved by the sol-electrospinning technique. The present study of  $\text{ZnTiO}_3$  nanorods has been compared with the previously reported bulk  $\text{ZnTiO}_3$  nanoparticles. The degradation rate constant ( $k$ ) has been compared with their counterparts of bulk  $\text{ZnTiO}_3$  prepared by the sol-gel method. The comparison

shows that the degradation rate constant ( $k$ ) has increased to  $0.01065 \text{ min}^{-1}$  in the presence of zinc titanate nanorods from value obtained with the bulk zinc titanate ( $0.00330 \text{ min}^{-1}$ ).

**Chapter 4:** In this chapter, we have prepared electrospun nitrogen-doped zinc titanate (N-ZnTiO<sub>3</sub>) nanoparticles by the novel sol-electrospinning technique. The prepared doped samples have been utilized for phenol degradation under visible light and the results have been compared with our previously published research article. The N-ZnTiO<sub>3</sub> has been well characterized to prove the nitrogen doping in ZnTiO<sub>3</sub>. The X-ray diffraction (XRD) pattern infers the hexagonal crystal structure in pure ZnTiO<sub>3</sub> and N-ZnTiO<sub>3</sub> samples. Furthermore, it investigates that the nitrogen doping induces microstrain in the ZnTiO<sub>3</sub> which estimated by the Williamson-Hall model. The BZT and EZT have been used for photocatalytic degradation of phenol under visible light irradiation. The rate constant ( $k$ ) has been found to improve from  $0.0033 \text{ min}^{-1}$  in BZT to  $0.01124 \text{ min}^{-1}$  in EZT samples. The ZTO samples were nitrogen-doped leading to a reduction in band gaps and a further improved photocatalytic efficiency. In nitrogen-doped samples with presumably highest nitrogen content, photocatalytic degradation rate constant ( $k$ ) further improved to  $0.02051 \text{ min}^{-1}$ .

**Chapter 5:** In the next set of study these oxide nanoparticles of ZTO were composited with polyaniline (PANI/ZTO). The composite showed excellent adsorption capacity giving a dramatic improvement in the adsorption performance towards dye molecules as compared to that observed with the PANI or the oxide nanoparticles separately as adsorbents. We attribute this effect to the increased accessibility of the PANI chains to the dye molecules due to their physisorption on to the nanoparticle surfaces. The prepared PANI/ZTO nanocomposite shows rapid adsorption and adsorbs 95% of CR dye (50 ppm-150 ppm) from its aqueous solution in 15 mins which compares much favourably with respect to adsorbent materials studied by other researchers. From the analysis of the kinetic data, the process is found to be intra-particle diffusion limited. The equilibrium data best fit to the Langmuir model suggesting physisorption of CR over PANI/ZTO and with maximum adsorption ( $Q_m$ ) being  $64.51 \text{ mg/g}$ .

**Chapter 6:** In this chapter, the bismuth ferrites (Bi<sub>2</sub>Fe<sub>4</sub>O<sub>9</sub>) was synthesized in different organic solvents. The effect of organic solvents was examined in the formation of Bi<sub>2</sub>Fe<sub>4</sub>O<sub>9</sub>. The morphological changes were observed on changing the solvents. The

nanorods formation of  $\text{Bi}_2\text{Fe}_4\text{O}_9$  with DMSO as solvents exhibits higher tendency of the methylene blue dye adsorption.

**Chapter 7:** In order to further test the idea that adsorption of the polyaniline on to the nanoparticles leads to better accessibility for the dye molecules and hence better adsorption, we also tried PANI/BFO composites for CR adsorption. The adsorption efficacy becomes even better than that in PANI/ZTO giving 95% removal (50 ppm-125 ppm) within 5 mins of adding the composite adsorbent. The Langmuir model suggests physisorption where the maximum adsorption ( $Q_m$ ) calculated 81.16 mg/g. The adsorption thermodynamics suggests spontaneous and exothermic adsorption which increases at the higher temperature.

**Chapter 8:** The thesis work has been concluded in this chapter. Some of the future work related to the thesis has been suggested here.



## Abbreviations/notations

|         |  |
|---------|--|
| B.E:    | Binding Energy   |
| BZT:    | Bulk Zinc Titanate   |
| BNZT:   | Bulk Nitrogen-doped Zinc Titanate  |
| BFO:    | Mixed phase of Bismuth Ferrite ( $\text{Bi}_2\text{Fe}_4\text{O}_9/\text{BiFeO}_3$ ) |
| BET:    | Brunauer–Emmett–Teller   |
| CB:     | Conduction Band  |
| DMSO:   | Dimethyl Sulfoxide   |
| DMF:    | N,N-dimethylformamide  |
| DMS-B5: | Bismuth Ferrite synthesized in DMSO at 525 °C  |
| DMF-B5: | Bismuth Ferrite synthesized in DMF at 525 °C   |
| DRS:    | Diffuse Reflectance Spectroscopy   |
| DLS:    | Dynamic Light Scattering   |
| D:      | Dark   |
| EDS:    | Energy Dispersive Spectroscopy   |
| EZT:    | Electrospun Zinc Titanate  |
| ENZT:   | Electrospun Nitrogen-doped Zinc Titanate   |
| EB:     | Emerldine Base   |
| ES:     | Emeraldine Salt  |
| eV:     | Electron Volt  |
| FTIR:   | Fourier Transform Infrared Spectroscopy  |
| FESEM:  | Field Emission Scanning Electron Microscopy  |
| L:      | Light  |
| MB:     | Methylene Blue   |
| mL:     | Milliliter   |
| NPs:    | Nanoparticles  |
| NRs:    | Nanorods   |
| N-ZTO:  | Nitrogen-doped Zinc Titanate   |
| nm:     | Nanometer  |
| PVA:    | Polyvinyl Alcohol  |
| PVP:    | Polyvinylpyrrolidone   |

|                 |  |
|-----------------|--|
| PANI:           | Polyaniline                                  |
| PANI/ZTO:       | Polyaniline-Zinc Titanate nanocomposite      |
| PANI/BFO:       | Polyaniline-Bismuth Ferrite nanocomposite    |
| PHS:            | Polyaniline Hydrogen Sulfate                 |
| PL:             | Photoluminescence Spectroscopy               |
| RT:             | Room Temperature                             |
| THF:            | Tetrahydrofuran                              |
| THF-B5:         | Bismuth Ferrite synthesized in THF at 525 °C |
| UV-Vis:         | Ultraviolet-Visible Spectroscopy             |
| VLPC:           | Visible Light Photocatalyst                  |
| VB:             | Valence Band                                 |
| XRD:            | X-Ray Diffraction                            |
| XPS:            | X-Ray Photoelectron Spectroscopy             |
| ZTO:            | Zinc Titanate ( $\text{ZnTiO}_3$ )           |
| $\mu\text{m}$ : | Micrometer                                   |
| Å:              | Angstrom                                     |

# Table of Contents

|            |  |           |
|------------|--|-----------|
| <b>1</b>   | <b>Chapter 1: Introduction and motivation .....</b>                      | <b>1</b>  |
| <b>1.1</b> | <b>Industrial pollutants and their treatment methods.....</b>            | <b>1</b>  |
| 1.1.1      | Brief historical development of dyes .....                               | 1         |
| 1.1.2      | Classification of dyes.....  | 2         |
| 1.1.3      | Impact of dyes on human being and environment .....                      | 3         |
| 1.1.4      | Use of dyes and management of its waste .....                            | 4         |
| 1.1.4.1    | Adsorption .....   | 6         |
| 1.1.4.2    | Adsorbent .....  | 8         |
| 1.1.4.3    | Photocatalysis/Visible light photocatalysis .....                        | 9         |
| 1.1.4.4    | Semiconductor photocatalyst.....   | 12        |
| <b>1.2</b> | <b>Nanomaterials and their nanocomposites.....</b>                       | <b>15</b> |
| 1.2.1      | Perovskite Structured materials .....                                    | 15        |
| 1.2.1.1    | Zinc titanate ( $ZnTiO_3$ ) .....  | 18        |
| 1.2.1.2    | Bismuth ferrite ( $BiFeO_3$ ) .....                                      | 19        |
| 1.2.2      | Conducting polymers .....  | 20        |
| 1.2.2.1    | Polyaniline (PANI) .....   | 20        |
| 1.2.3      | Heterostructured nanomaterials and their advantage .....                 | 21        |
| 1.2.4      | Electrospun nanofibers/nanowoven and their industrial applications ..... | 24        |
| 1.2.5      | Doping .....   | 26        |
| 1.2.6      | Rationale for selecting Zinc titanate and Bismuth ferrite .....          | 28        |

|            |  |           |
|------------|--|-----------|
| 1.2.7      | Overall objective of the thesis .....  | 30        |
| <b>2</b>   | <b>Chapter 2: Synthesis methods and characterization technique.....</b>                              | <b>31</b> |
| <b>2.1</b> | <b>Synthesis methods.....</b>  | <b>31</b> |
| 2.1.1      | Sol-gel method .....   | 31        |
| 2.1.2      | Electrospinning technique .....  | 32        |
| 2.1.3      | Sol-electrospinning technique .....  | 33        |
| 2.1.4      | Chemical oxidative polymerization technique .....  | 34        |
| <b>2.2</b> | <b>Characterization Technique.....</b>   | <b>35</b> |
| 2.2.1      | X-ray diffractogram (XRD) .....  | 35        |
| 2.2.2      | Fourier Transform Infrared (FTIR) spectroscopy .....   | 38        |
| 2.2.3      | Field Emission Scanning Electron Microscopy (FESEM)/ Energy-dispersive X-ray Spectroscopy (EDS)..... | 38        |
| 2.2.4      | UV-Visible spectroscopy .....  | 39        |
| 2.2.5      | Photoluminescence (PL) spectroscopy.....   | 40        |
| 2.2.6      | X-ray photoelectron spectroscopy (XPS)/ Auger electron spectroscopy (AES) 42                         |           |
| 2.2.7      | Dynamic light scattering (DLS) .....   | 43        |
| 2.2.8      | Thermogravimetric analysis (TGA) .....   | 44        |
| 2.2.9      | Raman spectroscopy analysis.....   | 45        |

|            |   |           |
|------------|---|-----------|
| <b>2.3</b> | <b>Materials and technical specifications of characterizing instruments .....</b>                         | <b>46</b> |
| 2.3.1      | Materials .....   | 46        |
| 2.3.2      | Characterizing materials .....  | 47        |
| <b>3</b>   | <b>Chapter 3: Comparing the photocatalytic property of zinc titanate nanorods and nanoparticles. ....</b> | <b>49</b> |
| <b>3.1</b> | <b>Abstract .....</b>   | <b>49</b> |
| <b>3.2</b> | <b>Introduction .....</b>   | <b>50</b> |
| <b>3.3</b> | <b>Experimental section .....</b>   | <b>52</b> |
| 3.3.1      | Synthesis of bulk zinc titanate (BZT) .....   | 52        |
| 3.3.2      | Synthesis of electrospun zinc titanate (EZT) .....  | 53        |
| 3.3.3      | Laboratory set-up for measuring the photocatalytic activity of ZnTiO <sub>3</sub> nanorods.....           | 54        |
| <b>3.4</b> | <b>Results and discussion.....</b>  | <b>55</b> |
| 3.4.1      | Field emission scanning electron microscopy (FESEM).....  | 55        |
| 3.4.2      | X-ray diffraction (XRD) .....   | 57        |
| 3.4.3      | Raman spectroscopy .....  | 59        |
| 3.4.4      | Fourier Transform Infrared Spectroscopy (FTIR) .....  | 61        |
| 3.4.5      | X-ray photoelectron spectroscopy (XPS) .....  | 62        |
| 3.4.6      | Diffuse reflectance spectroscopy (DRS).....   | 67        |
| 3.4.7      | Photoluminescence spectroscopy .....  | 70        |

|          |   |           |
|----------|---|-----------|
| 3.5      | Visible light photocatalytic activity.....  | 73        |
| <b>4</b> | <b>Chapter 4: Nitrogen-doped zinc titanate nanoparticles by electrospinning for visible-light photocatalytic degradation of phenol.....</b> | <b>77</b> |
| 4.1      | Abstract .....  | 77        |
| 4.2      | Introduction .....  | 78        |
| 4.3      | Experimental section .....  | 80        |
| 4.3.1    | Synthesis of zinc titanate (ZnTiO <sub>3</sub> ).....   | 80        |
| 4.3.2    | Synthesis of nitrogen-doped zinc titanate (ENZT) .....  | 80        |
| 4.4      | Results and discussion.....   | 82        |
| 4.4.1    | X-ray diffraction (XRD).....  | 82        |
| 4.4.2    | Raman Analysis.....   | 87        |
| 4.4.3    | Fourier Transform Infrared Spectroscopy (FTIR) .....  | 89        |
| 4.4.4    | Field Emission Scanning Electron Microscopy (FESEM) analysis.....   | 91        |
| 4.4.5    | X-ray Photoelectron Spectroscopy .....  | 94        |
| 4.4.6    | UV-Vis Diffuse Reflectance Spectroscopy .....   | 99        |
| 4.4.7    | Photoluminescence Spectroscopy .....  | 102       |
| 4.5      | Photocatalytic Activity of N-ZnTiO <sub>3</sub> nanopowder .....  | 103       |

|  |            |
|--|------------|
| <b>5 Chapter 5: Dramatic enhancement in adsorption of congo red dye in polymer-nanoparticle composite of polyaniline-zinc titanate .....</b> | <b>111</b> |
| <b>5.1 Abstract .....</b>  | <b>111</b> |
| <b>5.2 Introduction .....</b>  | <b>112</b> |
| <b>5.3 Experimental section .....</b>  | <b>115</b> |
| 5.3.1 Synthesis of ZnTiO <sub>3</sub> (ZTO) .....  | 115        |
| 5.3.2 Synthesis of Polyaniline by precipitation method .....   | 116        |
| 5.3.3 Synthesis of PANI/ZTO nanocomposite .....  | 116        |
| 5.3.4 Adsorption Experiments .....   | 117        |
| <b>5.4 Results and discussion.....</b>   | <b>118</b> |
| 5.4.1 X-ray Diffraction analysis .....   | 118        |
| 5.4.2 Dynamic light scattering analysis .....  | 120        |
| 5.4.3 Fourier transform infrared spectroscopy analysis.....  | 122        |
| 5.4.4 X-Ray photoelectron spectroscopy analysis .....  | 125        |
| 5.4.5 Field Emission Scanning Electron Microscopy analysis .....   | 130        |
| <b>5.5 Adsorption study .....</b>  | <b>131</b> |
| 5.5.1 Kinetics of adsorption .....   | 131        |
| 5.5.2 Mechanism of CR adsorption onto PANI/ZTO nanocomposite.....  | 137        |
| 5.5.3 Adsorption Isotherms.....  | 140        |

|            |   |            |
|------------|---|------------|
| 5.5.4      | Thermodynamic of adsorption .....   | 142        |
| <b>6</b>   | <b>Chapter 6: Solvent effect in synthesizing bismuth ferrite for methylene blue adsorption.....</b> | <b>147</b> |
| <b>6.1</b> | <b>Abstract .....</b>   | <b>147</b> |
| <b>6.2</b> | <b>Introduction .....</b>   | <b>148</b> |
| <b>6.3</b> | <b>Experimental section .....</b>   | <b>150</b> |
| 6.3.1      | Synthesis of Bismuth Ferrite Nanoparticles.....   | 150        |
| <b>6.4</b> | <b>Results and discussion.....</b>  | <b>151</b> |
| 6.4.1      | X-ray diffractogram.....  | 151        |
| 6.4.2      | Fourier Transform Infrared Spectroscopy analysis .....  | 153        |
| 6.4.3      | FESEM images and EDS analysis .....   | 155        |
| 6.4.4      | Raman Analysis.....   | 158        |
| 6.4.5      | BET Surface area analysis.....  | 161        |
| <b>6.5</b> | <b>Adsorption study .....</b>   | <b>163</b> |
| 6.5.1      | Adsorption experiments .....  | 163        |
| 6.5.2      | Amount of MB loading .....  | 165        |
| 6.5.3      | Effect of pH.....   | 167        |
| 6.5.4      | Adsorption Kinetics.....  | 169        |
| 6.5.5      | Adsorption Isotherms .....  | 174        |
| 6.5.6      | Thermodynamics of adsorption.....   | 177        |

|  |            |
|--|------------|
| <b>7 Chapter 7: Rapid adsorption of congo-red dye by polyaniline-bismuth ferrite nanocomposite .....</b> | <b>179</b> |
| <b>7.1 Abstract .....</b>  | <b>179</b> |
| <b>7.2 Introduction .....</b>  | <b>180</b> |
| <b>7.3 Experimental section .....</b>  | <b>182</b> |
| 7.3.1 Synthesis of PANI. ....  | 182        |
| 7.3.2 Synthesis of BFO. ....   | 182        |
| 7.3.3 Synthesis of PANI/BFO nanocomposite. ....  | 182        |
| 7.3.4 Batch Adsorption Experiments. ....   | 183        |
| <b>7.4 Result and discussion .....</b>   | <b>184</b> |
| 7.4.1 X-Ray Diffractogram analysis .....   | 184        |
| 7.4.2 Fourier Transform Infrared Spectroscopy (FTIR). ....   | 185        |
| 7.4.3 DLS analysis .....   | 188        |
| 7.4.4 XPS analysis .....   | 189        |
| 7.4.5 FESEM Imaging .....  | 194        |
| <b>7.5 Adsorption Study .....</b>  | <b>195</b> |
| 7.5.1 Adsorption kinetics .....  | 195        |
| 7.5.2 Adsorption Isotherms .....   | 202        |
| 7.5.3 Thermodynamics of adsorption .....   | 205        |
| <b>7.6 Reusability of adsorbent PANI/BFO .....</b>   | <b>208</b> |

|            |  |            |
|------------|--|------------|
| <b>8</b>   | <b>Chapter: 8 Conclusions and future work.....</b> | <b>209</b> |
| <b>8.1</b> | <b>Conclusions.....</b>                            | <b>209</b> |
| 8.1.1      | Chapter 3 .....                                    | 209        |
| 8.1.2      | Chapter 4 .....                                    | 209        |
| 8.1.3      | Chapter 5 .....                                    | 210        |
| 8.1.4      | Chapter 6 .....                                    | 210        |
| 8.1.5      | Chapter 7 .....                                    | 211        |
| <b>8.2</b> | <b>Future work.....</b>                            | <b>212</b> |
| <b>9</b>   | <b>References: .....</b>                           | <b>223</b> |

## List of Figures

|   |    |
|---|----|
| Figure 1.1. Classification of the dyes. ....  | 3  |
| Figure 1.2. Classification of various methods for dye treatment. ....   | 5  |
| Figure 1.3. The diagram for the energy of adsorption vs adsorbate's distance ( $d$ ) from the adsorbent; physisorption involving low enthalpy ( $\Delta H_p$ ) is represented by a solid line while chemisorption involving higher energy ( $\Delta H_c$ ) is depicted by a dashed line; and $\Delta E_{a,c}$ is the activation energy required for the chemisorption. .... | 7  |
| Figure 1.4. A schematic representation of an adsorbent with possible adsorption sites... 8  | 8  |
| Figure 1.5. Distribution of solar energy spectrum according to the wavelength. ....   | 11 |
| Figure 1.6. General mechanism of photocatalytic degradation of contaminants by a semiconductor photocatalyst. ....  | 11 |
| Figure 1.7. Classification of ternary metal oxides semiconductor photocatalyst. ....  | 13 |
| Figure 1.8. Classification of binary semiconductor photocatalyst. ....  | 15 |
| Figure 1.9. A schematic structural representation of $ABO_3$ type perovskite materials. 16  | 16 |
| Figure 1.10. Synthesis of polyaniline and its different forms. ....   | 21 |
| Figure 1.11. Two basic type coupled and capped heterostructure semiconductor photocatalyst. ....  | 23 |
| Figure 1.12. Applications of electrospun nanofibers in numerous fields. ....  | 25 |
| Figure 1.13. Mechanism of bandgap reduction in the doped semiconductor. ....  | 28 |
| Figure 2.1. A schematic diagram of X-ray diffractogram (XRD) represents the diffraction of incident x-rays from parallel planes having atoms in a regular pattern. ....   | 36 |
| Figure 2.2. Induced strain in the normal lattice changes the XRD pattern as represented. ....   | 37 |
| Figure 2.3. Jablonski diagram to define photoluminescence. ....   | 41 |

|  |    |
|--|----|
| Figure 2.4. Mechanism of photoelectron and Auger electron emission in XPS technique.<br>.....  | 43 |
| Figure 3.1. Schematic representation of synthesis process of electrospun zinc titanate (EZT).<br>.....   | 53 |
| Figure 3.2. Laboratory set-up for photocatalytic degradation of contaminants. ....   | 55 |
| Figure 3.3. The surface morphology represents (a) the nanoparticles of BZT, (b) as-spun EZT, (c) EZT nanorods, and (d) EZT nanofibers. ....  | 56 |
| Figure 3.4. XRD patterns of (a) BZT nanoparticles and (b) EZT nanorods. ....   | 59 |
| Figure 3.5. Raman analysis of BZT nanoparticles and EZT nanorods. ....   | 60 |
| Figure 3.6. Comparison of FTIR of BZT and EZT (a) From 4000 cm <sup>-1</sup> to 700 cm <sup>-1</sup> , and (b) Enlarge image from 1000 cm <sup>-1</sup> to 400 cm <sup>-1</sup> . .... | 62 |
| Figure 3.7. XPS of (a) Zn2p, (b) Ti2p, and (c) O1s for EZT and BZT.....  | 63 |
| Figure 3.8. XPS deconvoluted peaks of BZT components (a) Zn 2p, (b) Ti 2p, and (c) O 1s. ....  | 64 |
| Figure 3.9. XPS spectra of EZT components (a) Zn 2p, (b) Ti 2p, and (c) O 1s. ....   | 65 |
| Figure 3.10. Absorption spectra of BZT and EZT. ....   | 68 |
| Figure 3.11. (a) Kubelka-Munk function gives a bandgap of EZT (2.80 eV) which is smaller than (b) bandgap of BZT (2.90 eV). ....   | 70 |
| Figure 3.12. Cartoon representing (a) bandgap of ideal semiconductor, (b) surface states in between BZT bandgap, and (c) increase surface states in between EZT bandgap. ....          | 70 |
| Figure 3.13. The PL spectroscopy suggests the lower electron-hole recombination in EZT as compare to BZT. ....   | 73 |
| Figure 3.14. The photocatalytic degradation of phenol for its peak at (a) 210 nm (R <sup>2</sup> = 0.997) and (b) 270 nm (R <sup>2</sup> = 0.996) by BZT and EZT as indicated. ....    | 74 |

|  |     |
|--|-----|
| Figure 4.1. Schematic diagram represents the synthesis process of bulk zinc titanate (BZT) and electrospun Zinc titanate (EZT) and nitrogen-doped zinc titanate (bulk and electrospun: BNZT and ENZT). .....   | 81  |
| Figure 4.2. XRD analysis of (a) BZT, (b) EZT, (c) ENZT-0.25, and (d) ENZT-1. ....  | 83  |
| Figure 4.3. Microstrain calculation by WH-UDM in (a) BZT, (b) EZT, (c) ENZT-0.25, and (d) ENZT-1. ....   | 86  |
| Figure 4.4. Bar graph representation of (a) microstrain ( $\epsilon$ ) by WH-UDM, (b) crystallite size ( $D$ ) from the WH-UDM, and (c) average crystallite size ( $d_{avg}$ ) by Debye-Scherrer method for BZT, EZT, ENZT-0.25, and ENZT-1. ....  | 86  |
| Figure 4.5. Raman spectra of (a) BZT, (b) EZT, (c) ENZT-0.25, and (d) ENZT-1. ....   | 89  |
| Figure 4.6. FTIR spectra of BZT, EZT, ENZT-0.25, and ENZT-1.00 from (a) 4000 $\text{cm}^{-1}$ to 2000 $\text{cm}^{-1}$ , (b) 2000 $\text{cm}^{-1}$ to 700 $\text{cm}^{-1}$ . The peaks represented by $\bullet$ and $\blacklozenge$ suggest the incorporation of N into $\text{ZnTiO}_3$ lattice. .... | 91  |
| Figure 4.7. FESEM images of (a) BZT, (b) EZT, (c) ENZT-0.25, and (d) ENZT-1 at 50000 X magnification. ....   | 92  |
| Figure 4.8. FESEM images of (a) as-spun EZT (b) EZT at 50000 X magnification. ....   | 92  |
| Figure 4.9. Energy Dispersive X-Ray (EDS) of (a) EZT, (b) ENZT-0.25, and (c) ENZT-1 represents the presence of Zn, Ti, O and N in the respective samples. ....   | 93  |
| Figure 4.10. XPS of (a) N 1s of ENZT-1, (b) O 1s of EZT, and (c) O 1s of ENZT-1. ..  | 96  |
| Figure 4.11. XPS analysis of (a) Ti 2p of EZT, (b) Ti 2p ENZT-1, (c) Zn 2p EZT, and (d) Zn 2p ENZT-1. ....   | 97  |
| Figure 4.12. Plots of modified Kubelka-Munk function versus the energy of exciting light leading to the bandgap of (a) BZT, (b) EZT, (c) ENZT-0.25, and (d) ENZT-1.....  | 100 |

|   |     |
|---|-----|
| Figure 4.13. Representation of F(R) versus wavelength for BZT, EZT, ENZT-0.25, and ENZT-1. Increasing steepness in graphs for higher nitrogen doping suggests the surface states in samples. ....   | 101 |
| Figure 4.14. PL spectroscopy of BZT, EZT, ENZT-0.25, and ENZT-1.....  | 103 |
| Figure 4.15. The BET surface area and the pore size distribution in EZT ((a) and (b)), and in ENZT-1 ((c) and (d)). A significant change in the surface area and the pore size distribution is observed after nitrogenation, which bears an important effect on photocatalytic behavior. .... | 104 |
| Figure 4.16. (a) & (c): the first-order-rate kinetics, and (b) & (d): the plot of degradation constant ( <i>k</i> ) versus composition (N:Ti) of electrospun N-doped ZnTiO <sub>3</sub> samples and bulk N-doped ZnTiO <sub>3</sub> samples respectively. ....                                | 107 |
| Figure 4.17. Proposed scheme to represents the nitrogen electronic states, surface states in doped samples. ....  | 109 |
| Figure 5.1. Scheme represents synthesis process of polyaniline (PANI) and polyaniline/zinc titanate (PANI/ZTO) nanocomposite. ....  | 117 |
| Figure 5.2. XRD pattern of PANI, ZTO, and PANI/ZTO nanocomposite. Figure in inset represents the broadness in XRD of PANI/ZTO in the range of $2\theta = 10^\circ$ to $18^\circ$ .....  | 120 |
| Figure 5.3. The particle size distribution of (a) PANI, (b) ZTO, and (c) PANI/ZTO nanocomposite.....  | 121 |
| Figure 5.4. The FT-IR spectra of PANI, ZTO, and PANI/ZTO from (a) $4000\text{ cm}^{-1}$ to $2000\text{ cm}^{-1}$ , and (b) $2000\text{ cm}^{-1}$ to $500\text{ cm}^{-1}$ . ....   | 123 |
| Figure 5.5. Deconvoluted XPS peaks of (a) C 1s PANI, (b) N 1s PANI, and (c) Ti 2p ZTO. ....   | 127 |
| Figure 5.6. The XPS spectra of (a) C 1s PANI/ZTO, (b) N 1s PANI/ZTO, and (c) Ti 2p PANI/ZTO.....  | 130 |

|   |     |
|---|-----|
| Figure 5.7. FESEM images of (a&d) PANI, (b&e) ZTO, and (c&f) PANI/ZTO nanocomposite at 20000x and 100000x magnification respectively. ....  | 131 |
| Figure 5.8. The colour of CR solution after treatment with PANI, ZTO, and PANI/ZTO nanocomposite. ....  | 132 |
| Figure 5.9. UV-Vis adsorption kinetics of 50 ppm aqueous solution of CR onto (a) PANI, (b) ZTO, and (c) PANI/ZTO nanocomposite. ....  | 134 |
| Figure 5.10. A cartoon depicting the proposed scheme for adsorption explaining the dramatic enhancement of adsorption in polyaniline-nanoparticle composites. ZTO nanoparticles adsorb poorly (a). The adsorption sites which chiefly reside on the polyaniline chains, are accessible to dyes only at the surface in neat polymer suspensions, leaving the subsurface chains unutilized (b). This limitation is overcome in nanocomposites due to chains adhering to the nanoparticle surfaces (c) and opening up for adsorption. .... | 135 |
| Figure 5.11. (a) Adsorption $Q_t$ versus $t$ for four different dye concentrations by PANI and PANI/ZTO, and (b) Pseudo-second order plots of $t/Q_t$ versus time $t$ for the adsorption of the CR onto PANI/ZTO nanocomposite. ....  | 136 |
| Figure 5.12. Intra-particle diffusion plots of adsorption capacity $Q_t$ versus $t^{1/2}$ for the adsorption of CR onto PANI/ZTO for different concentrations (a) 50 ppm, (b) 75 ppm, (c) 100 ppm and (d) 150 ppm. ....   | 138 |
| Figure 5.13. Comparison of Intra-particle diffusion model of 50 ppm CR adsorption by (a) PANI, and (b) PANI/ZTO. ....   | 139 |
| Figure 5.14. Plot confirming the (a) Langmuir model of adsorption, and (b) D-R model. ....  | 140 |
| Figure 5.15. van't Hoff model fitting for CR adsorption by PANI/ZTO. ....   | 143 |
| Figure 6.1. Synthesis process for bismuth ferrite in different solvents. ....   | 151 |

|  |     |
|--|-----|
| Figure 6.2. XRD Pattern of BFO prepared with different solvent DMS, DMF, and THF (bottom to up).....   | 153 |
| Figure 6.3 The FTIR spectra from (a) 4000 $\text{cm}^{-1}$ to 1600 $\text{cm}^{-1}$ and (b) 1600 $\text{cm}^{-1}$ to 400 $\text{cm}^{-1}$ represents the chemical bonding of BFO prepared in different solvents. ....                    | 155 |
| Figure 6.4: The FESEM images of (a) and (b)-DMS-B5 showing nanorods on the surface; (c) and (d)- DMF-B5 representing nanoparticles; (e) and (f)-THF-B5 representing nanoflakes at two different scales 500 nm and 1 $\mu\text{m}$ . .... | 156 |
| Figure 6.5. The Energy Disperse Spectrum of (a)-DMS-B5, (b)-DMF-B5, and (c)-THF-B5 representing the presence of Bi, Fe, and O in all samples.....  | 157 |
| Figure 6.6: Raman Spectrum of BFO (a) DMS-B5, (b) DMF-B5, (c) THF-B5.....  | 159 |
| Figure 6.7. (a) Nitrogen adsorption-desorption isotherm for DMS-B5 showing the surface area of 3.46 $\text{m}^2/\text{g}$ , and (b) pore size distribution of DMS-B5. ....   | 162 |
| Figure 6.8: UV-Vis analysis shows the maximum adsorption of 15 ppm aqueous solution (100 mL) of Methylene Blue by DMS-B5 (adsorbent amount: 150 mg).....   | 164 |
| Figure 6.9: Diagram represents the percentage of removal efficiency of MB (15 ppm) from aqueous solution (100 mL) by BFO prepared in different solvents. ....  | 165 |
| Figure 6.10. Time-based adsorption kinetics of MB adsorption at different concentrations (a) 4.5 ppm, (b) 7.5 ppm, (c) 15 ppm, and (d) 22.5 ppm, by DMS-B5.....  | 166 |
| Figure 6.11. Graph represents that the higher dye loading (in 100 mL volume) decreases the adsorption by DMS-B5 (150 mg).....  | 167 |
| Figure 6.12. (a) Percentage of removal efficiency at different pH values, and (b) pH of MB aqueous solution before adsorption ( $\text{pH}_i$ ) and after adsorption ( $\text{pH}_f$ ) treatment....                                     | 168 |
| Figure 6.13. Fitting of pseudo-first-order equation for MB adsorption at different dye concentrations.....   | 171 |
| Figure 6.14: Pseudo second-order plots of $t/Q_t$ versus time $t$ . ....   | 172 |

|   |     |
|---|-----|
| Figure 6.15. Intra-particle diffusion model (plots between adsorption capacity $Q_t$ vs $t^{1/2}$ ) suggests film diffusion as rate controlling diffusion. ....   | 173 |
| Figure 6.16. (a) Boyd parameter $B_t$ versus time ( $t$ ) and (b) film diffusion model for the adsorption of MB on BFO. ....  | 174 |
| Figure 6.17: (a). Langmuir isotherm model suggests monolayer adsorption and (b). Separation factor $R_L$ versus initial concentration $C_0$ for the adsorption of MB represents minimum values of $R_L$ which suggests stronger interaction. .... | 175 |
| Figure 6.18. (a) Dubinin-Radushkevich (D-R) model infers physisorption and (b). UV-Vis adsorption data of MB adsorption at 70 °C. ....  | 177 |
| Figure 7.1. Pathway of synthesis of polyaniline/bismuth ferrite nanocomposite. ....   | 183 |
| Figure 7.2. XRD pattern of (a) PANI, (b) BFO, and (c) PANI/BFO nanocomposite. .   | 184 |
| Figure 7.3. FTIR spectra of PANI, BFO, and PANI coated BFO. ....  | 186 |
| Figure 7.4. DLS study of (a) PANI, (b) BFO, and (c) PANI/BFO. The larger particle size of PANI/BFO than BFO confirms the coating of PANI over BFO. ....   | 189 |
| Figure 7.5. XPS deconvolution spectra of (a) C 1s PANI, (b) C 1s PANI/BFO, (c) N 1s PANI, and (d) N 1s PANI/BFO. ....   | 191 |
| Figure 7.6. XPS spectrum of (a) Fe 2p of BFO, (b) Fe 2p of PANI/BFO, (c) Bi 4f of BFO, (d) Bi 4f of PANI/BFO. ....  | 192 |
| Figure 7.7. FESEM images of (a) PANI, (b) BFO, (c) PANI/BFO nanocomposite, and (d) CR-PANI/BFO. ....  | 194 |
| Figure 7.8. Time-dependent adsorption of 50 ppm CR dye (a) by PANI, (b) BFO, (c) 50 ppm CR solution by PANI/BFO; and (d) 125 ppm CR solution by PANI/BFO. ....  | 196 |
| Figure 7.9. (a) Adsorption capacity vs. time (s), and (b) percentage of 50 ppm CR (from 100 mL aqueous solution) removal by PANI, BFO, and PANI/BFO nanocomposite (150 mg of each adsorbent). ....  | 197 |

Figure 7.10. (a) Instantaneous concentration ( $C_t$ ) versus time ( $t$ ), and (b) Adsorption capacity  $Q_t$  versus time  $t$ ; for the adsorption of CR onto the PANI/BFO nanocomposites at a different initial concentration of 50 ppm, 75 ppm, 100 ppm, and 125 ppm. .... 197

Figure 7.11. The adsorption data fits pseudo-second order equation for the adsorption of the CR onto PANI/BFO nanocomposite. .... 198

Figure 7.12. Intra-particle diffusion model ( $Q_t$  versus  $t^{1/2}$ ) suggests film diffusion as rate-limiting process for the adsorption of CR onto PANI/BFO for different concentrations (a) 50 ppm, (b) 75 ppm, (c) 100 ppm, and (d) 125 ppm. .... 201

Figure 7.13. Plots of Boyd model parameter  $B_t$  versus time  $t$  for adsorption of CR onto PANI/BFO nanocomposite. .... 202

Figure 7.14. Plots of (a) Langmuir model infers monolayer adsorption, and (b) Separation factor  $R_L$  versus initial concentration  $C_0$ . .... 203

Figure 7.15. Linear fitting of (a) Freundlich model, and (b) D-R model. .... 205

Figure 7.16. (a) van't Hoff plot used to calculate thermodynamics parameters, and (b) Graph shows the CR (50 ppm) equally adsorbed at higher temperature by PANI/BFO. .... 206

Figure 7.17. The re-usability shows the higher capacity of the adsorbent towards CR removal. .... 208

## List of Tables

|   |     |
|---|-----|
| Table 3.1. XPS binding energy of BZT components (a) Zn 2p, (b) Ti 2p, and (c) O 1s; EZT components (a) Zn 2p, (b) Ti 2p, and (c) O 1s. .... | 66  |
| Table 3.2. The comparison of the bandgap energy of the ZnTiO <sub>3</sub> with the bandgap energy in previously reported articles.....      | 69  |
| Table 3.3. Listing of PL peaks in terms of wavelength and emission energy for BZT and EZT. ....   | 72  |
| Table 4.1. The nomenclature of samples. ....  | 81  |
| Table 4.2. The calculation of the percentage of hexagonal phase present in the samples. ....  | 84  |
| Table 4.3. The comparison of $d_{avg}$ , $d_m$ , $D$ , and $\varepsilon$ for BZT, EZT, ENZT-0.25, and ENZT-1. ....                          | 87  |
| Table 4.4. The lattice parameters and $c/a$ values of BZT, EZT, ENZT-0.25, and ENZT-1. ....   | 87  |
| Table 4.5. The representation of binding energy (B.E) and area % of the elements in ENZT-1 and EZT.....                                     | 98  |
| Table 4.6. The bandgap energy of BZT, EZT, ENZT-0.25, and ENZT-1.00.....  | 100 |
| Table 4.7. The calculation of the first-order-rate constant ( $k$ ) and % of photocatalytic degradation efficiencies. ....                  | 108 |
| Table 5.1. Comparison of time for achieving 90% adsorption of CR by previously reported adsorbents. ....                                    | 115 |
| Table 5.2 Assignment to the major peaks in FTIR of the PANI, ZTO, and PANI/ZTO nanocomposite. ....  | 124 |
| Table 5.3 Assignment to the XPS peaks of C, N, and Ti in PANI, ZTO, and PANI/ZTO nanocomposite. ....  | 128 |

|  |     |
|--|-----|
| Table 5.4. Kinetic parameters of the pseudo-second-order adsorption kinetic model for CR onto PANI/ZTO nanocomposite. .... | 136 |
| Table 5.5. Isotherms parameters for the adsorption of CR onto PANI/ZTO nanocomposite.....                                  | 142 |
| Table 5.6. Thermodynamic parameters for the adsorption of CR onto PANI/ZTO nanocomposites. ....                            | 145 |
| Table 6.1: Nomenclature of the samples. ....   | 151 |
| Table 6.2. Elemental analysis of DMS-B5, DMF-B5, and THF-B5.....   | 158 |
| Table 6.3. The identification and assignment of RAMAN peaks in all the samples. ...  | 161 |
| Table 6.4. The pH of MB aqueous solution before and after adsorption process.....  | 168 |
| Table 6.5. Adsorption parameters are calculated from the pseudo-first-order equation. ....                                 | 170 |
| Table 6.6. Adsorption parameters obtained from the modified pseudo-second-order equation. ....                             | 172 |
| Table 6.7. Parameters obtained from the isotherms models. ....   | 176 |
| Table 6.8. Thermodynamic parameter for the adsorption of MB onto BFO. ....   | 177 |
| Table 7.1. Summary of binding energy and area% of the XPS peaks for PANI, BFO, and PANI/BFO nanocomposite. ....            | 193 |
| Table 7.2. Kinetic parameters of the pseudo-second-order adsorption kinetic model..  | 199 |
| Table 7.3. Intra-particles diffusion model parameters for the adsorption of CR onto PANI/BFO nanocomposites.....           | 201 |
| Table 7.4. Isotherms parameters for the Langmuir model, and Dubinin-Radushkevich model.....                                | 204 |
| Table 7.5. Thermodynamic parameters for the adsorption of CR onto PANI/BFO nanocomposites. ....                            | 207 |





# Chapter 1: Introduction and motivation

## 1.1 Industrial pollutants and their treatment methods

### 1.1.1 Brief historical development of dyes

The dyes are a vital part of our life as these appear everywhere in our daily life. But, the dye's history is deep-rooted. The five natural dyes were reported earlier around pre-3000 BC in Egypt and the main sources of their extraction were vegetables, plants, and animals [1]. These five natural dyes were named *Archil* (*Cl natural red 28*), *Madder* (*Cl natural red 9*), *Kermes* (*Cl natural red 3*), *Kermes contains kermesic acid*, and *Woad* [1]. Since the origin of the dyes was natural at that time, therefore, these were biodegradable thereby was not caused harm to the environment. William Henery Perkin had innovated first synthetic dye '*Mauveine*' in 1856 which led to the revolutionary changes in the dye's history [2]. Thereupon, the discovery of *Mauveine* had triggered the development of the new dye industries. Although, *Mauveine* based industries were dominant until the end of the 20<sup>th</sup> century before the discovery of '*Phthalocyanines*' and '*reactive dyes*' [3]. The discovery of synthetic dyes reduced the use of natural dyes drastically. The increasing demand for synthetic dyes was tocsin of the danger to the environment. In the past, dyes were derived from organic materials. Currently, numerous methods and materials are available for coloring the textiles [2]. While today's methods are economically feasible and more efficient but always under the question of harmfulness to the environment and human beings.

Today's according to the data available around 700,000 tons of dyes are produced annually worldwide and used in different industries including textiles, printing, food, leather, etc [2]. Records say around 10-15% of total dye production lost as the dye effluent loaded with dyestuffs in the eco-system [2]. The released wastewater contains organic

molecules and metal complexes which are not acceptable worldwide and does not fulfill the environmental regulations [4–6]. The industrial effluent is a matter of concern as the dyestuffs persist in the environment due to less biodegradability, stability to the natural oxidizing agent, and photolysis [7]. Their presence in the environment is hazardous to the human and aquatic systems as most cytotoxic with proven carcinogenicity [8]. Moreover, the industrial waste dye effluents form a thin layer over the surface of receiving water bodies which consequently decreases the amount of oxygen dissolved and limits the penetration of the light in the water thereby affecting the food source of the aquatic organism by affecting the photosynthesis process [9].

### **1.1.2 Classification of dyes**

The dyes can be divided into many subcategories based on their source of origin, structure, application, and chemical composition as depicted in Figure 1.1 [10]. The azo dyes are most competent in all the dyes as these are using more than 50% for making colorant in the dye industries [10]. The azo dyes belong to the large class of aromatic molecules where its two nitrogen atoms are bonded with a double bond ( $-N=N-$ ) and the aromatic rings are attached to the available site of nitrogen atoms [10]. Besides it, the azo dyes can be further classified into cationic azo dyes, anionic azo dyes, and many more as shown in Figure 1.1 and these are the most studied dyes for adsorption and photocatalysis. The *methylene blue*, *cationic orange G*, *cationic black O*, *base yellow 21*, etc. are examples of cationic dye while the *congo red*, *ramazol black*, *ramazol red*, etc belongs to anionic dyes.

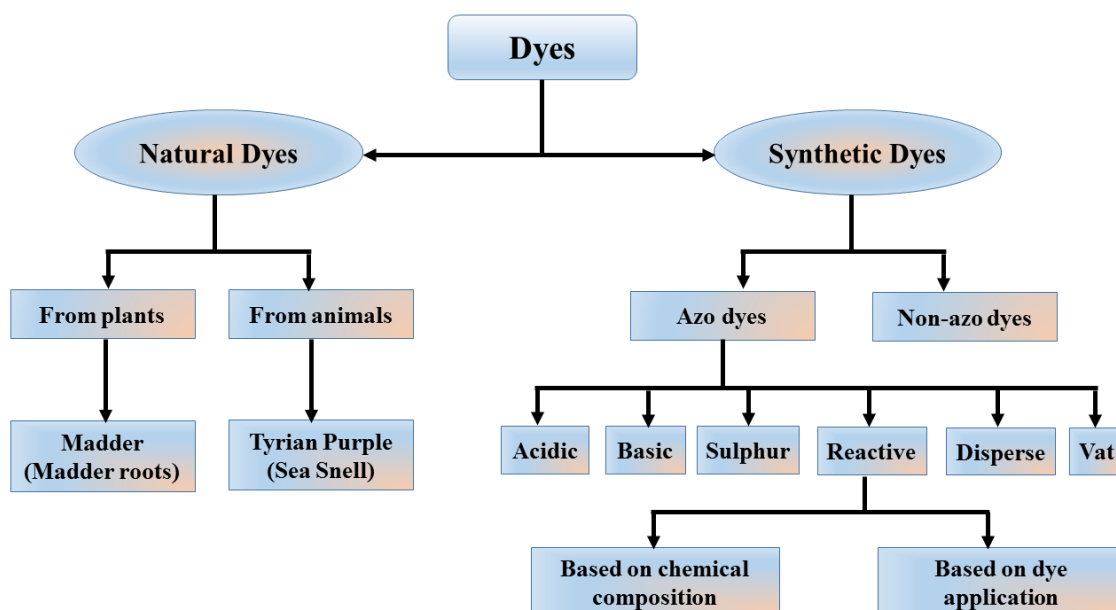


**Figure 1.1. Classification of the dyes.**

### **1.1.3 Impact of dyes on human being and environment**

During the coloration process, a huge amount of dyes does not bind to the fabric even after many cycles of fabrication and remain un-useful which discharge over the earth's surface and into natural water bodies like rivers and lakes, *etc* [11]. Approximately, 10-15% of the dye releases in the environment after the coloration process in the textile industries [12]. The long exposure of the dyes can be likely health hazards to the human being and they must be treated before release to the environment. Exposure of dyes can cause breathing problems due to the inhale of the dye molecules which affect the immune system of the human [13,14]. Other symptoms like itching, sore eyes, sneezing, coughing, and wheezing can also be the results of the impact of dye. On the other hand, in comparison with the other dyes, the anionic and cationic dyes can easily penetrate living body cells and can cause carcinogenic effects even at the low concentration [15]. The *congo red (CR)* and *methylene blue (MB)* are the two different classes of dyes belong to the anionic and the cationic family of the dyes respectively. Since the dyestuffs discharge

into the environment openly or release into water bodies therefore their particles are present in the environment near to their sources. Thereby, the migrated dye's particles in the environment can be inhaled and orally ingested into human beings causes serious health problems. For example, the inhalation of the *methylene blue (MB)* may give rise to the breathing problem while its oral consumption to the body may cause retching and initiate irritation, mental confusion, vomiting, perspiration, and methemoglobinemia [16]. *Congo red (CR)* is a diazo dye associated with benzidine which is a cancer-causing substance as declared by the *International Agency for Research on Cancer (IARC)*, *Department of Health and Human Services (DHHS)*, and *Environmental Protection Agency (EPA)* [17]. Therefore, *CR* is also known as a human carcinogen and toxic compound for animals and plants [18]. The toxicity of *Congo red* is primarily connected to its intermediary metabolites, which directly disturbed DNA and produce apoptosis in HL-60 cells (human promyelocytic leukemia cell line) [19]. Apart from dyes, *phenol and its derivatives* are also considered toxic to the human being if long term exposed. These cause mainly diarrhea, anorexia, vertigo, progressive weight loss, excessive salivation, dark colored urine, blood, and liver effects [20]. Knowing the bad impact of the dyes and toxic compounds on the human's life, plants, and animals, it is being crucial to eliminate the dyes from the wastewater prior to releasing into the environment.

#### **1.1.4 Use of dyes and management of its waste**

Industrial effluent is a big crisis all over the world as it contains metal complexes and dyes in high proportion [21,22]. The following industries such as the textile, paper and pulp, food, leather, pharmaceutical, pesticide, etc. have increased the use of synthetic dyes over the past years and continuing increasing due to the market demand of the items [23]. The cationic and anionic dyes are dedicated to dyeing acrylic fibers, polyester, nylon, polyacrylonitrile, paper, wool, silk, leather, cotton, etc [24]. In addition, the textile

industries release the waste at every step like printing, dyeing, and finishing. The released wastewater contains toxic heavy metals, high total dissolved solids (TDS), and non-biodegradable dyestuffs which demonstrate high chemical oxygen demands (COD) and biological oxygen demands (BOD) [11]. Moreover, the wastewater which is disposed into natural water bodies like rivers and lakes reduces the depth of sunlight penetration and results in to decrease in the photosynthesis process consequently decrease dissolved oxygen amount [25]. The contaminated and turbid water is harmful to the human being and the aquatic system. Several techniques are developed to treat the wastewater and reduced the contaminants dissolved in water before releasing into natural water resources. The different technologies are listed in Figure 1.2 [11].

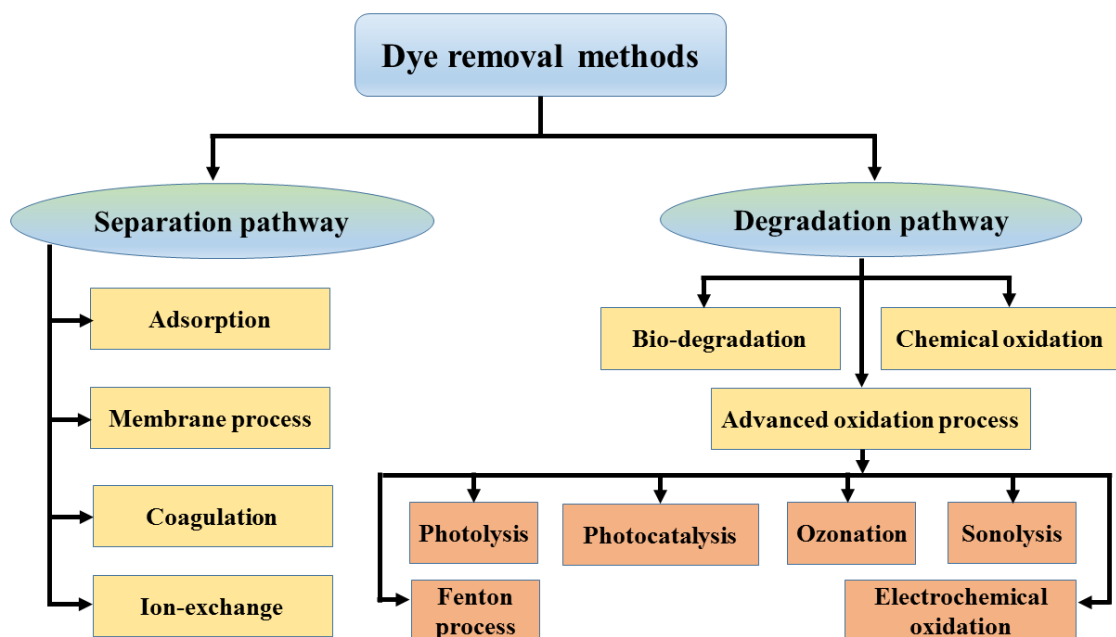


**Figure 1.2. Classification of various methods for dye treatment.**

Among various methods, the adsorption is considered simple and feasible for dye removal because of its high capacity and no secondary product results [25]. The adsorption process has been described in the next section.

#### 1.1.4.1 Adsorption

*Adsorption* is a dye treatment technique that defines when the molecules or ions in the solution or gaseous phase stick to the solid surface (porous surface as well) or rarely liquid through physical and chemical interaction [26]. The adsorbed molecular species are called ‘*adsorbate*’ while ‘*adsorbent*’ is the materials over which the adsorption occurs. While the reverse process is known as ‘*desorption*’ in which the adsorbate leaves the adsorbent under some conditions. The adsorption can be divided into three categories *physical adsorption (physisorption)*, *ion-exchange process*, and *chemical adsorption (chemisorption)* depending upon the force of interaction involved [27]. The adsorption is called physisorption if it occurs mainly due to physical interaction like *van der Waals forces* and *hydrogen bonding* between the adsorbate molecules and adsorbent surface [26,28]. In the physisorption mainly the adsorbate with the low energy hit the surface and this energy dissipated as the lattice vibration of the solids thereby the adsorbates adsorbs over the adsorbent [29]. On the other hand, if the molecules hit the adsorbent with high energy then the molecules with bounce back and will not stick to the surface [29]. The enthalpy of the physical adsorption is typically less than 20 kJ/mol which imparts no change in the chemical structure and does not form any new chemical bond [26]. The physisorption is highly liable which can revert easily. The multilayer adsorption results in physical adsorption until the adsorbate species are not shielded completely from the electrostatic potential of the adsorbent [26]. Of course, the enthalpy of the adsorption keeps continuously decreasing in the multilayer formation in physisorption.

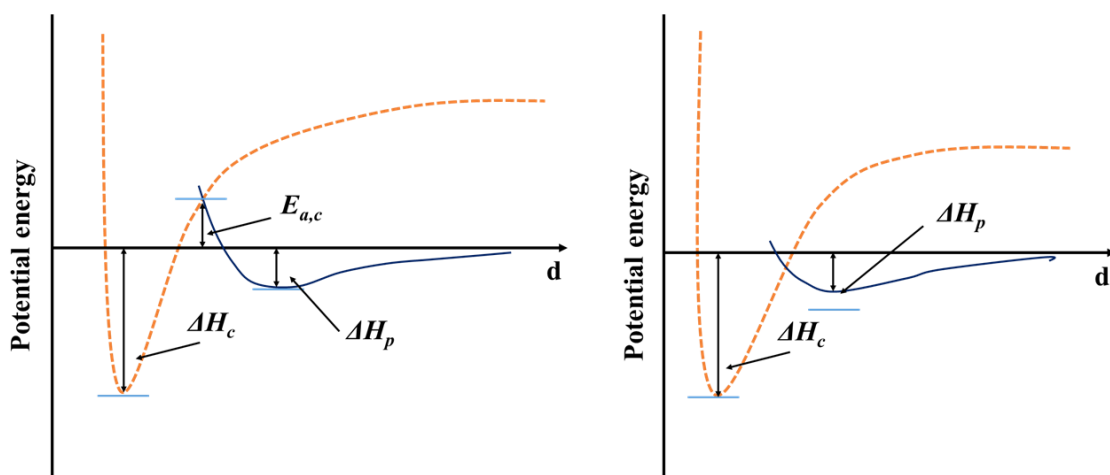


**Figure 1.3. The diagram for the energy of adsorption vs adsorbate's distance ( $d$ ) from the adsorbent; physisorption involving low enthalpy ( $\Delta H_p$ ) is represented by a solid line while chemisorption involving higher energy ( $\Delta H_c$ ) is depicted by a dashed line; and  $\Delta E_{a,c}$  is the activation energy required for the chemisorption.**

Contrary to the physical adsorption, the chemisorption results in new chemical bond formation between the adsorbent and adsorbate. Therefore, the change in enthalpy of chemisorption is in between -40 kJ/mol to -400 kJ/mol, and chemisorption is always a spontaneous process [26]. The chemisorption limits monolayer formation on the adsorbent's surface and restricts further adsorption if all the active sites are covered. Since the chemisorption is characterized by the real bonds (mostly covalent bonds) thereby, desorption is restricted at normal conditions and is an activated process. This is because desorption requires high energy for breaking the bonds to detach the molecules from the adsorbent's surface. The energy of adsorption vs distance ( $d$ ) of the adsorbate's particles from the adsorbent's surface has been depicted in Figure 1.3 [26]. Adsorption has been accepted as a green process for the removal of industrial pollutants as well as new emerging contamination [25]. Adsorption has proven a high uptake rate and minimum

secondary product. As the other chemical process, the adsorption is likely to influence by physical and chemical conditions such as temperature, pH, pressure, and redox conditions. As adsorption is a surface phenomenon so no doubt, it is more affected by the properties of the adsorbent's surface. The adsorption is more likely to occurs at porous materials where more surface sites are available resulting in a high uptake value [26].

#### 1.1.4.2 Adsorbent

The adsorbent is the materials that are capable of adsorption of foreign atoms, molecules, and ions by virtue of their surface properties.

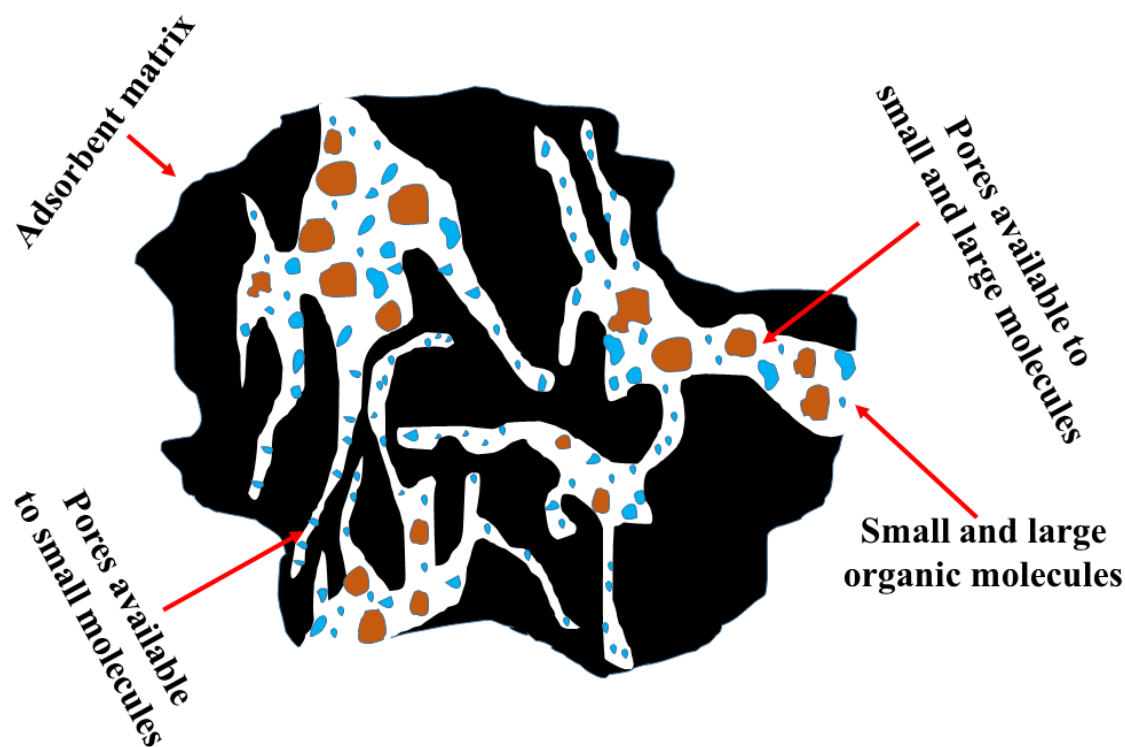


**Figure 1.4.** A schematic representation of an adsorbent with possible adsorption sites.

The surface of the adsorbent is more likely complex due to various kinds of pores and active sites that may exist in it. Figure 1.4 shows the matrix of the adsorbent where pores of different sizes have been shown. These pores are available for the adsorption of foreign

species of different sizes. The adsorbent molecules adsorb in the pores of the adsorbent. The pore sizes are classified into three categories as micropores (< 2 nm), mesopores (2-50 nm), and macropores (>50 nm) [30]. Besides the pores, the adsorbent is also characterized by the availability of active sites over the surface of the adsorbent. The active sites can be the atoms, molecules, or functional groups on the adsorbent's surface which have the capability of adsorption towards pollutant molecules. In addition to these, the surface charge of the adsorbent is an important factor in the adsorption process. The adsorbent with the opposite charge to their adsorbate is more active to adsorb due to electrostatic interaction. Therefore, complete knowledge of the nature of adsorbent help in deciding to choose the correct adsorbent for the adsorption process.

#### **1.1.4.3 Photocatalysis/Visible light photocatalysis**

Photocatalysis has been proven as an emerging tool for addressing water contaminants [10,31]. Photocatalysis accelerates in the presence of photocatalyst when exposing to the light for the remediation of the waste dyestuffs and contaminants [32,33]. Photocatalysis can be stated as the redox reaction in which oxidation and reduction process take place simultaneously in the presence of light [34]. Many researchers have reported tremendous photocatalysts but these are limited to the use of UV-Vis light energy. The shortcoming with the UV-Vis light is its low amount (4-7%) in the solar spectrum and can not harvest directly from the sunlight [35]. Therefore, researchers are seeking the solution in the visible light which is tremendously available in the solar spectrum and can be directly harvested. Because solar energy is an abundant renewable source of energy on the earth and can be harvested for carrying photocatalysis reaction where photonic energy converts into other forms of energy [36]. The percentage of the different radiation in the solar spectrum is depicted in Figure 1.5 [37]. The UV radiation is limited to 4-7 % in the solar spectrum therefore, the visible light photocatalysis has been widely attracted by the

researcher due to the availability of visible light in abundant amounts (40% to 45 %) in the solar spectrum [38]. Therefore, the term “*visible*” light photocatalysis is specifically used for the photocatalysis reaction if the visible light is being contributed. The photocatalytic reaction is already existing in nature as ‘photosynthesis by plants’, ‘photocatalysis by suspension’, ‘photocatalysis by microalgae’, and ‘photoelectrocatalysis’. The photocatalysis completes in four basic steps [33,39].

1. Electron-hole pairs generation in the photocatalyst after being exposed to the light.
2. Charge carriers separation where the electrons jump to the Conduction band (CB) and holes rest in the Valance band (VB).
3. The charge entities travel to the photocatalyst’s surface from their respective positions.
4. The charge carries react with the water and oxygen at the photocatalyst’s surface and forms hydroxyl radicals and superoxides ions by the redox reaction.

The bandgap of the semiconductor is the energy difference between the CB and VB, which is a vital property of the semiconductor. photocatalyst needs energy equal to bandgap energy to generate electrons and holes in CB and VB respectively [33]. The electrons and holes participate in the redox reaction occurring over the surface where electrons act as an oxidizing agent while holes as a reducing agent and they reduce and oxidize the compounds respectively [40]. The photogenerated charge carriers are short-lived and have a tendency of recombination on the surface’s sites or on the way to the surface [41]. Therefore, photocatalyst must migrate these charge carriers promptly to the surface before recombination and that can be achieved by nano-sized particles. Nevertheless, charge carriers recombine and lost the harvested energy as heat by a process called *non-radiative transition* or light emission which is known as *radiative transition* [40].

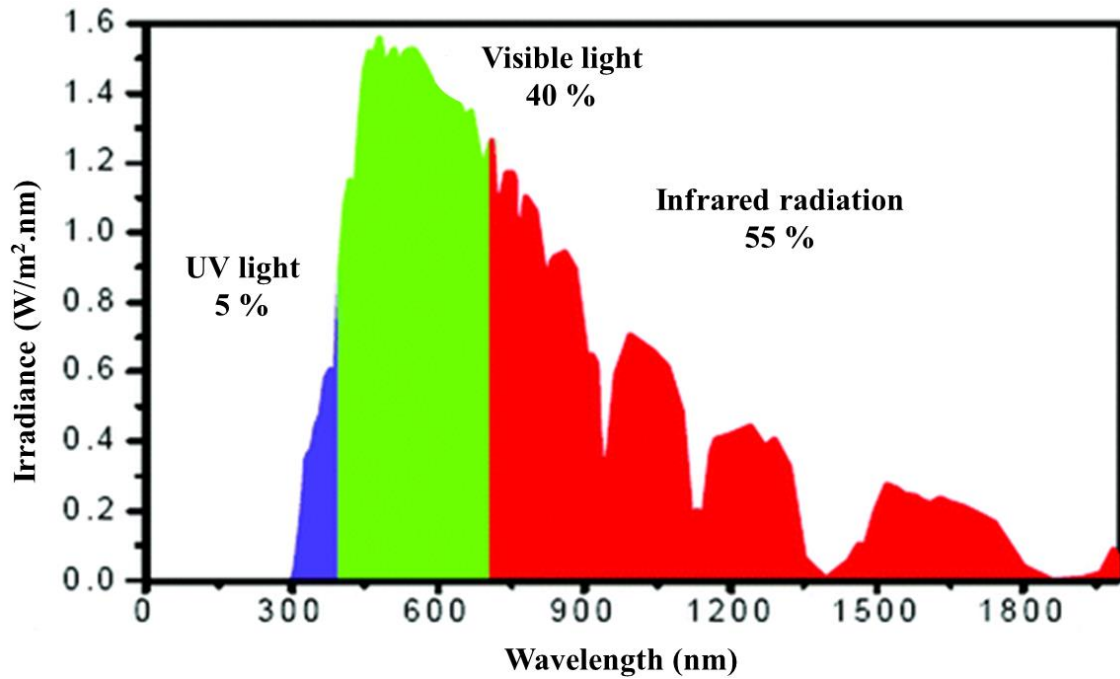


Figure 1.5. Distribution of solar energy spectrum according to the wavelength.

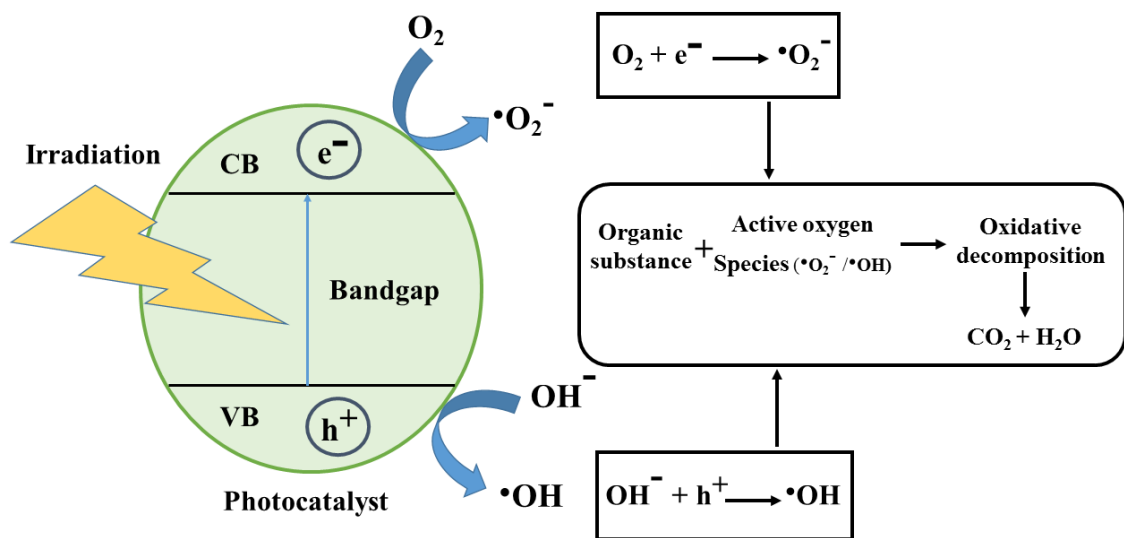


Figure 1.6. General mechanism of photocatalytic degradation of contaminants by a semiconductor photocatalyst.

The photocatalytic process is shown in Figure 1.6 [42]. The photogenerated electrons in CB react with available oxygen which produced oxygen superoxide while the holes into VB oxidizing the hydroxyl ions into hydroxyl radicals as represented in Figure 1.6 [42]. These superoxides and hydroxyl radicals have ample energy to break the pollutant's

molecules into complete mineralization [35]. Three processes are involved in the photocatalytic degradation of the pollutants such as oxidation, electron injection, and oxidation and reduction. Photocatalysis has a signature of the promising technology that has huge applications in the research area of water splitting, hydrogen generation, environment cleaning, water purification, air purification, water disinfection, elimination of several pollutants, and complete mineralization of the organic compounds, *etc* [43].

#### **1.1.4.4 Semiconductor photocatalyst**

Various semiconductors have been used as photocatalyst successfully in photocatalysis and other processes. These semiconductor photocatalysts are either be binary, ternary, or quadrilateral semiconductors. The types of ternary and binary semiconductors photocatalyst are represented in Figure 1.7 and Figure 1.8 respectively [43,44].

The photocatalysts with a d-transition metal are most studied semiconductor photocatalyst for the photocatalytic purpose for example  $\text{TiO}_2$ ,  $\text{ZnO}$ ,  $\text{Fe}_2\text{O}_3$ ,  $\text{V}_2\text{O}_5$ ,  $\text{ZrO}_2$ , and  $\text{WO}_3$ , etc. Among them, Degussa P-25 Titanium dioxide ( $\text{TiO}_2$ ) is a well-known photocatalyst due to its excellent photocatalytic activities. Since  $\text{TiO}_2$  owns properties such as high chemical stability, non-toxicity, relatively low cost, high oxidizing characteristics, and is environmentally safe, it has been established as a trusted photocatalyst [45].  $\text{TiO}_2$  is considered the most suitable photocatalyst for pollutant degradation due to its high oxidizing power in the UV-Vis range. Additionally,  $\text{ZnO}$  is the second most studied oxide photocatalyst after  $\text{TiO}_2$  due to its photochemical properties, low cost, and nontoxic nature. Even after they have compatible properties still both the photocatalyst ( $\text{TiO}_2$  and  $\text{ZnO}$ ) are limited to respond in the ultraviolet irradiation only because of their large bandgap (3.2 eV for  $\text{TiO}_2$  and 3.4 eV for  $\text{ZnO}$ ) [46,47]. But, the main objective of synthesizing the *binary* oxides such as  $\text{ZnTiO}_3$  is to develop photocatalysts that can harvest visible light from the solar spectrum, and even the poor

illumination can be sufficient to start photocatalysis. To overcome the wide bandgap of the semiconductors and to harvest the visible light, the researchers have modified the crystal structure of the materials also by doping, change in morphology of the materials, and preparing the heterostructure with the combination of two or more than two binary oxide semiconductors [48–51].

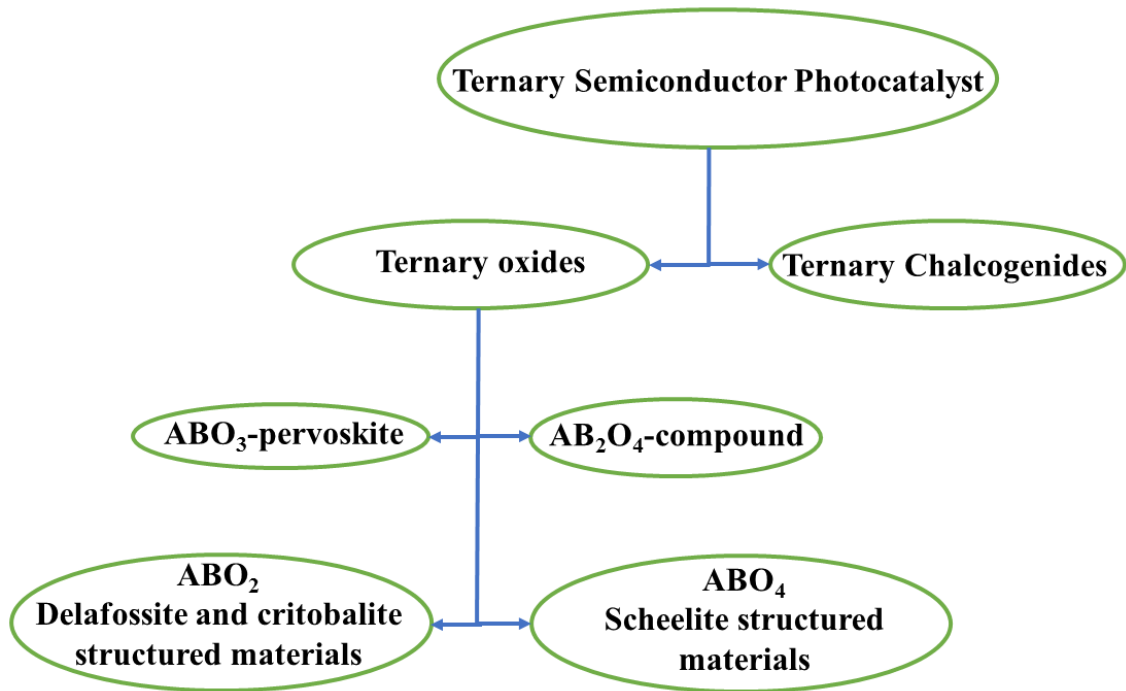


**Figure 1.7. Classification of ternary metal oxides semiconductor photocatalyst.**

In addition to this, Binary oxides are those which have two metallic/metal-like components. These are successfully utilized as photocatalyst for the degradation of organic pollutants under visible light irradiation. Various binary oxide catalysts seem to be potentially promising, since it is well-defined that binary oxide compounds often show higher catalytic activity and selectivity than what one can predict from the properties of their components [52]. Domen et al. showed that the photocatalytic activity of the SrTiO<sub>3</sub>-NiO compound is higher than the SrTiO<sub>3</sub> for the decomposition of water [53]. Bard et al. reported that the photocatalytic activity of ZnS.CdS/SiO<sub>2</sub> is higher than those of its component oxides for H<sub>2</sub> production [54]. Masakazu et al. presented that the

photocatalytic activity of TiO<sub>2</sub> in titanium-silicon oxides compound enhances photocatalytic reactions of alkenes and alkynes with water [52]. Similarly, many more researchers reported that the photocatalytic activity of TiO<sub>2</sub> remarkably increases when it forms binary compounds with ZnO, ZrO<sub>2</sub>, WO<sub>3</sub>, CeO<sub>2</sub>, Fe<sub>2</sub>O<sub>3</sub>, CdSe, etc [55]. It has been reported that binary oxide semiconductors seem to be attractive and feasible photocatalysts for the utilization of solar energy because of possibilities presented by inter-particle electron transfer, heterostructure, bandgap engineering, etc. [54]. As it is well established that the photocatalytic process is based on the generation and separation of electron-hole pairs by means of band-gap radiation [56]. It has been found that the binary oxide semiconductors play a crucial role in separating the generated charge carriers due to misalignment of the conduction band minimum and valance band maximum of the oxides components [57]. Consequently, the lifetime of the charge carriers increases therefore electrons and holes are available for a longer time for the redox reactions with the species adsorbed on the surface of the photocatalysts [56,58]. In principle, the binary oxide semiconductors are advantageous in order to absorb a wide range of solar radiation (UV and visible both) and to achieve a more efficient electron-hole pair separation, which results in higher photocatalytic activity [56,58].

Few properties are crucial for any materials for being a good photocatalyst as listed below.

1. The bandgap of the photocatalyst should be in the range 1.8 eV to 3.1 eV corresponds to the wavelength (400 nm to 700 nm) of visible light.
2. The maximum surface area of the photocatalyst.
3. Fast electron-hole pair separation.
4. The long lifetime of charge carriers.
5. Minimum recombination rate of the photogenerated charge carriers.

6. The CBM and VBM of the semiconductor should be appropriate to the band edge of the pollutant.

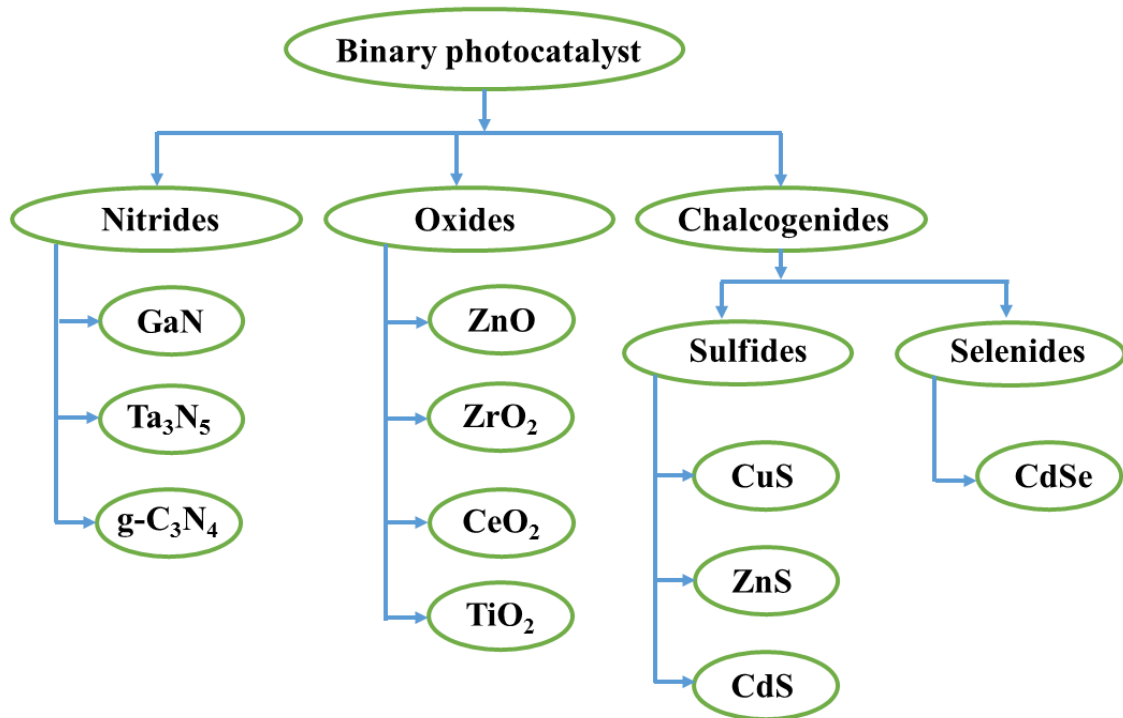


Figure 1.8. Classification of binary semiconductor photocatalyst.

## 1.2 Nanomaterials and their nanocomposites

### 1.2.1 Perovskite Structured materials

The Russian geologist ‘Count Lev Aleksevich von Perovski’ discovered the Perovskite structure of materials of the structural formula  $ABX_3$  [59]. Where  $A$  and  $B$  represent the cations and  $X$  denotes the anion. Cation  $A$  is bigger than cation  $B$ . The perovskite structure occurs in many sub crystal structures but the cubic crystal structure is considered as an ideal perovskite structure. The  $ABX_3$  forms a 3D crystal structure where 8 octahedra  $BX_6$  sitting on the corner of the structure centered  $A$ -cation. The  $A$ -cations are surrounded by 12 coordinated  $BX_3$  cavities and also by 12  $X$  anions whereas 6  $X$  anions are coordinated

to B-cations in the perovskite structure [60]. Figure 1.9 typically represents the cubic perovskite structure [61].

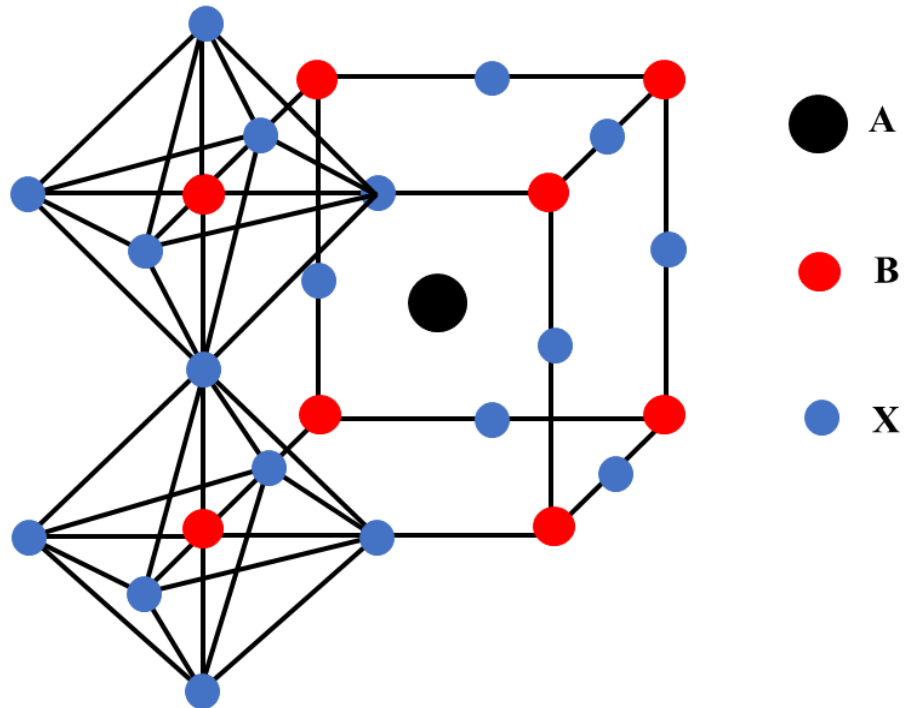


**Figure 1.9.** A schematic structural representation of ABO<sub>3</sub> type perovskite materials.

The following constancies are defining the perovskite crystal structure [62].

1. Tolerance factor ( $t$ ).
2. Octahedral factor
3. Ionic radii of A-cation and B-cation.

In 1926, Goldschmidt had proposed the idea of ‘**tolerance factor**’ to investigate the stability of the perovskite materials [63]. The tolerance factor ( $t$ ) is expressed in the below Equation (1-1).

$$t = \frac{r_A + r_B}{\sqrt{2}(r_B + r_X)} \quad (1-1)$$

Where  $r_A$ ,  $r_B$ , and  $r_C$  represent the ionic radii of the A-cation, B-cation, and C-anion respectively. Also, the perovskite structure is said to be an ideal if the bond length ratio between the bonds A-O and B-O is constant  $\sqrt{2}: 1$ . Roughly, if it is assumed that the sum of ionic radii is equal to the bond length then the tolerance factor will be 1. But, Goldschmidt found that the experimental value of the tolerance factor is between 0.815-0.965 somewhat smaller than 1 for perovskite structure [61,62]. However, for the distorted perovskite structure, the tolerance factor can be a wider range of  $t$ . Therefore, researchers have accepted the importance of tolerance factor ( $t$ ) to define the stability of the perovskite materials including oxides [61]. Apart from this, the stability of perovskite materials is not only defined by tolerance factor but one more factor known as octahedron factor is also recognized to define the stability and it is as much as important as tolerance factor [64]. The ratio of ionic radii of cation to the anion ( $r_B/r_X$ ) gives the value of the octahedron factor which lies in between 0.414-0.732. The third factor, ionic radii themselves use to calculate the stability of the perovskite  $ABX_3$  [64]. As perovskite and perovskite-type materials are sustainable at the high-temperature range, therefore, these are owing to various physical and chemical properties suitable for numerous applications [61,65]. Different theoretical schemes have been proposed to study the stability of the perovskite structures. Muller and Roy suggested a theoretical plot called “structural map” to study the stability of perovskite materials  $ABX_3$ ,  $A_2BX_4$ , and  $ABX_4$ . In that plot, Muller and Roy considered the ionic radii of A-cation and B-cation as the coordinate for the structural map [60]. The second model was proposed by Mooser and Pearson in 1959 based on the difference between the electronegativities of the cation and anion as well as the average principal quantum number [66]. Mooser and Pearson's model successfully discriminates between the different crystal structure type compounds for example AX, fluorides of  $ABX_3$ , and halides of  $AX_2$ .

### 1.2.1.1 Zinc titanate (ZnTiO<sub>3</sub>)

Zinc titanate (ZnTiO<sub>3</sub>: ZTO) is one of the family members of the ZnO-TiO<sub>2</sub> system [67]. Previously, only two compounds zinc orthotitanate (Zn<sub>2</sub>TiO<sub>4</sub>) and zinc metatitanate (ZnTiO<sub>3</sub>) were reported as the members of ZnO-TiO<sub>2</sub> family [67]. Later research (Lavy et. al.) shows the existence of three more zinc mesopentatitanate (Zn<sub>4</sub>Ti<sub>5</sub>O<sub>14</sub>), zinc orthodititanate (Zn<sub>3</sub>Ti<sub>2</sub>O<sub>7</sub>), and zinc paratitanate (ZnTi<sub>3</sub>O<sub>7</sub>) compounds in ZnO-TiO<sub>2</sub> family [67]. Therefore, so far, a total of five members in the ZnO-TiO<sub>2</sub> system have been discovered. However, experimental results show trivial confirmation of the formation of all five subtitanates. The ZnTiO<sub>3</sub> is one of the important material exists in two forms namely Cubic and Rhombohedral. ZnTiO<sub>3</sub> is a promising candidate in many areas such as paint pigment,[68] gas sensors [69], photocatalysis [70,71], a catalytic sorbent for the desulfurization of hot gases [72–75], lubricants [76], non-linear optics [77], luminescent materials [78], microwave dielectric [79], and microwave resonator [80]. Various synthesis processes such as sol-gel [81], hydrothermal methods [82], precipitation method [83], solid-state reactions [84], Pechini processes [85], sputtering [86], microwave heating [77], and physiochemical route [69], molten salt, *etc.*, methods have been widely adopted to synthesize ZnTiO<sub>3</sub> successfully. ZnTiO<sub>3</sub> was found to be a visible light photocatalyst (VLPC) and successfully degrade phenol and its derivatives dues to its physical and chemical properties in our previous research article and many others reported research articles [71]. The physicochemical properties such as the position of LUMO and HOMO, bandgap energy, carrier's lifetime, and low recombination rate of charge carriers are in the favor of ZTO to be the best visible light photocatalyst. ZnTiO<sub>3</sub> is an n-type semiconductor as reported previously [87].

### 1.2.1.2 Bismuth ferrite (BiFeO<sub>3</sub>)

Bismuth ferrite (BiFeO<sub>3</sub>: BFO) is a well-established single-phase multiferroic materials. Its temperature dependence of structure and magnetic order parameters: ferroelectricity, and antiferromagnetism (G-type) coexist at room temperature [88]. Its ferroelectric transition temperature ( $T_C$ ) is relatively high at 1100 K while antiferromagnetic transition temperature ( $T_N$ ) at around 643 K [88–90]. In recent years, numerous approaches have been used to synthesized BFO including sol-gel method [91], pulsed laser deposition [92], hydrothermal methods [93], electrospinning technique [94], solid-state reactions [95], microwaves hydrothermal reaction [96], magnetrons sputtering [97], and others [98]. BFO belongs to the rhombohedral distorted type perovskite structure of space group R3c [88,99]. The crystal structure of the BFO (rhombohedral perovskite structure) is distorted from the ideal perovskite structure because the octahedral BO<sub>6</sub> tilt around the *c* axis by a tilt angle  $\omega$  and the cations A and B are also dislocated from their ideal position [99]. The ferroelectricity and antiferromagnetism both are crucial properties of BFO which make it valuable in numerous applications. The origin of these properties is briefly explained. The displacement of cations A and B from their ideal position causes a positional imbalance in charges thereby an electric dipole moment generates which facilitates spontaneous electric polarization along one of the [111] axes in the BFO resulting in ferroelectricity at room temperature. The spontaneous polarization can switch into eight possible directions along the diagonals (both negative and positive) of the rhombohedral with angles 0°, 180°, 109°, and 71° [88]. On the other hand, G type antiferromagnetism is found in BFO which is due to the nearest Fe moments are aligned antiparallel to each other in all the cartesian direction. The antiferromagnetism in BFO arises due to the nearest Fe moments are aligned antiparallel to each other in all three

cartesian direction [100]. The tilt angle  $\omega$  is driven from the following Equation (1-2) [99].

$$\tan \omega = (4\sqrt{3})e \quad (1-2)$$

Where  $e$  is related to the rotation of an octahedron face about the triad axis [88,99].

## 1.2.2 Conducting polymers

### 1.2.2.1 Polyaniline (PANI)

PANI is conducting polymers that belong to the semi-flexible rod polymer family and is also known as ‘aniline black’[101]. PANI is a widely used conductive polymer due to its rich chemistry and ease of preparation, stability, and easily acid/base doped/dedoped properties [102]. It synthesizes mainly by the chemical oxidation polymerization or electrochemical polymerization of the aniline monomers and is found in three different oxidation states depending upon the preparation methods [101,103].

1. Leucoemeraldine

2. Emeraldine

3. Pernigraniline

Two forms of PANI are being synthesized know as emeraldine salt (ES) and emeraldine base (EB). The EB is neutral and being electrically conductive (ES) when doped with acid. The conductivity of the emeraldine salt increases with the level of acid doping in the insulating base [101,103,104]. The conductivity ( $\sigma$ ) of polyaniline rises from  $10^{-10}$  S/cm (EB form) to 1 S/cm (fully doped with acid, ES form) [103]. The conductivity of emeraldine salt can be tuned chemically or electrochemically by changing oxidation states. Chemically, the protonation of EB by acids results in ES [103]. Figure 1.10 represents the schemes of polyaniline in different oxidation states [101].

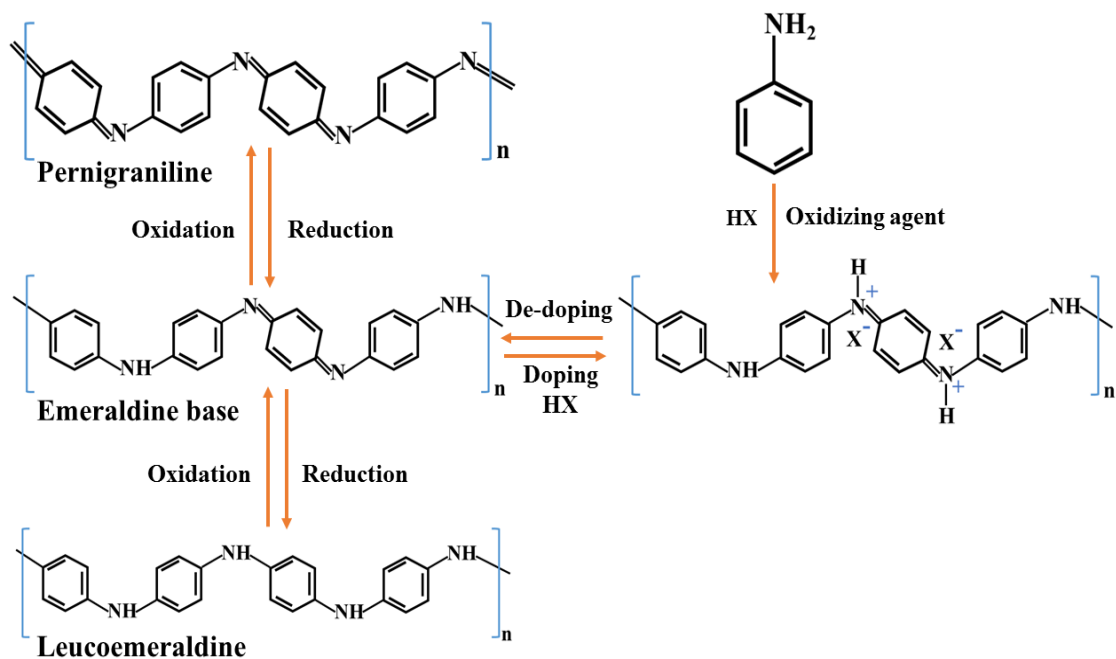


**Figure 1.10. Synthesis of polyaniline and its different forms.**

Polyaniline is known for its  $\text{sp}^2$  hybridization structure [105]. The backbone of the polyaniline has  $\pi$  conjugated chains which result in the delocalization of electrons along the entire chain. Consequently, polyaniline has special electrical properties [105]. The polyaniline is widely used in many areas of research such as sensors [106], batteries [107], fuel cell [108], adsorption [109], photocatalysis [110], and many more. The two forms of PANI can easily identify by observation as the EB is green color powder while the ES is a dark blue colored powder [111], The addition of PANI with other compounds, for example, metal oxides form the composites or heterostructures to assess its full potential towards the applications [112].

### 1.2.3 Heterostructured nanomaterials and their advantage

The combination of more than one nanocrystalline semiconductors led to the design of new heterostructure semiconductor materials. Heterostructured nanomaterials are

classified into five categories depending upon the type of materials used for heterostructure [35,43].

1. Metal/semimetal type heterojunction
2. Semimetal/insulator type heterojunction
3. Metal or semimetal/semiconductor type heterojunction
4. Semiconductor/semiconductor type heterojunction
5. Semiconductor/insulator type heterojunction

Among them, metal or semimetal/semiconductor and semiconductor/semiconductor type heterostructured nanomaterials gained much attention due to their advanced properties [113,114]. Besides the above heterojunction materials, the doped semiconductor (n-type or p-type) are also the other form of the heterostructure [115]. It is called isotype and anisotype depending upon the doping sides of host materials as the materials doped with the same or different materials respectively. The new heterostructured semiconductor materials recognize owing to their potential applications in water splitting, photocatalytic degradation of pollutants, adsorption, and others [43,116]. The two most important advantages result from the coupling of the semiconductors materials as underneath [43].

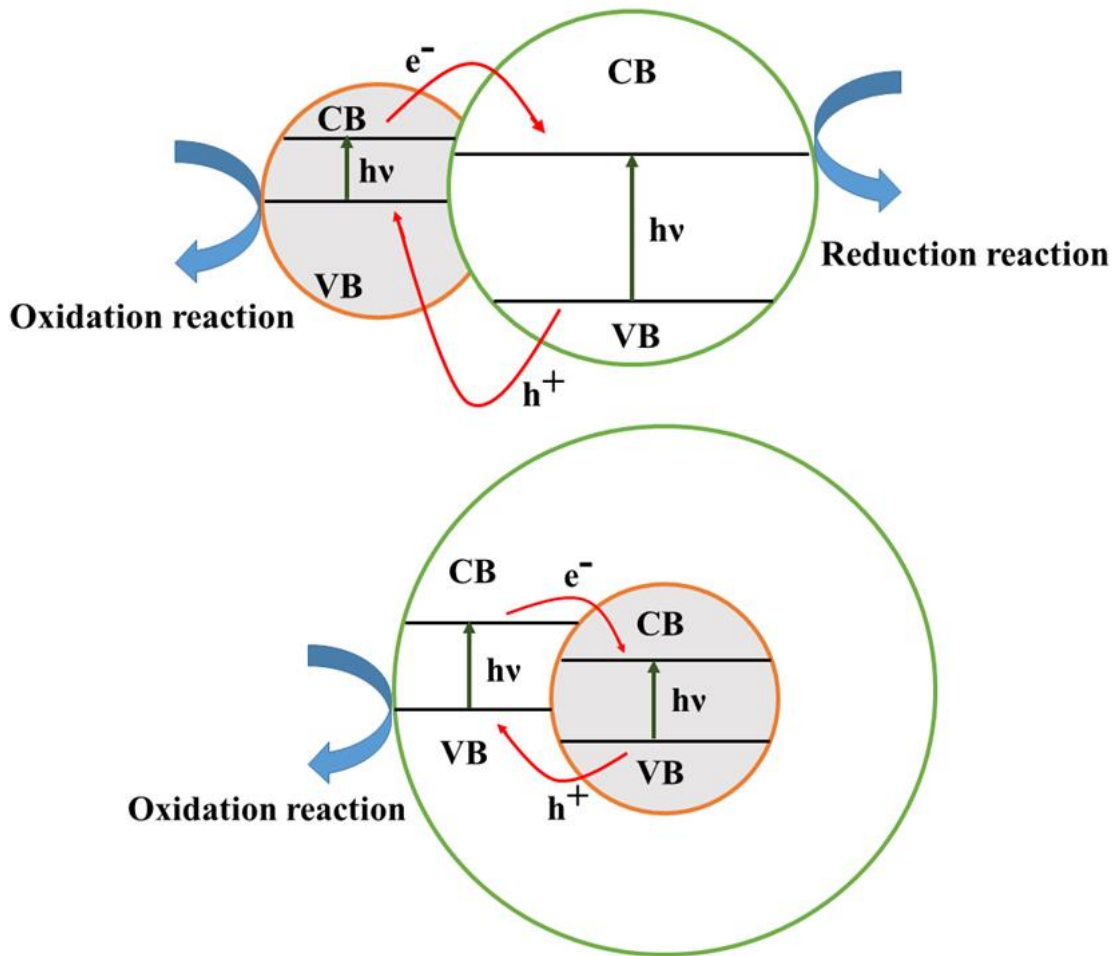


**Figure 1.11. Two basic type coupled and capped heterostructure semiconductor photocatalyst.**

1. Increases the photoresponse of the heterostructure by coupling large bandgap semiconductors to small bandgap semiconductors.
2. Decrease the recombination rate of the photogenerated electrons and holes by bypassing their direction of movement into CB and VB.

Figure 1.11 represents the two basic kinds of *capped* and *coupled* heterojunction configuration of the materials with the charge separation mechanism [116]. The charge separation mechanism is identical while the interfacial charge transfer mechanism is unlike in both the heterojunction materials [43]. In the coupled heterostructure as shown

in Figure 1.11(a), both the  $e^-$  and  $h^+$  are accessible at the semiconductor's surface thereby participating in the redox reaction [43]. In contrast to that, the capped heterojunction structure looks like a core-shell structure. The charge rectification occurs in capped heterojunction structure thereby only one kind of charged species is available for the redox reaction at the outer semiconductor's surface. Meanwhile, the other kind of charged species is getting trapped by the inner semiconductor [43].

#### **1.2.4 Electrospun nanofibers/nanowoven and their industrial applications**

The nanofibers have gained much interest in various applications due to their remarkable functional properties [117]. The electrospun nanofibers are advanced than their counterparts conventional fibrous due to their distinctive properties such as light-weight, small diameter, high porosity, controllable pore structure, appreciable mechanical strength, and high surface to volume ratio [117–119]. These properties make them unique for numerous applications. The nanofibers can be drawn from polymers and other materials with the help of polymers as guiding materials [120,121]. The size of the nanofibers varies from 1 nm to several nm depending upon the used polymers, processing methods, and other environmental conditions [122]. The nanofibers can be formed by natural or synthetic polymers [119]. Examples of natural polymers are gelatin, keratin, silk fibers, cellulose, collagen, and polysaccharides [117,119]. Meanwhile, the examples of synthetic polymers are polyvinyl alcohol (PVA), polyvinyl pyrrolidone (PVP), polyvinylidene fluoride (PVDF), polyvinyl chloride (PVC), polyvinyl acrylonitrile (PAN), *etc* [117,119]. The nanofibers have been made by various methods including electrospinning, template synthesis, drawing, self-assembly, and thermal-induced phase separation [123,124]. Among all the methods, electrospinning has attracted tremendous attention due to its advantages such as straight forwards setup, the capability of mass production of nanofibers from various polymers, mileage of forming ultrafine fibers with

the controllable diameter, easily tunable pore sizes and porosity, composition, and orientation of the nanofibers [117,118]. The electrospinning technology is flexible in producing different kinds of structures and morphology of the nanofibers such as nanoribbons, nanotubes, hollow nanofibers, solid nanofibers, nanobeads, core-shell nanofibers structures [125,126].

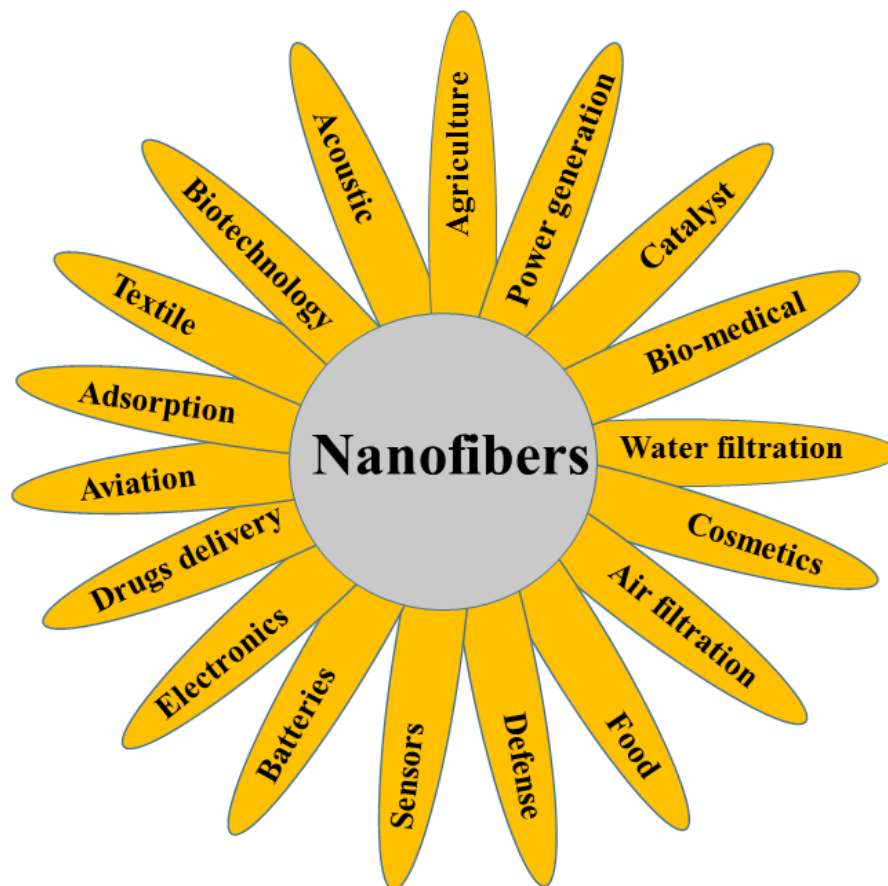


**Figure 1.12. Applications of electrospun nanofibers in numerous fields.**

Figure 1.12 depicts the application of nanofibers in different fields of industries, research, and technology. Few electrospun nanofibers examples are briefly described here. The electrospun nanofibers are commonly used in air filtration as a facemask, air purifier, vacuum cleaners, drug delivery, electrodes, *etc* [117,125,127–129]. Liu et al. reported that thin electrospun nanofibers were coated over metal mesh which could successfully

be used to accumulate more than 95% of PM<sub>0.25</sub> (Particulate matter 0.25) in a polluted environment area [130]. Further, the one-dimensional (1-D) nanofibers are used to prepare structures like a 2-D sheet and 3-D structures that have their significance in the applications [131]. Numerous studies previously proved that the electrospun nanofibers are in great use as photocatalyst because of their high surface area and porosity which enables tremendous reactive sites for the chemical reactions [71,132].

### **1.2.5 Doping**

In general, metal oxides are the most investigated materials as photocatalyst for environmental care applications by degrading pollutants on a large scale [133,134]. Metal oxides are characterized by their bandgap energy which makes them an appropriate material for photocatalytic degradation. The bandgap energy of the metal oxide semiconductors can range from UV to visible range of light [135]. The semiconductors that respond to UV light are called wide bandgap semiconductors. Since the UV light is only 4-7% in the solar spectrum therefore wide bandgap semiconductors are set their limit [136]. On the flip side, the availability of visible light in the solar spectrum opens the doors for new possibilities for the semiconductor photocatalyst. Therefore, new possibilities are to prepare the new visible-light photocatalyst as well as a lesson the bandgap of the wide bandgap semiconductors so that the longer wavelength of the solar spectrum can be harvested. Besides the wide bandgap, other shortcomings such as the high recombination rate of charge carriers, the short-lived lifetime of charge carriers, etc., restrict their use [35,135]. Many methods have been attempted to fix the above shortcomings. One of the methods called doping attracted the attention of the researcher. Doping is a process of adding a very small amount of foreign entities into the pure semiconductor materials (one dopant atom per  $1 \times 10^4$  to  $1 \times 10^8$  atoms of host semiconductor) [44]. Doping in the semiconductors is a vital approach to engineering the

various important properties of the semiconductor. A little amount of dopant can change the following properties of the semiconductor materials [135,137,138].

1. Narrowing the bandgap.
2. Addition of impurity energy levels and formation of oxygen vacancies.
3. Surface morphology, surface area, porosity, wettability, structure, and crystallinity.
4. Optical, electrical, and thermal properties.
5. Recombination rate of charge carriers, redox potential, and charge carriers mobility.

The dopants provide the new energy levels in between the bandgap of the SC which results in the narrowing of the bandgap [135]. Due to narrowing bandgap energy, a less amount of energy ( $h\nu$ ) is required to excite electrons and consequently create electron-hole pairs. It also helps to improve the trapping of electrons and consequently decreases the rate of recombination. Thus, overall, doping improves the photocatalytic reaction. Figure 1.13 represents the bandgap narrowing mechanism [39,137].

Both metal and non-metal atoms can be used as the dopant [44,135]. Metal doping can enhance photocatalytic activity either by a red-shift in the visible light absorption or modifying the potential of the photoexcited charge carriers [135,138]. Besides this, one of the shortcomings of thermal instability is always associated with metal doping [135,138]. Meanwhile, non-metal doping advances over metal doping as it can react with the metal-oxides in the following manners [139,140].

1. The dopant can hybridize with the oxides of SC.
2. The dopants substitute the oxygen sites which results in oxygen vacancies.
3. The addition of dopants at the oxygen-deficient sites acts as a blocker for reoxidation.

Thus, non-metal doping is more important as compare to metal doping. The non-metal doping also eliminates the possibility of thermal instability of the metal-doped SC [141].

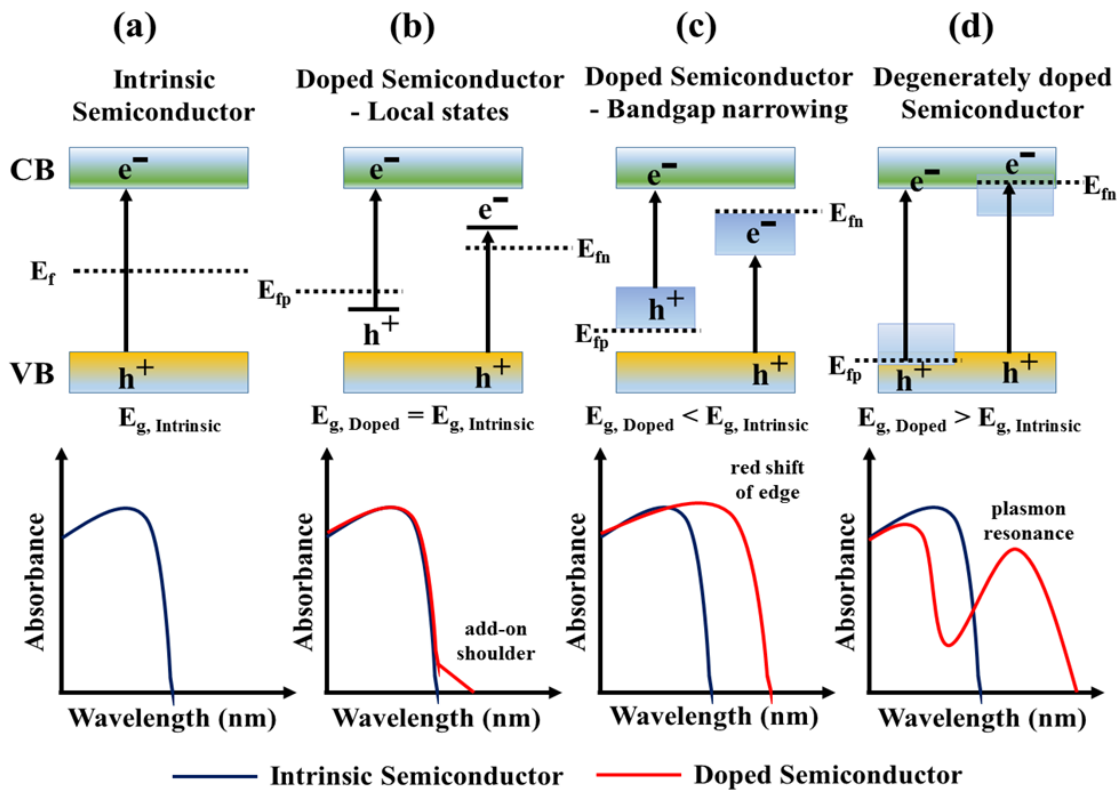


Figure 1.13. Mechanism of bandgap reduction in the doped semiconductor.

### 1.2.6 Rationale for selecting Zinc titanate and Bismuth ferrite

As we have already described the advantages and disadvantages of the  $\text{TiO}_2$  and  $\text{ZnO}$  as photocatalyst. The biggest disadvantage is that of a large bandgap (3.2 eV for  $\text{TiO}_2$  and 3.4 eV for  $\text{ZnO}$ ) due to which it is only active in UV irradiation. Our purpose is to harvest visible light for photocatalysis which is abundant on the earth. For that purpose, we have used a combination of the above two materials in the form of  $\text{ZnTiO}_3$  [142]. Also, in our earlier work, we have found the bandgap of  $\text{ZnTiO}_3$  prepared by the sol-electrospinning method to be 2.83 eV. Therefore ZTO is a promising material for visible light induced photocatalytic material overcoming the limitations in  $\text{ZnO}$  and  $\text{TiO}_2$ , and yet possessing

the best features of the two materials [71]. Besides this, ZTO offers a wide possibility of bandgap engineering by methods such as doping and by changing the morphology, so as to enhance its sensitivity to visible radiation. Many works of literature have reported that the lessening in the bandgap can be achieved by doping using metal and non-metal elements. However, non-metal doping is preferred due to its better thermal stability as compared to metal doping [143]. Picking this idea led us to further scaling down the bandgap energy by using nitrogen as a dopant. Since nitrogen is comparatively equal in size to oxygen therefore easily can replace oxygen in host materials and can be doped effectively. Hence, we have prepared nitrogen-doped zinc titanate by sol-gel and electrospinning technique. We have successfully degraded the phenol by nitrogen-doped zinc titanate in presence of visible light [144].

We have selected bismuth ferrite ( $\text{BiFeO}_3$ ) as another binary oxide material for visible light photocatalysis in my thesis work. In addition to being sensitive to visible light, bismuth ferrite is also has magnetic properties and the unit cell possesses a permanent dipole moment due to slight asymmetry in its structure [145,146]. Owing to its magnetic behaviour, in photocatalytic applications, it will be much easier to separate and recharge this catalyst after the reaction is over. Owing to its multiferroicity combined with its potential as a visible light catalyst, it is an attractive material to study. In this thesis, we have studied the effect of solvent on the catalyst prepared by solution route, in terms of its adsorption and catalytic behavior. We have prepared  $\text{BiFeO}_3$  with three different solvents DMSO, DMF, and THF. Interestingly, we have found that  $\text{BiFeO}_3$  synthesized in the DMSO as a solvent shows adsorption behavior towards methylene blue (MB) dye. Therefore, we continue with  $\text{BiFeO}_3$ . We have also modified the BFO nanoparticles by compositing it with polyaniline (PANI/BFO) which shows rapid adsorption behaviour towards congo red dye.”

### **1.2.7 Overall objective of the thesis**

Synthesis and characterization of zinc titanate particles and their applications in visible light induced photocatalytic degradation of environmental pollutants, specifically phenol.

- Nitrogen doping of zinc titanate for improving its photocatalytic performance.
- Synthesis and characterization of polyaniline-zinc titanate composite materials and its application as a highly adsorbent material for dye treatment in effluent wastewater.
- Study of effects of solvents used in the synthesis of bismuth ferrite, on its adsorption efficiency towards methylene blue.
- Synthesis and characterization of polyaniline-bismuth ferrite composites and its application as an adsorbent material for dye treatment.

# **Chapter 2: Synthesis methods and characterization technique**

## **2.1 Synthesis methods**

### **2.1.1 Sol-gel method**

The sol-gel method is a well-known synthetic approach to synthesize novel metal oxides, doped metal oxides as well as mixed composites nanomaterials [147]. The sol-gel method is subjected to three basic steps ‘hydrolysis’, ‘condensation’, and ‘drying (calcination)’ as listed below [148].

1. Sol formation: the hydrolysis of the metal precursors followed by the polycondensation process at room temperature.
2. Gel formation: the particles in the “sol” connecting in the three-dimensional networks in an aqueous medium.
3. Calcination or sinteration: the above products (gelation form) are calcined at a reasonable temperature so that the solvents evaporate and result in the final product.

The sol-gel is a quite versatile solution-based method useful in producing various kinds of shapes and microstructures of the materials [149]. For examples, the bulk materials synthesize by pouring the gelling sol into a matrix, the nanofibres of the viscous sol of the appropriate composition can be drawn by the electrospinning technology [150], the thin films of the sol can be fabricated by the spin coating or dip coating technology [77,151], membranes are prepared by pouring the sol onto porous oxides with coarse pores [147], and particles of different size distribution are prepared by simple control over the synthesis process by sol-gel method [152]. It is a simple method by which the properties of the materials can be engineered only just by changing its parameters such

as nature of the precursors, solvents, pH value of the medium, temperature, time of the reaction, reagent, concentration, catalyst nature, the addition of organic additives, gelation time, and calcination temperature during the reaction [153]. The sol-gel method is classified as 'aqueous' and 'non-aqueous' depending upon the solvent used. The aqueous sol-gel results if the water is taken as a solvent and non-aqueous sol-gel consists of organics as a solvent [154].

### **2.1.2 Electrospinning technique**

Electrospinning is a technique based on a *voltage-driven process* and governed by the *electrohydrodynamic* phenomena [119,155]. This technique is useful in producing the nanofibers and nanoparticles by polymeric solution and melt [119,155]. The electrospun nanofibers are advanced in their size and surface area as compared to the fibers produced by the other conventional techniques [119]. The most simple electrospinning setup consists of a source with a blunt needle or jet, a pump, a higher voltage power supply (several tens a DC voltage), and a collector. Electrospinning initiates when the repulsive forces between the charges (positive or negative) in the high electric field overcome the surface tension of the solution [156]. On applying high voltage, the solution droplets form a *Taylor cone* at the outlet of the jet [157]. The viscoelastic solution at the end of the Taylor cone stretches by the repulsive forces on the jet followed by the evaporation of the solvent led to the fabrication of fibers onto the collector [117]. The properties of the electrospun materials are significantly affected by electrospinning parameters and solution properties [122]. The parameters that affect electrospinning are solution feed rate, applied voltage, jet to collector distance, jet path, phases in electrospinning jet, nozzle diameter, electrospinning polarity, and speed of rotation of the drum [117,118,122]. While the solution properties that significantly affect electrospinning are the viscosity, concentration, conductivity/surface charge density, surface tension, solvent volatility,

solution temperature, the molecular weight of polymer, and solution phase transitions [118,158]. Currently, horizontal and vertical, two standard electrospinning setups are in utilization. Various nanostructures such as nanofibers, nanorods, nanoribbons, nanotubes, and nanoparticles, can be produced by this unique technique [71,159–162]. Time to time, modifications are done in basic electrospinning technique for example core-shell electrospinning technique, in order to enhance the properties and functionalities of the nanostructured materials [126,163]. In core-shell electrospinning, two unlike solutions are carried independently through the co-axial tubes to draw core-shell structured nanofibers. The core-shell electrospinning is found to be useful to make a different kind of core-shell nanostructures such as core-sheath nanofibers, hollow fibers, fibers from non-electrospinnable solutions, and microparticles encapsulated nanofibers [125,164–166]. Each different structure has led to a different application to enhance the functionalities of the materials and expands the scope of the electrospinning technique to meet the requirement of the next generation electrospun materials. Electrospinning nanotechnology is extensively used in various fields such as biomedical, environmental care, water filtration, air filtration, biotechnology, sensors, defence, catalysis, tissue engineering, and many more [121,122,171,125,159,160,162,167–170]. Thus, electrospinning is a simple, multipurpose, and cost-effective technique that produces non-woven fibers of high surface area to volume ratio, high porosity, and tunable porosity, *etc* [117]. These properties of the electrospinning technique make it a valuable technique in a wide range of applications.

### **2.1.3 Sol-electrospinning technique**

Sol-electrospinning technique is a rather forgiving technique to produce nanofibers of specific diameters and architectures of materials of choice [172,173]. This technique is widely used to prepare metal oxide nanomaterials with the help of spinnable polymers as

the guiding materials [172]. Sol-electrospinning technique is a combination of the sol-gel process and electrospinning process to prepare nanostructured materials of high surface area and high porosity. In the sol-electrospinning process, the precursor of the metal oxides is blended with a suitable polymer before electrospinning [120]. The addition of polymer into precursor provides necessary viscosity to the solution in order to make it spinnable [158].

Now, the solution is filled into a syringe and the syringe is being pumped at a very minimum flow rate (for example, 50  $\mu\text{L}/\text{min}$  to 1000  $\mu\text{L}/\text{min}$ ). The syringe to collector (counter-electrode) distance keeps constant around 10 cm (this is adjustable according to requirement). The positive potential is applied at the needle with respect to counter-electrode to maintain the high potential difference between them [117]. Adjusting the potential difference causes the change in fiber's diameters and morphology [122]. The high positive potential for example, of 10 kV is applied at the needle which led to creating a very strong electric field in between needle (source) and collector (counter-electrode). The solution starts to fabricate over the collector drum by the jet formation as the applied electric potential to overcome the surface tension of the droplets [156]. Once the jet is formed then it is an entanglement of the polymeric chains that prevent the dissection of the jet thereby maintaining the continuity of jet successfully led to the fabrication of electrospun materials[117].

#### **2.1.4 Chemical oxidative polymerization technique**

The chemical oxidative polymerization technique is a novel approach to synthesize polymeric products from various classes of monomers [174]. This technique is widely used to prepare conductive polymers such as polyaniline, polypyrrole, polythiophene, *etc* from their respective monomers [174,175]. Chemical polymerization of the monomers initiates in the presence of relatively strong oxidizing agents like permanganates,

ammonium peroxydisulfate (APS), bichromate ions, hydrogen peroxides, and ferric ions. The monomers used in the oxidative polymerization process are capable of pronounced electrons donate properties and high oxidation tendency [175,176]. The used monomers are oxidized in the presence of these strong oxidants and led to the formation of chemical active cation or radical cations in the appropriate solution [176]. The formed chemical active radical cations react back to the monomers in the solution results in the formation of oligomers or insoluble polymers [177]. In this way, the chemical oxidative process occurs continuously in the presence of strong oxidants in the bulk of the solution, yielding the resulting polymer as an insoluble solid [176]. It can be considered to the formation of a covalent bond between the monomer molecules at the expense of abstracting two protons [176]. Oxidative polymerization may have various kinds of linkage between the monomers. These linkages occur in the form of ‘head to head’, ‘head to tail’, and ‘tail to tail’, of active cations between the monomers during the polymerization [176].

## **2.2 Characterization Technique**

### **2.2.1 X-ray diffractogram (XRD)**

The X-ray powder diffraction analysis (XRD) is perhaps an extensively used analytical technique for characterizing materials. This technique is based on the phenomena of constructive interference of monochromatic X-rays [178]. X-rays are produced by the cathode ray tube which is further rectified by some means to produce a monochromatic X-ray beam, perfectly collimated, and exposed directly to the sample [178]. These X-rays interfere constructively after diffracted from the crystal’s plane and generate X-ray diffractograms [179]. The X-rays are diffracted from the crystal’s planes which follow Bragg’s law as given in the following Equation (2-1) [179].

$$2d \sin \theta = n\lambda \quad (2-1)$$

Where  $d$  denotes the interplanar spacing,  $\theta$  is the half of the diffraction angle,  $n$  is an integer that reflects the order of diffraction, and  $\lambda$  ( $1.54 \text{ \AA}$ ) represents the wavelength of the incident monochromatic X-ray beam. X-ray diffraction is shown in Figure 2.1.

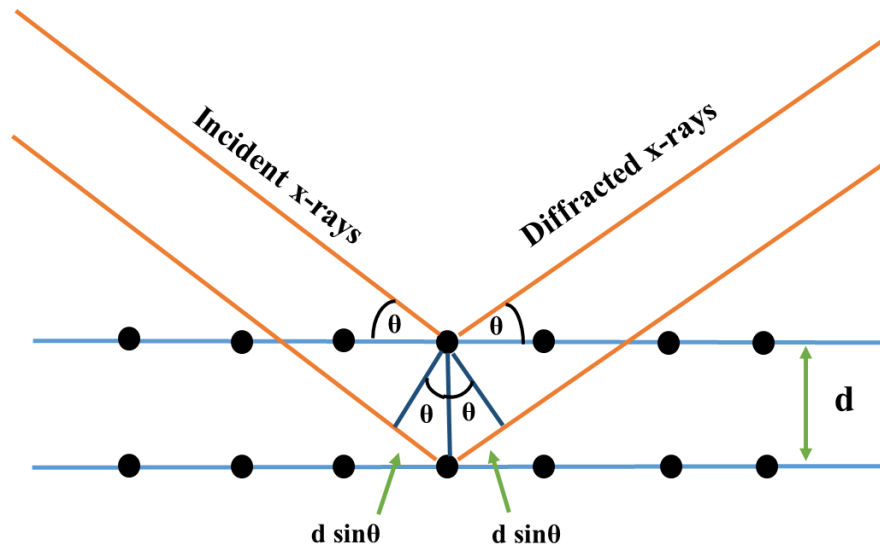


**Figure 2.1.** A schematic diagram of X-ray diffractogram (XRD) represents the diffraction of incident x-rays from parallel planes having atoms in a regular pattern.

The powder sample scans through the whole range of diffraction angle  $2\theta$  (typically  $5^\circ$  to  $90^\circ$ ). The detector collects all the possible diffraction peaks and counted them. The diffractogram plots the data intensity of diffracted peaks versus diffraction angle  $2\theta$ . The primary elements of the X-ray spectrometer are X-ray tube, a sample holder, and various detectors [178]. The X-ray beam of wavelength  $1.54 \text{ \AA}$  is produced by the Copper element.

Various important parameters can be investigated from the XRD pattern such as crystallite size, percentage of a particular phase of the materials, and microstrain in the sample [180–182].

The XRD technique is too important to analyze the strain-induced in the materials [182,183]. The XRD diffractogram can differ from the ideal sample in the terms of peak shifting and peak broadening according to the uniform and non-uniform strain-induced respectively [141,184,185]. The interstitials, substitution, dislocations, vacancies, and shear plans generate tensile and compressive forces in materials [141,184]. These tensile and compressive forces produce microstrain in the materials [186]. The microstrain-induced scheme is shown in Figure 2.2.

The application of XRD is widely found in various areas of research such as materials science, geology, environmental science, engineering, and biology to investigate the crystal structure of unknown materials and more.

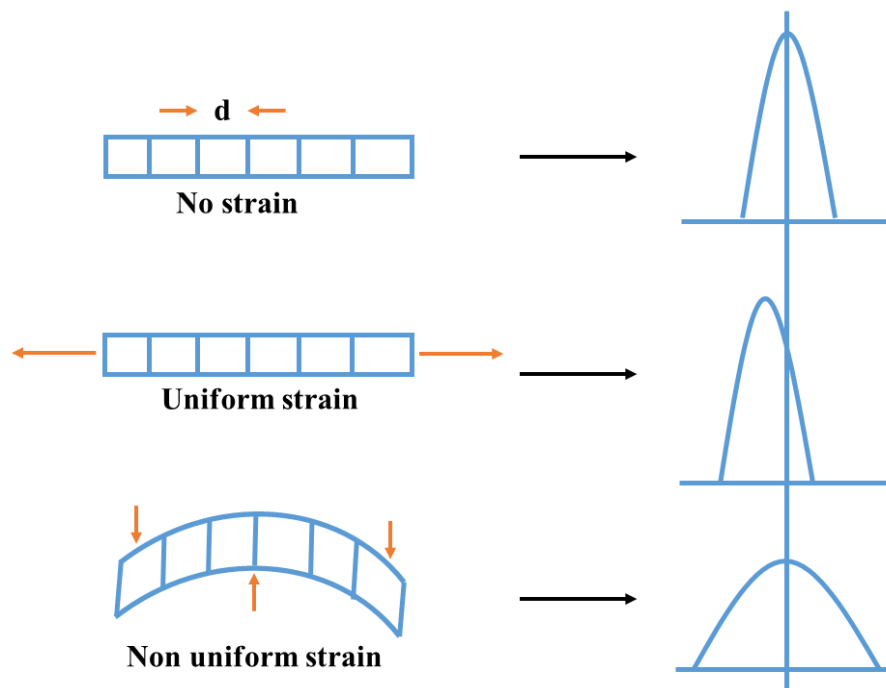


**Figure 2.2. Induced strain in the normal lattice changes the XRD pattern as represented.**

### **2.2.2 Fourier Transform Infrared (FTIR) spectroscopy**

FTIR is a widely used analytical technique to detect the functional (organic and inorganic) groups in the materials. FTIR is based on the Michelson Interferometer experiment where the vibrations in the molecules are detected after exposure to electromagnetic radiation [187]. The basic principle behind FTIR spectroscopy is that most of the molecules absorb infrared radiation (IR) which results in the vibrational motion of the bonds of the molecules [188]. The absorption of the IR radiation by a specific bond is the characteristic absorption of that bond [187]. The obtained IR spectra is analyzed between % Absorption or % Transmission versus wavenumber ( $400\text{ cm}^{-1}$  to  $4000\text{ cm}^{-1}$ ). The wavenumber is directly proportional to the energy of the IR radiation. All the molecules are not IR active irrespective of that, the molecules that have permanent dipole moment show FTIR spectra [43]. The basic IR spectrometer reads the samples in a complex, wave-like signal (called Interferogram) containing all the frequencies of vibration of the bonds [187]. The interferogram is a time-domain spectrum that changes into a frequency domain spectrum by a well-known Fourier transform operation. FTIR is a non-destructive technique that can use for any type of sample for example solids, liquids, gases, fibers, powders. The working of the FTIR is more advanced as it is associated with attenuated total reflectance (ATR) accessory equipped with ZnSe ATR crystal. FTIR spectroscopy is an extensively useful technique in many areas of research and industries.

### **2.2.3 Field Emission Scanning Electron Microscopy (FESEM)/ Energy-dispersive X-ray Spectroscopy (EDS)**

FESEM is an imaging technique used for the topographical analysis of the materials. FESEM uses the highly energetic electron beam to scan the surface of the specimen. A high accelerating voltage (0.1-30 kV) is applied at the cathode to generate an energetic electron beam [189]. The most important feature of FESEM images of their 3D

appearance because of its large depth of field [190]. In addition, the FESEM technique enables to provide a chemical composition and elemental analysis of the specimen when equipped with EDX (or EDS) [191]. A FESEM typically consists of a field emission electron gun, a series of electromagnetic lenses, condenser lenses, and one objective lens, various kinds of detectors, and a computer system [189]. The FESEM is useful to capture a highly magnified image of 1X to 500,000X and this magnification is the ratio of the linear size of the display to the linear size of the specimen scanned [190]. The image quality of the specimen is also associated with beam brightness which depends on the type of electron gun used [192]. The field emission gun has maximum brightness as compared to the tungsten thermionic gun (1000X) and LaB<sub>6</sub> thermionic gun (100X) [192]. When the high energetic electron beam strike over the sample's surface, it generates back-scattered electrons (BSEs) and scattered electrons (SEs) depends on the type of interaction: elastic scattering and inelastic scattering respectively [192]. Both SEs and BSEs are equally important for achieving topographical contrast and elemental composition contrast respectively [192]. When FESEM uses to scan a non-conductive sample then commonly the charging effect arising. In general, this is because of the gathering of static electric charges on the specimen surface. This results in many problems like blur image or swing of the sample. To overcome this problem, samples likely to be coated with gold coating. However, conductive samples are easily interpreted without prior gold coating.

#### **2.2.4 UV-Visible spectroscopy**

UV-Vis spectroscopy is the most popular and versatile analytical technique. This technique typically depends on the absorption of UV-Vis light by most of the molecules [193]. This technique works on the principle of Beer-Lambert law as given in Equation (2-2) [194].

$$A = \log \frac{I_0}{I} = \epsilon cl \quad (2-2)$$

Where  $A(\lambda)$  is absorbance,  $I_0$  and  $I$  are the intensity of the light incident upon sample cell and light leaving sample cell respectively,  $c$  ( $M = \text{mol dm}^{-3}$ ) is the solute's molar concentration,  $l$  is called the length of the sample cell in cm and  $\epsilon$  ( $M^{-1}\text{cm}^{-1}$ ) is known as molar absorptivity. As the name suggested, this technique scans the sample from the ultra-violet (UV) region (200 nm-400 nm) to the visible region (400 nm-700 nm). Generally, samples absorb this light energy and result in the UV-Vis spectrum. After absorbing energy by the molecules, the electrons promote from occupied orbitals of lower energy state (**HOMO**) to unoccupied orbitals of higher energy states (**LUMO**) [35]. The occupied orbitals are composed of  $\sigma$  orbitals,  $\pi$  orbitals, and nonbonding ( $n$ ) orbitals while the unoccupied orbitals are composed of antibonding orbitals ( $\pi^*$  and  $\sigma^*$ ) [35]. All transitions are not allowed between the orbitals but these are restricted by some selection rules. The allowed transitions must follow the conservation of the spin quantum number of electrons, if not, then the transition is called '**forbidden transition**' [35]. The UV-Vis spectrum generally records as a plot of absorbance ( $A$ ) (or Transmittance ( $T$ )) versus wavelength ( $\lambda$ ). The wavelength that corresponds to the highest absorption is referred to as the  $\lambda_{max}$  and this is a characteristic value of the specimen [35,193]. UV-Vis spectroscopy is crucial in the study of photocatalysis and adsorption because the kinetics of the reactions interprets by monitoring the concentration of the molecules.

### 2.2.5 Photoluminescence (PL) spectroscopy

The PL spectroscopy is a non-destructive and highly sensitive method to examine the electronic properties of the materials, especially in an excited state [35]. PL spectroscopy is a complementary technique to UV-Vis spectroscopy as it also provides electronic structural information from light excitation. The photoluminescence spectra obtain during the transition of the electrons from the excited state to the ground state [43]. During this

transition, the electrons emit extra energy that absorbed while jumping to an excited state from the ground state. This extra energy is used to plot PL spectra. Figure 2.3 depicts the basics of PL spectroscopy along with other phenomena [35]. PL is extensively used in the field of photocatalysis to study the rate of recombination of charge carriers indicating their lifetime. The intensity of PL spectra is proportional to the rate of recombination of the charge carriers. The fluorescence spectra obtain when the  $e^-$  from the CB recombine with the  $h^+$  in VB. Therefore, PL spectroscopy provides valuable information on the electron transfer kinetic in photocatalysis. PL is extensively useful for the determination of light-emitting materials, optical bandgap energy, detection of defects and impurity level, and study of recombination of charge carriers [43].

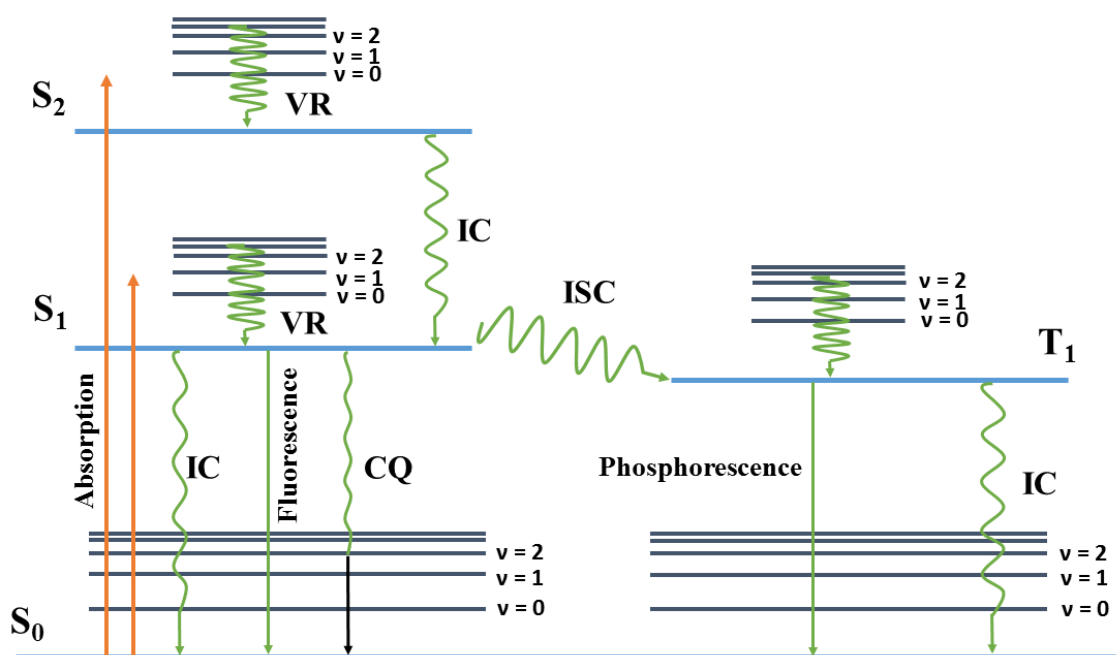


Figure 2.3. Jablonski diagram to define photoluminescence.

### 2.2.6 X-ray photoelectron spectroscopy (XPS)/ Auger electron spectroscopy (AES)

XPS and AES are the surfaces sensitive analytic techniques. XPS provides valuable quantitative and chemical state information of the sample under study [195]. XPS works on the phenomena of the ‘**photoelectric effect**’ in which the photoelectrons are emitted from the surface after absorbing incident radiation of suitable frequency [195]. Mg K $\alpha$  (1253.6 eV) and Al K $\alpha$  (1486.6 eV) cathodes are the two major sources for producing X-rays in XPS technique used for the analysis [43]. The XPS requires the ultra-high vacuum condition (UHV, pressure range: 10<sup>-8</sup> to 10<sup>-10</sup> mbar). The XPS is extensively used in the study of elemental compositional analysis of the sample. The obtained XPS data is compared with the standard database of the materials. The XPS directly calculates the kinetic energy of ejected photoelectron from the surface of the specimen by the X-ray radiation of constant energy  $h\nu$ . The kinetic energy of photoelectrons and X-ray radiation are connected by the following Equation (2-3) [43].

$$E_K = h\nu - E_{BE} - \phi \quad (2-3)$$

Where  $E_K$  is the K.E of the ejected photoelectrons,  $E_{BE}$  is known as the B.E of the electron in an orbital,  $h$  represents Plank’s constant,  $\nu$  is for the frequency of the incident radiation and  $\phi$  is known as the work function of the surface of materials. Typically, XPS spectra are plotted between counts/s (Intensity) versus binding energy. The photoelectrons are ejected from shells and subshells of different binding energy. The binding energy is used to identify an element as the binding energy of an atomic electron is a characteristic value for that element. The schematic representation of XPS and AES is given in Figure 2.4 [43].

In the AES technique, the highly energetic X-ray strikes on the inner shell’s electron ( $K$  shell) and knock out them [196]. The atom gets ionized and attained an excited state. This atom rapidly returns to its normal states by refilling the space by another shell’s electron

(for example L shell) [196]. Concurrently, this leads to the emission of an X-ray photon which imparts energy to the outer shell electron causes emission of Auger electron. The kinetic energy of an Auger electron is represented by the following Equation (2-4) [35]. Where  $E_{KL1L2,3}$  represents B.E of the Auger electron.  $E_{BK}$  is called B.E of the K shell electrons. Meanwhile,  $E_{BL1}$  and  $E_{BL2,3}$  represent the binding energy of the  $L_1$  and  $L_{2,3}$  subshells respectively.

$$E_{KL1L2,3} \approx E_{BK} - E_{BL1} - E_{BL2,3} \quad (2-4)$$

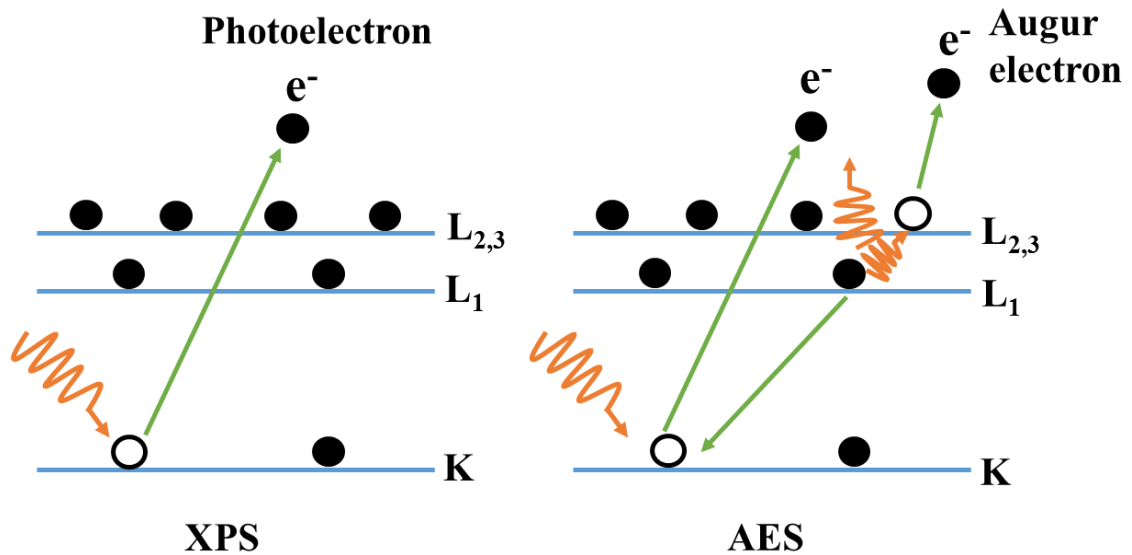


**Figure 2.4. Mechanism of photoelectron and Auger electron emission in XPS technique.**

### 2.2.7 Dynamic light scattering (DLS)

DLS is a valuable technique to find out the average size and size distribution of the nanoparticles in a colloidal system [197]. The surface charge of the nanoparticle so-called ‘Zeta potential’ is also measurable by this technique. DLS works on the principle

of ‘*Brownian motion*’ of the particles in colloids [195,197]. The solutes are in random motion in all directions and the motion depends on the size of the solute’s particles [197,198]. The small particles move faster than the bigger particles. The monochromatic light beam shining on the solution containing these particles executing Brownian motion causes scattering of the light thereby the light intensity changes. The intensity of scattered light depends on the particle’s velocity. The particles collide with each other during their random motion and transfer energy. This energy influences the motion of the particles. The hydrodynamic diameter of the particles can measure by using the Stokes-Einstein relation in Equation (2-5) [199].

$$D = \frac{k_B T}{6\pi\eta R_H} \quad (2-5)$$

Where  $D$  represents the translational diffusion constant,  $k_B$  is known as Boltzmann constant,  $T$  is the temperature. The viscosity of the solution represents by  $\eta$ , and  $R_H$  shows the hydrodynamic radius of the particle. The basic instrument of DLS is composed of monochromatic laser light, sample cell, and detectors [197]. The samples are illuminated in the monochromatic light and the light gets scattered by the particles present in the sample. The scattered light detects by the detectors at certain angles with time. The captured signals use to analyze the size of the particles. The surface charge of the particles (zeta potential) is also determined by this technique [195,200].

### **2.2.8 Thermogravimetric analysis (TGA)**

TGA is an important analytic technique used for the monitoring of change in mass of the sample in respect of the temperature at different times [201]. The Thermogravimetric Analyser or Thermobalance performs the TGA analysis. TGA uses a range of heat so that the thermal reaction can start and materials undergo physical changes, chemical changes, and thermal transitions. The thermal reaction in the TGA associates with the thermal

degradation of the materials thereby changes the materials' mass. The change in mass occurs due to decomposition, dehydration, and oxidation of the samples with temperature and time [202]. The TGA records the data at the uniform heating rate in a specific environment (air, N<sub>2</sub>, CO<sub>2</sub>, He, Ar, etc.) and the recorded data plots between the % mass (weight) loss or its derivatives versus temperature. This plot is known as the 'thermogravimetric curve' or 'thermogram'. The TGA provides information about the sample's thermal stability, the composition including volatiles such as water and solvents, thermal transitions of the materials, and inert additives or fillers [202]. In this technique, the mass loss is due to chemical reactions such as combustion whereas the physical changes such as melting do not contribute to the loss of mass [202,203]. Both mass gain and mass loss can be achieved by the TGA. The mass loss is due to the decomposition, reduction, evaporation, and desorption whereas the mass gain can be achieved due to adsorption, absorption, or oxidation of the materials in the specific environment [202].

### **2.2.9 Raman spectroscopy analysis**

Raman spectroscopy is an analytical technique based on the inelastic scattering process [204,205]. Raman spectroscopy uses the scattered light from the sample to measure the vibrational energy mode in a sample. Raman spectroscopy is indeed useful to obtain the chemical and structural information of the sample as well as provides the identification of the samples through their characteristic Raman 'fingerprints' [206]. The Raman fingerprints obtain through the detection of the Raman scattering from the sample. The Raman spectroscopy technique detects the vibrational modes of the molecules which involve a change in polarizability [205,206]. In this technique, the sample is excited by the monochromatic light source by different lasers. Raman spectroscopy uses lasers of different wavelengths ranging from UV-Vis to near IR including visible light [205]. The laser of the following wavelengths is used in the Raman spectroscopy; UV: 244 nm, 257

nm, 325 nm, 364 nm, Visible: 457 nm, 473 nm, 488 nm, 514 nm, 532 nm, 633 nm, 660 nm [205]. Raman technique detects scattered light from the samples versus the wavenumber shift. The scattered light is almost (~90%) having the same wavelength as the excitation source (Rayleigh or elastic scattering) [206]. However, scattered light of different wavelength detects in a very small fraction (~5-10%) other than the excitation light. This shift in the wavelength (wavenumber or frequency or energy) is called the Raman shift [205,206]. Raman shift is ascribed to the interaction between incident electromagnetic waves and vibrational energy levels in the molecules [43,205]. The Raman spectra of sample plots between the intensity of the Raman shift and frequency.

## **2.3 Materials and technical specifications of characterizing instruments**

### **2.3.1 Materials**

All the chemicals were of analytical grade and used without further purification. The zinc acetate dihydrate ( $\text{Zn}(\text{CH}_3\text{COOH})_2 \cdot 2\text{H}_2\text{O}$ : M.W = 219.50) was purchased from CDH Private Limited India. The tetrabutyl orthotitanate ( $\text{Ti}(\text{OC}_4\text{H}_9)_4$ : M.W = 340.32) was obtained from SRL Private Limited India. The acetic acid ( $\text{CH}_3\text{COOH}$ : M.W = 340.32) was obtained from HPLS Private Limited India. The cetyltrimethylammonium bromide (CTAB) ( $\text{C}_{19}\text{H}_{42}\text{BrN}$ : M.W = 364.45) and sulphuric acid ( $\text{H}_2\text{SO}_4$ : M.W = 98.07) were purchased from S D Fine Chem Limited India. The aniline ( $\text{C}_6\text{H}_5\text{NH}_2$ : M.W = 93.13) and potassium dichromate ( $\text{K}_2\text{Cr}_2\text{O}_7$ : M.W = 294.19) were obtained from the RFCL Private Limited and Merck Specialties Private Limited India. The bismuth nitrate pentahydrate ( $\text{Bi}(\text{NO}_3)_3 \cdot 5\text{H}_2\text{O}$ ) and ferric nitrate nonahydrate ( $\text{Fe}(\text{NO}_3)_3 \cdot 9\text{H}_2\text{O}$ ) were purchased from SRL Private Limited and RFCL Private Limited, India. Dimethyl sulfoxide and N, N-dimethyl formamide was purchased from Merck Specialties Private Limited, India. Tetrahydrofuran was purchased from Finar India.

### 2.3.2 Characterizing materials

Powder X-ray diffraction (XRD) data were collected from the prepared powder samples using a PANalytical X'pertpro MPD diffractometer with monochromatic Cu K $\alpha$  radiation ( $\lambda=1.54$  Å). The UV–Visible diffuse reflectance spectra were recorded in the range of 200 nm to 800 nm on an Agilent Cary 5000 UV–Vis–NIR spectrophotometer. Field Emission Scanning Electron Microscopy (FESEM) images of the calcined powder samples were taken by using a ZEISS/NOVA NANOSEM 450. The chemical composition was confirmed by elemental analysis on a ZEISS/NOVA NANOSEM 450 electron microscope equipped with an EDS analyzer. The thin gold coating was sputtered onto the samples to prevent charging prior to the analysis. The concentration of the phenol was evaluated during photocatalytic experiments by UV-Vis spectrophotometer (LAB INDIA Spectrometer). The Perkin Elmer Spectrum FT-IR spectrometer was used to record the FT-IR spectra of the samples as either solid or thin-film using with “attenuated total reflectance” (ATR) mode. The PIKE MIRacle single reflection horizontal ATR accessory equipped with a ZnSe ATR crystal was used for recording the FT-IR spectra. For Photoluminescence (PL), all the calcined powder samples were dispersed in DI-water and sonicated it for 15 min at room temperature, then the residue was collected for investigation. Steady-state PL spectra were recorded on a Varian Cary Eclipse fluorescence spectrophotometer with a Peltier temperature controller. The PL data was obtained by using excitation wavelength at 260 nm at room temperature. All the Raman spectra were recorded using an alpha 300 RA equipped with a diode laser for 532 nm excitation. The BET surface area analysis was performed by Micromeritics Flex 3 BET analyzer. The particle size calculation and zeta potential of the particles were examined by Zetasizer (model: Zetasizer Nano ZS) of Malvern Panalytical. The XPS measurements were performed on a PHI 5000 Versa Prob spectrometer with Al K $\alpha$  X-ray anode. The

binding energy correction was performed by using the C 1s peak of carbon at 284.6 eV as a reference peak. The electrospinning setup supplied by E-Spin Nanotech, India, consists of a spinneret, pump system, a high positive voltage power supply, and a grounded rotating drum collector, all arranged in a horizontal geometry. All the calcined powders samples have been used for the characterization in powder form.

## Chapter 3: Comparing the photocatalytic property of zinc titanate nanorods and nanoparticles.

### 3.1 Abstract

Aiming of the present work is to synthesized efficient photocatalyst that can harvest visible light for photocatalytic degradation of pollutants. Metal oxides photocatalyst of different geometry and shapes have proven their enhanced photocatalytic activity towards pollutant degradation in the presence of visible light. In this order, the current research has pursued the formation of electrospun zinc titanate nanorods and their application in the *visible light* photocatalytic degradation of the phenol. The degradation rate constant ( $k$ ) has been compared with their counterparts of bulk zinc titanate nanoparticles prepared by the sol-gel method. The comparison has proven that the degradation rate constant ( $k$ ) has been increased to  $0.01065 \text{ min}^{-1}$  in the presence of zinc titanate nanorods than by bulk zinc titanate ( $0.00330 \text{ min}^{-1}$ ). A series of experiments have been performed to characterize the materials and to reach a conclusion of enhanced photocatalytic activity of electrospun zinc titanate nanorods. The XRD and FESEM data have suggested the nanocrystalline nature of electrospun zinc titanate nanorods. The nanocrystalline nature of the electrospun zinc titanate nanorods induces quantum effect. The XPS, DRS, and PL suggest the surface states onto zinc titanate nanorods. They may lead to the capturing of excited electrons thereby decreasing the recombination rate of photo-generated charge carriers signifying enhanced photocatalytic activity.

**Keywords:** Electrospinning, zinc titanate nanorods, visible light photocatalysis, phenol degradation, quantum size effect.

## 3.2 Introduction

Electrospinning is an extensively used technique to fabricates the materials of various geometry, morphologies, and shapes [207]. The ceramic, polymers, gels, *etc* can be fabricated from the starting materials and electrospun materials show exceptional properties as compared to their bulk counterparts. Several varieties of materials of different morphologies and dimensionalities such as zero-dimensional (0D), one dimension (1D), two dimensional (2D), and three dimensional (3D) have been prepared by the electrospinning route [117]. Various nanostructures such as nanofibers, nanorods, nanoribbons, nanotubes, and nanoparticles, can be produced by this unique technique [71,160–162]. The properties and applications of various structured electrospun materials are broadly discovered in photocatalysis of pollutants [132], adsorption, drug delivery [208], membrane technology [209], air filtration, electronics [210], sensors [211], biomedical [212], *etc*. The sol-electrospinning is succeeded one step ahead then the electrospinning technique in order to get a nanofibrous structure of ceramic metal oxides. Sol-electrospinning technique is a combination of the sol-gel process and electrospinning process to prepare nanostructured materials of high surface area and high porosity [213]. In the sol-electrospinning process, the precursor of the metal oxides is blended with a suitable polymer before electrospinning [120]. The addition of polymer into the precursor provides necessary viscosity to the solution to make it spinnable [158].

Nowadays extremely uses of fossil fuels, textiles, paper, pesticides, *etc*. causes environmental pollutions such as water pollution and air pollution [214]. The increasing pollution level is a matter of public concern. Photocatalysis is considered one of the environmental remediations for the complete degradation of toxic contaminants present in water pollution and identified as an emerging technology for wastewater treatment

[215].  $\text{TiO}_2$  and  $\text{ZnO}$  both are considered a promising candidate as photocatalyst because of their exciting properties such as inexpensive, nontoxic, environmentally friendly, higher quantum efficiency, and high efficiency of contaminant degradation under UV-Vis light [46,143]. Having good properties still both  $\text{TiO}_2$  and  $\text{ZnO}$  are limited in their use as photocatalyst because of the following shortcomings [46,47].  $\text{TiO}_2$  and  $\text{ZnO}$  are wideband gap semiconductors of bandgap energy larger than 3 eV, therefore these are insufficient to harvest visible light for photocatalysis which limited their use to UV light only. Massive recombination of the photogenerated electrons and holes is also leading to the lower photocatalytic activity. Therefore, it is crucial to overcome these shortcomings of both semiconductors. This has been achieved by preparing mixed metal oxides of Zn and Ti such as zinc titanate ( $\text{ZnTiO}_3$ ).

Alloying of the  $\text{ZnO}$  and  $\text{TiO}_2$  advantage over their neat form separately in terms of their structural disadvantage and bandgap energy [216].  $\text{ZnTiO}_3$  has been considered as an emerging material for a variety of applications such as visible light photocatalysis [71], gas sensors [69], lubricants [76], luminescent materials [78], microwave dielectric [79], photochemical water splitting [217], *etc.* In the previous study, we prepared the bulk  $\text{ZnTiO}_3$  and electrospun  $\text{ZnTiO}_3$  [71]. The bulk  $\text{ZnTiO}_3$  was prepared by the sol-gel method while electrospun  $\text{ZnTiO}_3$  was prepared by the sol-electrospinning method. We investigated the bandgap energy of the bulk  $\text{ZnTiO}_3$  and electrospun  $\text{ZnTiO}_3$  was 2.90 eV and 2.80 eV respectively. The obtained bandgap energy was at the onset of visible light which is much better than the bandgap energy of  $\text{ZnO}$  and  $\text{TiO}_2$ . Due to lower bandgap energy, we showed the improved visible-light photocatalytic degradation of phenol. Polyvinyl alcohol (PVA) was used as a guiding polymer for the electrospinning of the  $\text{ZnTiO}_3$  sol. The as-spun  $\text{ZnTiO}_3$  sample showed nanofibrous structure meanwhile after

calcination nanofibrous structure could not retain and nanoparticles of electrospun ZnTiO<sub>3</sub> were obtained.

In the present study, ZnTiO<sub>3</sub> has been fabricated by the sol-electrospinning technique. The polyvinylpyrrolidone (PVP) has been used as the guiding polymer to assist in the fabrication during electrospinning by providing the required viscosity to the electrospinnable solution. We discovered that the as-spun ZnTiO<sub>3</sub> mat shows the nanofibrous structure. Meanwhile, after calcination, the nanofibers structures transform into ZnTiO<sub>3</sub> nanorods. The ZnTiO<sub>3</sub> nanorods have been focused in this study and their visible-light photocatalytic study towards phenol degradation has been evaluated. The present study of ZnTiO<sub>3</sub> nanorods has been compared with the previously reported bulk ZnTiO<sub>3</sub> nanoparticles.

### **3.3 Experimental section**

#### **3.3.1 Synthesis of bulk zinc titanate (BZT)**

BZT was prepared by the aqueous sol-gel route as represented in Figure 4.1. The titanium tetrabutyl orthotitanate (3.40 mL) was mixed with acetic acid (6.66 mL) under mild stirring for 30 minutes at room temperature (RT). A viscous, homogeneous, and white-colored solution was obtained. Thereafter, zinc acetate dihydrate (2.25 g) was added to the above solution while maintaining experimental conditions. The above mixture was further added with 10 mL DI-water resulting in a transparent and homogeneous solution. Now the temperature of the reaction increased to 50 °C and continue stirring for one hour. After one hour the temperature of the reaction and stirring was interrupted and obtained sol of zinc titanate was cooled to RT. Then, the above sol of zinc titanate was kept for several hours for gelation within the sol at RT. After that, the resultant was kept for sintering at 800 °C for 8 hours in an air furnace. The resultant

materials were crushed in a mortar pestle to make it fine powder called bulk zinc titanate (BZT).

### 3.3.2 Synthesis of electrospun zinc titanate (EZT)

The EZT was prepared by the sol-electrospinning method. The sol-electrospinning method is a combination of two consecutive processes (a) preparation of sol and (b) its electrospinning. Zinc titanate sol was prepared by the above method for BZT and succeeded by electrospinning.

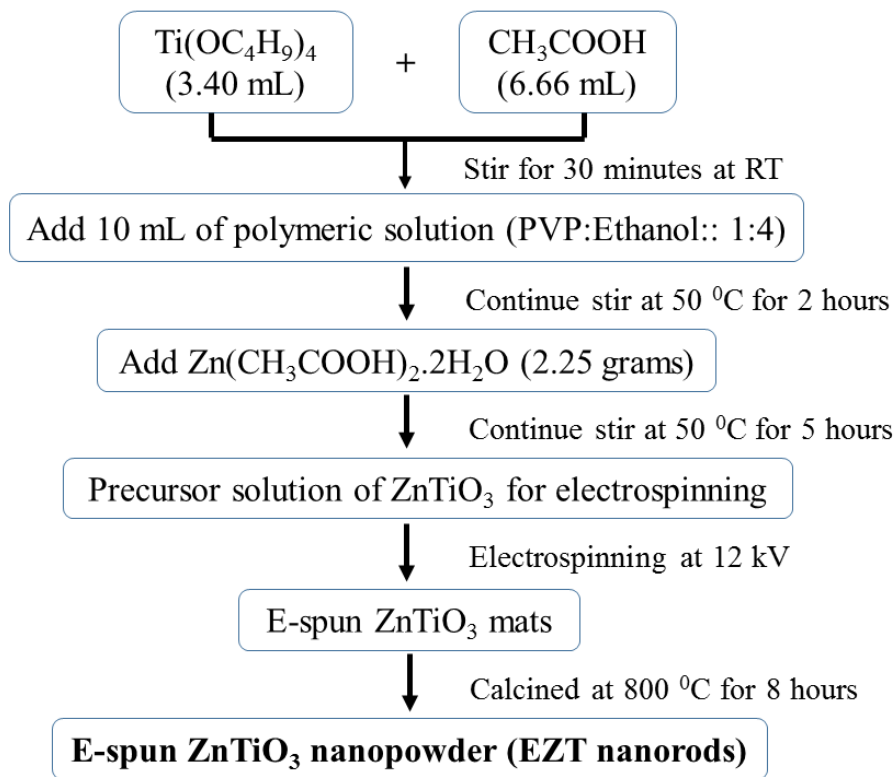


**Figure 3.1. Schematic representation of synthesis process of electrospun zinc titanate (EZT).**

The guiding polymer for electrospinning was prepared by the mixing of polyvinylpyrrolidone (PVP) and ethanol in a ratio of 1:4 at RT for one hour. The viscous polymeric solution was obtained and used in the synthesis process of sol of zinc titanate as follows. The 10 mL polymeric solution was used in the solution of tetrabutyl orthotitanate and acetic acid as defined in the above section at  $50\text{ }^\circ\text{C}$  under continuous

stirring for 2 hours for proper mixing. Then 2.25 g of zinc acetate dihydrate was added and the reaction was continued for the next 5 hours in order to get well mixing. The obtained sol was viscous and white-colored appeared. The precursor polymeric solution of zinc titanate was loaded into a 10 mL plastic syringe. The positive voltage of 12 kV was applied to the metallic needle of the syringe considering it as a positive electrode. The distance between the tip of the needle and the collector was fixed at 10 cm. A sufficient amount of polymeric zinc titanate sol was fabricated onto aluminum foil so that a thick electrospun mat can be peeled out. This electrospun mat was calcined at 900 °C for 8 hours in an air furnace. The resultant was crushed to get white fine power named electrospun zinc titanate (EZT). The synthesis process is best described in Figure 3.1.

### **3.3.3 Laboratory set-up for measuring the photocatalytic activity of ZnTiO<sub>3</sub> nanorods**

The photocatalytic reaction was conducted in a lab-made setup as represented in Figure 3.2. A double-walled glass chamber (made by borosilicate glass) was taken which connected with the chiller instrument. The chiller was used to maintain the temperature by circulating the normal water in the glass chamber during the photocatalytic process. An incandescent bulb of 100 watts was utilized as a visible light source. The distance between the glass chamber and the incandescent bulb was fixed at 15 cm. Phenol was chosen as the targeted pollutant. An aqueous solution of 100 µM phenol concentration was prepared and used for studying the photocatalytic activity of ZnTiO<sub>3</sub> nanorods/nanoparticles under visible light. 100 mg of prepared ZnTiO<sub>3</sub> nanorods/nanoparticles was taken as the photocatalyst. The aqueous solution of phenol was under continuous stirring in the presence of photocatalyst while exposing visible light to examine photocatalytic activity. Each time 2 mL of solution was taken out from the glass chamber. This solution was centrifuged so that photocatalyst gets settled.

Thereafter, the supernatant was taken and examined by UV-Vis spectroscopy. The UV-Vis spectroscopy recorded two peaks of phenol at 210 nm and 270 nm corresponding to the  $\pi$ - $\pi^*$  and  $n$ - $\pi^*$  transitions respectively. Both the peaks were monitored during photocatalysis and their absorption intensity was recorded. The concentration of the remnant phenol in the solution after 30 min was recorded and plotted against the wavelength. The photocatalytic activity was found by using the first-order kinetic equation.

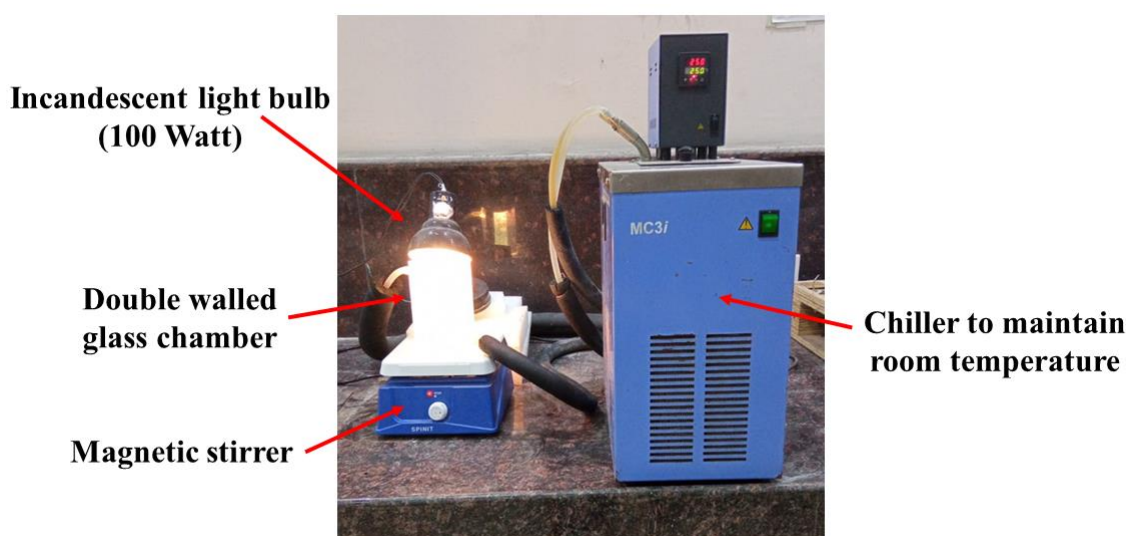


**Figure 3.2. Laboratory set-up for photocatalytic degradation of contaminants.**

## **3.4 Results and discussion**

### **3.4.1 Field emission scanning electron microscopy (FESEM)**

The surface morphology of BZT and EZT is depicted in Figure 3.3. All the micrographs have been captured at a magnification of nearly 7 kX. Figure 3.3a represents the micrograph of BZT suggesting the size of the nanoparticles in the range of 100 nm to 200 nm. It can be also noticed that the nanoparticles are highly aggregated and forming flake-like structure. The flake-like structures are visible in presenting the micrograph in Figure 3.3a. Figure 3.3b represents the surface morphology of the as-spun mat of ZnTiO<sub>3</sub>. The porosity in the as-spun mat of ZnTiO<sub>3</sub> can be seen in Figure 3.3b. Figure reveals the

nanofibers of as-spun  $\text{ZnTiO}_3$  are very smooth and their diameter can be calculated from 100 nm to 500 nm, meanwhile the length of nanofibers is several  $\mu\text{m}$ . The diameter of few nanofibers is nearly 1  $\mu\text{m}$  as can be seen in as-spun  $\text{ZnTiO}_3$  and the nanofibers are randomly oriented in the electrospun mats. The smoothness of the nanofibers is due to the presence of organics in the  $\text{ZnTiO}_3$  sol. The as-spun mat of  $\text{ZnTiO}_3$  calcined at 900  $^\circ\text{C}$  and the FESEM images is shown in Figure 3.3c. The well-formed nanorods are obtained after the calcination of the nanofibrous mat of  $\text{ZnTiO}_3$ . The length of nanorods is around 300 nm to 2  $\mu\text{m}$  while the diameter of the nanorods can be measured in the range of 100 nm to 500 nm. The formation of nanorods from nanofibers can be attributed to the burning of the organics presents over the surface of  $\text{ZnTiO}_3$  nanofibres [218].

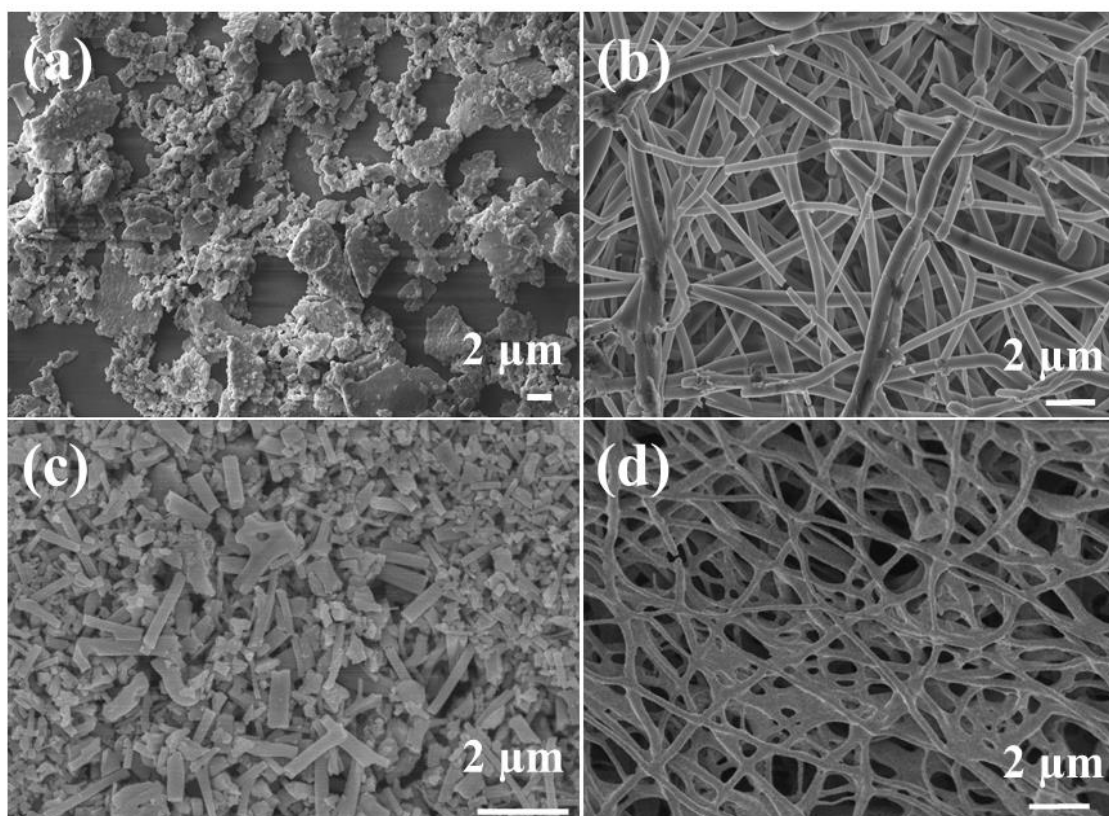


**Figure 3.3.** The surface morphology represents (a) the nanoparticles of BZT, (b) as-spun EZT, (c) EZT nanorods, and (d) EZT nanofibers.

Moreover, we have also determined the morphology of the  $\text{ZnTiO}_3$  nanofibres at a lower temperature of 700  $^\circ\text{C}$  in Figure 3.3d. Figure 3.3d represents the formation of the

nanofibers. The nanofibers are continuous similar to as-spun nanofibers but roughness is observed over the surface of  $\text{ZnTiO}_3$  nanofibers. The roughness can be attributed to the evaporation of the present organics of PVP under the calcination of the nanofibers mat. We can also notice that the nanofibers are made up of the aggregation of the small particles of  $\text{ZnTiO}_3$  in Figure 3.3d. Therefore, Figures conclude that the aspect ratio of EZT nanorods has been changed to a great extent as compare to BZT nanoparticles. The change in the aspect ratio plays a vital role in generating surface defects in the crystal and thereby improving the photocatalytic performance of the materials [219].

### 3.4.2 X-ray diffraction (XRD)

The XRD patterns of BZT and EZT are shown in Figure 3.4. The XRD pattern of BZT consists of several peaks indicating majorly  $\text{ZnTiO}_3$ . However, some residual impurities are also found as  $\text{Zn}_2\text{TiO}_4$  and rutile  $\text{TiO}_2$ . BZT diffraction peaks can be indexed to (101), (012), (104), (110), (113), (021), (202), (024), (116), (018), (214), (300), and (208) for hexagonal structure of zinc titanate from JCPDS card number 00-025-0671. Meanwhile, the XRD peaks at (110), (101), (210), and (211) can be assigned to the rutile  $\text{TiO}_2$  as well-matched with JCPDS card number 01-086-0147. The XRD peak indexed to (220) can be attributed to the cubic  $\text{Zn}_2\text{TiO}_4$  as confirmed from JCPDS card number 01-073-0578. Indexing of XRD peaks of EZT is similar to BZT signifying the hexagonal crystal structure of  $\text{ZnTiO}_3$  though few changes have been noticed in the XRD pattern of EZT. The suppressed intensity of XRD peaks in EZT indicates the formation of small crystallites as compare to BZT. XRD represents the FWHM of the EZT nanorods (for most intense peak  $0.1997^\circ$ ) is higher than the FWHM of BZT nanoparticles (for most intense peak  $0.1464^\circ$ ) signifying the lower crystallinity and small crystallites of the EZT nanorods. Secondly, the peak indexed to (220) of  $\text{Zn}_2\text{TiO}_4$  has been omitted in EZT revealing the decrease in impurities. However, XRD results of EZT suggest the

improvement of the rutile TiO<sub>2</sub> as impurities. The crystallite size (*d*) of ZnTiO<sub>3</sub> in BZT and EZT can be calculated by the Debye-Scherrer Equation (3-1) by choosing the most intense peak at 32.78° [180].

$$d = \frac{k\lambda}{\beta \cos \theta} \quad (3-1)$$

Where the shape constant is represented by *k*, the wavelength of X-ray is denoted by  $\lambda$ , FWHM of the most intense peak is given by  $\beta$ , and  $\theta$  denotes half of diffraction angle  $2\theta$ . The crystallite size of BZT and EZT is calculated at 56.52 nm and 41.44 nm respectively. The crystallite size of EZT is comparatively lowered than BZT. This can be attributed to the effect of electrospinning of ZnTiO<sub>3</sub> sol. The electrospinning of the ZnTiO<sub>3</sub> sol with PVP as guiding polymer led to the stretching of the ZnTiO<sub>3</sub> sol in the vicinity of the high applied voltage. This led to the fabrication of nanofibers of the nano-sized range which on calcination produced crystallites of smaller diameter.

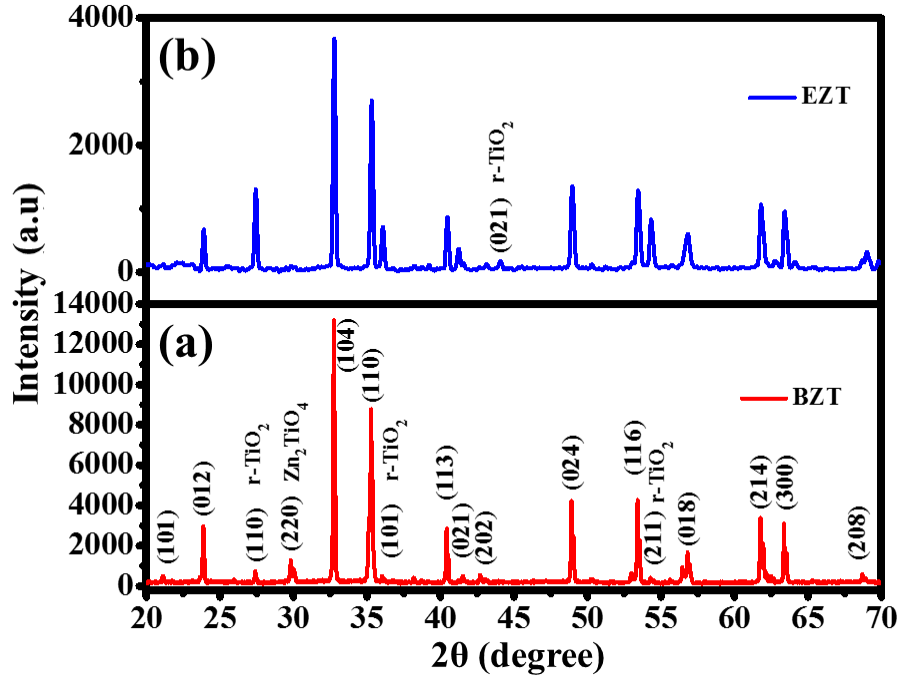


**Figure 3.4. XRD patterns of (a) BZT nanoparticles and (b) EZT nanorods.**

### 3.4.3 Raman spectroscopy

The chemical and structural analysis of BZT and EZT has been performed by Raman spectroscopy. The comparative analysis of Raman peaks of BZT and EZT is given in Figure 3.5. The Raman peaks are noticed at  $143\text{ cm}^{-1}$ ,  $178\text{ cm}^{-1}$ ,  $232\text{ cm}^{-1}$ ,  $266\text{ cm}^{-1}$ ,  $344\text{ cm}^{-1}$ ,  $392\text{ cm}^{-1}$ ,  $444\text{ cm}^{-1}$ ,  $481\text{ cm}^{-1}$ ,  $611\text{ cm}^{-1}$ , and  $709\text{ cm}^{-1}$  for BZT and EZT. The Raman peaks noticed at  $178\text{ cm}^{-1}$  [ $A_g$ ],  $232\text{ cm}^{-1}$  [ $E_g$ ],  $266\text{ cm}^{-1}$  [ $A_g$ ],  $344\text{ cm}^{-1}$  [ $A_g$ ],  $444\text{ cm}^{-1}$  [ $F_{1U}$ ],  $611\text{ cm}^{-1}$  [ $E_g$ ], and  $709\text{ cm}^{-1}$  [ $A_g$ ] are assigned for hexagonal phase of  $ZnTiO_3$  [82,220,221]. The remaining peaks can be assigned to the rutile  $TiO_2$  and  $Zn_2TiO_4$  present as impurities in the BZT and EZT. The Raman peaks of rutile  $TiO_2$  can be found at  $143\text{ cm}^{-1}$  [ $E_g$ ] and  $392\text{ cm}^{-1}$  [ $B_{1g}$ ] in BZT and EZT samples respectively which are in good agreement with XRD data [222].

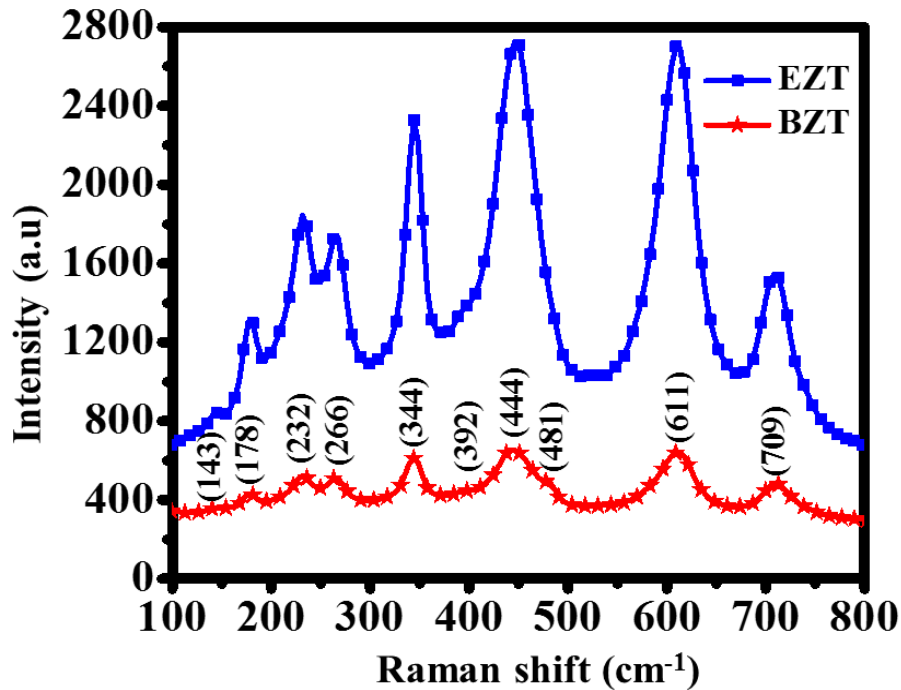


**Figure 3.5. Raman analysis of BZT nanoparticles and EZT nanorods.**

Meanwhile, a small hump at  $481\text{ cm}^{-1}$  [ $E_g$ ] is noticed in the BZT sample, attributing to the trace of  $\text{Zn}_2\text{TiO}_4$  as an impurity [223]. Raman peak corresponds to  $\text{Zn}_2\text{TiO}_4$  has been omitted in the EZT sample indicating no trace of  $\text{Zn}_2\text{TiO}_4$ . This can be also confirmed from the XRD data where the peak at  $29.86^\circ$  corresponding to  $\text{Zn}_2\text{TiO}_4$  excluded. By careful examination of the Raman spectra, we have noticed a blueshift of  $2.33\text{ cm}^{-1}$  in the peak at  $444\text{ cm}^{-1}$  of EZT as compare to BZT. Besides, the FWHM of the same peak of EZT is also decreased by  $1\text{ cm}^{-1}$  approximately. Researchers reported that the shift in the peak position and change in FWHM values represent the non-stoichiometry due to oxygen vacancy defects in several metal oxides and their composites [224,225]. Therefore, the observed blueshift and increase in FWHM signify the change in stoichiometry due to the presence of crystalline defects such as oxygen vacancies in the electrospun  $\text{ZnTiO}_3$  nanorods

#### 3.4.4 Fourier Transform Infrared Spectroscopy (FTIR)

The chemical structure of the BZT and EZT has been analyzed by the FTIR spectra as represented in Figure 3.6. The FTIR bands in the range of  $400\text{ cm}^{-1}$  to  $700\text{ cm}^{-1}$  are ascribed to the characteristic peaks of the metal-oxygen linkage in the metal oxides compounds [226,227]. The FTIR peak at  $447\text{ cm}^{-1}$  and  $608\text{ cm}^{-1}$  are the characteristic bands of ZnO and TiO<sub>2</sub> attributing to the vibrations of Zn-O and Ti-O bonds [227]. The FTIR bands appear at  $686\text{ cm}^{-1}$  and  $561\text{ cm}^{-1}$  are assigned for stretching vibration of the Ti-O bond in the TiO<sub>6</sub> network that exists in ZnTiO<sub>3</sub> and Zn<sub>2</sub>TiO<sub>4</sub> [228]. It is clear from Figure that BZT and EZT have a weak band in the range of  $3400\text{ cm}^{-1}$  to  $3700\text{ cm}^{-1}$  which can be ascribed for the presence of free -OH groups over the surface [229]. The three bands at  $2982\text{ cm}^{-1}$ ,  $2920\text{ cm}^{-1}$ , and  $2847\text{ cm}^{-1}$  are noticed in BZT indicating the stretching vibration of residual C-H from the organic compounds [229]. These FTIR bands have also appeared in EZT with very weak signal intensities signifying the little amount of residual C-H. A single band at  $2338\text{ cm}^{-1}$  in EZT can be assigned to the trace of C=O comes from PVP because PVP has been used for electrospinning the sample. Several FTIR bands are noticeable in the range of  $1800\text{ cm}^{-1}$  to  $1000\text{ cm}^{-1}$  in BZT and EZT. The bands at  $1744\text{ cm}^{-1}$ ,  $1573\text{ cm}^{-1}$ , and  $1427\text{ cm}^{-1}$  can be assigned to the surface adsorbed carbonyl (C=O and C-O) compounds in BZT [230].

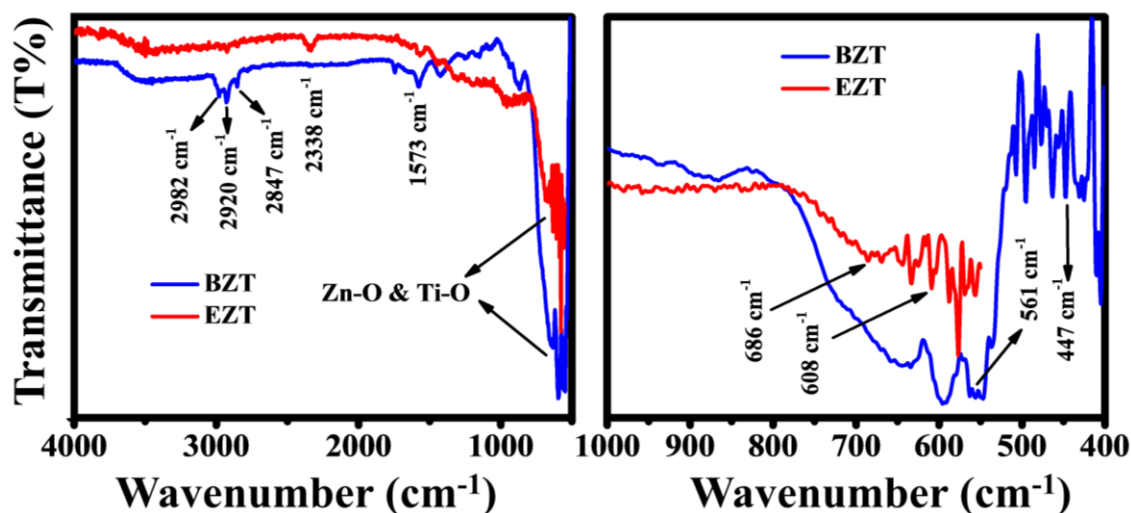
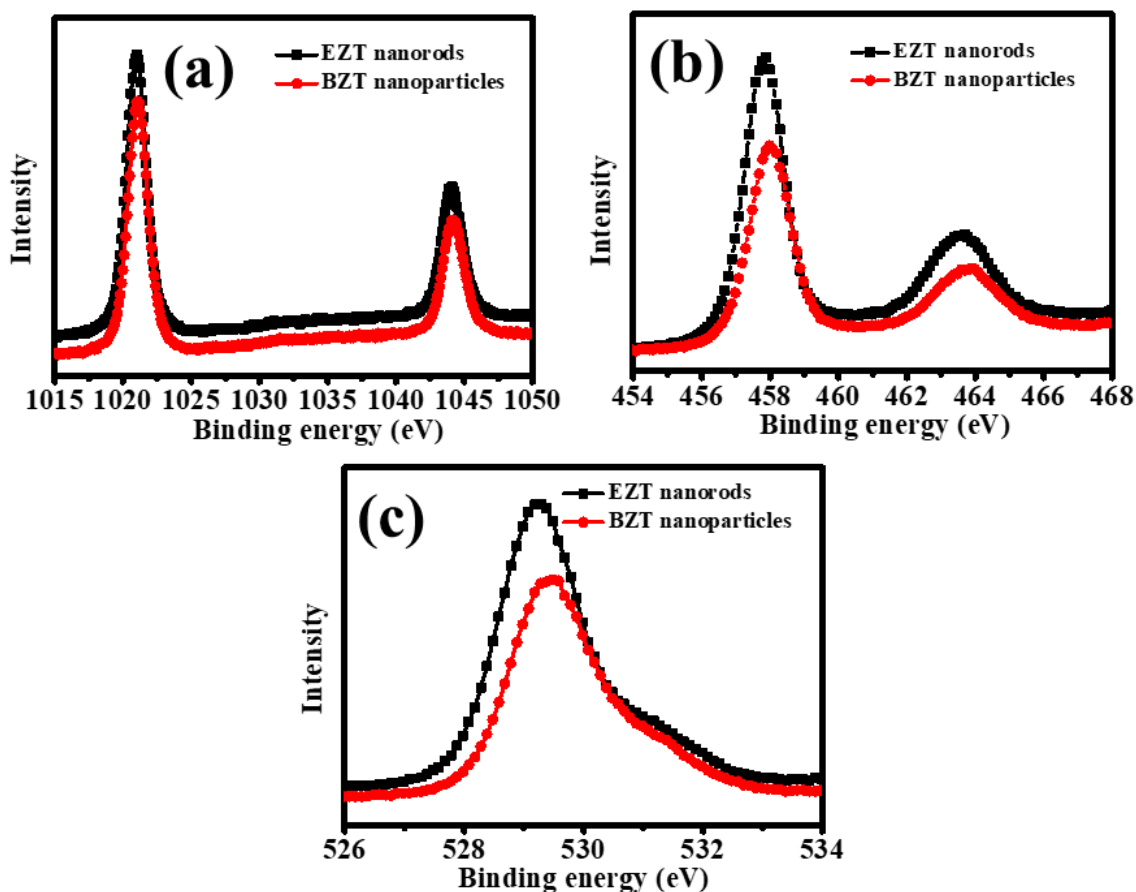


**Figure 3.6.** Comparison of FTIR of BZT and EZT (a) From  $4000\text{ cm}^{-1}$  to  $700\text{ cm}^{-1}$ , and (b) Enlarge image from  $1000\text{ cm}^{-1}$  to  $400\text{ cm}^{-1}$ .

These bands have also appeared in EZT excluding band at  $1744\text{ cm}^{-1}$  but their intensity is comparatively lower than BZT suggesting a lesser amount of surface adsorbed carbonyl compounds. This may be due to the calcination of the electrospun mat in the air furnace exposing higher surface area to the temperature for a longer time. Results show the formation of  $\text{ZnTiO}_3$  with some impurities of organics even at a higher temperature of  $900\text{ }^\circ\text{C}$ . In order to complete the removal of organic entities from the  $\text{ZnTiO}_3$  sintering above  $1000\text{ }^\circ\text{C}$  is required.

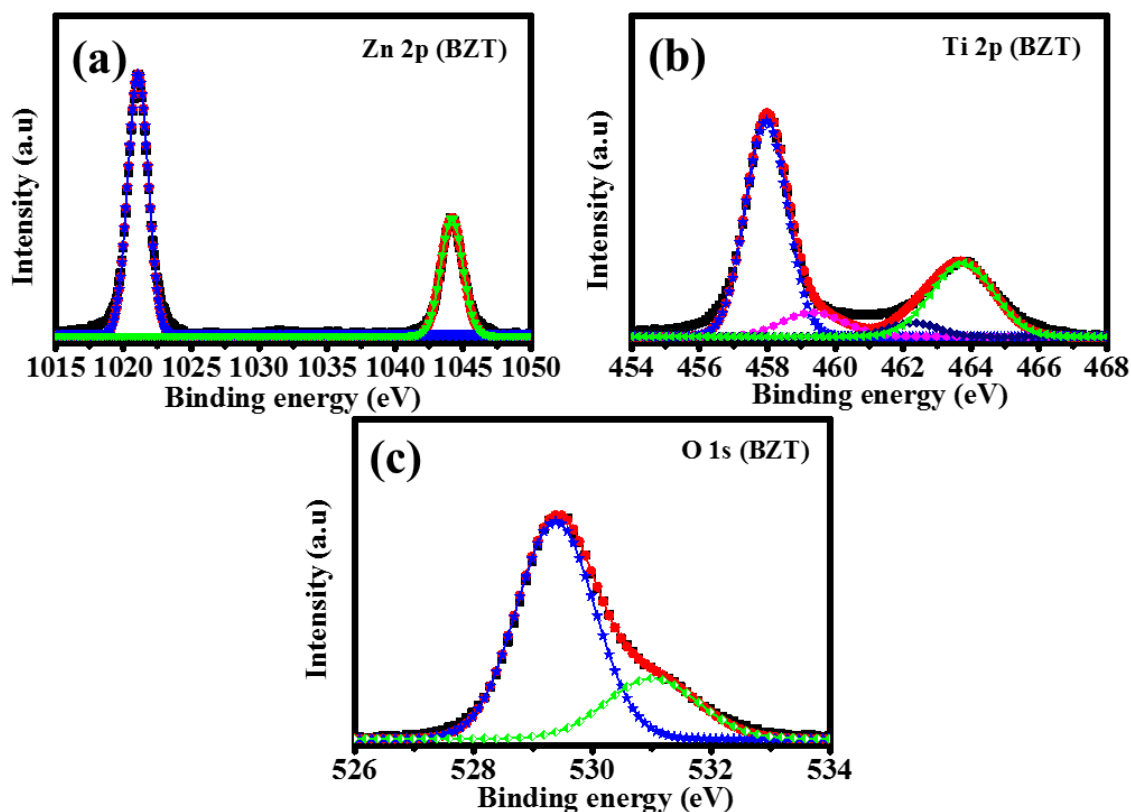
### 3.4.5 X-ray photoelectron spectroscopy (XPS)

The chemical analysis of the BZT and EZT has been investigated by the XPS technique. Figure 3.7 depicts the overlay of binding energy (B.E) of zinc (Zn), titanium (Ti), and oxygen (O) of the BZT and EZT which are different in two morphologies.



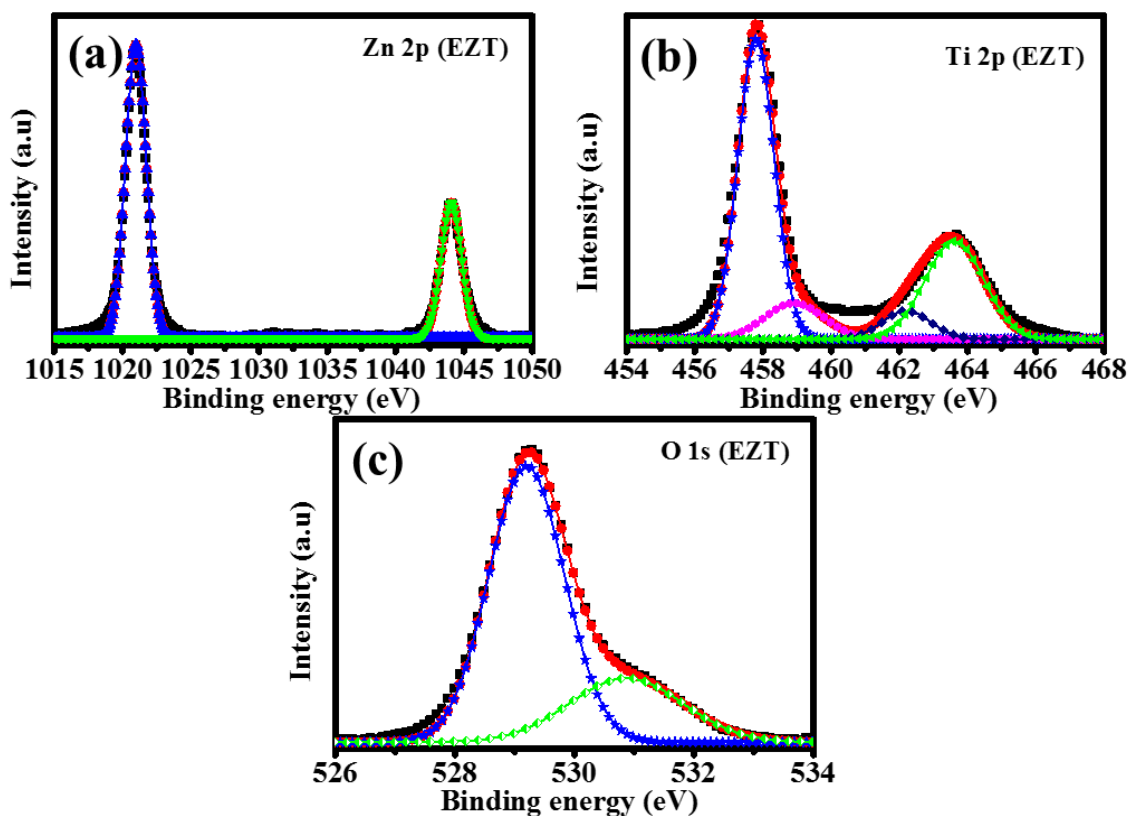
**Figure 3.7. XPS of (a) Zn2p, (b) Ti2p, and (c) O1s for EZT and BZT.**

Table 3.1 represents the binding energy of the elements in BZT and EZT along with their peak area%. The binding energy of the Zn, Ti, and O of EZT is significantly lower than BZT. Comparatively, the lower binding energy of the elements in the case of EZT nanorods can be attributed to the different morphologies. Gaashani et al. reported that the XPS binding energy of ZnO nanorods and nanoparticles are different owing to the different morphologies [231]. Zhou and Li also reported the same difference in XPS spectra for ZnO nanorods and nanoparticles [232]. The elemental analysis provides in-depth information about the chemical nature of the materials.



**Figure 3.8.** XPS deconvoluted peaks of BZT components (a) Zn 2p, (b) Ti 2p, and (c) O 1s.

Figure 3.8a and Figure 3.9a depict the Zn 2p orbital energy in BZT and EZT respectively. The two well-defined XPS peaks of Zn 2p can be seen at 1021.68 eV and 1044.18 eV in BZT attributing to  $2p_{3/2}$  and  $2p_{1/2}$  spin-orbit interaction [233]. The B.E difference in two peaks is 22.5 eV indicates the +2 oxidation state of Zn in BZT. Meanwhile, the same peaks have been shifted towards lower B.E in EZT as listed in Table 3.1. However, the B.E peak difference is found to increase at 23.1 eV. The high-resolution spectra of Ti 2p can be seen in Figure 3.8b and Figure 3.9b for BZT and EZT respectively. XPS peaks of Ti 2p can be deconvoluted into four peaks representing the presence of  $Ti^{+4}$  and  $Ti^{+3}$  simultaneously [234]. However,  $Ti^{+3}$  is very less than  $Ti^{+4}$  as suggested by Table 3.1. The existence of  $Ti^{+3}$  signifies the presence of oxygen vacancies [224]. The XPS peak positions of  $Ti^{+4}$  and  $Ti^{+3}$  are found to be redshifted in EZT as compare to BZT.



**Figure 3.9.** XPS spectra of EZT components (a) Zn 2p, (b) Ti 2p, and (c) O 1s.

It has been reported previously that the redshift of peak position is associated with the formation of oxygen vacancies [235]. Mosquera et al. reported that the redshift of the binding energy represents acceptor levels in the materials [236]. Therefore, on the behalf of the peak shifts in EZT, we can conclude that the oxygen vacancies are increased in EZT and these are situated at the acceptor levels in EZT. Further, the increment in the oxygen vacancies is identified by the change in peak area% as follows. We noticed the change in peak area% of the peaks attributing to  $Ti^{+4}$  and  $Ti^{+3}$ . The change in peak area indicates the change in stoichiometry [237]. Therefore, the peak area analysis is important here because electrospinning is known to change the morphologies thereby the surface states and bulk states of the materials can be affected [71]. The peak area of  $Ti^{+3}$  is increased by 26.72% and that of  $Ti^{+4}$  decreases by 4.80% in EZT. The increase in  $Ti^{+3}$  indicates the removal of oxygen from the lattice in the electrospun zinc titanate nanorods

[237]. On the other side, the decrease in the peak area of the  $Ti^{+4}$  infers the formation of oxygen vacancies onto the surface of EZT nanorods.

**Table 3.1. XPS binding energy of BZT components (a) Zn 2p, (b) Ti 2p, and (c) O 1s; EZT components (a) Zn 2p, (b) Ti 2p, and (c) O 1s.**

| Elements | BZT           |       | EZT           |       |
|----------|---------------|-------|---------------|-------|
|          | Peak position | Area% | Peak position | Area% |
| Zn 2p    | 1021.68       | 67.54 | 1020.98       | 68.70 |
|          | 1044.18       | 32.45 | 1044.08       | 31.29 |
| Ti 2p    | 457.97        | 57.32 | 457.79        | 54.00 |
|          | 459.34        | 9.51  | 458.91        | 10.53 |
|          | 462.30        | 4.15  | 462.20        | 6.78  |
|          | 463.75        | 29.00 | 463.61        | 28.67 |
| O 1s     | 529.38        | 75.33 | 529.19        | 74.11 |
|          | 531.01        | 24.66 | 530.86        | 25.88 |

The O 1s XPS spectrum of BZT and EZT is depicted in Figure 3.8c and Figure 3.9c respectively. The O 1s XPS peak can be deconvoluted into two peaks at 529.38 eV and 531.01 eV attributing to the lattice oxygen and non-lattice oxygen (surface adsorbed –OH groups) for BZT [87]. While for the EZT, the lattice oxygen and surface adsorbed –OH groups can be identified at 529.19 eV and 530.86 eV respectively. Further, we determine the area% for the quantitative analysis of the non-lattice oxygen present in BZT and EZT. An increase in peak area% of non-lattice oxygen in EZT by 4.95% then the BZT is obtained. So, the increment in the area% of non-lattice oxygen in EZT greatly suggests the formation of the oxygen vacancies in the zinc titanate lattice. Previously, the

formation of oxygen vacancies is also reported by researchers [224]. This obtained result is quite similar to the result of the decreased peak area% of  $Ti^{+r}$  by 4.80%. Hence, the fitted curve of the  $Ti^{+3}$  and O 1s of non-lattice oxygen suggests the enhancement of the oxygen vacancies in the EZT nanorods as compare to BZT nanoparticles.

### 3.4.6 Diffuse reflectance spectroscopy (DRS)

The optical properties of the BZT and EZT have been investigated by UV-Vis DRS spectroscopy. The absorption data has been collected from 200 nm to 800 nm as shown in Figure 3.10. Figure 3.10 suggests that the absorption cut-off edge of BZT and EZT is at 428 nm and 439 nm respectively. Absorption onset very closely corresponds to the energy 2.89 eV and 2.82 eV for both BZT and EZT. A comparatively small shift in the absorption onset of EZT towards higher wavelengths may attribute to the surface states present in the EZT. The bandgap of the BZT and EZT has been calculated by using the Kubelka-Munk method as given in Equation (3-2) [238,239].

$$F(R) = \frac{(1 - R)^2}{2R} \quad (3-2)$$

Where  $R$  represents the reflectance and  $F(R)$  is the Kubelka-Munk function. The bandgap energy ( $E_g$ ) has been obtained from the extrapolation of the linear plot between  $[F(R) \times hv]^{1/2}$  vs optical energy ( $hv$ ) to the ordinate as depicted in Figure 3.11. We have assumed the indirect transition for calculating bandgap energy as depicted in Figure 3.11. The bandgap energy is calculated at 2.90 eV and 2.80 eV for BZT and EZT which is consistent with the absorption data. EZT bandgap energy is comparatively lower than the BZT may suggest a lower bandgap due to the availability of the surface states presenting in the EZT producing by electrospinning.

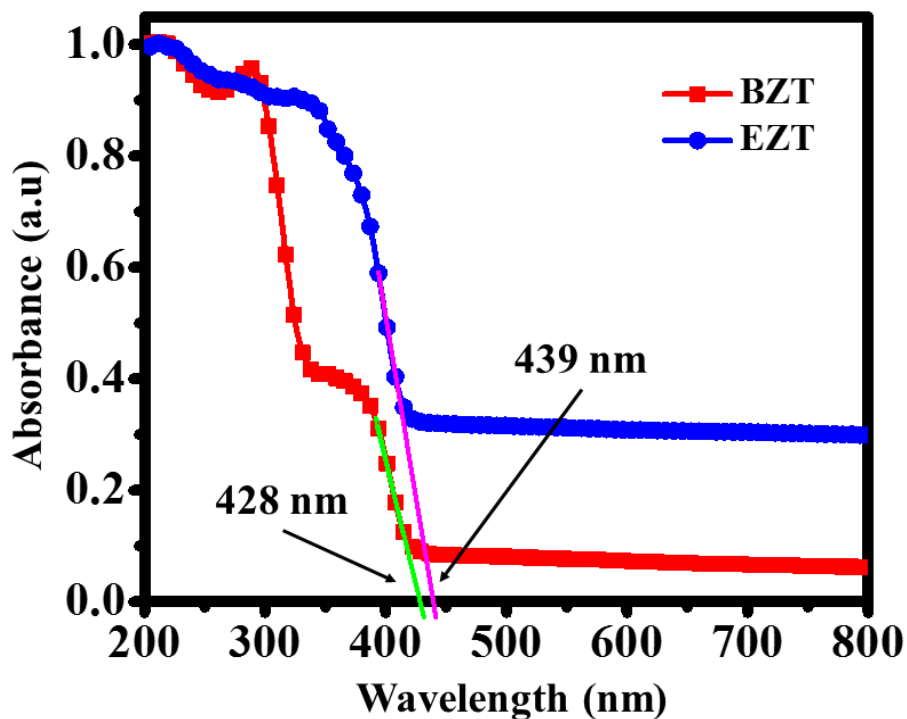


**Figure 3.10.** Absorption spectra of BZT and EZT.

In the current research, we are reporting an appreciable reduction in the bandgap energy of ZnTiO<sub>3</sub>. The obtained bandgap energy (2.90 eV and 2.80 eV) of ZnTiO<sub>3</sub> is minimum in our case. Previously, the same range of bandgap energy was also reported by us [71]. Several authors have reported the bandgap energy of ZnTiO<sub>3</sub> higher than 3 eV as listed in Table 3.2. Obtained binding energies lie in the domain of visible light energy (3.20 eV to 1.80 eV) leading to the use of ZnTiO<sub>3</sub> as a visible light photocatalyst in this study. Therefore, we could successfully harvest visible light for the visible light photocatalytic degradation of the phenol.

**Table 3.2. The comparison of the bandgap energy of the ZnTiO<sub>3</sub> with the bandgap energy in previously reported articles.**

| <b>Structure of ZnTiO<sub>3</sub></b> | <b>Method of preparation</b>     | <b>Bandgap energy (eV)</b> | <b>Ref.</b>                   |
|---------------------------------------|----------------------------------|----------------------------|-------------------------------|
| Cubic ZnTiO <sub>3</sub>              | Self-adjusting method            | 3.78                       | [240]                         |
| Cubic ZnTiO <sub>3</sub>              | Hydrothermal and reflux          | >3.18                      | [234]                         |
| Hexagonal ZnTiO <sub>3</sub>          | Sol-gel electrospinning          | 3.05                       | [241]                         |
| Cubic ZnTiO <sub>3</sub>              | Radiofrequency co-sputtering     | 3.70                       | [78]                          |
| Perovskite ZnTiO <sub>3</sub>         | Sol-gel                          | 3.20                       | [242]                         |
| Theoretical calculations              | Exchange-correlation Functionals | 3.8-4.1                    | [243]                         |
| Hexagonal ZnTiO <sub>3</sub>          | Sol-gel and sol-electrospinning  | 2.88 and 2.79              | [71]<br><b>Previous study</b> |
| Hexagonal ZnTiO <sub>3</sub>          | Sol-gel and sol-electrospinning  | 2.90 and 2.80              | <b>Current study</b>          |

As stated earlier, the trivial lessening bandgap energy of EZT is due to surface states. From presenting XPS data and previously reported articles, the XPS peaks shift due to acceptor levels as well. So, we can conclude that the bandgap reduction is accomplished with the acceptor levels of surface states below the conduction band as represented in Figure 3.12.

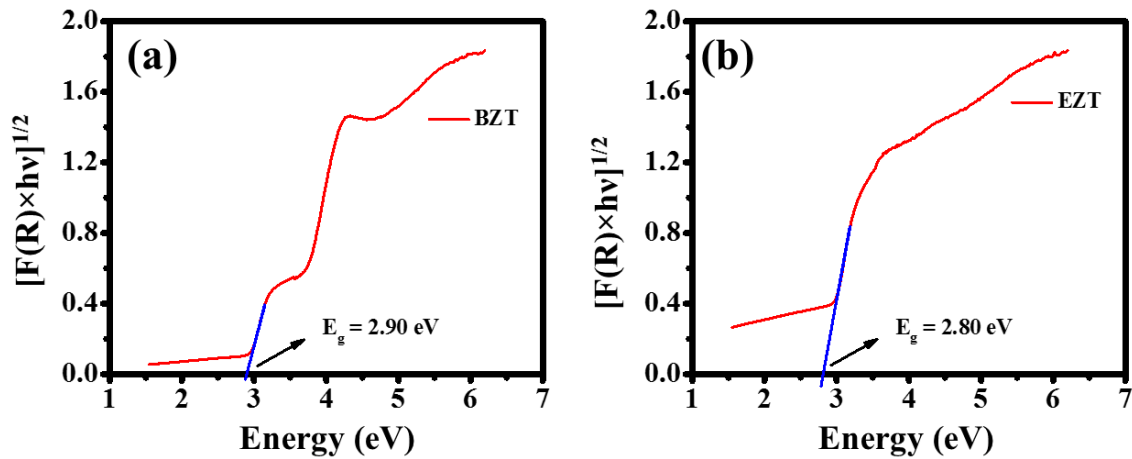


Figure 3.11. (a) Kubelka-Munk function gives a bandgap of EZT (2.80 eV) which is smaller than (b) bandgap of BZT (2.90 eV).

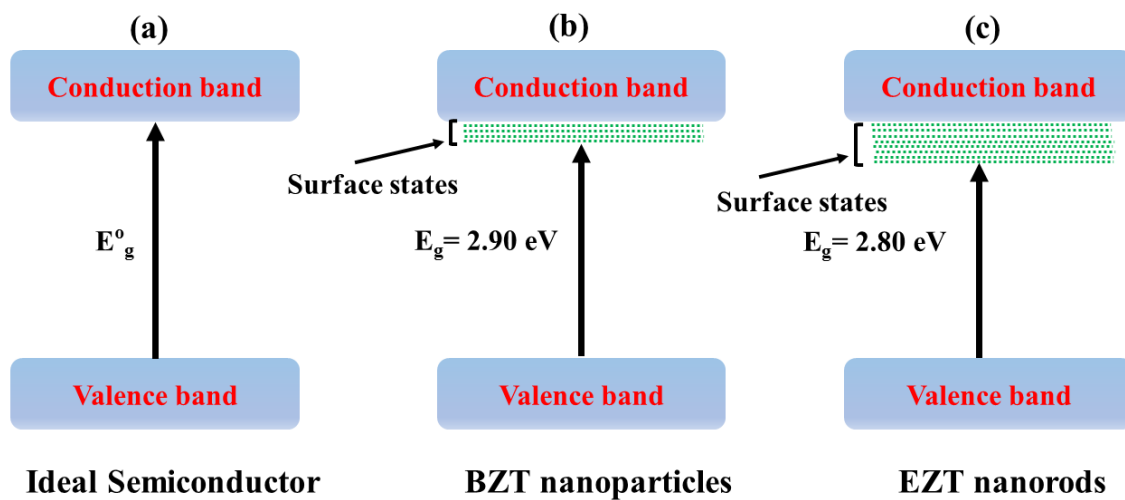


Figure 3.12. Cartoon representing (a) bandgap of ideal semiconductor, (b) surface states in between BZT bandgap, and (c) increase surface states in between EZT bandgap.

### 3.4.7 Photoluminescence spectroscopy

All the samples were investigated by the PL technique at room temperature and the results have shown in Figure 3.13. The photoluminescence spectra is resultant from the recombination of the free charge carriers. The PL spectroscopy extensively uses for the study of the charge carrier trapping, migration, and transfer and the density of the

electron-hole pairs in the semiconductor [87,244]. All the samples were excited at wavelength 260 nm and the spectra were recorded from 270 nm to 530 nm. We have noticed three precise emission bands in the PL spectra of BZT and EZT with varying peak intensities, representing the different charge carriers' lifetime. The peak position for BZT and EZT is represented in Table 3.3 along with their change in peak position in terms of wavelength and emission energy. For the first two PL peaks, a redshift (in terms of wavelength) in the UV region meanwhile a blue shift in the visible region is noticed for EZT as compared with BZT. However, the shift in the third PL peak is trivial that can be neglect therefore it can be assumed at the same position for BZT and EZT. The PL spectra of EZT can be described as follow. The emission peak observed at 418.80 nm corresponds to the bandgap energy 2.96 eV assigned to the band to band transition (direct transition) from the conduction band to the valance band. Whereas, the latter band at 488.12 nm can not be assigned to the band to band transition because the energy corresponding to this band (2.54 eV) is less than the bandgap energy. Meanwhile, this signal can be an emission signal originating from an oxygen vacancy trapped electron and the presence of defects [245]. Hence, the PL data also suggests the existence of surface states. The surface states may be  $Ti^{3+}$  or oxygen vacancies [78]. The maximum of the broad peak appears at 363.27 nm can be attributed to the emission from  $Zn_2TiO_4$  in BZT [246]. Meanwhile, the PL peaks of  $TiO_2$  emerge in the same range (at 364 nm and 369 nm) as well [247]. The  $Zn_2TiO_4$  and  $TiO_2$  are found as the impurities in  $ZnTiO_3$  as confirmed by XRD. So, the broadness of PL peak at 363.27 nm in BZT may be due to the overlapping of emission from  $TiO_2$  and  $Zn_2TiO_4$  as both are present in BZT. Moreover, the PL peak at 367.33 nm in EZT is due to  $TiO_2$  only because the EZT contains  $TiO_2$ , not  $Zn_2TiO_4$  as suggested by XRD. On comparing the PL spectra for peaks I and II, we have noticed the redshift emission in the UV region while blueshift emission in the visible region for EZT nanorods

as compare to the BZT nanoparticles. Although the III PL peak is almost in the same position. The corresponding shift is given in Table 3.3 and is in the range of previously reported values [248]. Contrary to the present situation, Demberga et al. reported the redshift of the visible emission and blueshift of the UV emission attributing to the band bending and quantum confinement effect respectively for varying ZnO film thickness [248]. So the shift in PL spectra for peaks I and II in the current study can be also assigned to the bend bending and quantum confinement effect in the EZT.

**Table 3.3. Listing of PL peaks in terms of wavelength and emission energy for BZT and EZT.**

| BZT                |                            | EZT                |                            | Change in peak's position       |   |
|--------------------|----------------------------|--------------------|----------------------------|---------------------------------|---|
| Wavelength<br>(nm) | Emission<br>energy<br>(eV) | Wavelength<br>(nm) | Emission<br>energy<br>(eV) | Change in<br>wavelength<br>(nm) | Change in<br>emission<br>energy<br>(eV) |
| 363.271            | 3.413                      | 367.336            | 3.375                      | 4.065                           | 0.038                                   |
| 421.155            | 2.944                      | 418.809            | 2.960                      | 2.346                           | 0.016                                   |
| 486.847            | 2.547                      | 488.127            | 2.540                      | 1.28                            | 0.007                                   |

The intensity of II and III PL peaks of EZT decreases as compare to BZT indicating the reduced recombination of electrons and holes. This may be due to electrons are trapped into existing surface states below the conduction band thereby recombination rate decreases and hence charge carriers are available for a longer time for the photocatalytic process [78]. The lower PL intensity of the EZT nanorods can also be defined as the EZT nanorods are closed packed structure of small nanoparticles as clearly visible from Figure 3.3d. The dense packing of the nanoparticles in EZT nanorods leads to efficient charge separation through interfacial charge transfer into the nanorods and thereby decreasing

electron-hole recombination [249]. Furthermore, the I PL peak of EZT shows opposite behaviour than the other two peaks as compare to BZT.

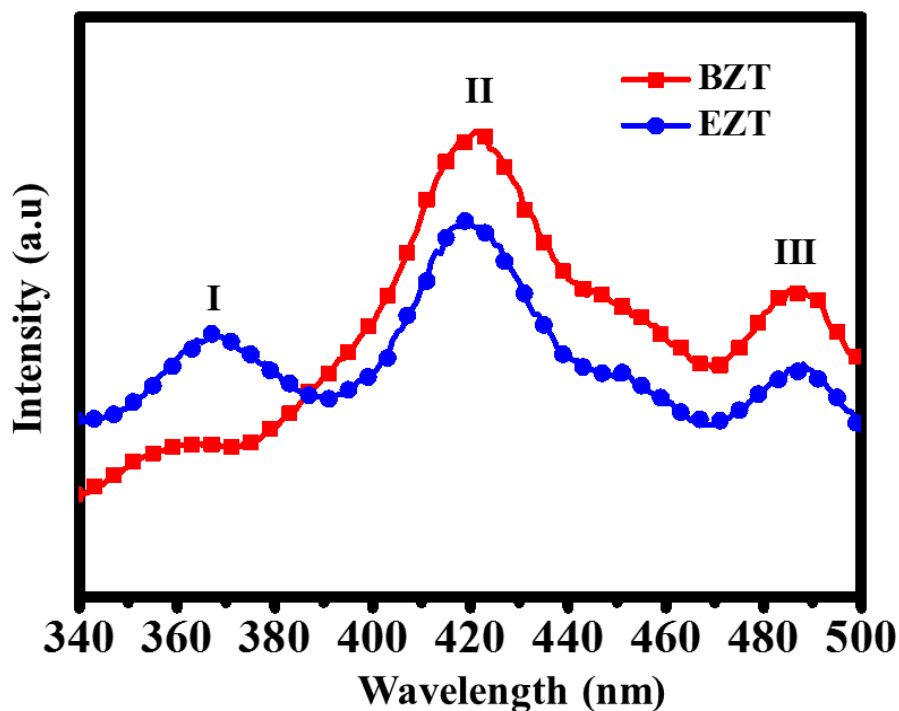


**Figure 3.13.** The PL spectroscopy suggests the lower electron-hole recombination in EZT as compare to BZT.

### 3.5 Visible light photocatalytic activity

The photocatalytic degradation of the pollutant in the presence of visible light is well established [35,250]. The semiconductor photocatalyst absorbs visible light upon exposing thereby creating electron-hole pairs. The electrons jump to the conduction band leaving holes in the valance band upon irradiation by visible light of suitable frequency. Further, the photogenerated electrons move to the surface of the photocatalyst without recombination. However, few of them also are recombined. The present electrons at the surface react with the oxygen ( $O_2$ ) in the aqueous media and produce superoxides ions ( $O_2^{\cdot-}$ ). Meanwhile, the holes available in the valance band react with hydroxide ions ( $-OH$ ) or water molecules to produce hydroxyl ( $\cdot OH$ ) radicals. The radicals are so energetic

that they are capable of degrading adsorbed species into lower molecular weight intermediates. These intermediates are finally broken into harmless environmentally friendly products such as water or carbohydrate.

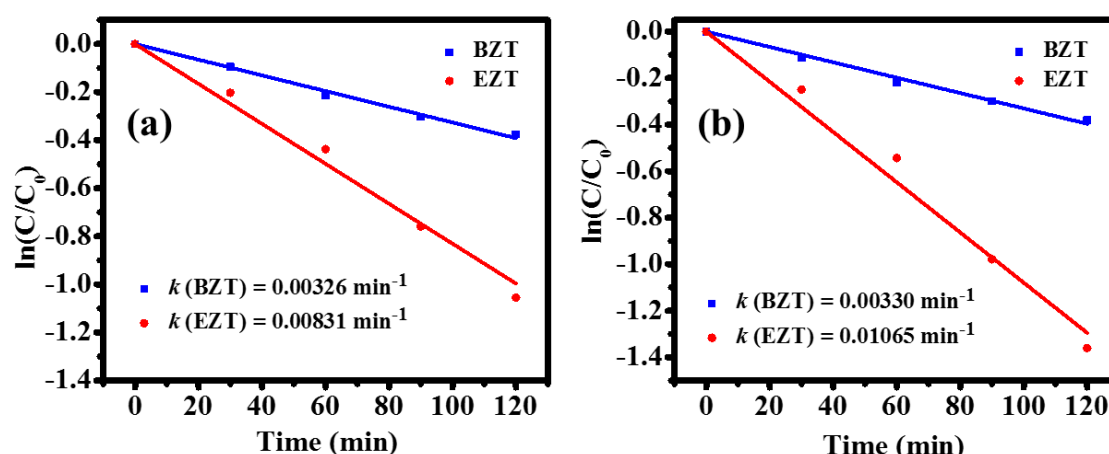


**Figure 3.14. The photocatalytic degradation of phenol for its peak at (a) 210 nm ( $R^2=0.997$ ) and (b) 270 nm ( $R^2=0.996$ ) by BZT and EZT as indicated.**

The kinetics of phenol degradation by BZT and EZT in the presence of visible light is investigated with the help of a first-order kinetic equation (3-3) [87,250].

$$\ln \frac{C}{C_0} = -kt \quad (3-3)$$

Where the concentration of phenol at the beginning and at time  $t$  is denoted by  $C_0$  and  $C$  respectively. The degradation rate constant is represented by  $k$  and time ( $t$ ) is measured in minutes. The degradation data is plotted between  $\ln(C/C_0)$  vs irradiation time ( $t$ ) as represented in Figure 3.14. The photocatalytic degradation rate constant ( $k$ ) is determined by the linear fitting of the data in Figure 3.14. Since the phenol is characterized by its two peaks at 210 nm and 270 nm. Therefore, both the peaks are monitored during the photocatalytic degradation and the degradation rate constant is evaluated for both peaks.

The values of  $k$  for the phenol degradation by EZT are calculated at  $0.00831 \text{ min}^{-1}$  and  $0.01065 \text{ min}^{-1}$  for the peaks at 210 nm and 270 nm respectively. These  $k$  values are compared with the  $k$  values of BZT at  $0.00326 \text{ min}^{-1}$  and  $0.00330 \text{ min}^{-1}$  for the peaks at 210 nm and 270 nm respectively. In comparison, it is clear that the degradation rate constant ( $k$ ) is increased by EZT nanorods then BZT nanoparticles. EZT nanorods increase the  $k$  values by 154.90% and 222.72% for the peaks at 210 nm and 270 nm respectively then the BZT nanoparticles. Many factors can be responsible for the improvement of photocatalytic degradation such as charge separation, recombination rate, high surface area to volume ratio, charge transport to the surface, *etc.* The appreciable improved results by EZT nanorods can be attributed to the following reasons.

(a) The EZT nanorods formation decreases the recombination rate by driving the charge carriers to the surface thereby photocatalytic activity increases, (b) the surface area to volume ratio may increase in EZT nanorods which offers more active sites for photocatalytic degradation, and (c) the increment in surface states capture photogenerated electrons thereby reducing electron-hole recombination resulting in enhanced photocatalytic activity.



# Chapter 4: Nitrogen-doped zinc titanate nanoparticles by electrospinning for visible-light photocatalytic degradation of phenol

## 4.1 Abstract

<sup>1</sup>Metal oxides nanomaterials are extensively used as photocatalyst for effectively decontaminant toxic organic compounds. But, the wide bandgap energy limits their use in UV-Vis irradiation only. Aiming to synthesize efficient lower bandgap photocatalyst that can harvest visible light for photocatalytic activity. Here, we report nitrogen-doped zinc titanate of bandgap energy 2.25 eV for photocatalytic degradation of phenol in the presence of visible light. The nitrogen doping in zinc titanate is confirmed by various characterization techniques. The XRD data infers that nitrogen doping induces compressive strain in the zinc titanate which is also confirmed by the Williamson-Hall method. Nitrogen doping hinders the crystallization of zinc titanate leading to the small crystallite as calculated by the XRD results. Other characterization technique such as Raman spectroscopy, FTIR, and XPS also suggests the nitrogen doping in zinc titanate. The FTIR results demonstrate that the nitrogen has doped at both substitutional and interstitial positions. The analysis of XPS and DRS data reveals that the surface states have been increased in doped zinc titanate. The bandgap energy of pure zinc titanate and nitrogen-doped zinc titanate is calculated at 2.90 eV and 2.25 eV (for maximum nitrogen content sample) respectively. Lessening in the bandgap energy is attributed to the extra electronic states provided by nitrogen in between the bandgap of zinc titanate and

---

<sup>1</sup> Singh. S, Perween. P, Ranjan. A; *Journals of Physics and Chemistry of Solids*: [doi.org/10.1016/j.jpccs.2021.110221](https://doi.org/10.1016/j.jpccs.2021.110221)

increasing surface states. Furthermore, the nitrogen-doped zinc titanate shows enhanced photocatalytic activity toward phenol degradation in the presence of visible light. The photocatalytic rate constant ( $k$ ) is increased to  $0.02051 \text{ min}^{-1}$  for nitrogen-doped zinc titanate as compare to  $0.00330 \text{ min}^{-1}$  for zinc titanate. The percentage increase in rate constant ( $k$ ) is about 520% is attributing to the nitrogen doping in zinc titanate.

**KEYWORDS:** Electrospinning, Nitrogen-doped  $\text{ZnTiO}_3$ , Visible light photocatalysis, Williamson-Hall Method

## 4.2 Introduction

Solar energy[136] is an abundant natural energy source on the earth, which can be harvested for many practical applications, for example, visible light photocatalysis [251–256] for degradation of organic pollutants, water splitting [257–260], electric energy generation [261], hydrogen generation, *etc* [262]. Visible light photocatalysis is a powerful method for degrading water-soluble organic pollutants, phenol and phenol derivatives, rhodamine-B, methylene blue, methylene orange, and congo red, *etc* present in the byproduct and wastewater of the industries, which are very hazardous to the environment and living beings [263]. Solar light-driven photocatalytic activity of the oxides attracts prevalent attention because of an unlimited source of solar light and recycled photocatalysts [181]. Among other oxides,  $\text{TiO}_2$  and  $\text{ZnO}$  are widespread studies photocatalysts.  $\text{TiO}_2$  is an appropriate photocatalyst for the pollutant and water remedy because of its high photochemical stability, non-toxicity, and inexpensiveness [264]. However,  $\text{TiO}_2$  has some drawbacks as it is active under UV light because of its high bandgap (3.2 eV), high recombination rates of photo-induced electrons and holes on its surface, and low quantum efficiency [181].  $\text{ZnO}$  is also a widespread photocatalyst having some merits over  $\text{TiO}_2$  as it has higher electron mobility and a longer lifetime of the charge carriers, however,  $\text{ZnO}$  is limited by low quantum yield [265,266].

However, the mixed oxide zinc titanate ( $\text{ZnTiO}_3$ ) of ZnO and  $\text{TiO}_2$  has some merits over the demerits of ZnO and  $\text{TiO}_2$  [181]. Much attention has been paid on perovskite-type  $\text{ZnTiO}_3$  as photocatalyst because of its low bandgap energy (2.79 eV-3.18 eV) as compared to  $\text{TiO}_2$  (3.20 eV-3.40 eV) and ZnO (3.40 eV) for visible light photocatalysis [71,135,241,263,267,268].  $\text{ZnTiO}_3$  is one of the candidates of the well-known ZnO- $\text{TiO}_2$  system [67,81].  $\text{ZnTiO}_3$  is an attractive material for the applications in photocatalysis of organic pollutants, electrodes for solid oxide fuels, metal-air barriers, gas sensors, microwave dielectric, paint pigments, and sorbent [67,181,269]. Several methods were employed for the preparation of the  $\text{ZnTiO}_3$  including sol-gel [229], solid-state reaction method [270], and hydrothermal method [271], *etc.* among all of them sol-gel method is vastly used and promising for the preparation of nanoscale particles of high purity, a high degree of homogeneity, high yield, and small processing time, cost-effective and eco-friendly [229]. The sol-electrospinning process associated with the electrospinning of the sol of the materials.

In our work [71], we reported a facile approach to produced  $\text{ZnTiO}_3$  with improved photocatalytic activity under visible light towards phenol degradation. We investigated the optical properties of  $\text{ZnTiO}_3$  where bandgap energy was reported at 2.88 eV and 2.79 eV for bulk  $\text{ZnTiO}_3$  (BZT) and electrospun  $\text{ZnTiO}_3$  (EZT) respectively [71]. The obtained bandgap energy of the  $\text{ZnTiO}_3$  was at the onset of the visible light energy spectrum. Therefore, still, there is a possibility to lessen the bandgap energy to make the  $\text{ZnTiO}_3$  more efficient visible-light photocatalyst. Considering it as the motivation for the current research work. The present work aims to develop a strategy to prepare nitrogen-doped zinc titanate ( $\text{N-ZnTiO}_3$ ) which led to strongly enhanced photocatalytic degradation of the phenol under visible light. The nitrogen doping has been achieved by the sol-gel process to synthesized nitrogen-doped zinc titanate ( $\text{N-ZnTiO}_3$ ) followed by

electrospinning. We have found interesting results where the bandgap of the electrospun nitrogen-doped ZnTiO<sub>3</sub> nanoparticles has been reduced to 2.25 eV for higher doping of the nitrogen in ZnTiO<sub>3</sub> (ENZT-1) and its visible-light photocatalytic rate has been enhanced appreciably.

### **4.3 Experimental section**

#### **4.3.1 Synthesis of zinc titanate (ZnTiO<sub>3</sub>)**

The synthesis process of the sol of zinc titanate is described in section 3.3.1. Further to make the solution spinnable, we proceed by adding 30 drops of 10% PVA (nearly 1.5 mL) solution dropwise by a plastic dropper in the sol of zinc titanate at the same experimental conditions as described in section 3.3.1. The resultant homogenous polymeric solution was used partially for (i) electrospinning process to fabricate fibrous structured ZnTiO<sub>3</sub> (EZT) and (ii) directly kept for the calcination process named bulk ZnTiO<sub>3</sub> (BZT). The process of synthesizing BZT and EZT is represented in Figure 4.1.

#### **4.3.2 Synthesis of nitrogen-doped zinc titanate (ENZT)**

In this procedure, the sol synthesis of ZnTiO<sub>3</sub> was identical as discussed in earlier section 3.3.1. Urea was used as a nitrogen source. The ZnTiO<sub>3</sub> was nitrogenated by urea at the time of the sol synthesis. The amount of urea was decided according to the initial nitrogen to titanium weight ratio (N:Ti =) 0.25, 0.50, 0.75, 1.00 in the raw materials. Thereafter, the solution was mixed with PVA solution as described in the ZnTiO<sub>3</sub> synthesis process and again the resultant solution was stable, homogeneous, and viscous that further used for partially (i) loaded for electrospinning and (ii) directly calcined at 900 °C for 8 h. The electrospinning process of the samples is described in section 3.3.2. The synthesis process is given in Figure 4.1. The nomenclature of the obtained samples is given in Table 4.1.

**Table 4.1. The nomenclature of samples.**

| Composition (N:Ti) in raw materials | Bulk ZnTiO <sub>3</sub> | Electrospun ZnTiO <sub>3</sub> |
|-------------------------------------|-------------------------|--------------------------------|
| Undoped                             | BZT                     | EZT                            |
| 0.25                                | BNZT-0.25               | ENZT-0.25                      |
| 0.50                                | BNZT-0.50               | ENZT-0.50                      |
| 0.70                                | BNZT-0.75               | ENZT-0.75                      |
| 1.00                                | BNZT-1.00               | ENZT-1.00                      |

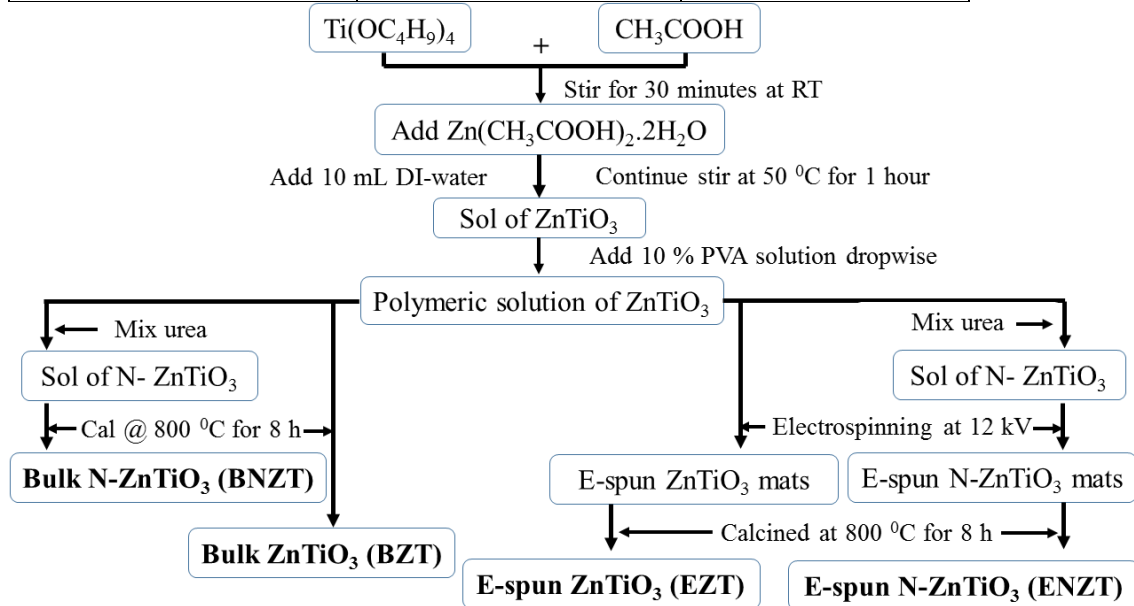


**Figure 4.1. Schematic diagram represents the synthesis process of bulk zinc titanate (BZT) and electrospun Zinc titanate (EZT) and nitrogen-doped zinc titanate (bulk and electrospun: BNZT and ENZT).**

We have represented the experimental data for BZT, EZT, ENZT-0.25, and ENZT-1 only in the text. Although, we have performed the visible light photocatalysis with all the samples and the degradation rate constant data have been listed in section 4.5.

## 4.4 Results and discussion

### 4.4.1 X-ray diffraction (XRD)

The X-ray diffraction patterns of BZT, EZT, ENZT-0.25, and ENZT-1 are represented in Figure 4.2. Indexing of XRD peaks in BZT infers the presence of  $\text{ZnTiO}_3$  with some residual impurities of  $\text{TiO}_2$  and  $\text{Zn}_2\text{TiO}_4$  in Figure 4.2a. The hexagonal crystal structure of  $\text{ZnTiO}_3$  (h- $\text{ZnTiO}_3$ ) can be confirmed from the JCPDS file number 25-0671. Meanwhile, the impurities of rutile- $\text{TiO}_2$  and cubic- $\text{Zn}_2\text{TiO}_4$  are also matched by the JCPDS database 01-086-0147 and 01-073-0578 respectively. EZT maintains its crystal structure similar to BZT as represented in Figure 4.2b. Next, we will examine the XRD data of doped samples and compare them with the BZT and EZT. Figure 4.2c-d infers that the ENZT-0.25 and ENZT-1 maintain the hexagonal structure of  $\text{ZnTiO}_3$ . But numerous observations can be noticed as compared to the BZT and EZT. (1) FWHM of peaks increases which signifies small crystallite. (2) Shifting of XRD peaks towards higher  $2\theta$  values indicates induced microstrain. (3) The relative intensities of XRD planes (104) and (110) have been interchanged in doped samples. (4) Relatively, % of  $\text{ZnTiO}_3$  decreases thereby impurities increases. Based on these observations we assume that nitrogen has been successfully doped in  $\text{ZnTiO}_3$ . To prove it, further characterization data will be presented. An increase in FWHM of the peaks indicates the small crystallite. The crystallite size ( $d_m$ ) has been calculated by the Debye-Scherrer Equation (3-1). The most intense peaks have been chosen to calculate the crystallite size in each sample. We have also calculated the average crystallite size ( $d_{avg}$ ) of each sample after considering each peak in XRD data. Table 4.3 compares both the parameters. Table 4.3 suggests comparatively small crystallites in doped samples which attributes to the interrupting of the  $\text{ZnTiO}_3$  crystallization after N doping [272].

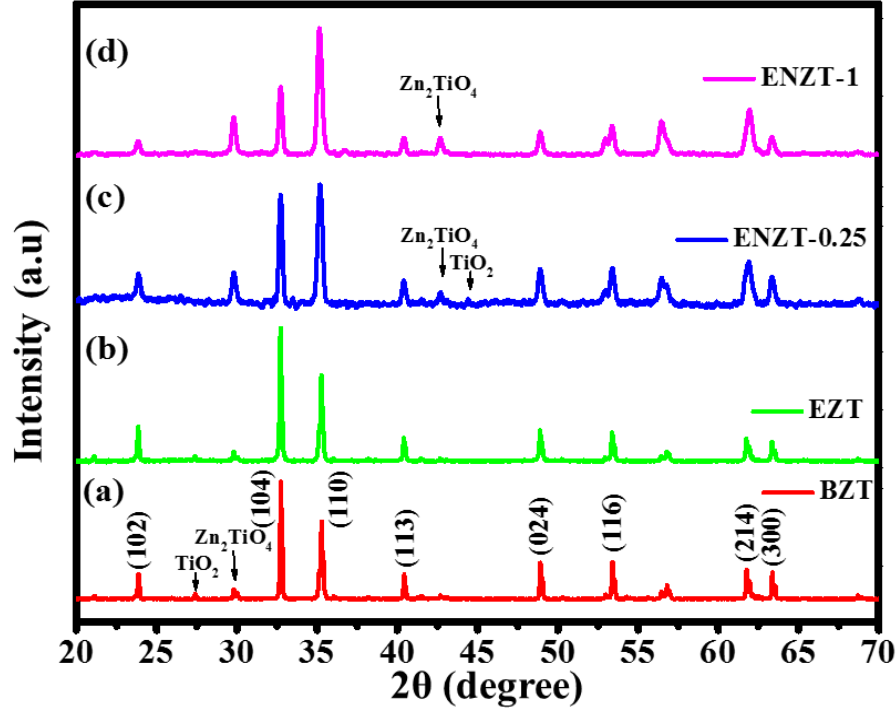


**Figure 4.2.** XRD analysis of (a) BZT, (b) EZT, (c) ENZT-0.25, and (d) ENZT-1.

Previous studies suggest nitrogen doping in metal oxides causes the creation of oxygen vacancies (surface states) to maintain charge neutrality thereby decreasing crystallite size [135,273]. Later in section 4.4.6, DRS data also supports increments in surface states in doped samples. We have found the crystallites of the equal size in ENZT-0.25 and ENZT-1 irrespective of nitrogen content. However, the average crystallite size ( $d_{avg}$ ) decreases regularly. An in-depth analysis of XRD reveals that nitrogen doping suppresses h-ZnTiO<sub>3</sub> meanwhile increasing impurities of Zn<sub>2</sub>TiO<sub>4</sub>. Therefore, the percentage of h-ZnTiO<sub>3</sub> (%*H*) has been calculated by the following Equation (4-1) [181].

$$\% H = \left[ \frac{A_h}{A_{all}} \times 100 \right] \% \quad (4-1)$$

Here,  $A_h$  and  $A_{all}$  represent the area of XRD peaks relating to the h-ZnTiO<sub>3</sub> and the area of all the peaks respectively. The %*H* is listed for each sample in Table 4.2.

**Table 4.2. The calculation of the percentage of hexagonal phase present in the samples.**

| Sample    | % Hexagonal phase |
|-----------|-------------------|
| BZT       | 90.09             |
| ENZT      | 92.46             |
| ENZT-0.25 | 84.76             |
| ENZT-1.00 | 78.90             |

Table 4.2 concludes that the h-ZnTiO<sub>3</sub> decreases consequently impurities increases after nitrogen doping.

Shifting in the peaks has been noticed in ENZT-0.25 and ENZT-1. Generally, the peaks shift due to lattice distortion caused by defects (vacancies, interstitial, substitution, local structure transformation, etc.) [141,184]. Shifting of the peaks determines the type of microstrain as compressive strain or tensile strain [141,184]. In the current study, the XRD peaks shift towards a higher diffraction angle indicating the compressive strain. Also, the broadening in the peaks is in favor of microstrain in the doped samples. This may be due to the higher ionic radii of nitrogen ( $r^{2+} = 1.46 \text{ \AA}$ ) as compare to oxygen ( $r^{2+} = 1.38 \text{ \AA}$ ). The induced microstrain can be calculated by using the Williamson-Hall model based on Uniform Deformation Model (WH-UDM). This WH-UDM model is given by the following Equation (4-2) [182,274].

$$\beta_{hkl} \cos \theta = \frac{k\lambda}{D} + 4\varepsilon \times \sin \theta \quad (4-2)$$

Where  $\beta_{hkl}$  denotes FWHM of the peaks,  $D$  represents the crystallite size,  $\varepsilon$  is microstrain, and  $k$  is known as shape constant. The linear fitting between  $\beta_{hkl} \cos \theta$  and  $4 \sin \theta$  of the Equation gives the value of slope and intercept thereby microstrain and crystallite size calculates. The comparison of the calculated microstrains is represented in Figure 4.3.

Also, all calculated values are listed in Table 4.3. The BZT and EZT show the positive slope which can be assigned to tensile strain attributing to the oxygen vacancies and surface states. Comparatively, EZT is stressed more than BZT, this can be attributed to the increasing number of surface defects induced by electrospinning. However, the doped samples show the opposite behaviour than undoped samples. The negative slope values represent compressive strain in ENZT-0.25 and ENZT-1 moreover the more negative slope indicates the higher compressive strain in ENZT-1. The peaks shift towards a higher value of  $2\theta$  also supports the compressive microstrains in doped samples. Thus, the nitrogen atoms reside in  $\text{ZnTiO}_3$  lattice resulting in compression of the lattice planes. We have calculated lattice parameters of hexagonal  $\text{ZnTiO}_3$  and doped- $\text{ZnTiO}_3$  as listed in Table 4.4. The lattice parameters are in good agreement with the previously reported article [275]. The  $c/a$  values 2.68, 2.73, and 2.79 for EZT, ENZT-0.25, and ENZT-1 respectively are increasing. These numbers may show that the ENZT-0.25 and ENZT-1 structures are more open comparatively than EZT. This may be assigned to the existence of surface states due to nitrogen doping.

Figure 4.4 compares the microstrain and crystallite size of the samples.

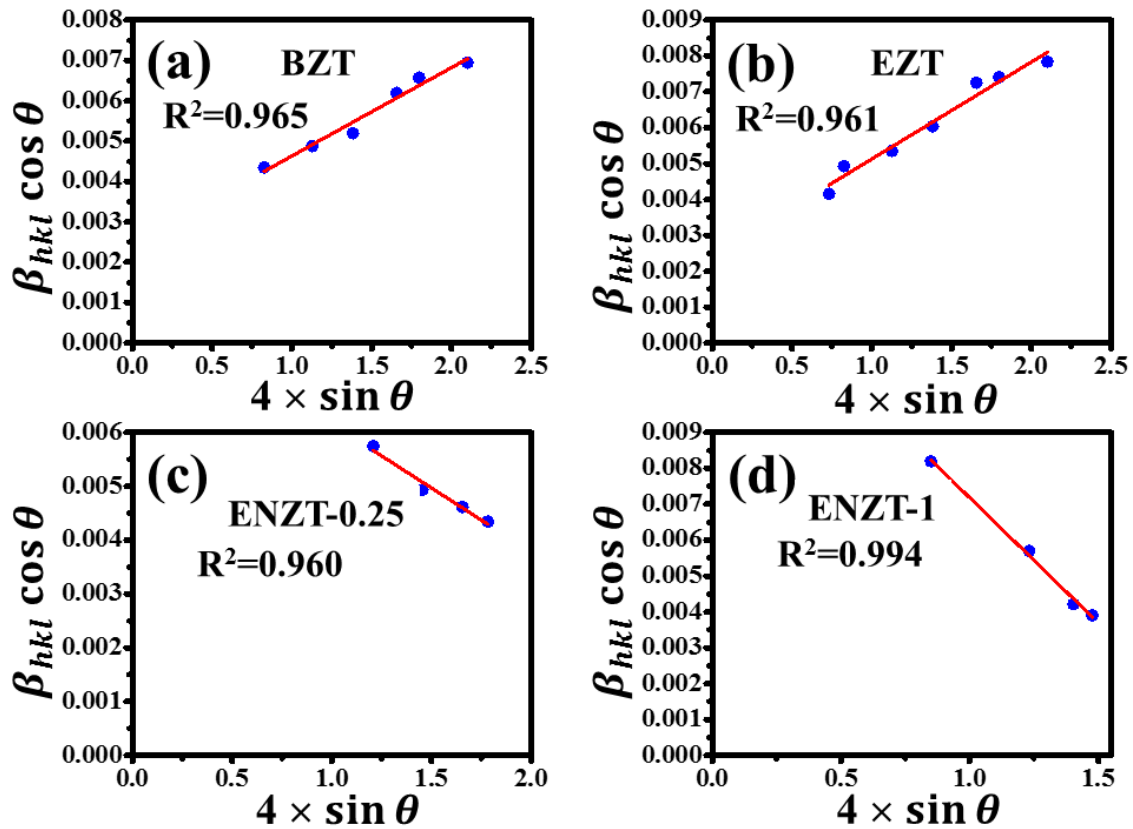


Figure 4.3. Microstrain calculation by WH-UDM in (a) BZT, (b) EZT, (c) ENZT-0.25, and (d) ENZT-1.

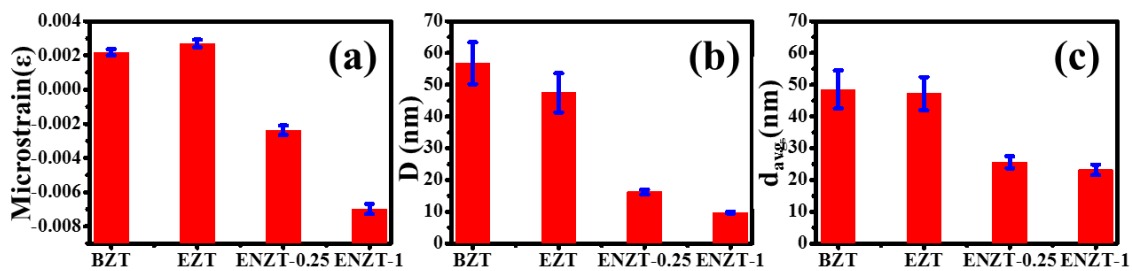


Figure 4.4. Bar graph representation of (a) microstrain ( $\epsilon$ ) by WH-UDM, (b) crystallite size ( $D$ ) from the WH-UDM, and (c) average crystallite size ( $d_{avg}$ ) by Debye-Scherrer method for BZT, EZT, ENZT-0.25, and ENZT-1.

**Table 4.3. The comparison of  $d_{avg}$ ,  $d_m$ ,  $D$ , and  $\varepsilon$  for BZT, EZT, ENZT-0.25, and ENZT-1.**

| Sample    | $d_{avg}$ (average) | $d_m$ (from maximum intense peak) | $D$ (WH-ISM)        | $\varepsilon$ ( from WH-ISM model) |
|-----------|---------------------|-----------------------------------|---------------------|------------------------------------|
| BZT       | $48.54 \pm 12.32\%$ | 57.34                             | $56.80 \pm 11.61\%$ | $0.00219 \pm 8.35\%$               |
| EZT       | $47.18 \pm 11.05\%$ | 52.23                             | $47.46 \pm 13.06\%$ | $0.00270 \pm 8.11\%$               |
| ENZT-0.25 | $25.62 \pm 7.35\%$  | 24.33                             | $16.22 \pm 4.99\%$  | $-0.00238 \pm 11.63\%$             |
| ENZT-1    | $23.20 \pm 7.19\%$  | 24.28                             | $9.78 \pm 2.67\%$   | $-0.00698 \pm 4.29\%$              |

**Table 4.4. The lattice parameters and c/a values of BZT, EZT, ENZT-0.25, and ENZT-1.**

|           | a (Å) | c (Å) | c/a  |
|-----------|-------|-------|------|
| BZT       | 5.09  | 13.94 | 2.73 |
| EZT       | 5.16  | 13.87 | 2.68 |
| ENZT-0.25 | 5.13  | 14.05 | 2.73 |
| ENZT-1    | 4.97  | 13.87 | 2.79 |

#### 4.4.2 Raman Analysis

The Raman spectrum was recorded using a YAG laser of 532 nm laser line as an excitation source. Figure 4.5 represents the Raman spectra of synthesized BZT, EZT, ENZT-0.25, and ENZT-1. The Raman peaks detected at  $176 \text{ cm}^{-1}$  [ $A_g$ ],  $230 \text{ cm}^{-1}$  [ $E_g$ ],  $265 \text{ cm}^{-1}$  [ $A_g$ ],  $344 \text{ cm}^{-1}$  [ $A_g$ ], and  $709 \text{ cm}^{-1}$  [ $A_g$ ] are assigned for hexagonal phase of  $\text{ZnTiO}_3$  [82,220,276]. The peaks at  $390 \text{ cm}^{-1}$  and  $614 \text{ cm}^{-1}$  can be assigned to rutile- $\text{TiO}_2$  (r- $\text{TiO}_2$ ) meanwhile the Raman peak at  $468 \text{ cm}^{-1}$  is ascribed for  $\text{Zn}_2\text{TiO}_4$  respectively

[82,277]. Most of the Raman peaks are well matched in all the samples. Besides, few changes have been noticed in doped samples as compared to undoped samples. We have noticed a significant hump at  $483\text{ cm}^{-1}$  in ENZT-0.25 associated with a peak at  $468\text{ cm}^{-1}$  which can be assigned for  $\text{Zn}_2\text{TiO}_4$  [278]. Meanwhile, both the above peaks are merged in ENZT-1 as represented in Figure 4.5. The emergence of this new peak at  $483\text{ cm}^{-1}$  in ENZT-0.25 and ENZT-1 might be due to the nitrogen doping in  $\text{ZnTiO}_3$  lattice. As nitrogen doping suppresses the formation of h- $\text{ZnTiO}_3$  thereby increasing impurities of  $\text{Zn}_2\text{TiO}_4$ . It has been noticed that the peaks at  $390\text{ cm}^{-1}$  and  $614\text{ cm}^{-1}$  of r- $\text{TiO}_2$  were suppressed in ENZT-0.25 after that omitted in ENZT-1. This is in good agreement with the XRD data where the XRD peak at  $27.40^\circ$  of r- $\text{TiO}_2$  disappeared in nitrogen-doped samples. However, a weak peak at  $44.40^\circ$  in XRD of ENZT-0.25 shows the presence of r- $\text{TiO}_2$  causes r- $\text{TiO}_2$  peaks in the Raman spectra of ENZT-0.25 as depicted in Figure 4.5. We have detected a weak peak at  $320\text{ cm}^{-1}$  and a broad hump at  $565\text{ cm}^{-1}$  (represented by  $\times$ ) in ENZT-1 which can be assigned to vibration of Ti-N bond in doped  $\text{ZnTiO}_3$  [245,279]. However, the same peaks are not detectable in ENZT-0.25 may be due to least nitrogen present in the sample. The Raman peak at  $709\text{ cm}^{-1}$  corresponds to hexagonal  $\text{ZnTiO}_3$  has been appeared in BZT, EZT, and ENZT-0.25. However, the same peak in ENZT-0.25 is wider than the BZT and EZT. Meanwhile, the same peak has been shifted and appeared at  $724\text{ cm}^{-1}$  (represented by  $\bullet$ ) in ENZT-1 as represented in Figure 4.5. The broadening and shifting in the peaks suggest nitrogen doping in the  $\text{ZnTiO}_3$  nanoparticles [280]. Previously, it has been reported that higher nitrogen doping causes larger shifts in Raman peaks [281]. Therefore, Raman data also concludes the nitrogen doping in  $\text{ZnTiO}_3$ .

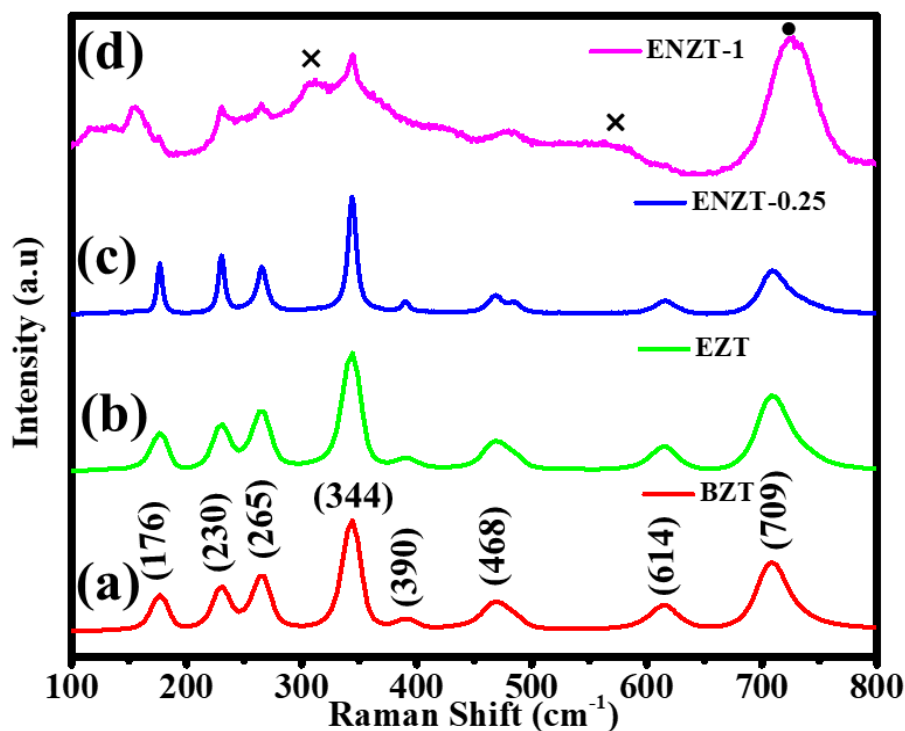


**Figure 4.5. Raman spectra of (a) BZT, (b) EZT, (c) ENZT-0.25, and (d) ENZT-1.**

#### 4.4.3 Fourier Transform Infrared Spectroscopy (FTIR)

The FTIR spectra of BZT, EZT, ENZT-0.25, and ENZT-1 have been represented in Figure 4.6. The low range FTIR bands from  $650\text{ cm}^{-1}$  to  $600\text{ cm}^{-1}$  are assigned for stretching vibration of Ti-O bonds in the  $\text{TiO}_6$  octahedra exist in  $\text{ZnTiO}_3$  [241,282]. It is also seen that the main characteristic peak of  $\text{ZnTiO}_3$  at  $562\text{ cm}^{-1}$  and  $590\text{ cm}^{-1}$  shifted to higher wavenumber region in the N doped samples as shown in Figure 4.6 [228]. The blue shift of these peaks indicates the change in bond strength of Zn-Ti-O, suggesting the successful N doping in the  $\text{ZnTiO}_3$  crystals [283]. This is in good agreement with the published article by Surendar et. al, where they have reported the redshift in the La-doped  $\text{ZnTiO}_3$  nanoparticles [283]. Further, we have reported higher wavenumber FTIR peaks as following. It is clear from Figure 4.6a that all the samples have common bands in the range of  $3700\text{ cm}^{-1}$  to  $3400\text{ cm}^{-1}$  which can be ascribed for the presence of free -OH groups over the surface of the nanoparticles [229]. Moreover, the FTIR bands at  $2981\text{ cm}^{-1}$

<sup>1</sup>, 2928 cm<sup>-1</sup>, and 2952 cm<sup>-1</sup> can be assigned to the stretching vibration of residual C-H from the organic compounds [229]. We have noticed a common band at 2361 cm<sup>-1</sup> in EZT, ENZT-0.25, and ENZT-1 while this band is missing in the BZT sample. This FTIR band at 2361 cm<sup>-1</sup> may be due to the residual organics from PVA. However, Babu et al, assigned this peak at 2361 cm<sup>-1</sup> to the incorporation of the nitrogen in the octahedral of TiO<sub>2</sub> to form O-Ti-N bonds [272]. Several FTIR bands are detectable in the range of 1800 cm<sup>-1</sup> to 800 cm<sup>-1</sup> in nitrogen-doped samples, among them some bands are common to both ENZT-0.25 and ENZT-1. However, the band intensities in the ENZT-0.25 sample is lower than the ENZT-1. Meanwhile few extra bands are also noticed for higher nitrogen-doped sample ENZT-1. The FTIR shows the N-ZnTiO<sub>3</sub> may have two kinds of N species; at ZnTiO<sub>3</sub> surface and incorporated into ZnTiO<sub>3</sub> lattice. The band at 1544 cm<sup>-1</sup>, 1516 cm<sup>-1</sup>, and 1383 cm<sup>-1</sup> in the nitrogen-doped samples could be assigned to the N-O bond vibration of surface adsorbed NO<sub>3</sub><sup>-1</sup> as represented by (●) in Figure 4.6b [228,282]. Meanwhile, the two peaks at 1070 cm<sup>-1</sup> and 1106 cm<sup>-1</sup> can be assigned to the nitrogen (hyponitrite: (N<sub>2</sub>O<sub>2</sub>)<sup>2-</sup>) adsorbed to the ZnTiO<sub>3</sub> surface [284,285]. Also, the peaks at 1315 cm<sup>-1</sup> and 1608 cm<sup>-1</sup> can be assigned to the symmetric stretching and bending of N-O bond in NO<sub>2</sub><sup>-1</sup>[281]. Thus urea promotes the formation of NO<sub>3</sub><sup>-1</sup>, (N<sub>2</sub>O<sub>2</sub>)<sup>2-</sup>, and NO<sub>2</sub> in the ENZT-1 samples. The FTIR spectra also exhibit peaks at 1152 cm<sup>-1</sup>, 1280 cm<sup>-1</sup>, 1234 cm<sup>-1</sup>, 1164 cm<sup>-1</sup>, and 1436 cm<sup>-1</sup> can be related to the N incorporated into TiO<sub>2</sub> network as N-Ti bond in the ENZT-0.25 and ENZT-1 (represented by ♦) [282,285,286]. However, few peaks are noticed to be shifted in the ENZT-1 as compare to ENZT-0.25 samples. Moreover, extra FTIR bands have been observed in a highly N doped sample (ENZT-1) as compared to other samples. These bands suggest the presence of organic molecules on the ENZT-1. Hence, FTIR suggests nitrogen doping in ZnTiO<sub>3</sub> at both the interstitial positions and substitutional positions.

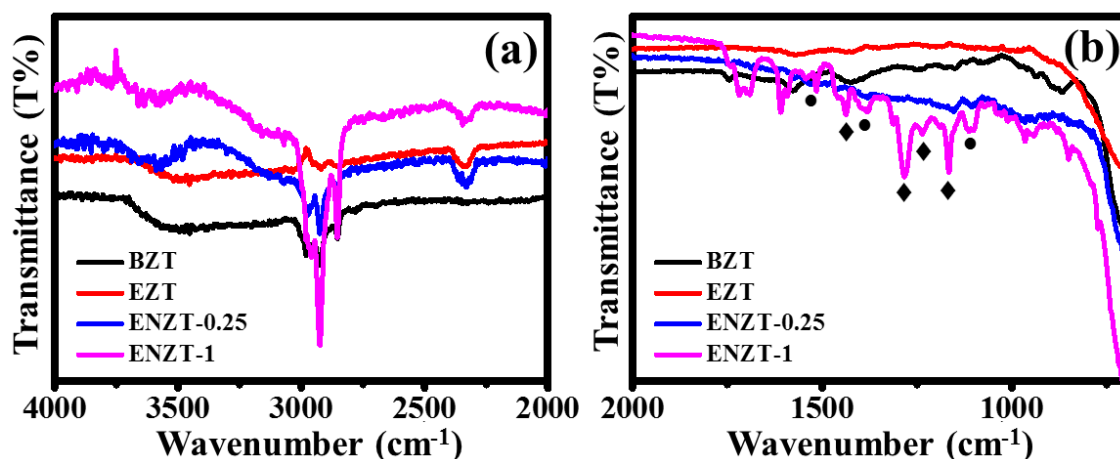
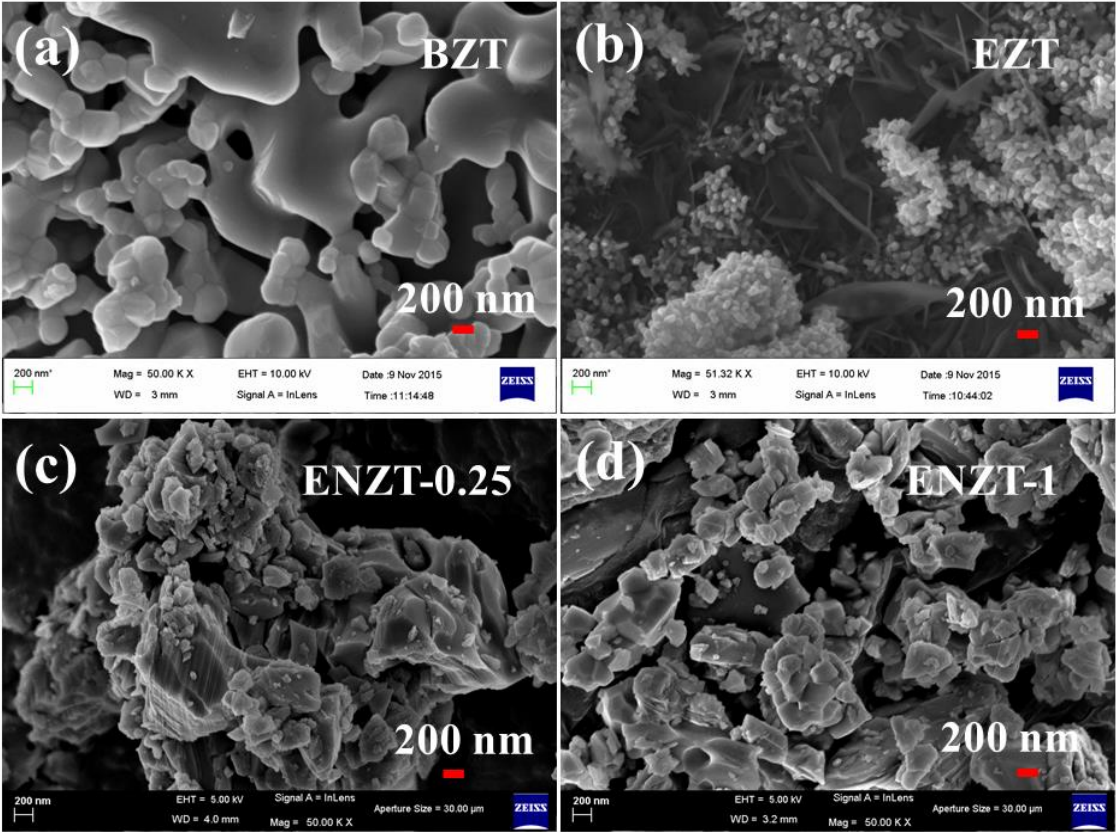


Figure 4.6. FTIR spectra of BZT, EZT, ENZT-0.25, and ENZT-1.00 from (a) 4000  $\text{cm}^{-1}$  to 2000  $\text{cm}^{-1}$ , (b) 2000  $\text{cm}^{-1}$  to 700  $\text{cm}^{-1}$ . The peaks represented by ● and ◆ suggest the incorporation of N into  $\text{ZnTiO}_3$  lattice.

#### 4.4.4 Field Emission Scanning Electron Microscopy (FESEM) analysis

The FESEM is a technique to visualize the topographic details of the surface of nanoscale samples. Figure 4.7 shows FESEM images of BZT, EZT, ENZT-0.25, and ENZT-1. The particle size of the BZT is larger than 200 nm as can be seen in Figure 4.7a. However, the particle size of the EZT in Figure 4.7b decreases drastically and lies in the range of 20 nm to 50 nm attributing to the electrospinning of the sample. But, electrospinning of nitrogenated sol of  $\text{ZnTiO}_3$  results in bigger particles upon calcination. On the comparison

between the doped samples with EZT, bigger size particles (200 nm-600 nm) have



**Figure 4.7. FESEM images of (a) BZT, (b) EZT, (c) ENZT-0.25, and (d) ENZT-1 at 50000 X magnification.**

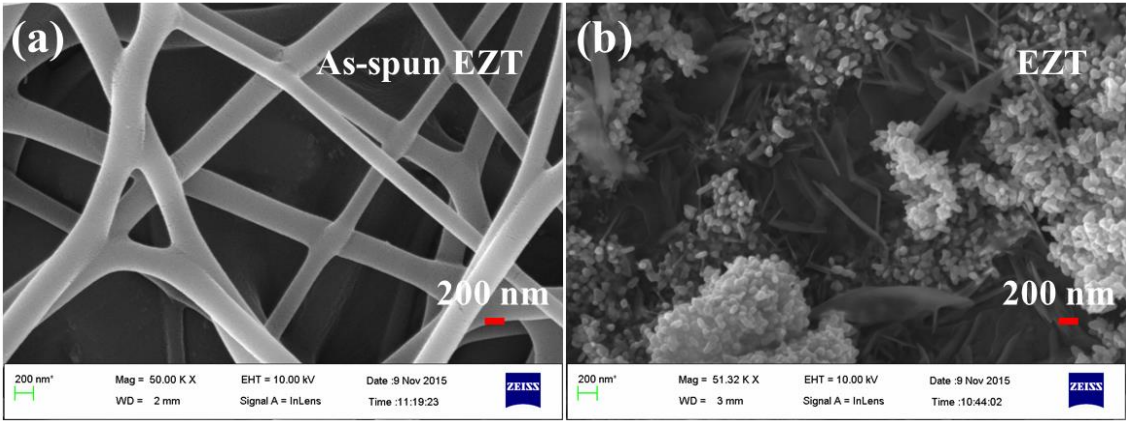


**Figure 4.8. FESEM images of (a) as-spun EZT (b) EZT at 50000 X magnification.**

appeared in ENZT-0.25 and ENZT-1 as depicted in Figure 4.7c-d. It can be observed that the particles are aggregated in ENZT-0.25 and ENZT-1. In addition, the electrospinning of ZnTiO<sub>3</sub> sol successfully fabricates the nanofibrous structure as seen in Figure 4.8a.

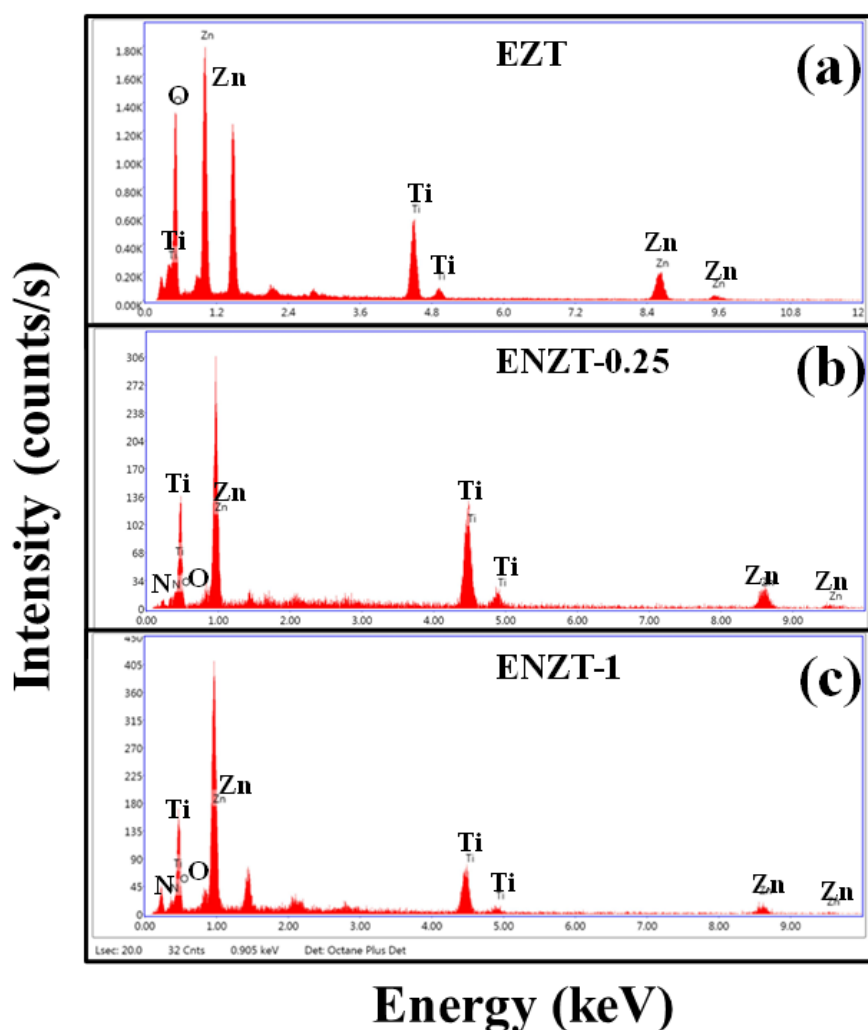


**Figure 4.9. Energy Dispersive X-Ray (EDS) of (a) EZT, (b) ENZT-0.25, and (c) ENZT-1 represents the presence of Zn, Ti, O and N in the respective samples.**

The diameter of the as-spun nanofibers is around 200 nm to 400 nm while the length is in several micrometers. The morphology in Figure 4.8a suggests a smooth surface which indicates the presence of the organics. The as-spun nanofibers are calcined at 900 °C in an air furnace which results in nanoparticles of 20 nm-50 nm in size as seen in Figure 4.8b. Thus, the nanofibers could not retain their fibrous structure upon calcination which is due to the burning of organics from the surface, crystallization of EZT nanoparticles, and coalescence of the grains [287].

The elemental compositional analysis is performed by Energy Dispersive X-ray Spectroscopy (EDS). The EDS of EZT is depicted in Figure 4.9a confirming zinc (Zn),

titanium (Ti), and oxygen (O) elements in the samples. Besides this, Figure 4.9b-c asserts the presence of zinc (Zn), titanium (Ti), oxygen (O), and nitrogen (N) elements in ENZT-0.25 and ENZT-1. So it is concluded that nitrogen is successfully incorporated in the  $\text{ZnTiO}_3$  lattice.

#### 4.4.5 X-ray Photoelectron Spectroscopy

The elemental analysis of the EZT and ENZT-1 is represented in Figure 4.10 and Figure 4.11. The chemical state of N can be identified by deconvolution of its XPS peak. The N1s orbital energy can be deconvoluted into two peaks at 397.36 eV and 399.37 eV in Figure 4.10a. Previously reported articles infer that the N1s peaks in the range of 396 eV-397.5 eV have been identified as the substitutional nitrogen ( $\text{N}_s$ ) which replace the oxygen in the lattice and making Ti-N-Ti linkage [143,288,289]. Therefore, the peak at 397.36 eV in the current research can be assigned to the substitutional nitrogen ( $\text{N}_s$ ) at the oxygen lattice sites indicating Ti-N-Ti linkage. The other deconvoluted peak of N1s appears at 399.37 eV in Figure 4.10a. Researches have assigned the binding energy of interstitial nitrogen (in the atomic form) in  $\text{TiO}_2$  octahedra in the range of 399-401 eV [290–292]. Also, it is reported experimentally and theoretically the same range of binding energy (399-401 eV) of the interstitial nitrogen in different kinds of environmental species such as hyponitrite ( $\text{N}_2\text{O}_2$ )<sup>2-</sup> to nitrite ( $\text{NO}_2^-$ ), and nitrate ( $\text{NO}_3^-$ ) [285,288]. Therefore, specific identification of interstitial position occupied by atomic nitrogen is difficult. Thus, we attribute the peak at 399.37 eV for interstitial nitrogen and assume that both atomic nitrogen and oxidized nitrogen are present in ENZT-1. Moreover, the probability is higher to occupy interstitial positions by oxidized nitrogen. This is also supported by the FTIR data where ( $\text{N}_2\text{O}_2$ )<sup>2-</sup>, ( $\text{NO}_2^-$ ), and nitrate ( $\text{NO}_3^-$ ) peaks are present.

Figure 4.10b-c represents the O 1s spectra for EZT and ENZT-1. The XPS peaks are deconvoluted into two peaks at 530.85 eV and 532.61 eV in the EZT. These peaks

can be attributed to the lattice oxygen (in Zn-O and Ti-O) and oxygen in surface adsorbed hydroxyl groups [233]. However, XPS spectra of core level O 1s can be deconvoluted into three peaks at 529.77 eV, 531.04 eV, and 532.25 eV in ENZT-1. The peaks at 529.77 eV and 532.25 eV are assigned to lattice oxygen ( $O_L$ ) as Zn-O and Ti-O and oxygen in surface adsorbed hydroxyl groups ( $O_{OH}$ ) [233]. Moreover, these peaks are noticed to be shifted toward lower binding energy as compared to EZT. This observation is consistent with the earlier reported articles [281,288]. The shift in binding energy can be due to the electronegativity difference between oxygen and nitrogen [233]. As the electronegativity of the oxygen is higher than nitrogen, therefore, the substituted nitrogen will lead to decrease electron density on anions. This increases the electron density of the other ions. Due to the change in electron density over other ions, the electron screening effect would be prominent subsequently, XPS peaks will shift to the lower binding energy [233]. In addition to this, one extra XPS peak appears at 531.04 eV in the ENZT-1. This peak may be assigned to the oxygen ( $O_N$ ) in hyponitrite ( $N_2O_2$ )<sup>2-</sup>, nitrite ( $NO_2^-$ ), and nitrate ( $NO_3^-$ ) [288]. Feng et. al, have suggested the peak at 531.5 eV to the formation of hyponitrite ( $(N_2O_2)^{2-}$ ) [288]. Further, to acquire in-depth information, we have calculated the area% of deconvoluted O 1s peaks as given in Table 4.5. The area percentage of  $O_L$  and  $O_{OH}$  is 72.96% and 27.03% respectively in EZT. This area% has decreased to 68.10% and 13.34% for  $O_L$  and  $O_{OH}$  in ENZT-1. The decrease in area% of lattice oxygen in the doped sample may denote that the oxygen has been substituted by nitrogen and also may give an indication of increasing oxygen vacancies. The formation of nitrates may decrease the surface hydroxyl groups thereby the area% of  $O_{OH}$  reduces. Area% of  $O_N$  is calculated at 18.64% in ENZT-1.

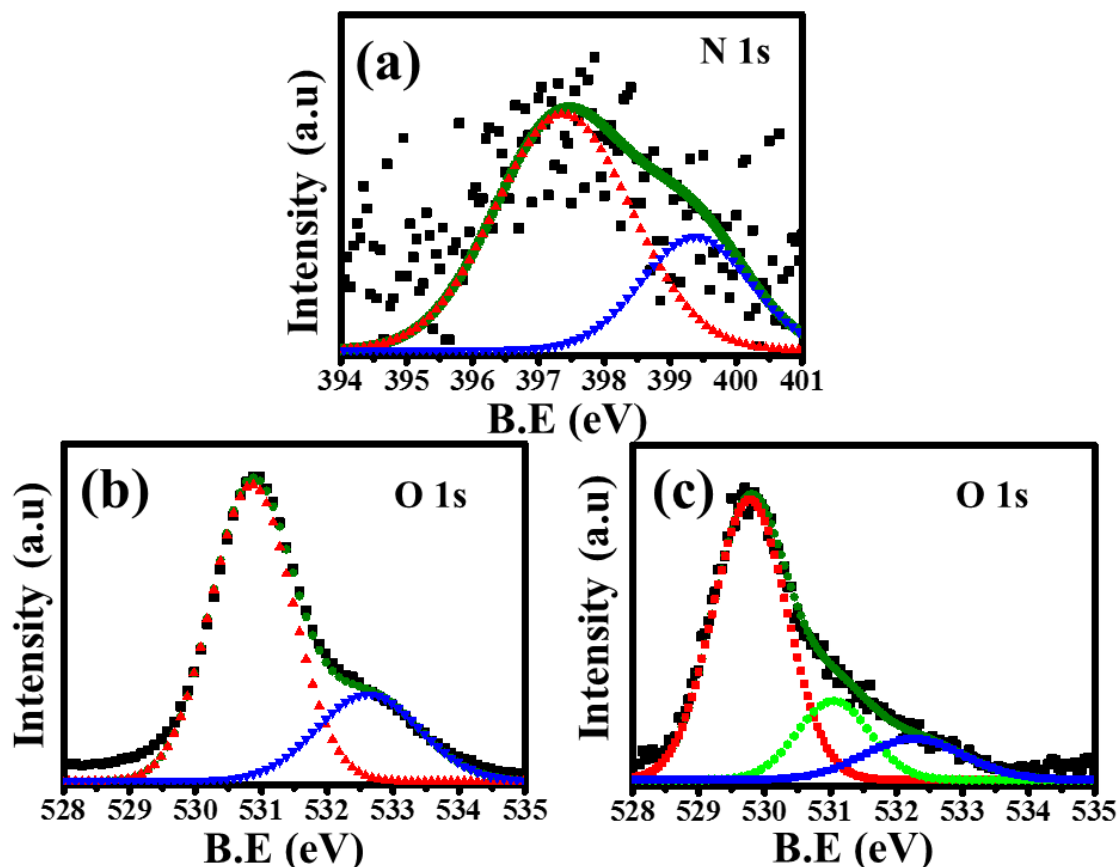


**Figure 4.10.** XPS of (a) N 1s of ENZT-1, (b) O 1s of EZT, and (c) O 1s of ENZT-1.

The titanium and zinc core-shell level XPS spectra are depicted in Figure 4.11. The Ti 2p can be deconvoluted into four peaks at 459.28 eV, 460.38 eV, 464.08 eV, and 465.16 eV in EZT as represented in Figure 4.11a. The core-level peaks at 459.28 eV and 465.16 eV represent  $\text{Ti}^{4+}$  2p<sub>3/2</sub> and  $\text{Ti}^{4+}$  2p<sub>1/2</sub> orbital respectively attributing to the presence of  $\text{Ti}^{4+}$  in EZT [293]. Also, the EZT contains  $\text{Ti}^{3+}$  in a significant amount as confirmed by the peaks at 460.38 eV, 464.08 eV assigned for  $\text{Ti}^{3+}$  2p<sub>3/2</sub>, and  $\text{Ti}^{3+}$  2p<sub>1/2</sub> respectively [293,294]. Whereas in ENZT-1, the core level XPS peaks of Ti 2p have appeared at 458.24 eV, 459.47 eV, 463.01 eV, and 464.18 eV as represented in Figure 4.11b. The data are given in Table 4.5. These peaks suggest the presence of  $\text{Ti}^{4+}$  and  $\text{Ti}^{3+}$  in ENZT-1. It is noticed that the Ti 2p core-level XPS peaks have been shifted towards lower binding energy in ENZT-1. Moreover, the comparison between the area% in EZT and ENZT-1 indicates that  $\text{Ti}^{4+}$  decreases and  $\text{Ti}^{3+}$  increases in ENZT-1 as compare to EZT.

This can be attributed to the partial reduction of  $Ti^{4+}$  to  $Ti^{3+}$  by doped nitrogen. This further confirms the doping of nitrogen at interstitial and substitutional positions. These changes in XPS of Ti are emerged due to the electronegativity difference between oxygen and nitrogen and the proper reason has been given above.

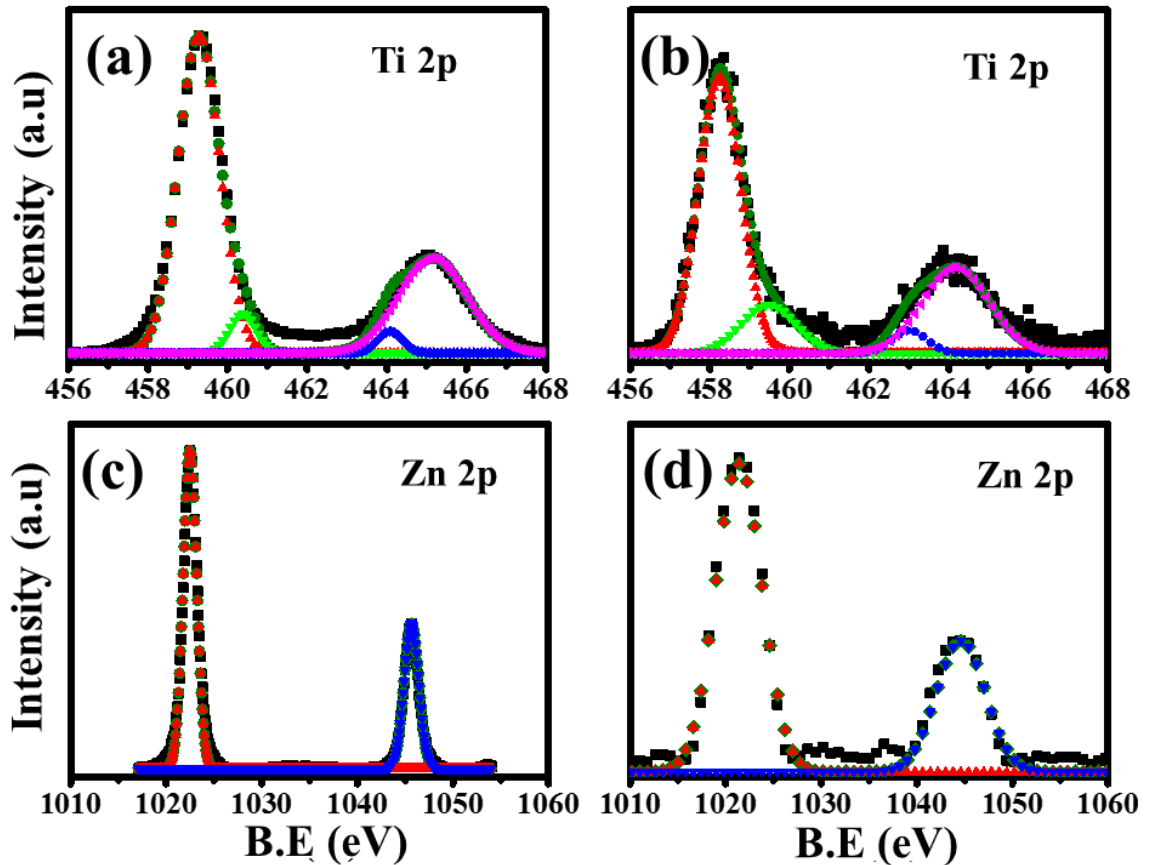


**Figure 4.11.** XPS analysis of (a) Ti 2p of EZT, (b) Ti 2p ENZT-1, (c) Zn 2p EZT, and (d) Zn 2p ENZT-1.

The high-resolution XPS spectra of Zn 2p are given in Figure 4.11c-d for EZT and ENZT-1 respectively. XPS peak of Zn 2p can be deconvoluted into two peaks at 1022.48 eV, 1045.65 eV attributing to Zn  $2p_{3/2}$ , and Zn  $2p_{1/2}$  respectively in EZT [233,295]. However, Zn  $2p_{3/2}$  and Zn  $2p_{1/2}$  appear at 1021.36 eV and 1044.60 eV respectively in ENZT-1. This confirms the +2 oxidation state of Zn in EZT and ENZT-1 samples [295]. We noticed a shift of around 1 eV towards lower binding energy in ENZT-1. This is due to the nitrogen doping in ENZT-1 and somewhat due to the above reason. The FWHM of

the Zn signal in ENZT-1 increases as compare to EZT may be due to N<sup>3-</sup> substitution of O<sup>2-</sup> [233].

**Table 4.5. The representation of binding energy (B.E) and area % of the elements in ENZT-1 and EZT.**

|              | ENZT-1   |        | EZT      |        |
|--------------|----------|--------|----------|--------|
|              | B.E (eV) | Area % | B.E (eV) | Area % |
| <b>N 1s</b>  | 397.36   | 72.01  |          |        |
|              | 399.37   | 27.98  |          |        |
| <b>O 1s</b>  | 529.77   | 68.10  | 530.85   | 72.96  |
|              | 531.04   | 18.64  | -        | -      |
|              | 532.25   | 13.34  | 532.61   | 27.03  |
| <b>Ti 2p</b> | 458.24   | 56.13  | 459.28   | 62.24  |
|              | 459.47   | 12.67  | 460.38   | 4.84   |
|              | 463.01   | 3.78   | 464.08   | 2.53   |
|              | 464.18   | 27.40  | 465.16   | 30.40  |
| <b>Zn 2p</b> | 1021.36  | 69.00  | 1022.48  | 66.87  |
|              | 1044.60  | 30.99  | 1045.65  | 33.12  |

#### 4.4.6 UV-Vis Diffuse Reflectance Spectroscopy

The UV-Vis DRS data was recorded to elucidate the bandgap engineering of ZnTiO<sub>3</sub> after nitrogen doping. The bandgap energy has been calculated for all the samples by using the modified Kubelka-Munk function given in Equation (3-2). Figure 4.12 represents the bandgap energy for all the samples by assuming indirect transition. We have noticed a remarkable decrease in the bandgap of the doped samples as listed in Table 4.6. The bandgap energy has been calculated at 2.89 eV, 2.83 eV, 2.63 eV, and 2.25 eV for BZT, EZT, ENZT-0.25, and ENZT-1 respectively. The little decrease in EZT bandgap energy ( $E_g=2.89$  eV) compare to BZT bandgap energy ( $E_g=2.83$  eV) attributes to the surface defects generated by electrospinning of ZnTiO<sub>3</sub> [71]. However, the sharp decrease in bandgap energy of ENZT-0.25 and ENZT-1 can attribute to the extra electronic states provided by nitrogen doping in ZnTiO<sub>3</sub> [135].

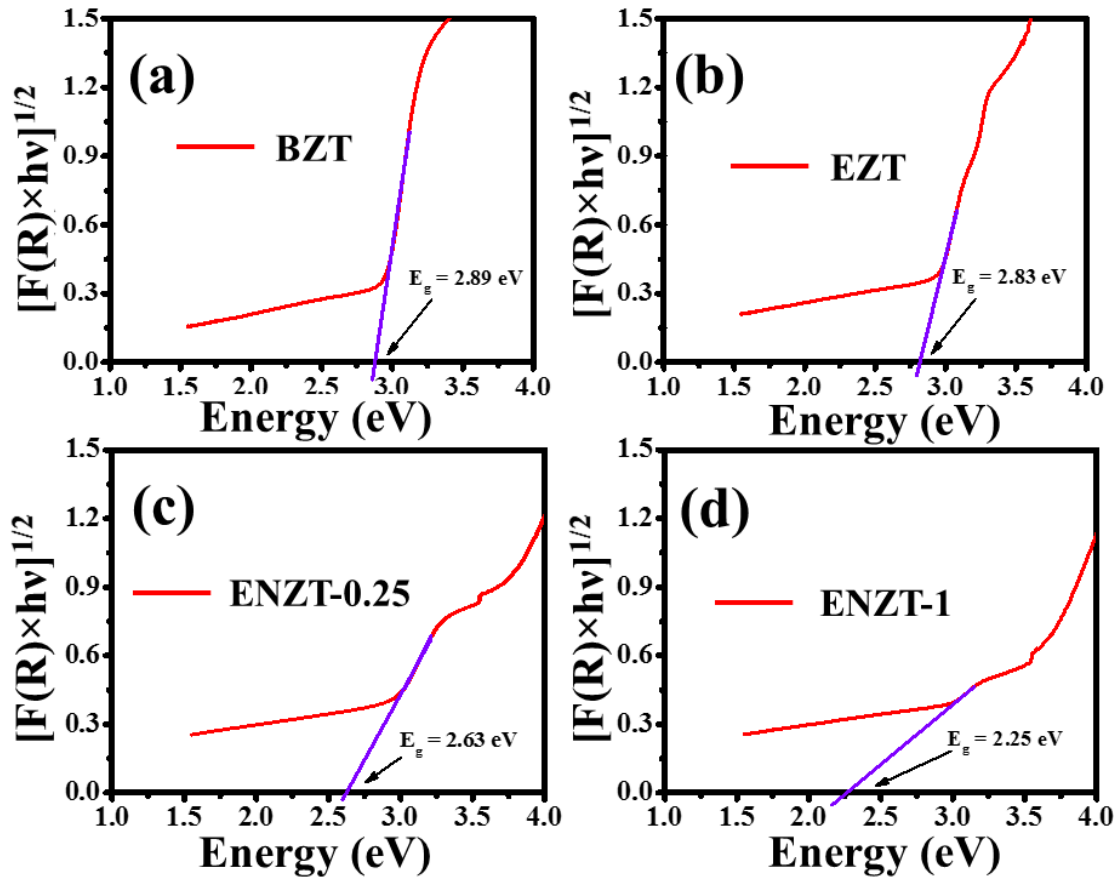
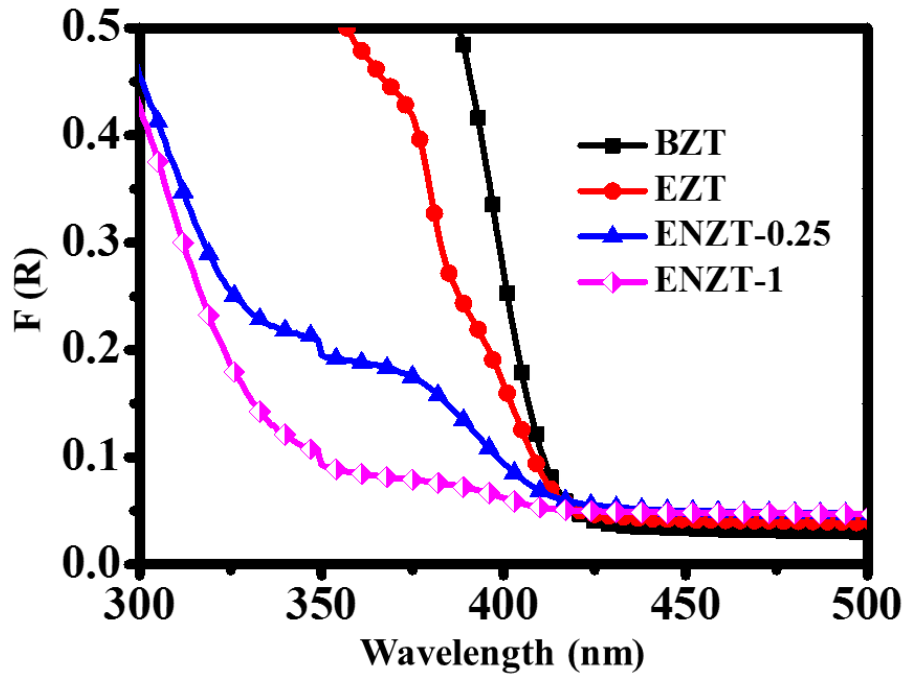


Figure 4.12. Plots of modified Kubelka-Munk function versus the energy of exciting light leading to the bandgap of (a) BZT, (b) EZT, (c) ENZT-0.25, and (d) ENZT-1.

Table 4.6. The bandgap energy of BZT, EZT, ENZT-0.25, and ENZT-1.00

| Sample Name | Bandgap Energy ( $E_g$ ) |
|-------------|--------------------------|
| BZT         | 2.89 eV                  |
| EZT         | 2.83 eV                  |
| ENZT-0.25   | 2.66 eV                  |
| ENZT-1      | 2.25 eV                  |

Next, we have explained the existence of surface states by DRS data. Figure 4.13 represents the plot between  $F(R)$  versus wavelength ( $\lambda$ ) which reveals that the absorption onset is steep in all the samples.



**Figure 4.13. Representation of  $F(R)$  versus wavelength for BZT, EZT, ENZT-0.25, and ENZT-1. Increasing steepness in graphs for higher nitrogen doping suggests the surface states in samples.**

However, the absorption onset is maximum steeper in BZT and continuously decreases for the other samples in a regular pattern. This represents the availability of the surface defects and anion vacancies that generate localized intra-bandgap states, the so-called *surface states* [35]. Therefore,  $ZnTiO_3$  is reported as an n-type semiconductor [87]. The flat absorption shoulders are conspicuous in the case of EZT as compared to BZT. This might be due to the creation of more surface defects arising due to mesoporosity as the electrospinning technique reduces the size of the materials [71]. The fast decreasing steepness in nitrogen-doped samples may indicate much-increasing surface states (surface defects and anion vacancies) along with other reasons (will discuss later in the same section). The decreasing steepness in ENZT-0.25 and ENZT-1 can chiefly attribute

to the increasing oxygen vacancies create upon nitrogen doping to maintain charge neutrality as also supported by the XRD data. However, surface defects generated by electrospinning may be considered approximately equal in EZT, ENZT-0.25, and ENZT-1 because the samples were electrospun under constant experimental conditions. Therefore, it can be concluded that the shrinkage of the bandgap upon nitrogen doping is due to the synergic effect that comes from the creation of mid-gap energy states in between VB and CB, surface defect, and oxygen vacancies.

#### 4.4.7 Photoluminescence Spectroscopy

**All the samples were investigated by the PL technique at room temperature and the results have shown in**

Figure 4.14. The photoluminescence spectra is generated from the recombination of the free charge carriers. The PL spectroscopy extensively uses for the study of the charge carrier trapping, migration and transfer, and the density of the electron-hole pairs in the semiconductor [87,244]. All the samples were excited at wavelength 260 nm and the spectra were recorded from 270 nm to 530 nm. Three emission bands have originated at 357 nm, 420 nm, and 487 nm in all the samples with varying peak intensities, representing the different charge carrier's lifetime. The emission peak at 420 nm corresponds to the bandgap energy 2.9 eV can be assigned to the band to band transition (direct transition) from the conduction band to the valance band. Whereas, the latter band at 487 nm corresponds to bandgap energy 2.54 eV is an emission signal originating from an oxygen vacancy trapped electron and the presence of defects [245]. Also, the emission peak at 357 nm corresponding to 3.5 eV can be attributed to the presence of  $Zn_2TiO_4$  impurities. The PL examination suggests that the PL intensity of the doped samples is quite lower than the undoped sample in the order of  $BZT > EZT > ENZT-0.25 > ENZT-1$ . This reveals that the recombination rate of electron-holes is also in the above order. The lower recombination rate of electron-hole pairs demonstrates that the electrons and holes are

available for a longer time for photocatalytic degradation. Thus, the PL results demonstrate that the doped samples enable efficient separation of photoinduced electron-hole compared with undoped samples. Thus, the nitrogen doping in the  $\text{ZnTiO}_3$  quenches the photoluminescence of the materials and this can be achieved by the two routes: (1) The oxygen vacancies trap the electrons thereby reducing recombination rate. (2) The excited electron transfer from the conduction band to the new defect levels that exist near the conduction band minimum thereby decreases the PL intensity [296].

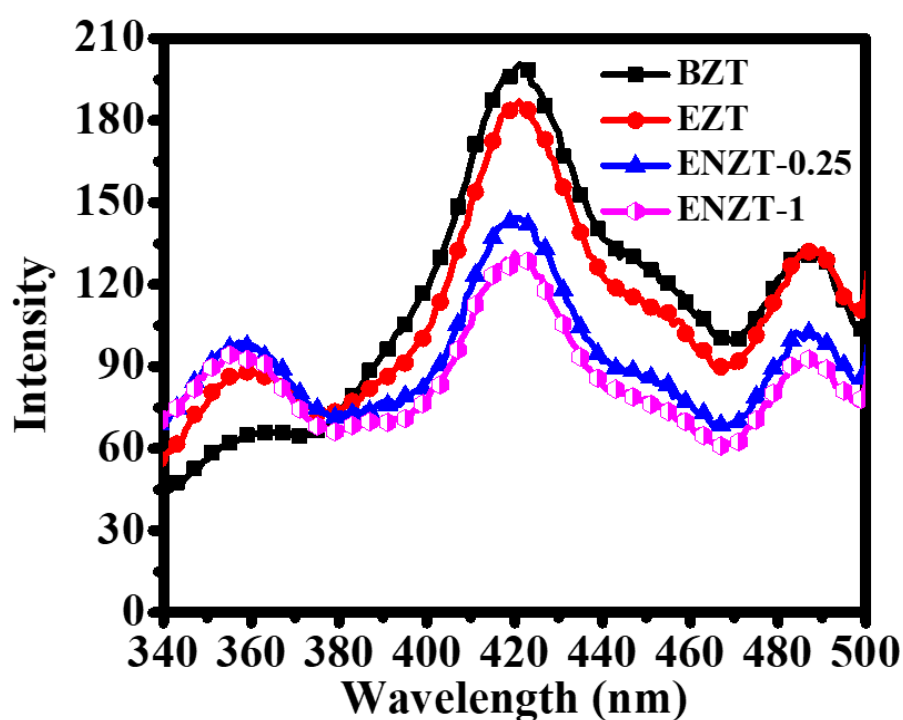
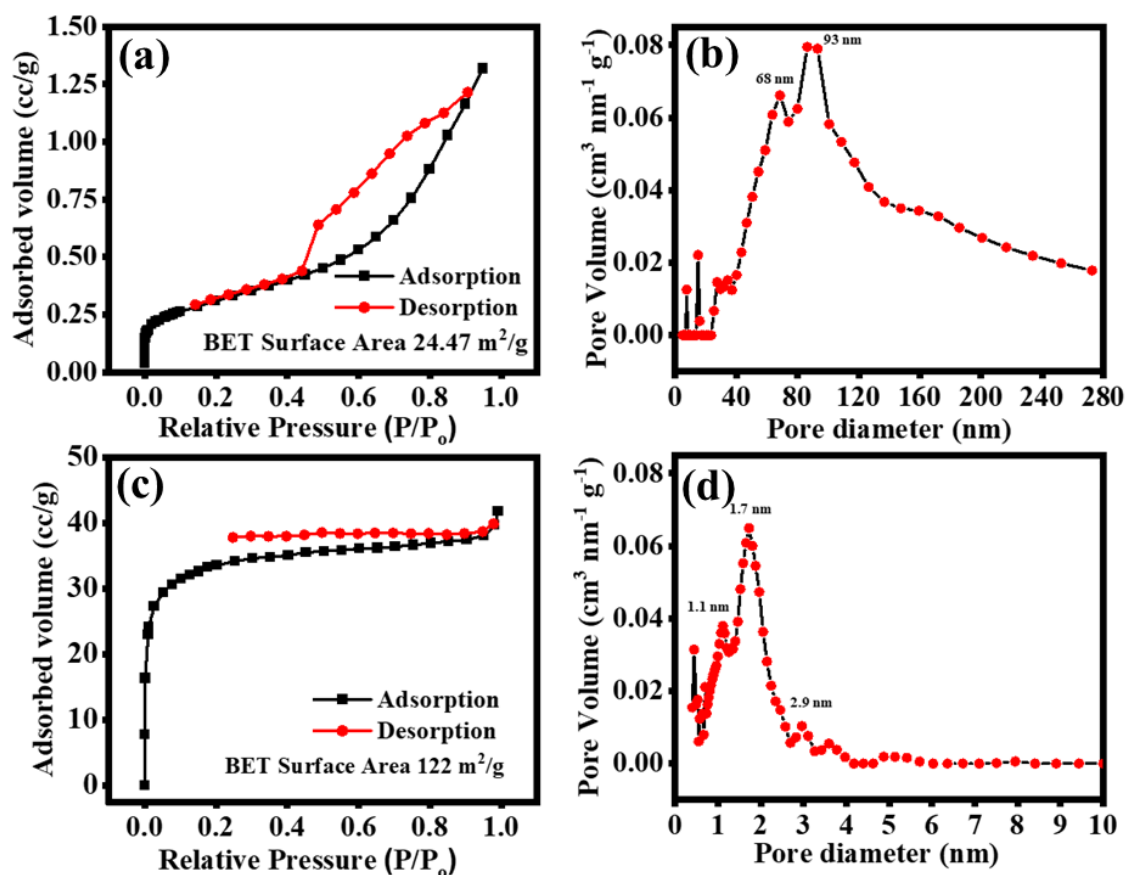


Figure 4.14. PL spectroscopy of BZT, EZT, ENZT-0.25, and ENZT-1.

#### 4.5 Photocatalytic Activity of N- $\text{ZnTiO}_3$ nanopowder

The photocatalytic degradation of phenol has been studied in the aqueous suspension of N- $\text{ZnTiO}_3$  nanopowder under visible light illumination. One important consideration here is the possibility of adsorption of the phenol molecules onto the catalyst powder, so that the disappearance of phenol from the solution can be mistakenly interpreted as photocatalytic degradation. To avoid this error, we have performed the surface area analysis of the electrospun samples with and without nitrogen incorporated, and also

measured the phenol concentration dependence with time under dark conditions. Even though the specific surface area in nitrogenated electrospun samples was relatively much larger ( $122 \text{ m}^2/\text{g}$ ) than that in the un-nitrogenated electrospun samples ( $24.47 \text{ m}^2/\text{g}$ ) as shown in Figure 4.15, the change in phenol concentration with time in presence of these two catalyst samples under dark conditions was negligible. This confirms that adsorption contribution can be ignored and all the degradation observed in presence of light can be attributed to photocatalysis. We speculate that the degradation of the urea molecule during calcination, which may lead to the formation and escape of gaseous nitrogenous compounds, is aiding in the formation of highly porous oxide material.



**Figure 4.15.** The BET surface area and the pore size distribution in EZT ((a) and (b)), and in ENZT-1 ((c) and (d)). A significant change in the surface area and the pore size distribution is observed after nitrogenation, which bears an important effect on photocatalytic behavior.

The photocatalytic degradation process has been conducted in a homemade photoreactor (please see 3.3.3). 50 ml aqueous solution of phenol (100  $\mu\text{M}$ ) has been taken into quartz photo-reactor vessel with 100 mg of ENZT-0.25 and ENZT-1 nanopowder (2 mg/ml) followed by continued stirring. Each time a 2 ml solution has been taken after 30 minutes of time-interval and centrifuged at 1200 rpm for 10 minutes to settle down the photocatalyst. The supernatant has been collected and use for the study of the concentration of phenol by monitoring its UV-Vis peak at 270 nm. First of all, the adsorption experiment has been performed in the dark for one hour to confirm adsorption on the nanopowder surface. The data suggests no adsorption onto the photocatalyst surface. The UV-Vis spectra of the phenol show two absorption peaks at 210 nm and 270 nm corresponding  $\pi$ - $\pi^*$  and n- $\pi^*$  transitions respectively. The photocatalytic activity of phenol has been evaluated after recording the intensities of main absorption peaks at 270 nm and accordingly, concentration has been plotted against time. As stated in the beginning that the four nitrogen-doped samples have been prepared named ENZT-0.25, ENZT-0.50, ENZT-0.75, and ENZT-1 along with this, their counterpart bulk nitrogen-doped samples (BNZT-0.25, BNZT-0.50, BNZT-0.75, and BNZT-1) have been also prepared. All the prepared samples have been examined for phenol degradation in the presence of visible light. The UV-Vis data fit into first-order kinetic Equation (3-3) to study the kinetics of photocatalytic degradation of phenol [297]. The data is plotted between  $\log(C/C_0)$  vs time ( $t$ ) as shown in Figure 4.16 (a & c). The linear fit to the data generates slope which is the degradation rate constant ( $k$ ). The degradation rate constants are listed in Table 4.7 and compare with the BZT and EZT. From Table 4.7, it can be noticed that the degradation rate is increasing for doped samples. Thus, nitrogen doping improved the degradation of phenol. We also calculate the degradation efficiency of the

samples towards phenols degradation and data is compared with the BZT and EZT. The degradation efficiency ( $\eta\%$ ) is calculated by Equation (4-3).

$$\eta\% = \left[ \frac{A_0 - A_t}{A_0} \times 100 \right] \% \quad (4-3)$$

where  $A_0$  and  $A_t$  are the initial absorbance and absorbance at the time  $t$  respectively. The calculated degradation efficiencies are given in Table 4.7. The data in Table 4.7 represents that nitrogen doping contributes to the increment in phenol degradation by visible light photocatalysis. The visible light photocatalysis is well established for the metal oxides as photocatalyst [250,264,297]. In short, the photocatalysis process is associative with (1) generation of charge carriers upon irradiating with light energy greater than the bandgap ( $E_g$ ) of the photocatalyst, (2) transfer of photogenerated charge carriers, and (c) consumption of the photogenerated electrons and holes in the CB and VB respectively [297,298]. Our previous study indicates the bandgap energy of BZT and EZT at 2.89 eV and 2.83 eV respectively [71]. EZT samples may have comparatively more surface states than BZT thereby reducing bandgap energy trivially. Also, it is clear from the DRS and XPS data that nitrogen doping in  $ZnTiO_3$  lattice increases  $Ti^{3+}$  defects. Moreover, the DRS data suggests bandgap lessening. Based on the above analysis of EZT and ENZT-1 by DRS and XPS, the schematic diagram for the effective photocatalysis charge transfer mechanism has been shown in Figure 4.17. It is reported that the position of  $Ti^{3+}$  defects levels and N 2p orbital depends upon the synthesis process [273]. Therefore, the level of the  $Ti^{3+}$  defects will appear below the conduction band (CB) and N 2p orbitals will be formed above the valance band (VB) edge thereby reducing the bandgap energy of the doped zinc titanate [273]. This bandgap energy further decreases for higher nitrogen content sample ENZT-1 as calculated by DRS data. The electrons in VB and N 2p states absorb energy on excitation and jump to the  $Ti^{3+}$  states and CB, leaving holes behind. The excited electrons trap in  $Ti^{3+}$  states leading to the delaying in the recombination of

electrons and holes. Trapping of the excited electrons in  $\text{Ti}^{3+}$  increases the lifetime of both charge carriers thereby these are available for photocatalysis reaction at the photocatalyst surface. This may be a reason behind improved phenol degradation in visible light by ENZT-0.25 and ENZT-1.

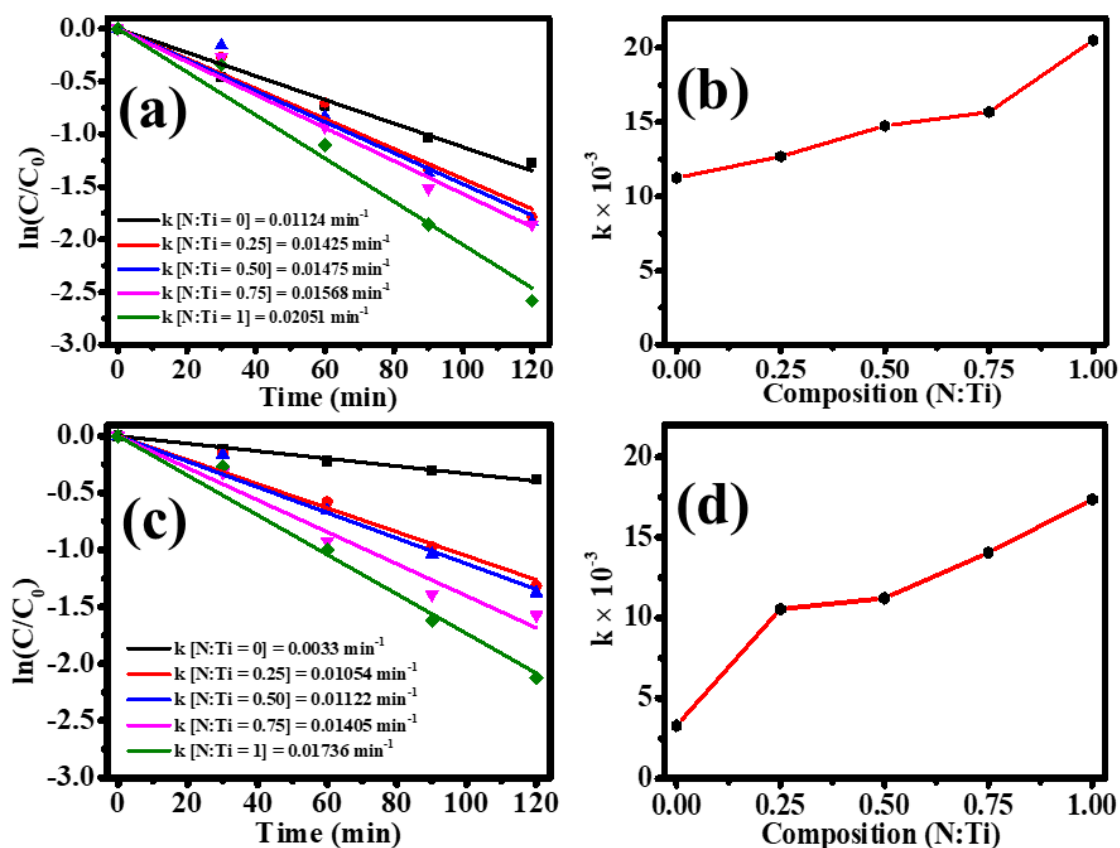
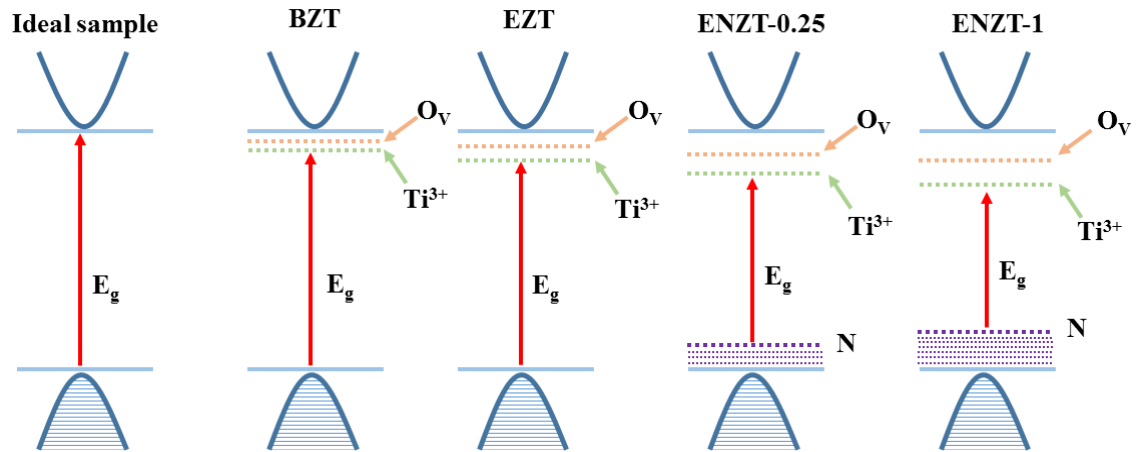


Figure 4.16. (a) & (c): the first-order-rate kinetics, and (b) & (d): the plot of degradation constant ( $k$ ) versus composition (N:Ti) of electrospun N-doped ZnTiO<sub>3</sub> samples and bulk N-doped ZnTiO<sub>3</sub> samples respectively.

**Table 4.7. The calculation of the first-order-rate constant ( $k$ ) and % of photocatalytic degradation efficiencies.**

| <b>Sample</b> | <b><math>k</math> (min<sup>-1</sup>)</b> | <b><math>\eta</math> % (270 nm)</b> |
|---------------|--|-------------------------------------|
| BZT           | 0.0033                                   | 31.65                               |
| BNZT-0.25     | 0.01054                                  | 73.59                               |
| BNZT-0.50     | 0.01122                                  | 74.39                               |
| BNZT-0.75     | 0.01405                                  | 79.25                               |
| BNZT-1.00     | 0.01736                                  | 87.56                               |
| EZT           | 0.01124                                  | 71.92                               |
| ENZT-0.25     | 0.01425                                  | 75.53                               |
| ENZT-0.50     | 0.01475                                  | 84.01                               |
| ENZT-0.75     | 0.01568                                  | 84.34                               |
| ENZT-1.00     | 0.02051                                  | 92.42                               |



**Figure 4.17.** Proposed scheme to represents the nitrogen electronic states, surface states in doped samples.



## **Chapter 5: Dramatic enhancement in adsorption of congo red dye in polymer-nanoparticle composite of polyaniline-zinc titanate**

### **5.1 Abstract**

<sup>2</sup>Adsorbent materials with high and rapid adsorption properties are required always. We found dramatic enhancement in the adsorptive removal of Congo Red (CR) dye by polyaniline-zinc titanate (PANI/ZTO) nanocomposite as compared with that when PANI or ZTO are used separately. The dye exhibited little adsorption in the presence of lab-synthesized pristine ZnTiO<sub>3</sub> (ZTO) powder as adsorbent and somewhat moderate adsorption in the presence of neat polyaniline whereas an excellent and much faster adsorption was exhibited in the presence of PANI/ZTO nanocomposite. The composite was prepared by carrying out the polymerization of aniline in the presence of ZTO suspensions. The composite samples were characterized using X-Ray diffraction, FT-IR Spectroscopy, field emission scanning electron microscopy (FESEM), X-ray photoelectron spectroscopy (XPS), and dynamic light spectroscopy (DLS), and the adsorption kinetics were studied using UV-vis spectroscopy. The characterization data suggest that the adsorption of the CR dye gets enhanced because PANI chain molecules which are chiefly responsible for adsorption through  $\pi$ - $\pi$  interactions with the dye, get adsorbed/tethered on to the ZTO nanoparticles, and thereby overcome the mass transfer limitation by being better exposed to the dye molecules. The kinetics of adsorption followed the pseudo-second-order rate equation and the rate of adsorption was controlled by intra-particles diffusion. The isotherm was best described by the Langmuir model and

---

<sup>2</sup> **Singh. S, Perween. S, Ranjan. A**; *Journal of Environmental Chemical Engineering*: [doi.org/10.1016/j.jece.2021.105149](https://doi.org/10.1016/j.jece.2021.105149)

the maximum adsorption was calculated to be 64.51 mg/g. The value of 7.80 kJ/mole obtained from the Dubinin-Radushkevich (DR) model suggested the physisorption of CR onto PANI/ZTO nanocomposite. These results suggest that the mass of a polymeric substance in general can be better utilized for adsorption by suitably dispersing them over the surface of appropriate support nanoparticles.

## 5.2 Introduction

Polymer nanoparticle composites have been utilized for a range of engineering applications such as visible light photocatalysis, adsorption, energy storage, dielectric applications, water treatment, electrical energy storage, anticorrosion, solar cells, fuels cells, *etc.*, in recent past [299–304]. Polymer strands tethered or adsorbed on the nanoparticle surfaces can impart desired functionalities to the nanoparticulate materials. Treatment of chemicals in wastewater through adsorption could be an important area of application of such composites. The polymer chains can provide appropriate interaction sites for a given adsorbate molecule and thereby serve as good adsorbent materials. The adsorption can be facilitated and tuned by suitably modifying the monomer chemistry and their interaction with the adsorbing species. A polymeric substance designed so as to exhibit good adsorption capacity towards a particular compound can be utilized as an adsorbent material, and adsorption is ordinarily carried out by heterogeneous routes with adsorbent present in the solid phase and adsorbing species in liquid. In heterogeneous adsorption, it is easy to separate the treated liquid but the subsurface polymer chains in the solid adsorbent particles may not be efficiently utilized for adsorption due to mass transfer limitations. One may envision homogeneous adsorption where the *dissolved* strands are utilized for adsorption, but here separation of the dissolved polymers after the treatment becomes a necessary but difficult step. One possible way to overcome both these limitations in ease of separation and effective utilization of the adsorbent mass is to

distribute the polymer strands over inorganic nanoparticle surfaces. In this approach, most polymeric matter is present at the surface, and therefore is better accessible to the adsorbate species present in the liquid phase. And moreover, the nanoparticles carrying the polymers along with the adsorbed species on its surface can be easily separated from the parent liquid. In this paper, we report designing such a novel system and demonstrate that our approach gives a dramatic enhancement in the adsorption rate.

Here, we have chosen the Congo Red (CR) dye as the adsorbing species. The dyes currently in industrial use are generally non-biodegradable and highly toxic, and in spite of being important chemicals that concern routine human lives, create serious environmental problems [25]. Waste discharge effluents from textile, pesticide, pharmaceutical, food, and leather industries frequently contain dyes and pollute the water resources [305]. Turbid water resulting from the dyes present in water resists the sunlight penetration which directly affects the photosynthesis process useful for the aquatic system [8]. Therefore, the removal of dyestuffs from the wastewater is highly desirable before their discharge in natural water bodies [25]. Many methods and technologies such as membrane treatment [305], coagulation/flocculation [306], ozone treatment [307], ion exchange [308], photocatalysis [71,309], biological and chemical oxidation [310], and adsorption [311,312], *etc.* have been used to remove the dyestuffs from the effluent. Among the available techniques, *adsorption* is widely recognized as a promising method because of its flexibility, ease of operation, low capital investment, the simplicity of design, insensitivity towards toxic materials, and the ability to remove the pollutants effectively [313,314]. In a previous study, the authors have shown the ZnTiO<sub>3</sub> (ZTO) nanomaterials synthesized *via* a novel method show high degradation of aqueous phenol in visible light [71]. In this paper, we have used the ZTO as our base nanoparticle.

PANI is a conducting polymer and has been of great interest to the academic and industrial community [315]. This polymer is easy to prepare, inexpensive, has good thermal stability, can offer large surface area, and its properties can be manipulated easily by doping-dedoping reversibility [315]. PANI has attracted considerable attention for adsorption application due to the nitrogen-containing protonic amine group in its backbone which has a tendency to attract heavy metal ions such as Cu, Zn, Ti, Pb, As, *etc.* as well as anionic pollutants through the electrostatic attraction, hydrogen bonding,  $\pi$ - $\pi$  interaction, and dipole-dipole interaction [316]. But, the use of PANI as an adsorbent is limited owing to its low mass density due to which its tendency to settle down and hence its recovery from the solution is restricted [315].

Here, we report that ZTO nano-particles with polyaniline (PANI) as the adsorbing polymer on its surface form an excellent adsorbent material for removal of Congo Red (CR) dye from liquid phase as compared to that when ZTO or PANI nanoparticles are used separately. The ZTO/PANI is rational choice for the design of nanocomposite material since the ZTO can stabilize conjugated polymers via donor-acceptor interaction [317], and properties like insolubility in water, high mass density, high porosity, and easy recovery can make it a suitable candidate material for the adsorption [69].

As suggested by the data presented in this paper, relatively enhanced adsorption of the CR dye onto the composite particles can be attributed to the tethering/adsorption of the polyaniline molecules onto the ZTO particles thereby exposing more adsorption sites on the polymer. Our findings suggest that a suitable particle-polymer composite can be designed so as to affect the adsorption of a particular kind of dye or chemical pollutant that is present in the solution phase.

The PANI/ZTO nanocomposite was synthesized through chemical polymerization of aniline in the presence of as-prepared ZTO nanoparticles by sol-gel route. The kinetics of

adsorption and equilibrium isotherms for CR dye adsorption have been investigated with variations in process parameters such as dye concentration, contact time, and temperature. Table 5.1 shows a comparison of the approximate time to achieve 90% adsorption of CR by various previously reported polyaniline-based adsorbents. In the current study, we achieved approximately 90% adsorption of (50 ppm-75 ppm) CR within 15 min by PANI/ZTO nanocomposites.

**Table 5.1. Comparison of time for achieving 90% adsorption of CR by previously reported adsorbents.**

| <b>Adsorbent</b>                              | <b>Initial adsorbate (CR) concentration</b> | <b>Time taken to achieve 90% adsorption</b> | <b>Reference</b>    |
|---|---|---|---------------------|
| PANi/Bi <sub>2</sub> WO <sub>6</sub>          | 25 ppm-200 ppm                              | 30 min                                      | [318]               |
| $\alpha$ -MoO <sub>3</sub> /Polyaniline       | 10 ppm-50ppm                                | 30 min                                      | [319]               |
| Polyaniline@MoS <sub>2</sub>                  | 10 ppm-100 ppm                              | 30 min                                      | [316]               |
| Polyaniline                                   | 20 ppm                                      | 30 min                                      | [320]               |
| <i>p</i> TSA doped polyaniline@graphene oxide | 200 ppm                                     | 150 min                                     | [321]               |
| CNT/Mg(Al)O                                   | 100 ppm                                     | 90 min                                      | [322]               |
| PANI/ZTO                                      | 50 ppm-150 ppm                              | 15 min                                      | <b>Present work</b> |

### **5.3 Experimental section**

#### **5.3.1 Synthesis of ZnTiO<sub>3</sub> (ZTO)**

The synthesis process of the zinc titanate is given in section 3.3.1.

### **5.3.2 Synthesis of Polyaniline by precipitation method**

Polyaniline (PANI) was synthesized by the chemical polymerization method. To synthesize PANI, three main solutions (solution-1, solution-2, and solution-3) were prepared as follows. The solution-1 was prepared by mixing 2 mL of aniline into 73 mL of DI-H<sub>2</sub>O (equivalent to 0.3 M) at room temperature (RT) for 1 h. The solution-2 was a 3 M H<sub>2</sub>SO<sub>4</sub>. Then the final solution-3 was prepared by adding 0.294 g K<sub>2</sub>Cr<sub>2</sub>O<sub>7</sub> in 10 mL of DI-H<sub>2</sub>O followed by the addition of 2-3 drops of 3 M H<sub>2</sub>SO<sub>4</sub>. The PANI was prepared by the following process stepwise: 7.5 mL of solution-2 was mixed in 75 mL of solution-1 containing aniline monomers, resulting in anilinium cations. The H<sub>2</sub>SO<sub>4</sub> contained in the solution-2 acted as the dopant for the aniline monomers. To initiate polymerization of aniline monomers, 7.5 mL of solution-3 containing K<sub>2</sub>Cr<sub>2</sub>O<sub>7</sub> which act as a polymerizing agent was slowly added to the above solution dropwise. The resulting process was kept under continuous stirring at RT for 12 h. The PANI was precipitated in the above solution which was further filtered and washed it several times with ethanol and water, respectively. Later, the residue was dried at 90°C for 5 h which finally obtained powder was dark blue. The synthesis process of PANI is represented in Figure 5.1.

### **5.3.3 Synthesis of PANI/ZTO nanocomposite**

The PANI/ZTO nanocomposite was synthesized by the chemical polymerization process. First of all, a synthesized calcined sample of 2g ZTO powder was dispersed in solution-1 (as defined in section 2.3) under continuous magnetic stirring at RT for 10 min. Solution-2 and solution-3 were then added to the above mixture, respectively. The resultant solution was kept under continuous stirring at RT for 12 h. The final suspension was filtered and the collected residue was washed several times with ethanol and water respectively. The residue was dried at 90°C for 5 h in the oven. Finally, the collected

materials were crushed into a fine powder. The scheme of the synthesis process of PANI/ZTO nanocomposite is represented in Figure 5.1.

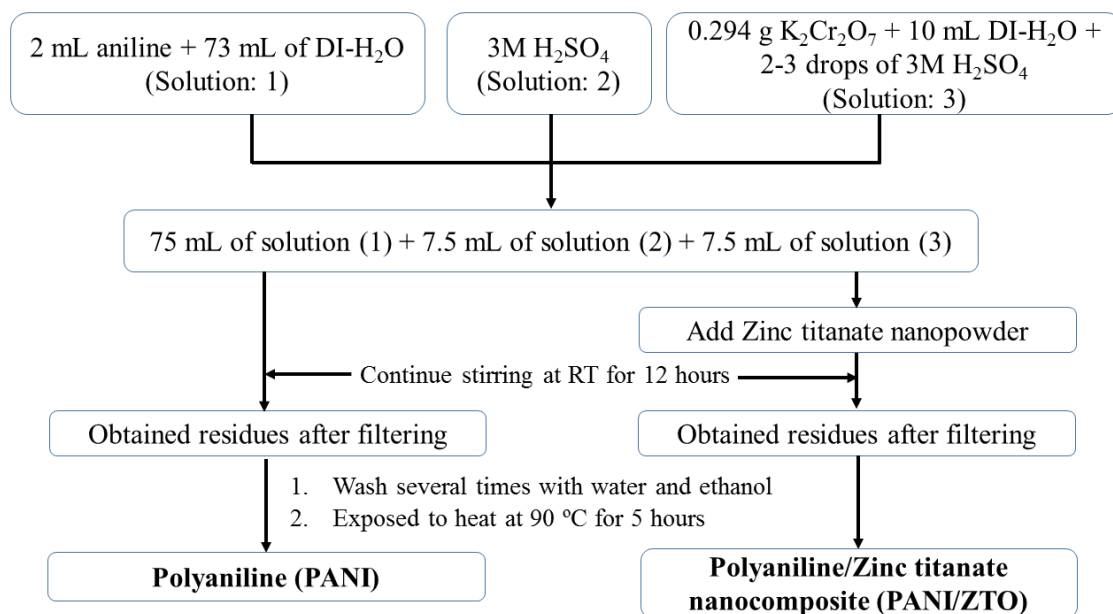


**Figure 5.1. Scheme represents synthesis process of polyaniline (PANI) and polyaniline/zinc titanate (PANI/ZTO) nanocomposite.**

### 5.3.4 Adsorption Experiments

The batch adsorption experiments were carried out in a double-walled glass chamber which facilitates the circulation of the water with the help of a chiller to maintain the constant temperature during experiments. To study the dye uptake by the PANI, ZTO, and PANI/ZTO, 200 mg of adsorbent was added into a 100 mL aqueous solution of CR dye of desired initial concentration of 50 ppm, 75 ppm, 100 ppm, and 150 ppm at natural pH and agitated at 600 RPM at RT. At a time interval of 15 min, the 2 mL solution was taken and the adsorbent was separated by a centrifuge process for the UV-Vis analysis. The characteristic absorption peak of CR dye was found to be at 498 nm by the UV-Vis spectrophotometer. This peak was used for monitoring adsorption studies. The concentration of the dye at different times was calculated from their UV-Vis absorbance spectra to further study the adsorption kinetics. For the adsorption isotherms, the CR solution of four different concentrations of 50 ppm, 75 ppm, 100 ppm, and 150 ppm was

agitated until the equilibrium was achieved. The adsorption (or adsorption capacity,  $Q_t$ ) defines the value of the amount of adsorbed substance (adsorbate) onto adsorbent in the solid-liquid interface solution system and, if equilibrium achieves in the solution then it is called equilibrium adsorption (or equilibrium adsorption capacity  $Q_e$ ) [323] The adsorption ( $Q_t$ ) has been defined by the following Equation (5-1) [312,319].

$$Q_t = (C_0 - C_t) \frac{V}{m} \quad (5-1)$$

where  $Q_t$  (mg/g) is the adsorption at time  $t$ ,  $C_0$  (mg/L) and  $C_t$  (mg/L) are the CR concentration at beginning and time  $t$ ,  $V$ (L) is the volume of solution, and  $m$  (g) is the mass of adsorbent. The equilibrium adsorption ( $Q_e$ ) corresponding to equilibrium concentration  $C_e$  was calculated also by the above Equation (5-1).

## 5.4 Results and discussion

### 5.4.1 X-ray Diffraction analysis

The crystal structure of as-prepared samples has been confirmed by an X-ray diffractogram. Figure 5.2 shows the XRD pattern of polyaniline where the two broad diffraction peaks centered at  $20.89^\circ$  and  $25.0^\circ$  corresponds to (100) and (110) plane respectively, are assigned to the semi-crystalline PANI [324,325]. Presence of diffused peaks implies a suppressed crystallinity in the pure polyaniline samples. It was also observed that the polyaniline powder samples, when suspended in water, made the suspension acidic. This can be attributed to the presence of protonated nitrogen centers which suppresses the native crystallinity which would have otherwise resulted from packing of neutral polyaniline chains as suggested by rather broad XRD peaks observed in polyaniline powders. The XRD pattern corresponds to the rhombohedral structure, as confirmed by matching with the standard rhombohedral structure of ZTO (JCPDS PDF: 25-0671) [229]. The high intensity of the diffraction peaks indicates the good crystallinity

of as-prepared ZTO. The XRD pattern of PANI/ZTO nanocomposite shows that the crystallinity of the ZTO is maintained, whereas the PANI has lost its semi-crystalline nature as evidenced by the disappearance of its peaks after compositing. A change in FWHM of the ZTO Bragg peaks is also noticed. The average crystallite size ( $d$ ) of ZTO and PANI/ZTO nanocomposite is calculated by the Debye Scherrer Equation (3-1). This relation gives  $d$  values of 40.29 nm and 43.26 nm respectively in ZTO and the composites. The most prominent Bragg peak at  $35.22^\circ$  corresponding to (110) plane is chosen to calculate the crystallite sizes. The small increase in the crystallite size can be attributed to the layer of polyaniline molecules adsorbed on the surface of the ZTO particles, which is also in agreement with other characterization data as presented in later sections. In summary, XRD results suggest that the polymerization of polyaniline in the presence of ZTO inhibits the crystallization of PANI and yields the ZTO nanoparticles decorated with the polyaniline molecules. Next, we present the results that establish the nature of physico-chemical interactions that lead to these structural modifications in polyaniline which subsequently improves the adsorption in composites.

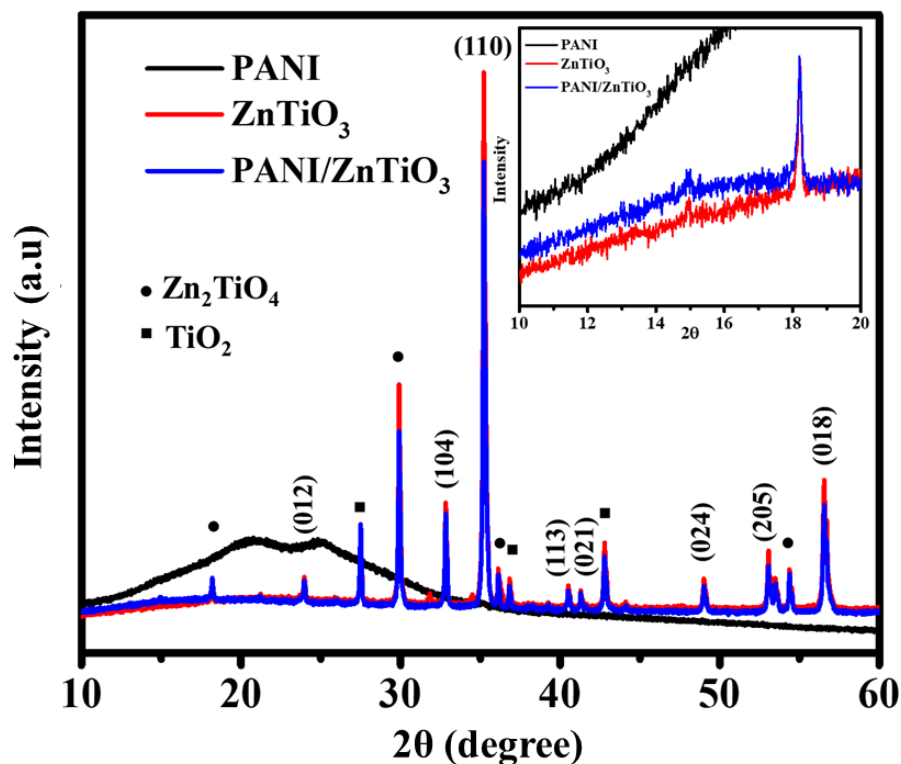


**Figure 5.2.** XRD pattern of PANI, ZTO, and PANI/ZTO nanocomposite. Figure in inset represents the broadness in XRD of PANI/ZTO in the range of  $2\theta = 10^\circ$  to  $18^\circ$ .

#### 5.4.2 Dynamic light scattering analysis

As mentioned earlier, the aqueous suspension of the synthesized polyaniline powder was acidic in nature which may be due to the presence of polyaniline present in the form of polyaniline hydrogen sulphate [326]. The zeta potential of the polyaniline powder samples was found to be -7.54 mV. The negative charge on the polyaniline develops due to the release of protons by the PHS chains [326]. The zeta potential measurements of the samples PANI, ZTO, and PANI/ZTO nanocomposite shows that all the samples acquire negative surface charges in water and have been measured to be -7.54 mV, -30.2 mV, and -21.2 mV for PANI, ZTO, and PANI/ZTO nanocomposite respectively.

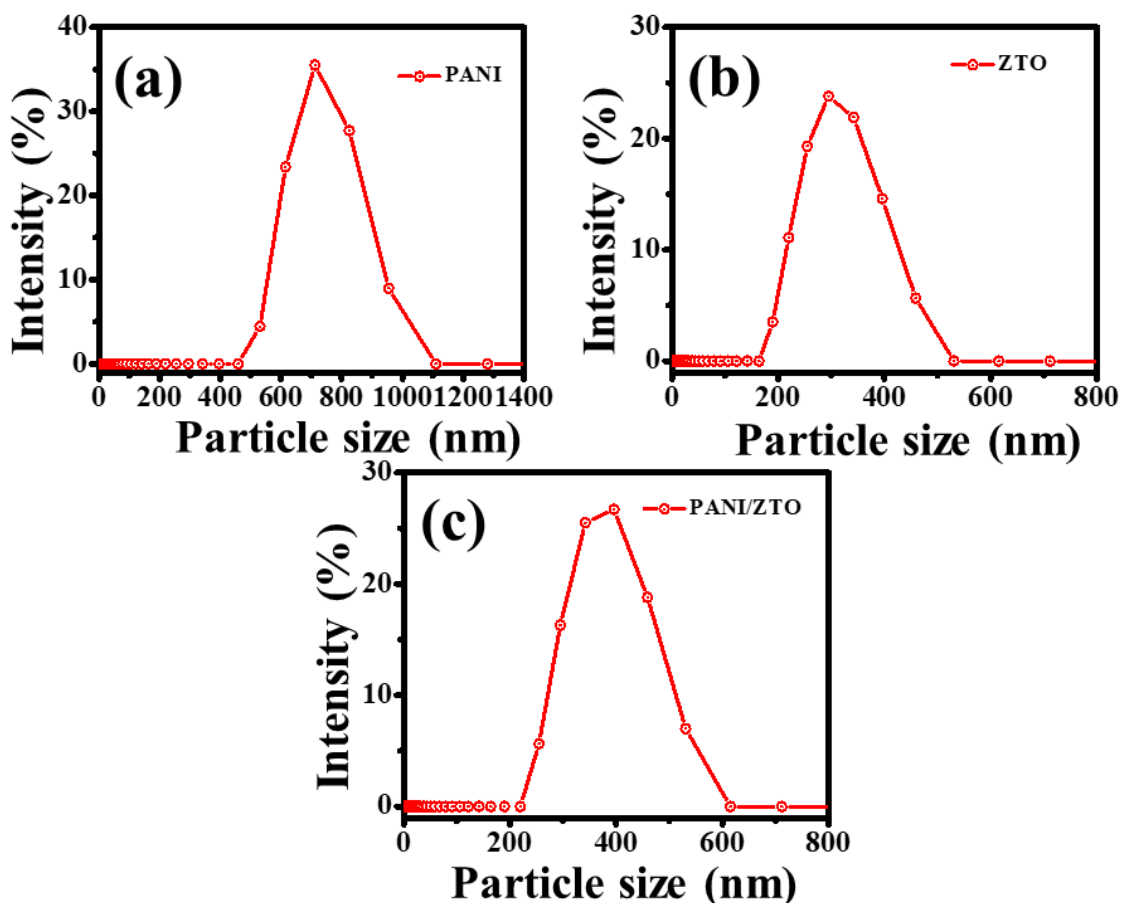


**Figure 5.3.** The particle size distribution of (a) PANI, (b) ZTO, and (c) PANI/ZTO nanocomposite.

The moderate adsorption of the CR found with PANI which is absent in ZTO arises mainly due to  $\pi$ - $\pi$  interaction and hydrogen bonding [316]. Although polyaniline has an affinity to adsorb CR, owing to agglomeration (confirmed by less charge as measured from zeta potential measurement) polyaniline is not best utilized for adsorption because agglomeration and crystallinity causes a reduction in surface area. However, carrying out the polymerization of polyaniline in the presence of ZTO helps in overcoming this shortcoming. The presence of ZTO in the solution causes polyaniline molecules (in the form of PHS) to adsorb onto the ZTO particles. The surface charge on the ZTO is negative because of the accumulation of the  $\text{OH}^-$  ions on to ZTO surface [327]. The binding between the PHS and ZTO is mediated by the electrostatic attraction between the positive

charge center on the PHS and the negatively charged surface of ZTO. The electrostatic pull between the ZTO particles and polyaniline molecules suppress the latter's tendency to crystallize and agglomerate (also corroborated by the XRD data discussed earlier) and causes polyaniline to get adsorbed in the molecular form on to the ZTO thereby exposing more sites of  $\pi$ - $\pi$  interaction and hydrogen bonding for adsorption of CR. Thus the presence of ZTO essentially leads to higher availability of surface area with active adsorption sites and helps in efficiently utilizing the polyaniline molecules for CR adsorption. The particle's size of the PANI, ZTO, and PANI/ZTO has been found  $734 \pm 109.5$  nm,  $267.4 \pm 58.57$  nm, and  $379.1 \pm 72.48$  nm respectively as depicted in Figure 5.3. As expected the particle size of the nanocomposite is higher than the ZTO and smaller than the PANI.

#### **5.4.3 Fourier transform infrared spectroscopy analysis**

FT-IR spectroscopy of all the samples was conducted to understand how the nature of chemical bonding is influenced in composite samples as compared to parent materials of ZTO and polyaniline. The FT-IR results also help us to explain the enhanced adsorption of CR in composite powder materials. The standard peaks for C-H and N-H (around  $3000\text{ cm}^{-1}$ ), OH stretch (near  $3650\text{ cm}^{-1}$ ), metal-oxygen bonds (near  $540\text{ cm}^{-1}$ ), and bands specific to polyaniline (from  $1000\text{ cm}^{-1}$  to  $1550\text{ cm}^{-1}$ ) (please see in section 7.4.2 for FT-IR of polyaniline) are observed as shown in Figure 5.4 [185,328–330]. The assignments of various peaks to associated chemical bonds are presented in Table 5.2. The bands at  $537\text{ cm}^{-1}$  and  $547\text{ cm}^{-1}$  are the characteristic peaks of Ti-O and Zn-O in ZTO respectively which are present in ZTO and composites but absent in polyaniline [70,127].

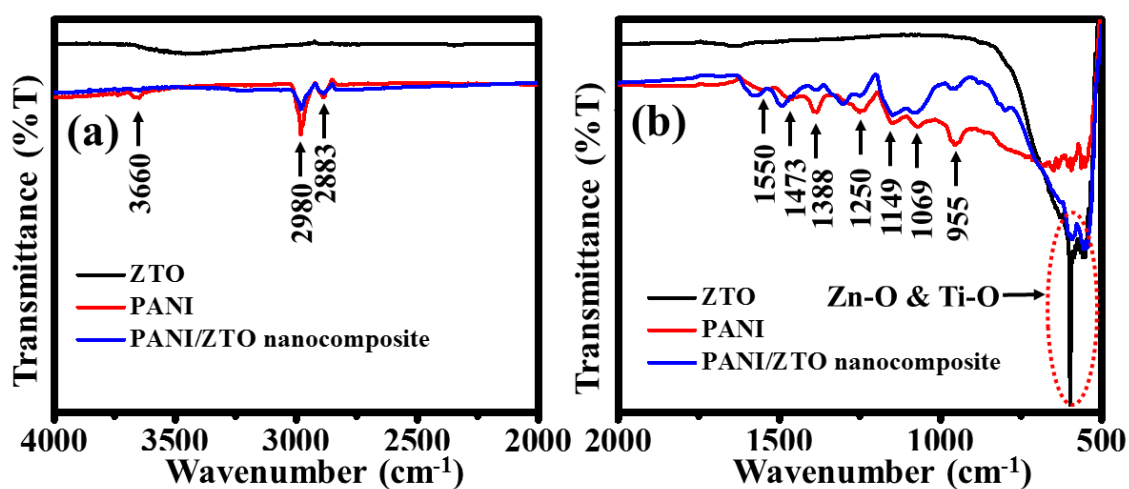


**Figure 5.4.** The FT-IR spectra of PANI, ZTO, and PANI/ZTO from (a) 4000  $\text{cm}^{-1}$  to 2000  $\text{cm}^{-1}$ , and (b) 2000  $\text{cm}^{-1}$  to 500  $\text{cm}^{-1}$ .

The presence of a band due to the stretching mode of relatively mobile  $\text{OH}^-$  ions at around 3650  $\text{cm}^{-1}$  is observed in both polyaniline and the PANI/ZTO nanocomposite powders. This can be attributed to the presence of  $\text{OH}^-$  ions due to the formation of PHS as dictated by the electroneutrality since PHS has a positively charged backbone. In addition a broad and weak hump around 3600  $\text{cm}^{-1}$  is observed in ZTO samples, suggesting the presence of adsorbed hydroxyl ions on to the ZTO surface. The ZTO may be acquiring a negative charge, as corroborated from zeta potential measurements, due to these adsorbed  $\text{OH}^-$  ions [327]. The peaks at 1250  $\text{cm}^{-1}$  due to C-N stretching and 1473  $\text{cm}^{-1}$  due to C=C stretching in benzenoid rings in PANI are noticed to shift towards higher wavenumber in the nanocomposite. We attribute these shifts to the binding of positively charged protonated nitrogen centers on to the negatively charged ZTO surfaces thereby leading to a change in the C-N and C=C band frequencies. We notice one stronger band at 1301  $\text{cm}^{-1}$  and a weak band at 1250  $\text{cm}^{-1}$  in PANI/ZTO nanocomposite as tabulated in Table 5.2. The band at 1301  $\text{cm}^{-1}$  in PANI/ZTO corresponds to the C-N stretching of the benzenoid unit is due to the shifting of a peak originally at 1250  $\text{cm}^{-1}$  in neat PANI. The peak at 1250  $\text{cm}^{-1}$  may be assigned to the Ti-N bond in nanocomposite [282,286].

**Table 5.2 Assignment to the major peaks in FTIR of the PANI, ZTO, and PANI/ZTO nanocomposite.**

| S.No | Peaks position   | Assignment to the functional groups  |
|------|--|--|
| 1    | 3653 cm <sup>-1</sup>  | “Free” O-H   |
| 2    | 2980 cm <sup>-1</sup> and 2883 cm <sup>-1</sup>                        | N-H stretching vibration of the amine groups   |
| 3    | 1550 cm <sup>-1</sup> and 1473 cm <sup>-1</sup>                        | C-C and C=C stretching vibration of quinonoid and benzenoid ring respectively  |
| 4    | 1388 cm <sup>-1</sup>  | N-H bending vibration of the benzenoid ring  |
| 5    | 1250 cm <sup>-1</sup>  | C-N stretching mode of the benzenoid unit and Ti-N bond  |
| 6    | 1149 cm <sup>-1</sup>  | N=Q=N unit (where Q denotes the quinonoid unit)  |
| 7    | 1068 cm <sup>-1</sup>  | Stretching mode of Q-NH <sup>+</sup> B   |
| 8    | 858 cm <sup>-1</sup> , 955 cm <sup>-1</sup> , and 790 cm <sup>-1</sup> | Deformation of aromatic C-H out of the plane in 1,2,4-trisubstituted and 1,4-disubstituted benzene ring respectively |
| 9    | 537 cm <sup>-1</sup> and 547 cm <sup>-1</sup>                          | Ti-O and Zn-O in ZTO   |

The comparison of the relative positions of the FT-IR peaks and their shifts thus supports the physical picture of the process as proposed earlier based upon the XRD data. The polyaniline molecules are responsible for adsorption, and polymerization in the presence of ZTO particles disrupts their crystallization and causes them to adhere to the ZTO surfaces.

#### 5.4.4 X-Ray photoelectron spectroscopy analysis

. In this work, analyzing the XPS spectra from C1s, N1s, and Ti2p electrons help us gain an understanding of the origin of the significant enhancement in the adsorption of the CR dye in PANI/ZTO composites as compared to that in PANI and ZTO separately. The XPS spectra of the C1s, N1s, and Ti2p are presented in Figure 5.5 and Figure 5.6. The peak positions and the area fractions of the various deconvoluted peaks, and the chemical environments pertaining to the orbitals responsible for producing these peaks are listed in Table 5.3. The overall ratio of carbon to nitrogen in polyaniline samples is found to be nearly 5:1 which is close to the ratio of 6:1 expected for polyaniline [331]. The small variation may be attributed to a higher cross-section of photo-electron generation in nitrogen as compared to carbon [331]. This ratio reduces to a value of nearly 3.5:1 in PANI-ZTO composite powders. We suspect that the reduction in the ratio that signals a higher fraction of nitrogen is caused by the presence of nitrogen atoms incorporated into the ZTO matrix during the calcination step performed under ambient conditions.

A comparison of the total areas under the XPS peaks from C1s, N1s, and Ti2p levels shows that the signal strengths from C1s and N1s increase in PANI/ZTO composites as compared to PANI, whereas the signal strength from Ti2p in the composite decreases as compared to that in ZTO. This suggests that in the composite samples, the polyaniline chains are better exposed so that the interaction of X-rays with the carbon and nitrogen atoms is increased. This, in turn, suggests that the polyaniline molecules which aggregate and form crystalline particles in absence of ZTO, tend to anchor on the ZTO surfaces in molecular form when polymerized in presence of ZTO particles. Exposure of a relatively larger number of carbon and nitrogen atoms to X-rays, when adsorbed on to the ZTO

surfaces as compared to that when present in crystalline particulate form, may lead to an enhanced signal strength of C1s and N1s signals in PANI-ZTO composites. The Ti2p signal gets reduced as Ti centers become sub-surface species and are less accessible to X-rays due to the presence of a layer of anchored chains on the ZTO surface. Hence these data suggest that the polyaniline has adhered to the ZTO surface. In what follows, we present an analysis of the deconvoluted peaks which also confirms this conclusion.

Examining the deconvoluted peaks in terms of their peak positions and area fractions show that in polyaniline the N1s peaks can be deconvoluted into four component peaks, and reveal the presence of four kinds of chemical environment the nitrogen atoms can experience. These belong to nitrogen on imine ( $-N=$ ), amine ( $-NH-$ ), protonated imine ( $-NH^+=$ ), and semiquinone cation radical ( $-N^{*+}H-$ ) units [332]. The imine nitrogen is easily protonated and yields protonated imine and semiquinone cation radicals. In our samples, we ascribe peaks corresponding to these four species respectively at the binding energies of 398.77 eV, 399.5 eV, 400.40 eV, and 401.63 eV in polyaniline samples. These peaks show a blue shift to the binding energies of 398.94 eV, 399.82 eV, 400.94 eV, and 402.48 eV in PANI/ZTO composite samples. Li *et al.* have observed a red-shift in these peaks in polyaniline composited with titania [333]. The blue shift is attributed to the binding of the nitrogen atoms to the  $Ti^{4+}$  ions present in the ZTO crystals. The binding may be affected by the partial sharing of the nitrogen lone pair with the titanium ions which will lead to the development of additional small positive charge on the protonated nitrogen ions thereby increasing the binding energy of the 1s electrons of nitrogen.

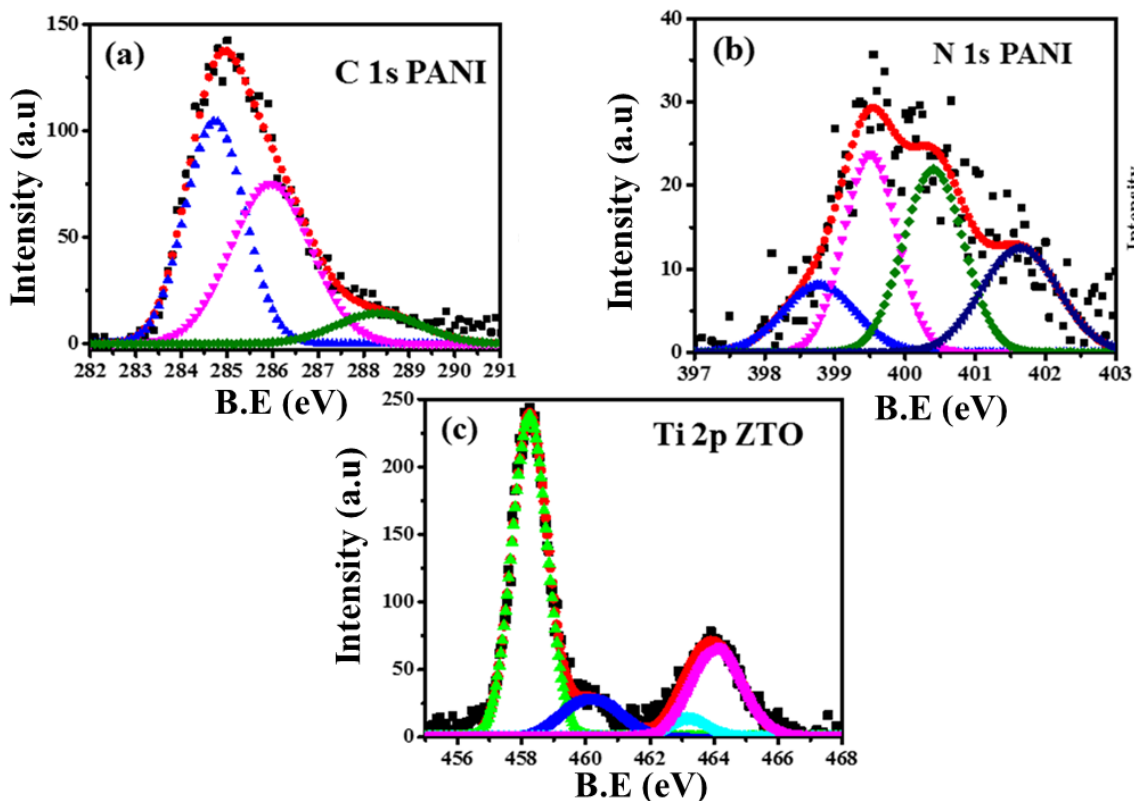


**Figure 5.5. Deconvoluted XPS peaks of (a) C 1s PANI, (b) N 1s PANI, and (c) Ti 2p ZTO.**

Although all the nitrogen peaks show a blue shift, the highest blue shift is observed in the semiquinone cation free radicals and protonated imine peaks, suggesting that these form the predominantly adsorbed species. The area fraction of amine nitrogen is relatively unaltered whereas the imine nitrogen signal is enhanced with an accompanying decrease in the signals from the two protonated units. Thus polyaniline in the composite samples undergoes a reduced protonation. Formation of the Ti-N bond, also suggested from FT-IR peaks at  $1080$  and  $1250\text{ cm}^{-1}$  will lead to loosening of the N-H bond, thereby making the adsorbed chains less susceptible to protonation [282]. As a result, the formation of the salt form is suppressed and leads to a reduction in  $\text{N}^+$  signals resulting from the protonation of imine nitrogen.

Analysis of Ti2p spectra in PANI/ZTO and ZTO samples as shown in Figure 5.6c and Figure 5.5c and with details listed in Table 5.3. Titanium signal could be deconvoluted in

**Table 5.3 Assignment to the XPS peaks of C, N, and Ti in PANI, ZTO, and PANI/ZTO nanocomposite.**

| S.No | Element | PANI  |        | ZTO   |        | PANI/ZTO |        |
|------|---------|---|--------|---|--------|----------|--------|
|      |         | B.E (eV)  | % Area | B.E (eV)  | % Area | B.E(eV)  | % Area |
| 1    | C 1s    | 284.73<br>(C-C or C-H)                            | 46.29  |   |        | 284.84   | 39.66  |
|      |         | 285.96<br>(C-N or C=N)                            | 44.72  |   |        | 285.92   | 43.99  |
|      |         | 288.32<br>(C-N <sup>+</sup> or C=N <sup>+</sup> ) | 8.97   |   |        | 287.64   | 16.34  |
| 2    | N 1s    | 398.77 (=N-)                                      | 14.33  |   |        | 398.94   | 21.04  |
|      |         | 399.50 (-NH-)                                     | 30.58  |   |        | 399.82   | 29.83  |
|      |         | 400.40 (-N <sup>+</sup> H-)                       | 31.81  |   |        | 400.94   | 29.43  |
|      |         | 401.63 (-NH <sup>+</sup> -)                       | 23.26  |   |        | 402.48   | 19.67  |
| 3    | Ti 2p   |   |        | 458.24<br>(Ti <sup>4+</sup> 2p <sub>3/2</sub> ) | 60.17  | 458.05   | 52.82  |
|      |         |   |        | 460.17<br>(Ti <sup>3+</sup> 2p <sub>3/2</sub> ) | 11.69  | 459.97   | 11.31  |
|      |         |   |        | 463.21<br>(Ti <sup>3+</sup> 2p <sub>1/2</sub> ) | 3.70   | 462.67   | 3.37   |
|      |         |   |        | 464.06<br>(Ti <sup>4+</sup> 2p <sub>1/2</sub> ) | 24.47  | 463.93   | 32.48  |

four constituent Gaussian-shaped peaks from  $Ti^{4+}2p_{3/2}$ ,  $Ti^{4+}2p_{1/2}$ ,  $Ti^{3+}2p_{3/2}$ , and  $Ti^{3+}2p_{1/2}$  with peak positions respectively at the binding energy values of 458.24 eV, 460.17 eV, 463.21 eV, and 464.06 eV in ZTO samples suggesting the presence of 4+ and 3+ oxidation states of Ti [293]. However, a comparison of the area fractions of the constituent peaks suggests that the 4+ state is the predominant state. Whereas a blue shift is observed in nitrogen 1s peaks owing to the development of small positive charge arising due to sharing of lone pair as discussed earlier, a redshift is observed in all the Ti2p peaks in PANI/ZTO composite samples as compared to the ZTO samples. The redshifts in the Ti2p peaks can be attributed to the complementary reduction in the positive charge on  $Ti^{4+}$  caused by the lone pair sharing. Kim *et al.* have ascribed the shift in  $Ti^{4+}$  XPS peak near 458 eV of binding energy to the binding of  $Ti^{4+}$  with the nitrogen of  $-NH_2$  [334]. However, binding with  $Ti^{3+}$  can also be not ruled out since the XPS signal from our samples show the presence of a small fraction of  $Ti^{3+}$ . Authors have suggested that  $Ti^{3+}$  may form during calcination and have proposed a mechanism of formation of  $Ti^{3+}$  [294]. DFT calculations by Koch and Manzhos have also suggested that titanium may be present in the  $Ti^{3+}$  oxidation state [293].

The XPS spectra of PANI/ZTO show the prominent splitting of Zn 2p spectra into two peaks centered at 1021.04 eV and 1043.90 eV corresponding respectively to  $2p_{3/2}$  and  $2p_{1/2}$  respectively, indicating the +2 oxidation state of Zn into ZTO [295]. It is noticed that the binding energy of Zn in PANI/ZTO nanocomposite is the same as in ZTO. Therefore, PANI in our samples has interacted with ZTO through nitrogen-titanium interaction only while the Zinc atoms have not participated directly in PANI/ZTO nanocomposite formation.

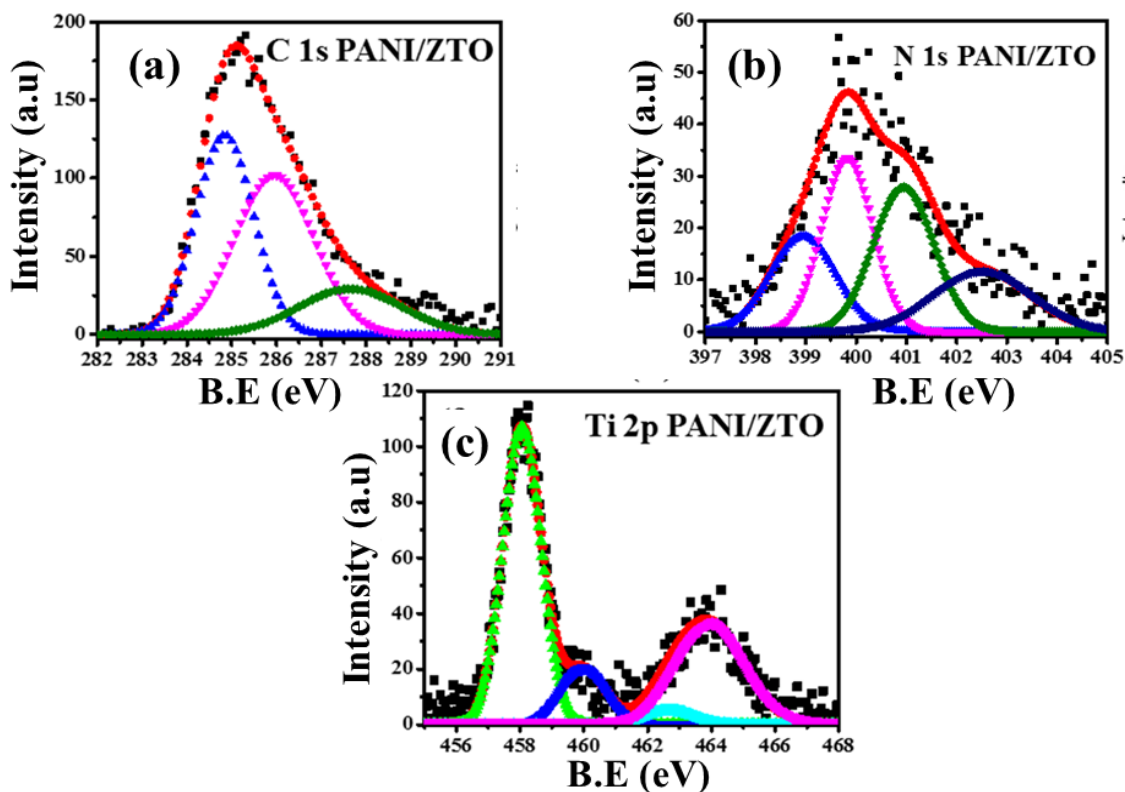


**Figure 5.6.** The XPS spectra of (a) C 1s PANI/ZTO, (b) N 1s PANI/ZTO, and (c) Ti 2p PANI/ZTO.

#### 5.4.5 Field Emission Scanning Electron Microscopy analysis

The surface morphology of the samples has been analyzed by FESEM. Figure 5.7 represents the FESEM images of the three samples (a) PANI, (b) ZTO, and (c) PANI/ZTO nanocomposite at two different magnification 20000X and 100000X respectively. The micrograph of pristine PANI in Figure 5.7a and Figure 5.7d reveals that the pristine PANI is highly agglomerated and its particles are well interconnected to each other which suggested that they have enough binding energy to interconnect with neighbour molecules [319]. Figure 5.7b and Figure 5.7e depicts the ZTO nanoparticles, those are uniform in size and randomly distributed all over the surface. The surface morphology of PANI/ZTO nanocomposite has been investigated as shown in Figure 5.7c and Figure 5.7f. Figure 5.7 and Figure 5.7 infer that the ZTO nanoparticles are embedded into the PANI matrix or it can be stated that the PANI has been coated over the ZTO surface as most of the ZTO nanoparticles are appeared to be shielded by PANI. Thus it is concluded that

PANI has been coated onto ZTO nanoparticles and assists them to interconnect with each other.

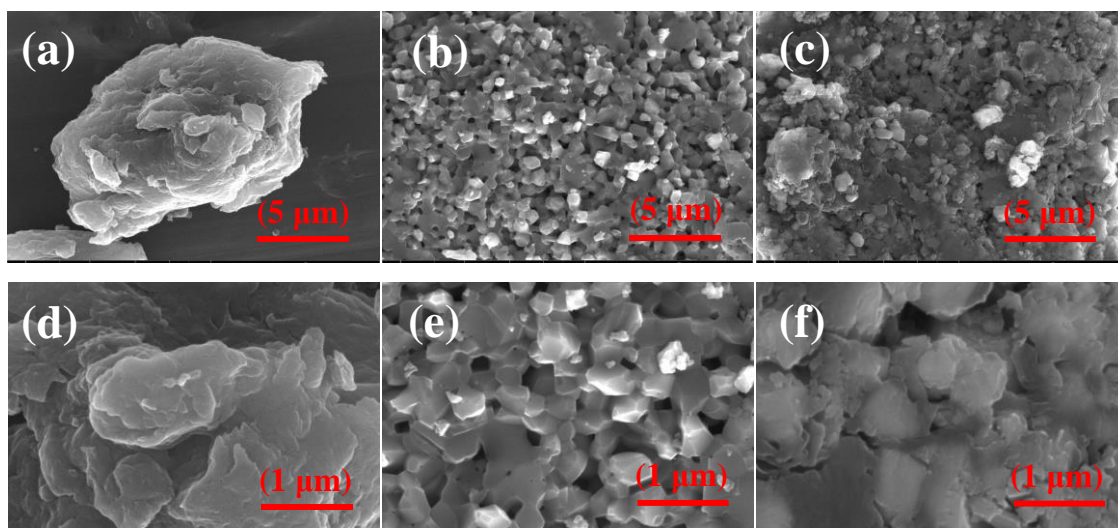


**Figure 5.7.** FESEM images of (a&d) PANI, (b&e) ZTO, and (c&f) PANI/ZTO nanocomposite at 20000x and 100000x magnification respectively.

## 5.5 Adsorption study

### 5.5.1 Kinetics of adsorption

In this work, we report the adsorption behavior of PANI/ZTO nanocomposites for CR dye, in comparison with adsorption in the presence of polyaniline and ZTO separately. The adsorption behavior is quantified using UV-Visible spectroscopy monitoring the absorption peak of the dye. The vials of CR solutions after treating them with ZTO powder, PANI powder, and PANI/ZTO composite are shown in Figure 5.8.

It was observed that when CR dye was brought in contact with the aqueous suspension of PANI powder, there was a shift in the absorption peak and that the adsorption was moderate (around 50%) as represented in Figure 5.9a. A color change in the solution was observed suggesting that the medium was acidic. The acidity in the medium is attributed to the PANI present in the polyaniline hydrogen sulfate (PHS) form [326]. This form results from the synthesis protocol of aniline polymerization carried out in the presence of  $H_2SO_4$ . The release of the protons from PHS makes the solution acidic. The adsorption

of the dye in the presence of ZTO was very low (nearly 15%). However, the composites showed a 98% adsorption and the adsorption rate was also found significantly higher compared to the other two cases.

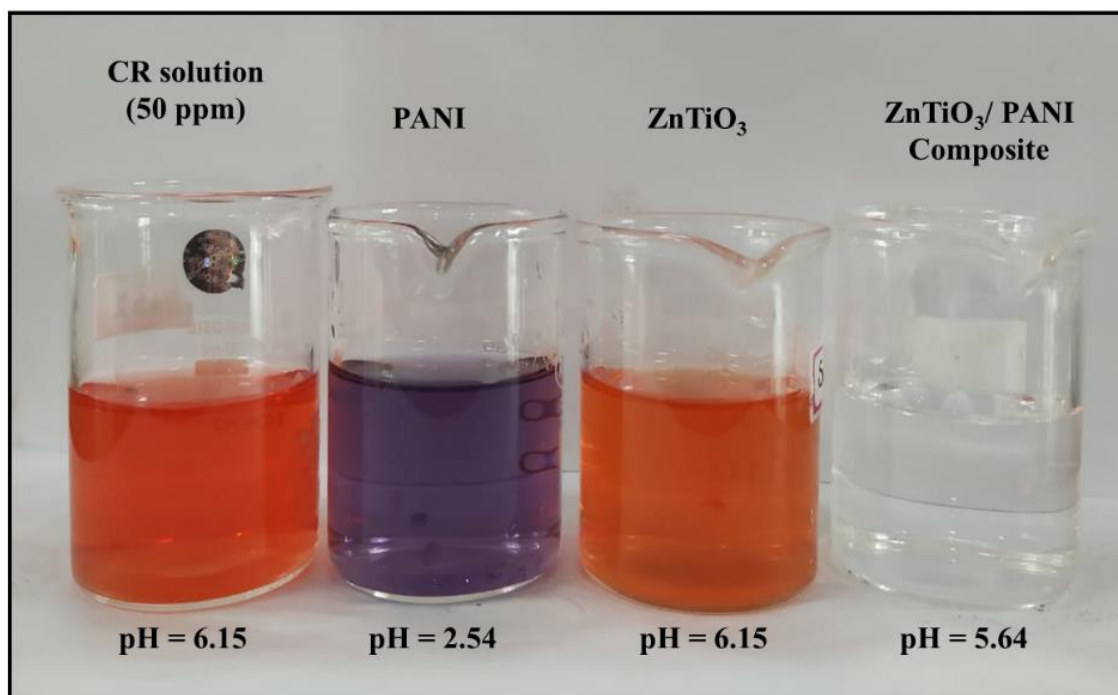


**Figure 5.8. The colour of CR solution after treatment with PANI, ZTO, and PANI/ZTO nanocomposite.**

Analysis of all characterization data suggests the following picture (see Figure 5.10) as to the dramatic increase in the adsorption of CR dyes in presence of PANI/ZTO composite: When aniline monomers are polymerized in presence of ZTO particles, the aggregation and crystallization of the polymer chains are suppressed and the chains are instead adsorbed in the molecular form on to the ZTO particles. Owing to the presence of adsorbed polyaniline chain in the composite materials, their accessibility to the CR molecules is significantly enhanced, and as a result, the interaction of CR molecules with the polyaniline is more efficiently utilized towards adsorption of the CR dyes in the composites.

The adsorption of CR has been examined with three adsorbents PANI, ZTO, and PANI/ZTO. The adsorption kinetics have been represented for three adsorbents PANI, ZTO, and PANI/ZTO in Figure 5.9a-c respectively. The characteristic absorbance peak of CR appears at 343 nm and 498 nm corresponds to  $\pi$ - $\pi^*$  transition and  $n$ - $\pi^*$  transition respectively [335]. Here adsorption of CR dye is examined by monitoring the intensity of peak at 498 nm. On the addition of the PANI into the CR aqueous solution, this peak shifts to 564 nm which is due to the acidic nature of the solution [336]. In the acidic medium, the CR dissociates into its ionic form due to which the color of solution changes from red to green [337]. Thereafter, the anionic group ( $-\text{SO}_3$ ) of CR could lead to the chemical interaction with the positively charged backbone of PANI (as has been observed in adsorption of orange-G dye on polyaniline [337]) thereby leading to results into the adsorption of CR onto PANI and causing the reduction in the peak intensity. It has been found that pure PANI could not adsorb all the CR dye molecules and the adsorption equilibrium is achieved after 90 min as shown in Figure 5.9. Figure 5.9b shows negligible adsorption of CR on ZTO and hence establishes that ZTO is not responsible for adsorption in the composite. The result in Figure 5.9c shows that PANI/ZTO nanocomposite acts as an excellent adsorbent material with rapidly adsorbing the 95% of 50 ppm of CR dye within 15 min. The amount of the adsorbent used in the three cases were the same as discussed earlier, this dramatic enhancement in the adsorption rate can be due to the PANI molecules which are better distributed in the medium by tethering to the surface of the suspended ZTO particles.

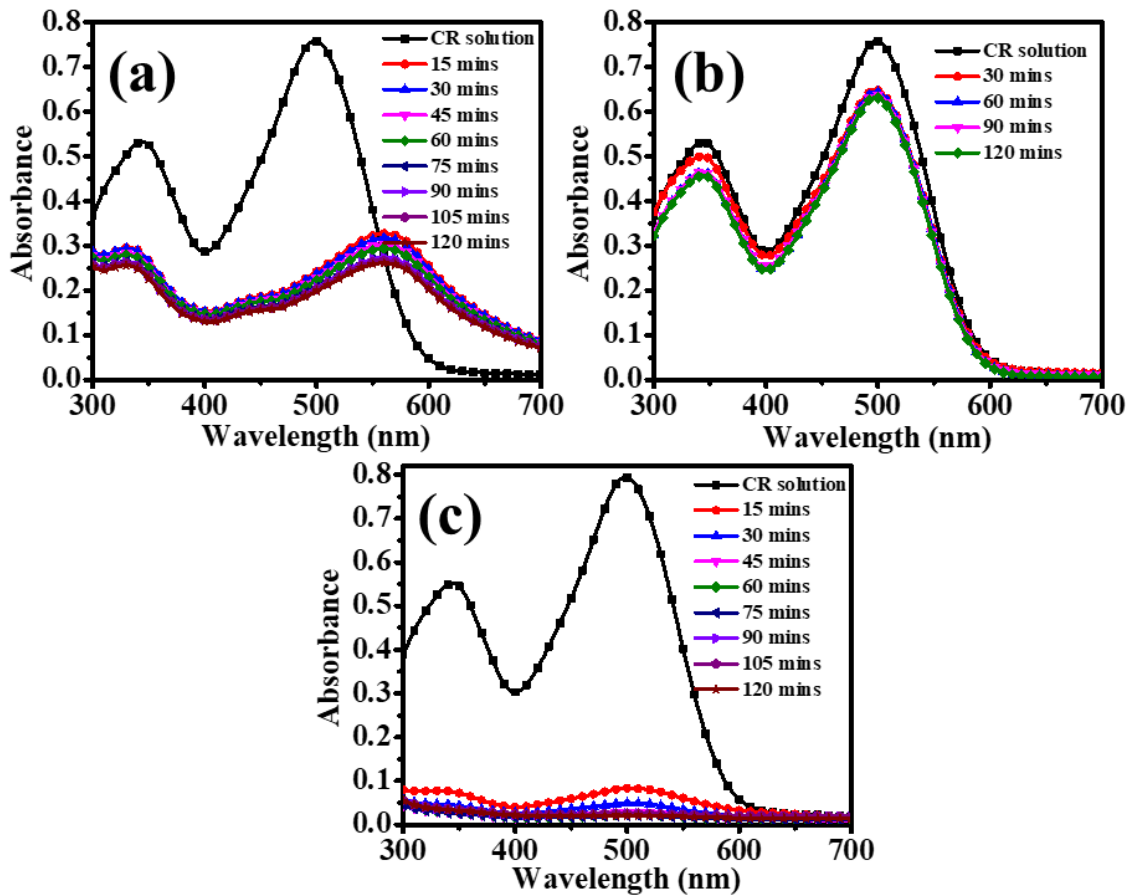


**Figure 5.9.** UV-Vis adsorption kinetics of 50 ppm aqueous solution of CR onto (a) PANI, (b) ZTO, and (c) PANI/ZTO nanocomposite.

Dye concentration is calculated from the UV-Vis absorbance using Beer-Lambert's law and the  $Q_t$ , the adsorption capacity at time  $t$  as defined in equation (5-1), is plotted against time to analyze the kinetics of adsorption. Further, the adsorption kinetics have been examined for different dye concentrations (50 ppm, 75 ppm, 100 ppm, and 150 ppm) at RT.

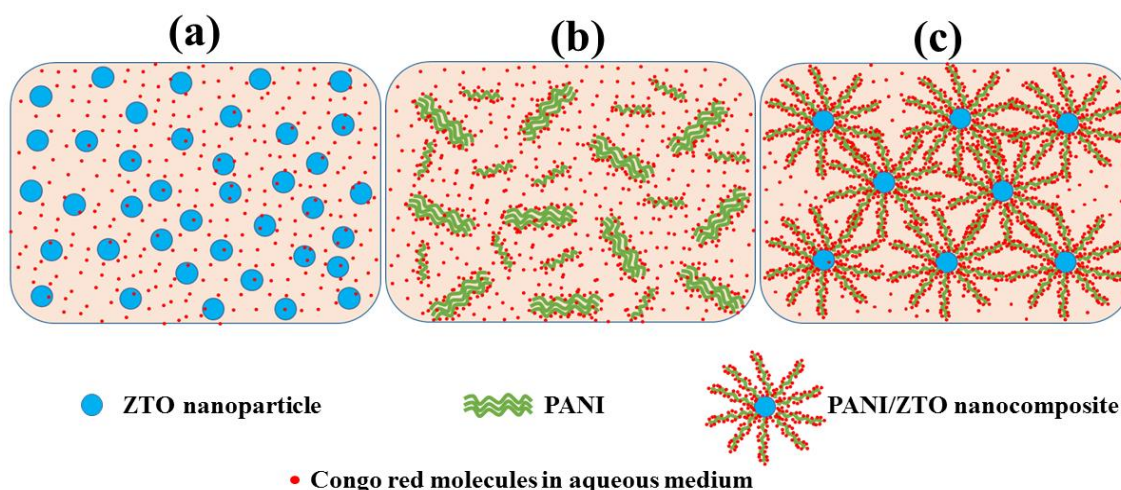


**Figure 5.10.** A cartoon depicting the proposed scheme for adsorption explaining the dramatic enhancement of adsorption in polyaniline-nanoparticle composites. ZTO nanoparticles adsorb poorly (a). The adsorption sites which chiefly reside on the polyaniline chains, are accessible to dyes only at the surface in neat polymer suspensions, leaving the subsurface chains unutilized (b). This limitation is overcome in nanocomposites due to chains adhering to the nanoparticle surfaces (c) and opening up for adsorption.

Figure 5.11a shows the adsorption equilibrium (saturation coverage) for different values of the initial dye concentration. The data could be fitted to the following second-order kinetics Equation (5-2) [338].

$$\frac{t}{Q_t} = \frac{1}{k_2 Q_e^2} + \frac{t}{Q_e} \quad (5-2)$$

where  $Q_t$  is the coverage (mg/g) at time  $t$  (sec), and  $k_2$  is the pseudo-second-order rate constant in  $\text{g}\cdot\text{sec}^{-1}/\text{mg}$ . The values of  $Q_e$  and  $k_2$  are calculated from the linear fitting between  $t/Q_t$  versus  $t$  as shown in Figure 5.11b. The value of equilibrium adsorption ( $Q_e$ ) can also be calculated directly from the kinetics data in Figure 5.11b. The values of equilibrium adsorption ( $Q_e$ ) are approximately the same when calculated by Equation (5-1) (named  $Q_e$  (Exp)) and by Equation (5-2) (named  $Q_e$  (cal)) as given in Table 5.4.

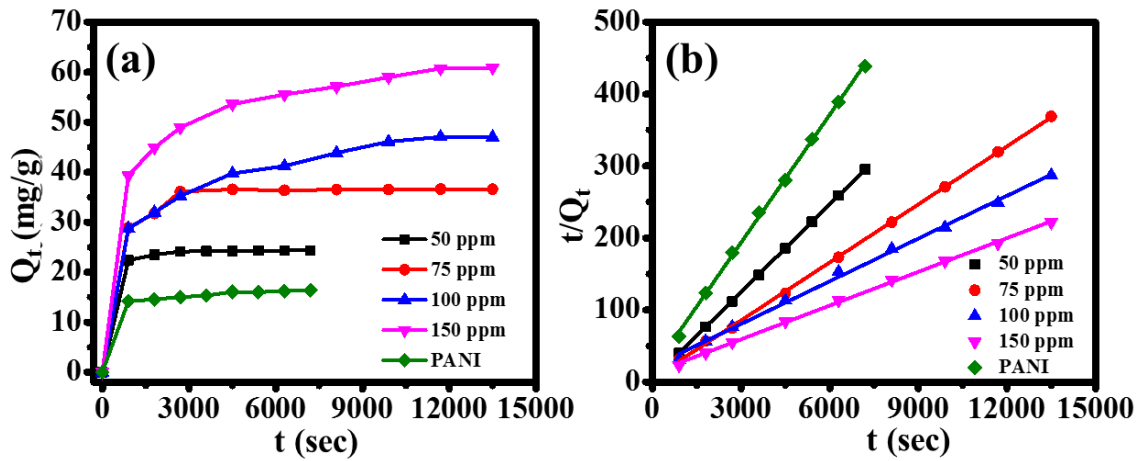


**Figure 5.11.** (a) Adsorption  $Q_t$  versus  $t$  for four different dye concentrations by PANI and PANI/ZTO, and (b) Pseudo-second order plots of  $t/Q_t$  versus time  $t$  for the adsorption of the CR onto PANI/ZTO nanocomposite.

**Table 5.4.** Kinetic parameters of the pseudo-second-order adsorption kinetic model for CR onto PANI/ZTO nanocomposite.

| Concentration | $k_2$ (g.sec <sup>-1</sup> /mg) | $Q_e$ (Cal)<br>(mg/g) | $Q_e$ (Exp)<br>(mg/g) |
|---------------|---------------------------------|-----------------------|-----------------------|
| 50 ppm        | 0.000509                        | 24.6426               | 24.3578               |
| 75 ppm        | 0.000144                        | 37.2300               | 36.5384               |
| 100 ppm       | 0.000018                        | 50.5561               | 47.0446               |
| 150 ppm       | 0.000019                        | 64.0204               | 60.7616               |

The value of equilibrium adsorption  $Q_e$  increases whereas the rate constant decreases as the initial concentration of the dye increases. The saturation coverage increases because higher initial dye concentration affords extra driving force to overcome the mass transfer resistance of the dye molecules between the liquid phase and the solid phase, whereas the rate constant ( $k_2$ ) decreases because of the strike hindrance of the dye molecules at higher concentrations [339].

### 5.5.2 Mechanism of CR adsorption onto PANI/ZTO nanocomposite

The experimentally observed overall adsorption kinetics of dyes from their aqueous solutions over solid adsorbent is governed by the following three steps that includes transport of the adsorbate molecules and actual adsorption at the active sites: (a) In *film diffusion*, the adsorbate transports to the exterior surface of the adsorbent particles through a liquid film region; (b) In *intra-particle diffusion*, the transportation of the adsorbate occurs from the exterior surface of the particles to the pores of the adsorbent; and (c) *Adsorption* over active sites occurs as the last step [312]. The third step does not contribute to the rate-controlling step because this corresponds to the equilibrium stage where no dye molecules are left for the adsorption [312]. This may happen due to the reversible process with fast kinetics. During the remaining two processes which are diffusive in nature, coverage is directly proportional to  $t^{1/2}$ , and can be modeled by the following Equation (5-3) [312,340].

$$Q_t = k_i t^{1/2} + C \quad (5-3)$$

where  $k_i$  (mg.sec<sup>-1/2</sup>/g) denotes intra-particle diffusion rate constant and  $C$  (mg. g<sup>-1</sup>) is the constant related to the boundary layer effect [341]. Dependence of  $Q_t$  on  $t^{1/2}$  shown in Figure 5.12 clearly establishes multilinearity in the curves in all the cases and the three linear regions can be identified from the fitting of Equation (5-3). The first (earliest) linear region corresponds to the film diffusion in which the CR particles diffuse over the external surface of the PANI/ZTO through the liquid film and form layers onto the surface of the adsorbent. The second linear region is ascribed for the intra-particle diffusion where the CR dye molecules diffuse to the exterior or interior pores of the PANI/ZTO. The third (latest) linear region is assigned for the adsorption of the CR dye onto active sides of the adsorbent where very few CR dye molecules left into the aqueous solution corresponds to the almost equilibrium stage. Due to a lack of concentration data during the first fifteen

minutes (which includes film diffusion regime), the first two points in Figure 5.12a-d are joined by a dashed line. Therefore the slope of the coverage vs  $t^{1/2}$  curves in Figure 5.12 during the initial time corresponding to the *film diffusion* is definitely larger than the dashed lines shown in Figure 5.12. The dashed lines represent the lower bound on the diffusion coefficient of the film diffusion process. The second region with a reduced slope pertains to intraparticle diffusion wherein dye molecules diffuse into the particles. As is evident from Figure 5.12a-d, the duration of intraparticle diffusion is longer at higher dye concentrations.

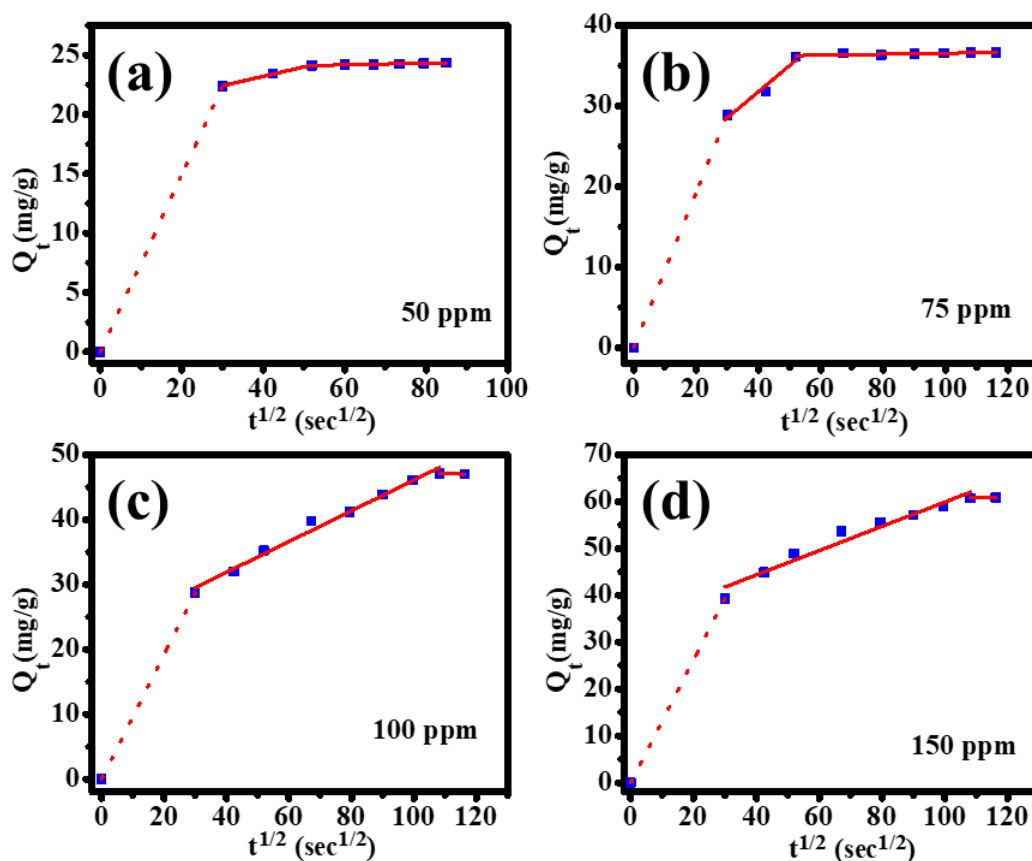


**Figure 5.12.** Intra-particle diffusion plots of adsorption capacity  $Q_t$  versus  $t^{1/2}$  for the adsorption of CR onto PANI/ZTO for different concentrations (a) 50 ppm, (b) 75 ppm, (c) 100 ppm and (d) 150 ppm.

This is consistent with the previously noted conclusion that larger strike hindrance at

higher crowding, while the dye molecules diffuse inside the pores of the adsorbent particles, slows down the net adsorption process. A comparison of the plot of  $Q_t$  vs  $t^{1/2}$  plots with PANI and PANI/ZTO chosen as adsorbent materials for 50 ppm dye concentration is presented in Figure 5.13. Figure 5.13 clearly shows that the diffusion coefficient determining the intraparticle diffusion is larger and saturation occurs much early on in nanocomposite samples. This suggests that in the nanocomposite samples, the crowding of the dye molecules which impedes the net rate of adsorption is significantly reduced. This may be attributed to our early conclusion that the pure polyaniline adsorbent material is mostly semicrystalline in nature with denser packing of the polyaniline molecules, whereas in the composites the chains are distributed on the oxide particle surfaces with a considerable reduced degree of packing. Therefore the composites offer less crowded pathways for the diffusion of the dye molecules which yields the behavior observed in Figure 5.13.

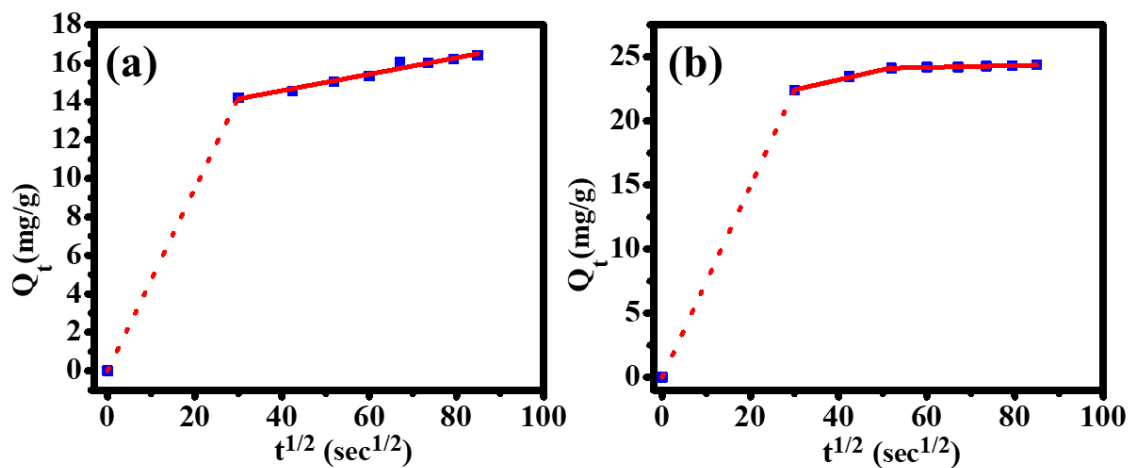


**Figure 5.13. Comparison of Intra-particle diffusion model of 50 ppm CR adsorption by (a) PANI, and (b) PANI/ZTO.**

It is evident from Figure 5.13 that the film diffusion is faster than the intraparticle diffusion in all cases, and among the two diffusive processes, the intraparticle diffusion is relatively slower and will determine effective kinetics of adsorption.

### 5.5.3 Adsorption Isotherms

In the foregoing section, we analyzed the kinetic aspects of the adsorption process. In this section, we will do the same for the equilibrium aspects by applying the Langmuir isotherms and Dubinin-Radushkevich (D-R) isotherms models to the adsorption data. The Langmuir isotherms model is given by the following Equation (5-4) [342,343].

$$\frac{C_e}{Q_e} = \frac{1}{bQ_m} + \frac{C_e}{Q_m} \quad (5-4)$$

where  $C_e$  (mg/L) and is the equilibrium concentration of the dye molecules in the solution after achieving equilibrium.  $Q_e$  (mg/g) is the equilibrium adsorption capacity of the adsorbent at equilibrium.  $Q_m$  (mg/g) is the maximum coverage and  $b$  (L/mg) is the Langmuir constant signifying the strength of adsorption which is determined by the energy of adsorption [26]. The adsorption data has been well-fitted to the Langmuir model as depicted in Figure 5.14a suggesting adsorption proceeds in monolayer form, with active sites homogeneously distributed on the surface. The corresponding fitting parameters are presented in Table 5.5. (Fitting the adsorption data to the Freundlich model gave a much smaller value of  $R^2$ ).

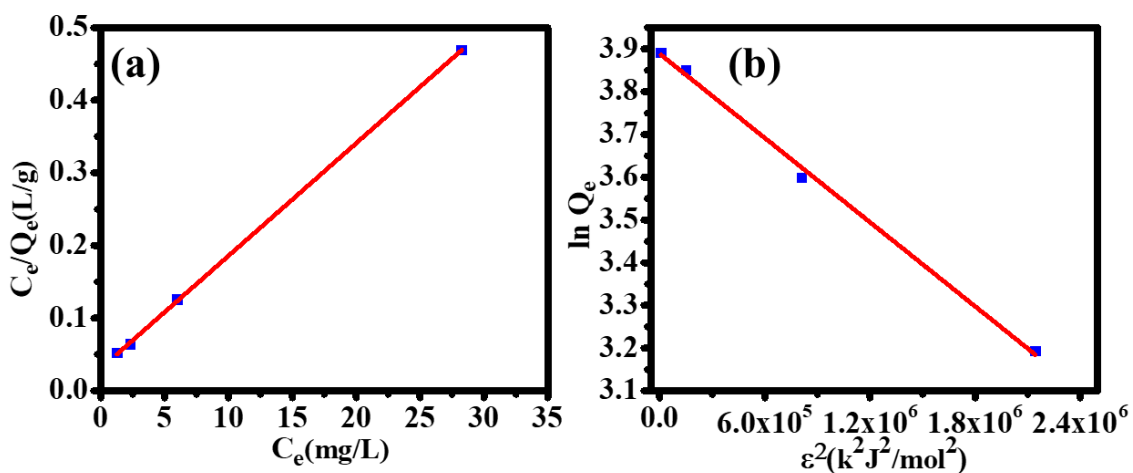


Figure 5.14. Plot confirming the (a) Langmuir model of adsorption, and (b) D-R model.

The value of  $Q_m$ , the monolayer adsorption capacity, extracted from fitting the Langmuir model can be used to estimate the specific surface area also by using the following Equation (5-5) for the surface coverage ( $S_c$ ) [316].

$$S_c = \frac{6.023 \times 10^{23} \times A_m \times Q_m}{M.W.} \quad (5-5)$$

Here,  $S_c$  ( $\text{m}^2/\text{g}$ ) is the total surface coverage,  $A_m$  ( $\text{m}^2$ ) is the molecular surface area of CR,  $M.W.$  is for molecular weight (696.66 g/mol) of the CR dye. The value of  $Q_m$  is obtained to be 64.51 mg/g (Table 5.5) and the size of the CR molecule is about 2.3 nm whereby the surface area is estimated to be around 6  $\text{nm}^2$  [316]. Substituting these values in the above Equation (5-5), the total surface coverage is found to be around 300  $\text{m}^2/\text{g}$ . A high value of  $S_c$  is another reason why the nanocomposite shows excellent CR removal through adsorption.

We next turn our attention to estimating the energy of adsorption using the D-R isotherm model. Equation (5-6) of the D-R model is given as follows [344,345].

$$\ln Q_e = \ln Q_m - B\varepsilon^2 \quad (5-6)$$

Where,  $\varepsilon$  is the Polanyi potential related to the initial and equilibrium concentrations through the following Equation (5-7):

$$\varepsilon = RT \ln \frac{C_0 - C_e}{C_e} \quad (5-7)$$

And the mean energy of adsorption  $E$  can be extracted from  $B$  using the following Equation (5-8):

$$E = \frac{1}{\sqrt{2B}} \quad (5-8)$$

Figure 5.14b represents the D-R model fitting of adsorption data and the corresponding extracted parameters are listed in Table 5.5.

**Table 5.5. Isotherms parameters for the adsorption of CR onto PANI/ZTO nanocomposite.**

| Model                              | Parameters   | Values   |
|------------------------------------|--|----------|
| Langmuir model                     | $b$ (L/g)  | 0.503    |
|                                    | $Q_m$ (mg/g)   | 64.51    |
|                                    | $R^2$  | 0.999    |
| Dubinin -<br>Radushkevich<br>model | $B$ (mol <sup>2</sup> /k <sup>2</sup> J <sup>2</sup> ) | 0.008212 |
|                                    | $Q_m$ (mg/g)   | 68.37    |
|                                    | $E$ (kJ/mol)   | 7.80     |
|                                    | $R^2$  | 0.989    |

The extracted value of the mean free energy of adsorption from the D-R model is 7.80 kJ/mole, suggesting that adsorption is weak physisorption [28,346]. Which is what we expect from our proposition that the dye molecules get adsorbed chiefly on to polyaniline molecules due to dipolar and  $\pi$ -  $\pi$  interactions.

#### 5.5.4 Thermodynamic of adsorption

To understand in-depth of adsorption, the thermodynamic parameters associated with the inherent energy changes have been determined by van't Hoff Equation (5-9) [347].

$$K_d = \frac{C_{Ae}}{C_e} \quad (5-9)$$

where  $K_d$  represents distribution coefficient and  $C_{Ae} = C_o - C_e$  (mg/L) denotes the quantity of dye adsorbed per liter of the aqueous solution at equilibrium by the adsorbent.

The changes in Gibbs free energy ( $\Delta G^\circ$ ) can be calculated by using Equation (5-10).

$$\Delta G^\circ = -RT \ln K_d \quad (5-10)$$

Where,  $T$  (K) represents temperature,  $R$  designates as gas constant (8.3145 J/mole.K). The changes in entropy ( $\Delta S^\circ$ ) and change in enthalpy ( $\Delta H^\circ$ ) can be determined by Equation (5-11).

$$\ln K_d = \frac{\Delta S^\circ}{R} - \frac{\Delta H^\circ}{RT} \quad (5-11)$$

The van't Hoff equation fitting is shown in Figure 5.15, where slope and intercept of the linear fit to the data between  $\ln K_d$  and  $T^{-1}$  give the values of  $\Delta S$  and  $\Delta H$ . Table 5.6 represents the calculated values of thermodynamic parameters in which the negative values of Gibbs free energy reveal the adsorption is favorable at the higher temperature.

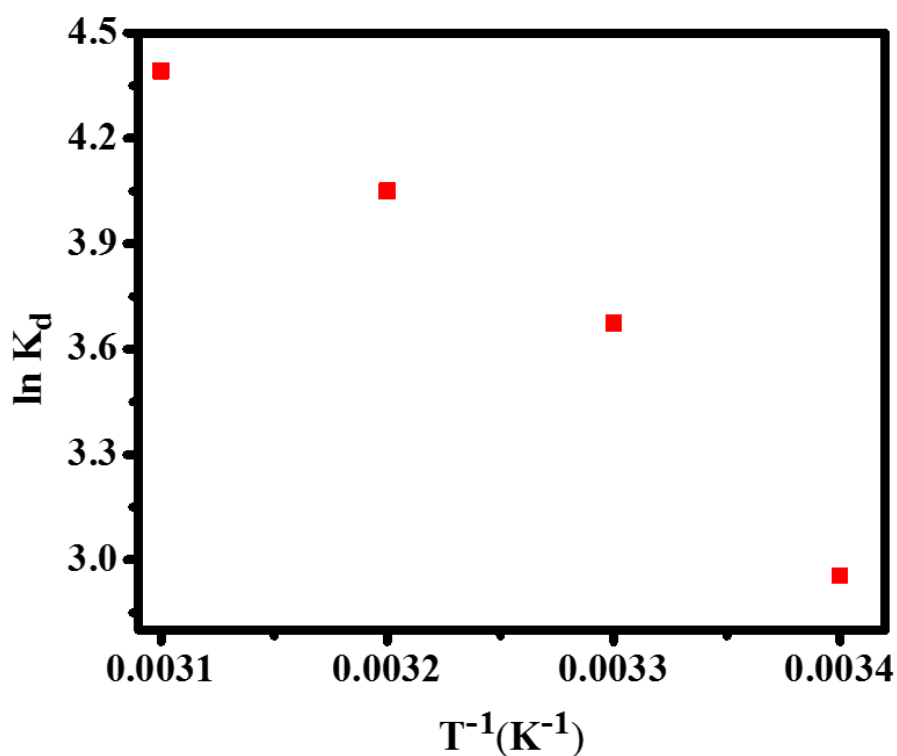


**Figure 5.15.** van't Hoff model fitting for CR adsorption by PANI/ZTO.

Generally,  $\Delta G^\circ$  helps in determining the type of adsorption as physisorption (-20 to 0 kJ/mol), physisorption with chemisorption (-20 to -80 kJ/mol) and chemisorption (-80 to

-400 kJ/mol) [348]. Therefore, the obtained value of  $\Delta G^\circ$  in the current research is between -9 to -3 kJ/mol which strongly in the favor of physisorption of CR onto PANI/ZTO nanocomposite. The  $\Delta S^\circ$  (185.69 J.mol<sup>-1</sup>.K<sup>-1</sup>) indicates the randomness at the solid-liquid interfaces during the adsorption. The randomness at the solid-liquid interface might be due to the selectivity of CR molecules from its aqueous solution by PANI/ZTO adsorbent. During the adsorption process, the CR molecules strongly attract by the PANI/ZTO adsorbent through various physical forces and simultaneously water have been repelled from the adsorbent surface due to which the randomness increases at the solid-liquid interface results into net entropy of the system increased. The typical number of the polyaniline monomers can be calculated from the striking entropy value 185.69 J.mol<sup>-1</sup>.K<sup>-1</sup>. The total change in entropy can be expressed in terms of monomer numbers as  $\Delta S^\circ = N_{av} \times k \times N$ . Where  $N_{av}$  is the Avogadro number (6.023×10<sup>23</sup>/mol),  $k$  is Boltzmann constant (1.38×10<sup>-23</sup> J/K) and  $N$  represents number of polyaniline monomers. The above equation turns out to be as  $\Delta S^\circ = R \times N$  where  $R$  (=kN) denotes gas constant. This equation gives a total number of  $N = 22$  monomers in a polyaniline chain. This is also in agreement with the previously reported data [349]. This number can also be justified from XRD data as the XRD peaks in PANI/ZTO nanocomposite related to PANI has been disappeared which suggested that the addition of ZnTiO<sub>3</sub> hinders the polymerization of PANI over its surface. This might be in result of short polymeric chains of less number of monomers. The enthalpy change  $\Delta H^\circ$  (45.58 kJ/mol) is positive which indicates the endothermic adsorption [350]. The endothermicity of the adsorption is also confirmed experimentally as the adsorption increases at a higher temperature [312]. The endothermicity of the reaction can be explained as follows. The glass transition temperature of the polyaniline has been reported between 30°C to 70°C in both polyaniline film and polyaniline (EB and ES) powder [351–353]. It is also reported that as the temperature of the polymer raises

near to its glass transition temperature then a liquid-like layer exists over the glassy film of polymer which ruling out the chain confinement and the size of the polymer chain divers [354]. This might increases the degree of freedom of the polyaniline chain due to which the randomness increases at the surface of the nanocomposite resulting in endothermic adsorption. Various driving forces are involved in the adsorption process and these can be identified with the help of the magnitude of  $\Delta H^\circ$  [341,355]. Therefore, it can be concluded from the  $\Delta H^\circ$  value that the adsorption is due to the electrostatic interaction,  $\pi$ - $\pi$  interaction, hydrogen bond forces, and dipole-dipole interaction forces. The endothermicity of the adsorption suggests that the entropy of the adsorption increases over a higher temperature range (20°C to 60°C). This could be explained as the presence of short polymeric chains (in between 20 to 30) onto the ZnTiO<sub>3</sub> surface in the nanocomposite. Despite having  $\Delta H^\circ > 0$  as the temperature increases, the entropy of polymeric chains dominates resulting in the adsorption.

**Table 5.6. Thermodynamic parameters for the adsorption of CR onto PANI/ZTO nanocomposites.**

| S.No. | T   | $\Delta G^\circ$        | $\Delta H^\circ$        | $\Delta S^\circ$                        |
|-------|-----|-------------------------|-------------------------|---|
| Unit  | (K) | (kJ×mol <sup>-1</sup> ) | (kJ×mol <sup>-1</sup> ) | (J×mol <sup>-1</sup> ×K <sup>-1</sup> ) |
| 1     | 293 | -8.88                   | 45.558                  | 185.69                                  |
| 2     | 303 | -8.68                   |                         |   |
| 3     | 313 | -7.20                   |                         |   |
| 4     | 323 | -3.89                   |                         |   |



## **Chapter 6: Solvent effect in synthesizing bismuth ferrite for methylene blue adsorption**

### **6.1 Abstract**

Herein, the synthesis and characterization of mixed-phase of  $\text{BiFeO}_3$  and  $\text{Bi}_2\text{Fe}_4\text{O}_9$  (represented as BFO) have been reported. Three different organic solvents Tetrahydrofuran (THF), N, N-dimethylformamide (DMF), and Dimethyl sulfoxide (DMS) have been used in the BFO synthesis process. The structural and morphological studies of the BFO have been examined. Further, the adsorption capacities of BFO synthesized in different organic solvents have been exposed. The BFO has been characterized by X-ray Diffraction (XRD), Fourier Transform Infrared (FTIR) spectroscopy, Field Emission Scanning Electron Microscopy (FESEM), Energy Dispersive X-ray Diffraction spectroscopy (EDX), X-ray Photoelectron Spectroscopy (XPS), Raman Spectroscopy, and Brunauer-Emmett-Teller (BET) analysis, etc. The interpretation of the kinetics, isotherms, and thermodynamics are also carried out of the adsorption of MB onto BFO nanoparticles which suggests that the adsorption process follows the pseudo-first-order rate kinetic equation and simultaneously thermodynamic parameter standard Gibbs energy ( $\Delta G^\circ$ ) has been calculated. The negative values (-24.8 kJ/mol to -16.8 kJ/mol) of standard Gibbs energy ( $\Delta G^\circ$ ) favors the physisorption of MB onto BFO, which is also confirmed by the Dubinin – Radushkevich model as the energy of adsorption is obtained 10.29 kJ/mol. The adsorption data is fitted to Langmuir isotherms results in the adsorption process is physisorption as well as favorable. The adsorption of MB onto BFO was examined with various parameters such as the effect of pH, amount of dye loading, contact time, and temperature.

## 6.2 Introduction

Organic solvents have their importance in the metal oxides synthesis process. The non-aqueous sol-gel synthesis of metal oxides in organic solvents have their advantage over the aqueous sol-gel synthesis. The advantage of the organic components is due to their manifold role such as solvents, surfactants, organic ligands, etc. The organic solvents also act as the oxygen supplier in the metal oxides formation which strongly determines the particle shape, particle size, and surface properties of the particles because of their coordination properties [356]. The nature of the solvent is important for growing the particles and gives rise to its particular morphology if the other factors are constant [357]. The above properties of the particles are crucial in many applications such as dye treatment through photocatalysis and adsorption.

$\text{BiFeO}_3$  is a perovskite material having the rhombohedral structure of space group  $R3c$  [358]. It is a multiferroic material having an electric and magnetic ordering that exists simultaneously at room temperature.  $\text{BiFeO}_3$  shows outstanding performance due to its high Curie temperature ( $T_c = 1100^\circ\text{C}$ ) and G-type ferromagnetic ordering below the Neel temperature ( $T_N = 643^\circ\text{C}$ ) [359].  $\text{BiFeO}_3$  has its potential applications in many areas such as spintronics, memory devices, information storage, sensors, and magnetoelectronics, *etc* [360–362]. In addition to its multiferroic properties, the  $\text{BiFeO}_3$  shows fascinating physio-chemical properties such as photocatalysis due to its narrow bandgap (2.18 eV) and chemical stability [146,363].  $\text{Bi}_2\text{Fe}_4\text{O}_9$  is another Bi-containing compound that is also widely used as a visible light photocatalyst due to its narrow double bandgap energy of 1.53 eV and 2.01 eV [364].  $\text{Bi}_2\text{Fe}_4\text{O}_9$  is obtained during the formation of  $\text{BiFeO}_3$  and adopted as a secondary phase or impurity in  $\text{BiFeO}_3$  materials [365]. In our work, we obtained a mixed phase of  $\text{BiFeO}_3$  and  $\text{Bi}_2\text{Fe}_4\text{O}_9$  and for convenience, we named BFO for the mixed phase of  $\text{BiFeO}_3$  and  $\text{Bi}_2\text{Fe}_4\text{O}_9$ .

In the present study, we have synthesized BFO by a non-aqueous sol-gel route in which three different organic solvents tetrahydrofuran (THF), N, N-dimethylformamide (DMF), and dimethyl sulfoxide (DMS) have been used. We have observed ample adsorption of methylene blue before examine visible-light photocatalytic activity by BFO. The adsorption of MB is also varied with the BFO prepared in different solvents. We found that the maximum adsorption occurs by BFO prepared in DMS while the least adsorption is by BFO prepared in DMF. For further study, we have considered BFO to show maximum adsorption. Currently, the synthesis and characterization of the materials have been exposed and their application for the adsorption before the visible light photocatalysis is also investigated. Later in the separate study, we will discover the visible-light photocatalytic activity of BFO.

Nowadays, dyes are the common materials in human life as these are applicable in the human's basic needs such as textiles, paper, food, printing, pulp mills, dyestuffs, plastic, and lather, etc. and these have been a serious environmental problem for human beings and aquatic organism [366,367]. The production of dyes all over the world is a great deal and dyes are produced on a large scale. Therefore, the production of dyes becomes industrial environment pollutants before production and after their uses in various applications. The industrial waste dye effluents can form a thin layer over the surface of receiving water bodies which consequently decreases the amount of oxygen dissolved and limits the penetration of the light in the water thereby affecting the food source of the aquatic organism by affecting the photosynthesis process [9]. Undoubtedly, the eviction of the dyes from the wastewater is indispensable as the dyes are persistent in the water and these are considered as Xenobiotic. So far, various methods and technologies have been introduced for the removal of dyes from the wastewater including photocatalysis [71,309], chemical oxidation [310], ion exchange [308], membrane filtration,[305] ozone

treatment,[307] coagulation/ flocculation,[306] metal-organic framework [368], and adsorption [311,312]. Among them, the adsorption was well-founded due to its simplicity, easy to use, high efficiency, and easy availability of a wide range of adsorbents (e.g., clay, zeolites, polymers, biomass, activated carbon, and nanomaterials such as metal oxides) [312].

### **6.3 Experimental section**

#### **6.3.1 Synthesis of Bismuth Ferrite Nanoparticles.**

The nanoparticles of BFO were synthesized by a non-aqueous sol-gel route as represented in Figure 6.1. The Bismuth nitrate pentahydrate and ferric nitrate nonahydrate were taken in 1.2: 1 wt. %. The following three solvents were tested N, N-dimethyl formamide (DMF), tetrahydrofuran (THF), and dimethyl sulfoxide (DMS) for the synthesis of BFO. First,  $\text{Bi}(\text{NO}_3)_3 \cdot 5\text{H}_2\text{O}$  was mixed in 20 mL of solvent in each set of experiments respectively in 50 ml one neck round bottom flask at room temperature with constant stirring. The solution was found to be colorless. Immediately,  $\text{Fe}(\text{NO}_3)_3 \cdot 9\text{H}_2\text{O}$  was mixed in the solution followed by continuous stirring by a magnetic stirrer for 12 hours at room temperature. Here are the observations during the mixing of  $\text{Fe}(\text{NO}_3)_3 \cdot 9\text{H}_2\text{O}$  in the above solution of  $\text{Bi}(\text{NO}_3)_3 \cdot 5\text{H}_2\text{O}$  and respective solvents. The final solution was brownish in color with solvents DMF and THF but the color of the final solution changed to be greenish with solvent DMS. The resultant solutions were found viscous, homogeneous, and stable. The resultant solution was sintered at 525 °C for 12 hours followed by the cooling till room temperature. The resultant was collected and grinding in a mortar pestle to make it a fine powder. The fine powder of BFO is appeared brownish. The fine powder was used to further study and these are named as given in Table 6.1 with their specifications. In the results and discussion part the “BFO” is written for DMS-B5 otherwise noted.

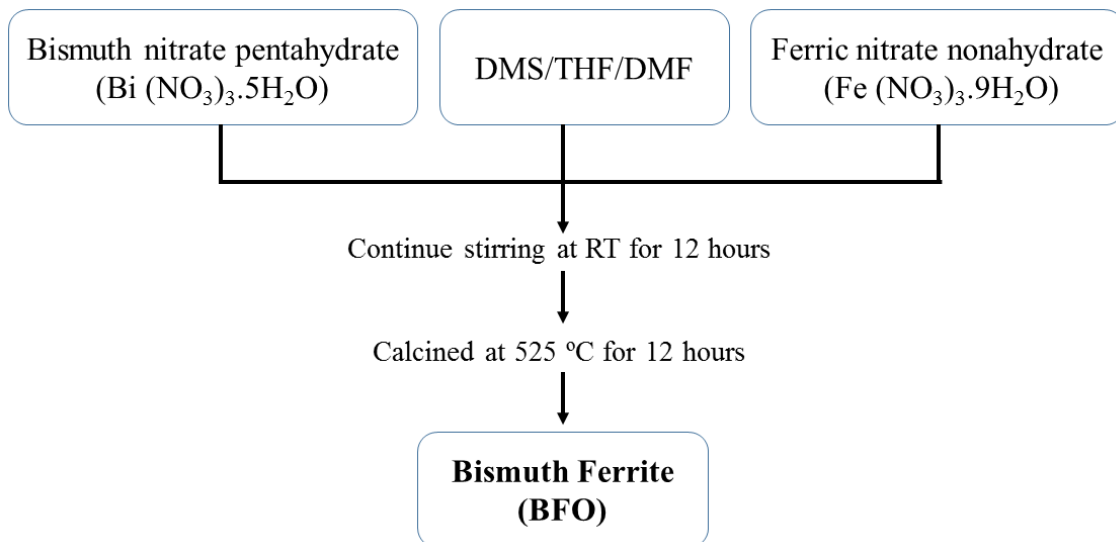


**Figure 6.1.** Synthesis process for bismuth ferrite in different solvents.

**Table 6.1:** Nomenclature of the samples.

| Samples       | Name   |
|---------------|--------|
| BFO with DMSO | DMS-B5 |
| BFO with THF  | THF-B5 |
| BFO with DMF  | DMF-B5 |

## 6.4 Results and discussion

### 6.4.1 X-ray diffractogram

The XRD patterns in Figure 6.2 depict the crystal structure of the prepared samples. The main characteristic peaks are well-matched within each sample. XRD confirms the mixed phase of  $\text{BiFeO}_3$  and  $\text{Bi}_2\text{Fe}_4\text{O}_9$  in samples. The peaks in case of DMS-B5 obtained at  $31.68^\circ$ ,  $32.06^\circ$ ,  $39.46^\circ$ ,  $51.26^\circ$ , and  $57.14^\circ$  can be assigned to (012), (110), (021), (113), and (300) plane respectively of the rhombohedral structure of  $\text{BiFeO}_3$  which is well agreed with the JCPDS file 00-020-0169. While few of the peaks at  $22.36^\circ$ ,  $35.67^\circ$ , and  $45.65^\circ$  belongs to the XRD planes (200), (022), and (132) respectively of the orthorhombic structure of  $\text{Bi}_2\text{Fe}_4\text{O}_9$ . The one most intense peak at  $27.86^\circ$  is close to the

most intense peak of  $\text{Bi}_{24}\text{Fe}_2\text{O}_{39}$  at  $27.97^\circ$  according to the JCPDS file 00-042-0201, but it is also close to the most intense peak of  $\text{Bi}_2\text{Fe}_4\text{O}_9$  at  $28.20^\circ$  according to the JCPDS file 00-042-0201. In this present study of the sample DMS-B5, the most intense peak was found at  $27.86^\circ$  which we are proposed to assign for  $\text{Bi}_2\text{Fe}_4\text{O}_9$  rather than  $\text{Bi}_{24}\text{Fe}_2\text{O}_{39}$ . The reason to assign this peak to  $\text{Bi}_2\text{Fe}_4\text{O}_9$  is described in the EDS section. The XRD patterns of THF-B5 and DMF-B5 are well-matched with the XRD pattern of DMS-B5 except for a few new peaks. The newly emerged peaks at  $66.31^\circ$ ,  $67.03^\circ$ ,  $70.52^\circ$ ,  $71.46^\circ$ , and  $75.81^\circ$  can be ascribed for (060), (220), (015), (303), and (214) planes of the rhombohedral structure of  $\text{BiFeO}_3$  in DMF-B5 and THF-B5. Two major changes have been noticed in DMS-B5 as compared to DMF-B5 and THF-B5. One of them is the variation of the peaks intensity which may be due to the mass fraction of the samples under characterization. Secondary, most of the peak's position in all three samples is the same irrespective of the peak in the range of  $27^\circ$ - $28^\circ$ . The XRD peaks positioned in this range at  $27.37^\circ$ ,  $27.70^\circ$ , and  $27.86^\circ$  for DMF-B5, THF-B5, and DMS-B5 respectively. In order to get an explanation for this variation, we can fix the XRD peak at  $27.37^\circ$  of THF-B5 as the reference peaks for the other two samples because the solvent tetrahydrofuran (THF) is composed of carbon, hydrogen, and oxygen only no other elements such as nitrogen or sulphur is to present as in case of dimethyl sulfoxide (DMS) and dimethylformamide (DMF). Now, the variation in the peak position of DMS-B5 and DMF-B5 can understand as follows. Since the DMS-B5 sample was prepared in dimethyl sulfoxide solvent where the sulphur (S) is one of the elements. Therefore, it is a possibility of capturing the sulphur in the DMS-B5 sample lattice during the calcination process. As the atomic size of the sulphur is bigger than the oxygen so captured sulphur might produce the strain in the samples which might be the cause for the peak shifting in XRD pattern. The same concept could be applied to the DMF-B5 sample where nitrogen is the main source in the

dimethylformamide solvent. Therefore, the sample DMS-B5 and DMF-B5 may be doped with sulfur and nitrogen respectively attributing to the peak shift.

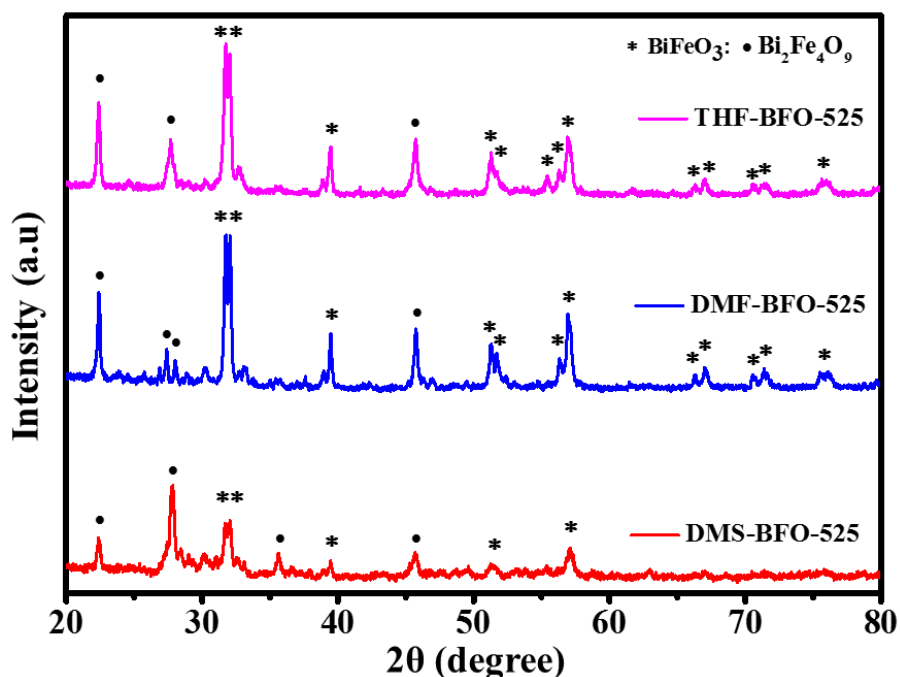


**Figure 6.2.** XRD Pattern of BFO prepared with different solvent DMS, DMF, and THF (bottom to up).

The crystallites size ( $d$ ) is calculated by using the Debye-Scherrer Equation (3-1) for the peak at  $22.4^\circ$  for all the samples. The  $d$  calculates at 29.15 nm, 33.68 nm, and 38.87 nm for DMS-B5, THF-B5, and DMF-B5 respectively.

#### 6.4.2 Fourier Transform Infrared Spectroscopy analysis

Figure 6.3 shows the FTIR spectra of the perovskite-type vibration in the mixed-phase of  $\text{BiFeO}_3$  and  $\text{Bi}_2\text{Fe}_4\text{O}_9$ . The bands at around  $3660\text{ cm}^{-1}$  in the DMS-B5 sample can be assigned to the O-H stretching of the intramolecular hydrogen bonds or hydroxyl ions [369]. The C-H stretching vibration can be identified at  $2980\text{ cm}^{-1}$  to  $2887\text{ cm}^{-1}$ , which are common to all the samples [370]. Too many small sharp peaks obtained between  $400\text{ cm}^{-1}$  to  $520\text{ cm}^{-1}$  could be attributed to the characteristic peaks of BFO as follow. The

FTIR bands in between  $400\text{ cm}^{-1}$ - $410\text{ cm}^{-1}$ ,  $410\text{ cm}^{-1}$  to  $425\text{ cm}^{-1}$ , and  $425\text{ cm}^{-1}$  to  $440\text{ cm}^{-1}$  can be assigned to bending vibration of O-Fe-O, asymmetric stretching of Fe-O-Fe, and deformations of  $\text{FeO}_6$  octahedral respectively in BFO [371]. The FTIR bands at  $452\text{ cm}^{-1}$  and  $547\text{ cm}^{-1}$  can be identified as the bending and stretching vibration of Fe-O bonds in  $\text{FeO}_6$  octahedral [372]. The vibrations corresponding to Bi-O bonds of  $\text{BiO}_6$  octahedral also detect in the range of  $450\text{ cm}^{-1}$  to  $500\text{ cm}^{-1}$  [371]. It is reported that the two different sites ( $\text{Fe}_1$  and  $\text{Fe}_2$ ) are occupied by four Fe atoms in  $\text{Bi}_2\text{Fe}_4\text{O}_9$  [372].  $\text{Fe}_1$  occupies a tetrahedral position and makes a  $\text{FeO}_4$  tetrahedral while  $\text{Fe}_2$  occupies an octahedral position and makes  $\text{FeO}_6$  octahedral. Therefore, both the tetrahedral  $\text{FeO}_4$  and octahedral  $\text{FeO}_6$  exist simultaneously in  $\text{Bi}_2\text{Fe}_4\text{O}_9$  [372]. The FTIR bands at  $633\text{ cm}^{-1}$  and  $692\text{ cm}^{-1}$  are assigned to the stretching vibration of Fe-O bond of  $\text{FeO}_4$  tetrahedra which are the characteristic peaks of  $\text{Bi}_2\text{Fe}_4\text{O}_9$  [373]. The band at  $583\text{ cm}^{-1}$  is assigned to the Fe-O-Fe bending vibration of the tetrahedron  $\text{FeO}_4$  pairs in  $\text{Bi}_2\text{Fe}_4\text{O}_9$  [374]. Thus these peaks are also in good agreement with XRD data which in the favor of the presence  $\text{Bi}_2\text{Fe}_4\text{O}_9$ . A band at  $1474\text{ cm}^{-1}$  common to all samples can be attributed to the presence of carbonates ions may be in the form of  $\text{FeCO}_3$  [372]. The common band located at  $1388\text{ cm}^{-1}$  in all the samples is assigned to the existence of nitrate ions from the metal ions precursor[282]. The obtained FTIR patterns are not common in the range of  $900\text{ cm}^{-1}$  to  $1200\text{ cm}^{-1}$  for all three samples, this might be attributed to the used different solvents.

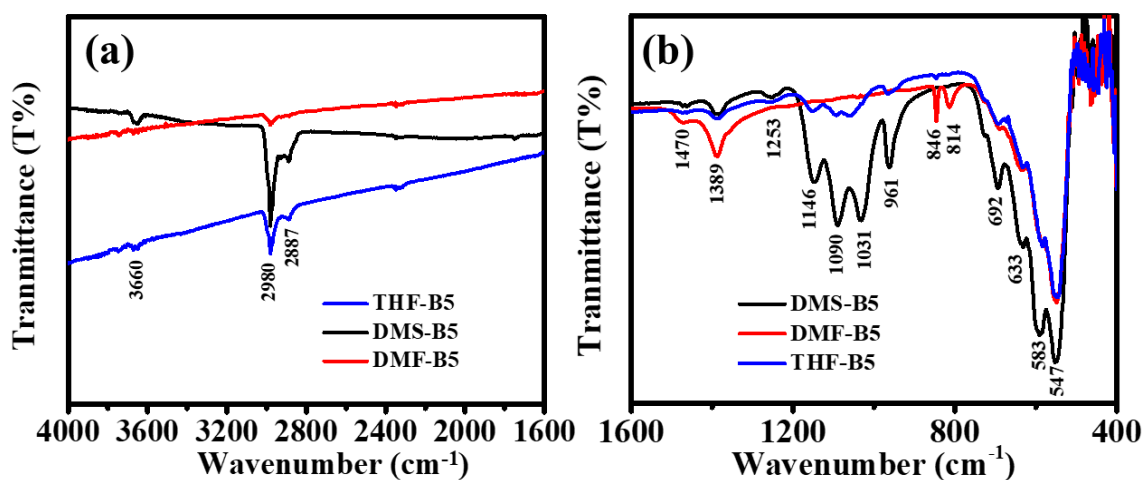


**Figure 6.3** The FTIR spectra from (a) 4000  $\text{cm}^{-1}$  to 1600  $\text{cm}^{-1}$  and (b) 1600  $\text{cm}^{-1}$  to 400  $\text{cm}^{-1}$  represents the chemical bonding of BFO prepared in different solvents.

In the FTIR spectra of DMF-B5, two peaks at 814  $\text{cm}^{-1}$  and 846  $\text{cm}^{-1}$  can be assigned to the nitrate ions ( $\text{NO}_3^-$ ) [375]. While the FTIR spectra of DMS-B5 in the range of 900  $\text{cm}^{-1}$  to 1200  $\text{cm}^{-1}$  can be assigned to the sulfate ions, as the DMSO is a source of sulfur. The FTIR spectrum of the sample DMS-B5 consists of characteristic peaks at 1031  $\text{cm}^{-1}$  and 1090  $\text{cm}^{-1}$ , which can be assigned to the symmetrical vibration of  $\text{SO}_4^{2-}$  while the bands at 961  $\text{cm}^{-1}$  and 1146  $\text{cm}^{-1}$  can be assigned to S-O and S=O in  $\text{SO}_3^{2-}$  respectively [376]. However, the FTIR peaks in the same region at 961  $\text{cm}^{-1}$ , 1057  $\text{cm}^{-1}$ , and 1091  $\text{cm}^{-1}$  represent the C-O bond, and the band at 1151  $\text{cm}^{-1}$  represents surface adsorbed  $\text{NO}_3^-$  [226,285,377]. These peaks are also noticed in THF-B5 samples. The FTIR spectrum of DMF-B5 does not show any peak in the range of 900  $\text{cm}^{-1}$  to 1200  $\text{cm}^{-1}$  but instead of that, the intensity of nitrate band at 1388  $\text{cm}^{-1}$  is larger than the other two samples. This peak enhancement might be due to the addition of nitrogen through the DMF solvent.

#### 6.4.3 FESEM images and EDS analysis

Figure 6.4 represents the FESEM image analysis of the samples at the two different scales at 500 nm and 1  $\mu\text{m}$  respectively. The FESEM images of DMS-B5 are

depicted in Figure 6.4a-b. It is interesting to find the nanorods over the surface. These nanorods are embedded onto the surface of DMS-B5 and their orientations are random in all directions.

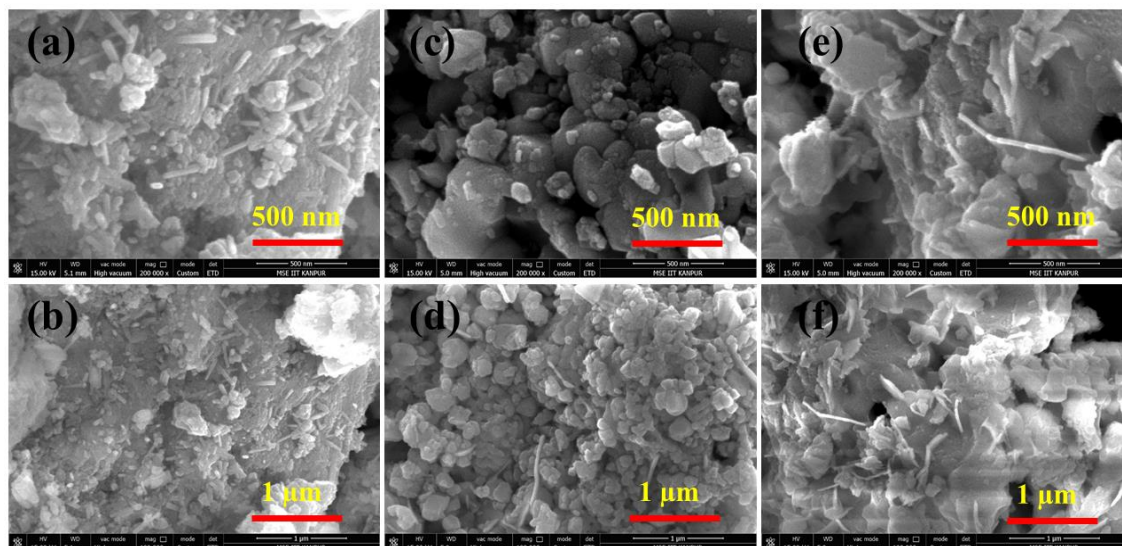


**Figure 6.4:** The FESEM images of (a) and (b)-DMS-B5 showing nanorods on the surface; (c) and (d)- DMF-B5 representing nanoparticles; (e) and (f)-THF-B5 representing nanoflakes at two different scales 500 nm and 1  $\mu$ m.

The typical length of the nanorods is calculated from 100 nm to 300 nm while the diameter around 20 to 50 nm. The surface morphology of DMF-B5 is presented in Figure 6.4c-d which shows the well-formation of BFO crystallites in a few nanometres ranges to hundreds of nanometre ranges. As can be observed from the micrograph, the BFO nanoparticles synthesized in DMF are aggregated. In contrast, the BFO prepared in THF shows the nanoflakes in the micrographs Figure 6.4(e)-(f), and these nanoflakes are also grown vertically on the surface. As observed, from micrograph Figure 6.4 that the BFO synthesized in different solvents DMSO, DMF, and THF show the different morphology which might be attributed to their different chemical nature which plays their vital role during the BFO synthesis.

The EDS is used to determine the elemental composition of synthesized samples. This technique is employed here to ascertain the presence of Bismuth (Bi), Iron (Fe), and Oxygen (O) in BFO. Figure 6.5a-c represents Bi, Fe, and O elements in DMS-B5, DMF-B5, and THF-B5 samples respectively. In addition, at% and wt% of the respective elements are listed in Table 6.2. Table refers that the Bi:Fe ratio is 1:2, we claim here that our samples composed of  $\text{Bi}_2\text{Fe}_4\text{O}_9$ , not  $\text{Bi}_{24}\text{Fe}_{20}\text{O}_{39}$ .

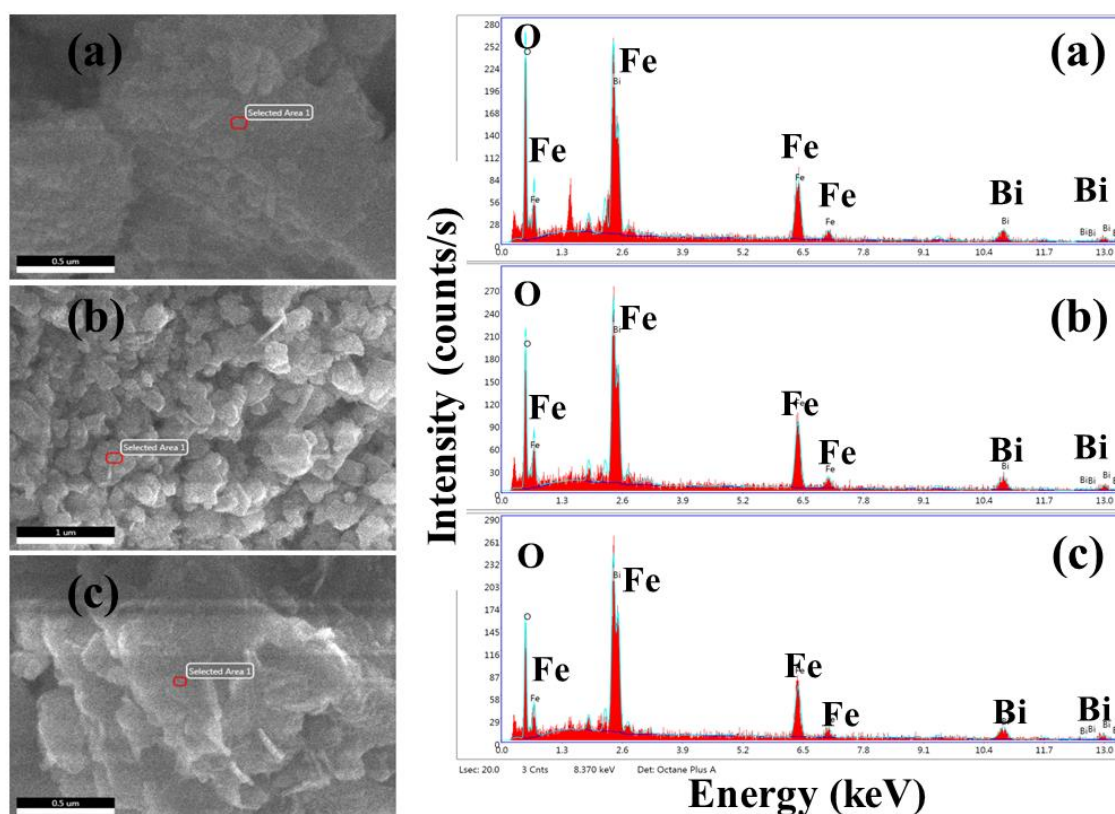


**Figure 6.5. The Energy Disperse Spectrum of (a)-DMS-B5, (b)-DMF-B5, and (c)-THF-B5 representing the presence of Bi, Fe, and O in all samples.**

**Table 6.2. Elemental analysis of DMS-B5, DMF-B5, and THF-B5.**

| <b>Sample</b> | <b>Elements</b> | <b>wt%</b> | <b>at%</b> |
|---------------|-----------------|------------|------------|
| <b>DMS-B5</b> | Bi              | 52.68      | 12.77      |
|               | Fe              | 27.72      | 25.14      |
|               | O               | 19.61      | 62.09      |
| <b>DMF-B5</b> | Bi              | 53.28      | 14.17      |
|               | Fe              | 30.86      | 30.71      |
|               | O               | 15.87      | 55.12      |
| <b>THF-B5</b> | Bi              | 58.18      | 16.60      |
|               | Fe              | 27.25      | 29.10      |
|               | O               | 14.57      | 54.30      |

#### 6.4.4 Raman Analysis

Raman spectroscopy is a valuable technique to provide a local electronic structure within the materials. The Raman spectra of all the samples have been recorded by a laser source of 532 nm and are represented in Figure 6.6. It is well known that the Bi atoms are low wavenumber modes active up to  $167\text{ cm}^{-1}$  and the Fe atoms are the dominates in the modes between  $152\text{ cm}^{-1}$  and  $261\text{ cm}^{-1}$  meanwhile the modes above  $262\text{ cm}^{-1}$  ascribed for the motion of the oxygen atoms [378]. Since the samples are composed of two distinct phases of  $\text{BiFeO}_3$  and  $\text{Bi}_2\text{Fe}_4\text{O}_9$ , therefore the Raman spectra have contained the bands of two phases simultaneously. The  $\text{BiFeO}_3$  has a distorted perovskite structure, rhombohedral with space group  $R3c$ , and  $C_{3v}$  point group which contains a total of 13 Raman active modes (4  $A_1$  modes and 9 E modes) [379]. The Raman active modes with  $A_1$  and E can be recapitulated as in the irreducible representation  $\Gamma = 4A_1 + 5A_2 + 9E$ , however,  $A_2$  modes are Raman inactive for  $\text{BiFeO}_3$  while for  $\text{Bi}_2\text{Fe}_4\text{O}_9$ , the irreducible

representation is formulated by  $\Gamma = 12A_g + 12 B_{1g} + 9 B_{2g} + 9B_{3g}$  [379]. The Raman modes of the local structure of the as-prepared samples are listed in Table 6.3. Raman bands for the DMS-B5 sample have been described as follows. The Raman band at  $99 \text{ cm}^{-1}$  can be attributed to the  $A_g$  mode of  $\text{Bi}_2\text{Fe}_4\text{O}_9$  where the Bi atom vibrates in the xy plane [380]. The signal at  $145 \text{ cm}^{-1}$  can be assigned to the  $A_1$  mode of  $\text{BiFeO}_3$  [381]. In addition, the signal at  $214 \text{ cm}^{-1}$  can be attributed to the  $A_g$  mode of Fe1 atom which vibrates in the xy plane and the Raman band at  $294 \text{ cm}^{-1}$  can be assigned to the  $B_{3g}$  mode of Fe2 atom vibrates along the y-direction in  $\text{Bi}_2\text{Fe}_4\text{O}_9$  [382].

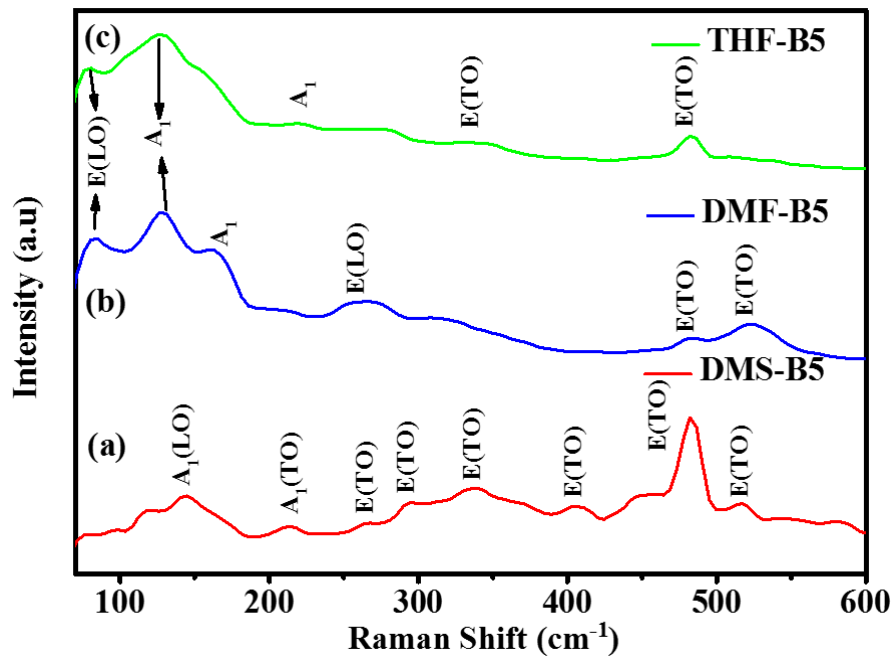


**Figure 6.6: Raman Spectrum of BFO (a) DMS-B5, (b) DMF-B5, (c) THF-B5.**

The Raman bands at the higher Raman shift can be assigned to the oxygen vibration. Therefore, the Raman bands at  $337 \text{ cm}^{-1}$ ,  $404 \text{ cm}^{-1}$ ,  $482 \text{ cm}^{-1}$ ,  $516 \text{ cm}^{-1}$ ,  $544 \text{ cm}^{-1}$ ,  $580 \text{ cm}^{-1}$ ,  $662 \text{ cm}^{-1}$ , and  $731 \text{ cm}^{-1}$  can be assigned to the vibration of oxygen atoms positioned at the different location in  $\text{Bi}_2\text{Fe}_4\text{O}_9$  and  $\text{BiFeO}_3$  lattice [378]. The Raman signals at  $337 \text{ cm}^{-1}$  and  $731 \text{ cm}^{-1}$  can be assigned to the  $A_g$  modes of oxygen atoms ( $\text{O}_3$ ) move along the xy direction while the band at  $404 \text{ cm}^{-1}$  can be assigned to the  $B_{3g}$  mode of  $\text{O}_3+\text{O}_2$  oxygen

atoms vibrates in the xy direction [382]. A shoulder at  $544\text{ cm}^{-1}$  and a band at  $662\text{ cm}^{-1}$  can be assigned to the  $B_{1g}$  modes of O4+O3 and O2+O4 oxygen atoms simultaneously in xy direction [382]. Few of the Raman bands are originated from the  $\text{BiFeO}_3$  crystal structure and these bands can be assigned for the various atoms vibration as follows. The Raman bands at  $145\text{ cm}^{-1}$  and  $516\text{ cm}^{-1}$  belong to  $A_1$  (LO), and  $A_1$  (TO) modes respectively [383–385]. The Raman peaks at  $267\text{ cm}^{-1}$ ,  $337\text{ cm}^{-1}$ ,  $482\text{ cm}^{-1}$ , and  $517\text{ cm}^{-1}$  are ascribed for the E(TO) modes of phonons [379,384–386]. The Raman band at  $482\text{ cm}^{-1}$  is common to all samples which might be attributed to the  $\text{FeO}_6$  octahedral of the  $\text{BiFeO}_3$  compound. With the other samples, as the positions of the peaks have been listed in Table 6.3 show the shift in the corresponding Raman peaks, and also the emergence and disappearance of the new peaks. With these, two major phenomena are also noticed as the change in peak intensity and peak broadening. These phenomena noticed in the Raman peaks can be understood on the behalf of the solvents used. Raman spectroscopy is a very sensitive technique and it is sensitive to atomic displacement. So, it can be proposed here as the BFO has been synthesized in the different solvents which they have their properties and atomic arrangement which directly affected the crystal structure and results in the different Raman spectrum. The Raman peaks broadening occur in the DMS-B5 samples as compare to the others can be described as the degree of disorder in the DMS-B5 increased and some of the symmetry was destroyed might be due to sulphur insertion during calcination. This data also supported by the XRD and FTIR data.

**Table 6.3. The identification and assignment of RAMAN peaks in all the samples.**

| DMS-B5 | DMF-B5 | THF-B5  | Mode              | Atomic motion         | Compound                                       |
|--------|--------|---------|-------------------|-----------------------|--|
| 99     | 85     | 80      | A <sub>g</sub>    | Bi (xy plane)         | Bi <sub>2</sub> Fe <sub>4</sub> O <sub>9</sub> |
| 145    | 131    | 127     | A <sub>1</sub> -1 | Bi (z-direction)      | BiFeO <sub>3</sub>                             |
|        | 163    |         | A <sub>1</sub> -2 | Fe (z-direction)      | BiFeO <sub>3</sub>                             |
| 214    | 212    | 222     | A <sub>g</sub>    | Fe1 (xy plane)        | Bi <sub>2</sub> Fe <sub>4</sub> O <sub>9</sub> |
| 267    | 270    | 277     | E (TO)            | O (xy plane)          | BiFeO <sub>3</sub>                             |
| 294    |        |         | B <sub>3g</sub>   | Fe2 (y-<br>direction) | Bi <sub>2</sub> Fe <sub>4</sub> O <sub>9</sub> |
| 337    | 316    | 334/348 | A <sub>g</sub>    | O3 (xy)               | Bi <sub>2</sub> Fe <sub>4</sub> O <sub>9</sub> |
| 404    |        | 408     | B <sub>3g</sub>   | O3 (z) +<br>O2(xy)    | Bi <sub>2</sub> Fe <sub>4</sub> O <sub>9</sub> |
| 482    | 483    | 483     | E (TO)            | O (xy plane)          | BiFeO <sub>3</sub>                             |
| 517    | 522    | 509     | E (TO)            | O (xy plane)          | BiFeO <sub>3</sub>                             |
| 544    |        | 535     | B <sub>1g</sub>   | O4(xy) +<br>O3(xy)    | Bi <sub>2</sub> Fe <sub>4</sub> O <sub>9</sub> |
| 580    |        |         |                   |                       |  |
| 662    | 680    | 626     | B <sub>1g</sub>   | O4(xy) +<br>O2(xy)    | Bi <sub>2</sub> Fe <sub>4</sub> O <sub>9</sub> |
|        |        | 710     |                   |                       |  |
| 729    | 738    | 731     | A <sub>g</sub>    | O4(xy)                | Bi <sub>2</sub> Fe <sub>4</sub> O <sub>9</sub> |

#### 6.4.5 BET Surface area analysis

The Brunauer-Emmett-Teller (BET) surface area measurement has been carried out via a multi-point BET method by using nitrogen adsorption and desorption. The isotherms of

the DMS-B5 and its pore size distribution can be seen in Figure 6.7. As can be observed from micrograph 5 that the DMS-B5 sample exhibits type (IV) adsorption-desorption isotherm accompanied by an H<sub>4</sub>-type hysteresis loop which shows the capillary condensation occurs in a mesoporous range of the pores at relatively high pressure (P/P<sub>0</sub>) [387]. The existence of type (IV) isotherm reveals the interaction of the DMS-B5 with the N<sub>2</sub> and also it shows the interaction between the molecules in the condensed state. Figure 6.7a shows the initial monolayer and multilayer adsorption onto mesoporous walls in the relative pressure (P/P<sub>0</sub>) range 0-0.8 and then followed by the pore condensation at a relatively high-pressure range 0.8-1.0. The capillary condensation infers the existence of canonical and cylindrical mesoporous over the surface of DMS-B5. At pressure 0.8-1, the hysteresis loop obtained of type H<sub>4</sub> can be ascribed to the narrow slit-like pores due to large inter aggregated pores.

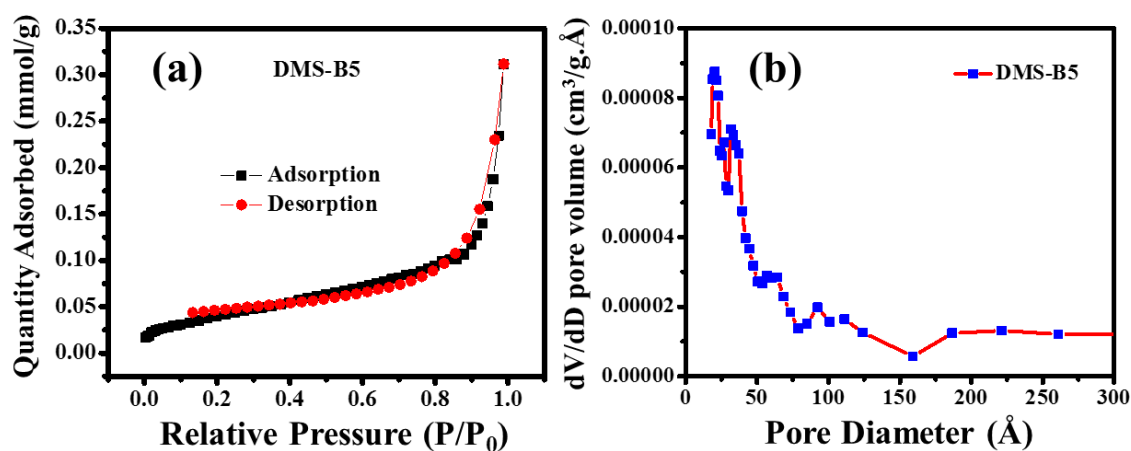


**Figure 6.7. (a) Nitrogen adsorption-desorption isotherm for DMS-B5 showing the surface area of 3.46 m<sup>2</sup>/g, and (b) pore size distribution of DMS-B5.**

The one important phenomenon that can be noticed in the desorption data that the monolayer desorption part is absent from Figure 6.7a only multilayer desorption data is present. This observation can be attributed to the monolayer adsorption of N<sub>2</sub> onto the DMS-B5 surface during the experiment and the adsorbate and adsorbent interaction is strong enough which does not allow the monolayer desorption. Analysis of the adsorption

data with the BET method gives a surface area of 3.46 m<sup>2</sup>/g and a total BJH pore volume 0.00568 cm<sup>3</sup>/g. The pore size distribution of DMS-B5 has been calculated by employing Barret-Joyner-Halender (BJH) desorption method and it is evident that the DMS-B5 sample presents quite an extended pore size distribution range 2 nm to 9.2 nm as represented in Figure 6.7b. Thus, the pore size distribution suggests the mesoporosity in the sample and it is also very close to the edge of microporosity as well. The mesoporosity in the sample can be attributed to the aggregation of the BFO crystallites due to its magnetic nature.

## **6.5 Adsorption study**

### **6.5.1 Adsorption experiments**

The batch adsorption study of the MB onto BFO nanoparticles was carried out in a 250 mL beaker. Initially, adsorption by all the three samples DMS-B5, DMF-B5, and THF-B5 was examined for 100 ml of 7.5 ppm MB solution by the constant amount of 150 mg of the adsorbent. The suspension was magnetically stirred at 800 rpm in the dark environment. 2 mL suspension was collected at a predetermined time interval and further centrifuged at 4000 rpm for 10 minutes to separate nanoparticles from the suspension. The supernatant was collected for recording the UV-Vis data. The characteristic peak of MB appears at 664 nm corresponding to n- $\pi^*$  transition and this peak has been monitored to calculate adsorption. Initially, the adsorption properties of BFO prepared with three different solvents have been studied onto a 7.5 ppm MB aqueous solution. Figure 6.8 suggests that the maximum adsorption has been achieved by the DMS-B5.

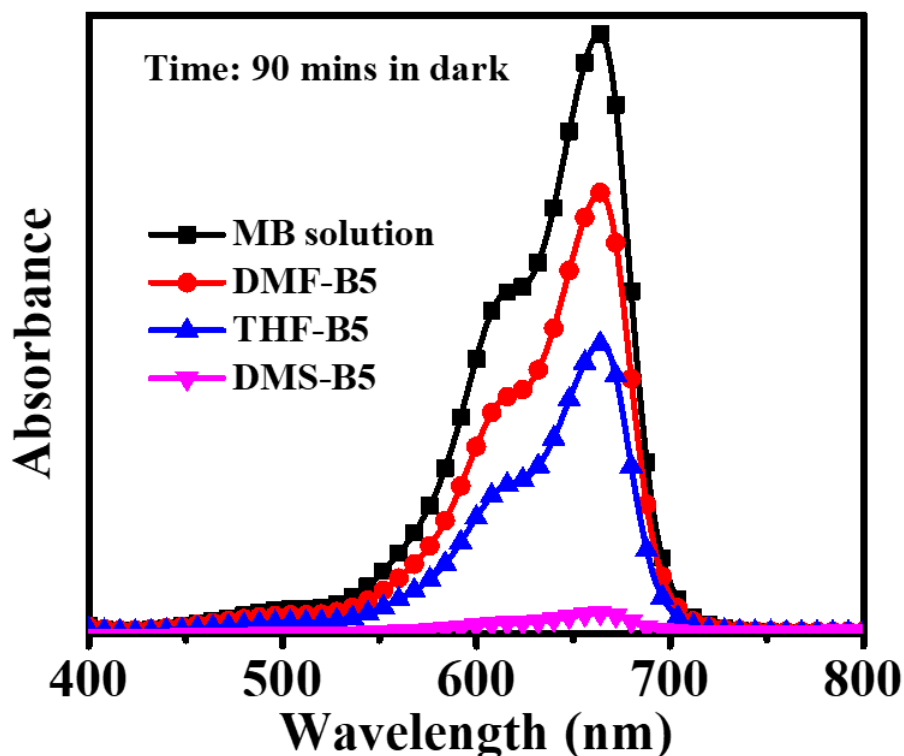


**Figure 6.8:** UV-Vis analysis shows the maximum adsorption of 15 ppm aqueous solution (100 mL) of Methylene Blue by DMS-B5 (adsorbent amount: 150 mg).

Simultaneously, we calculate the % of dye removal efficiency by the following Equation (6-1).

$$\%R = \left[ \frac{C_0 - C_t}{C_0} \times 100 \right] \% \quad (6-1)$$

Where,  $C_0$  represents initial dye concentration and  $C_t$  represents final dye concentration in an aqueous solution. Figure 6.9 interprets the dye removal efficiency of the BFO thereby the maximum removal efficiencies are calculated 96.54%, 51.63%, and 26.48% for DMS-B5, THF-B5, and DMF-B5 respectively corresponding to the equilibrium adsorption. We noticed that the BFO prepared in different solvents offers different adsorption. It is quite interesting to tune the adsorption properties of the materials by just changing the solvent during the synthesis process. Appreciating the maximum adsorption of MB by the DMS-B5 sample, we further continued the batch adsorption experiments with the DMS-B5 sample only. Now, the effect of different parameters such as dye

loading, pH of the solution, and temperature has been investigated. The adsorption mechanism has been studied over a pH scale from 1 to 13. The pH of the aqueous solution of MB has been adjusted by adding HCl and NaOH. In Figure 6.10a-d, the abbreviate use as the first letter “D” means the reaction was carried out in dark and the numerical values denote the time in minutes.

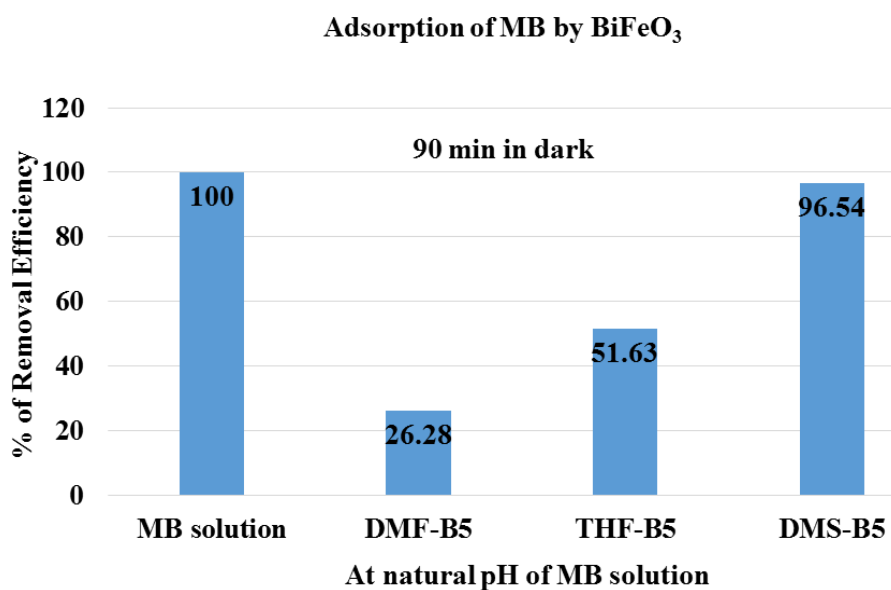


**Figure 6.9:** Diagram represents the percentage of removal efficiency of MB (15 ppm) from aqueous solution (100 mL) by BFO prepared in different solvents.

### 6.5.2 Amount of MB loading

The adsorption kinetics have been studied over the four different dye concentrations 4.5 ppm, 7.5 ppm, 15.2 ppm, and 22.8 ppm for the time 120 minutes as shown in Figure 6.10.

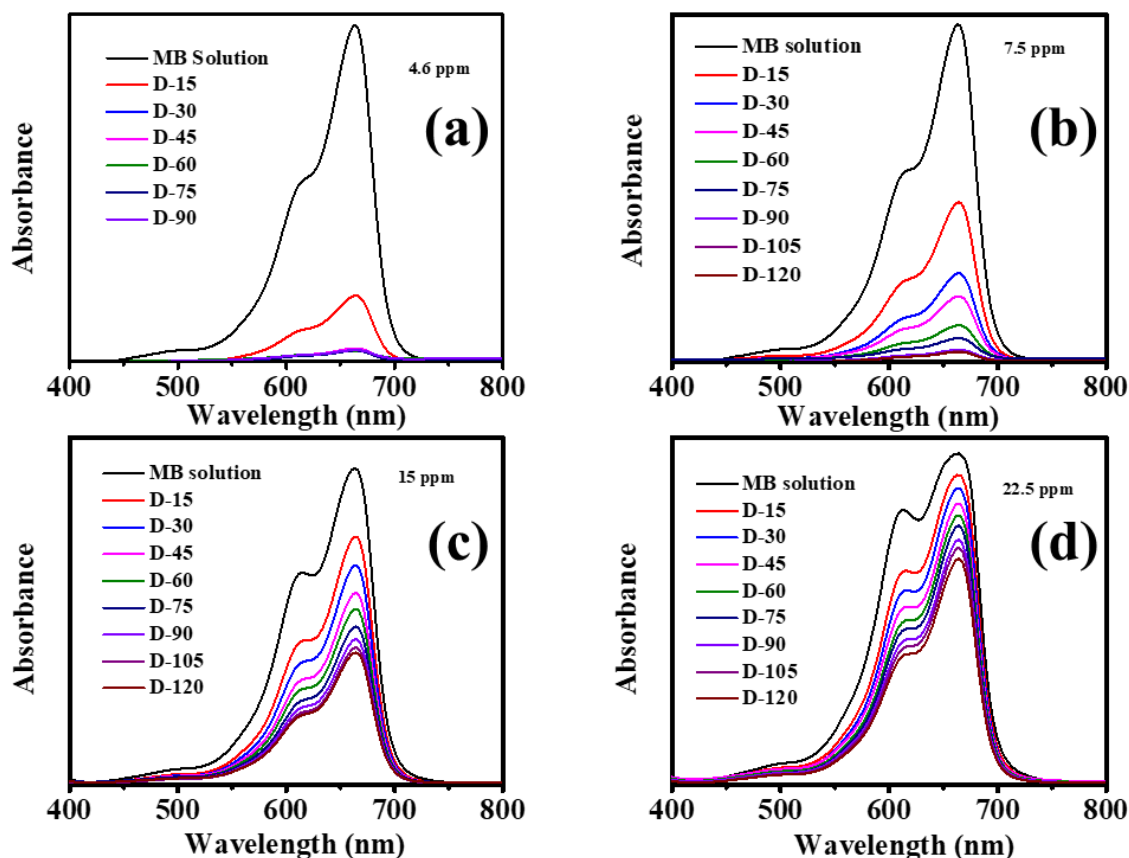


**Figure 6.10. Time-based adsorption kinetics of MB adsorption at different concentrations (a) 4.5 ppm, (b) 7.5 ppm, (c) 15 ppm, and (d) 22.5 ppm, by DMS-B5.**

Figure 6.10 infers that the adsorption decreases with the increase in dye concentration. This might be due to the strike hindrance of the dye molecules at the higher concentration. The % of dye removal efficiency is calculated for the respective dye concentrations as represented in Figure 6.11 where the dye removal efficiency for the 4.5 and 7.5 ppm is almost constant at 96.6 %. Meanwhile, for the two higher concentrations 15 ppm and 22.5 ppm, the % removal efficiency has been decreased sharply at 54.26 % and 26.4 % respectively. This can be attributed as with the agitation at lower dye concentration, the mass transfer coefficient increases which results in fast adsorption. However, attaining equilibrium adsorption is delayed with higher dye concentration.

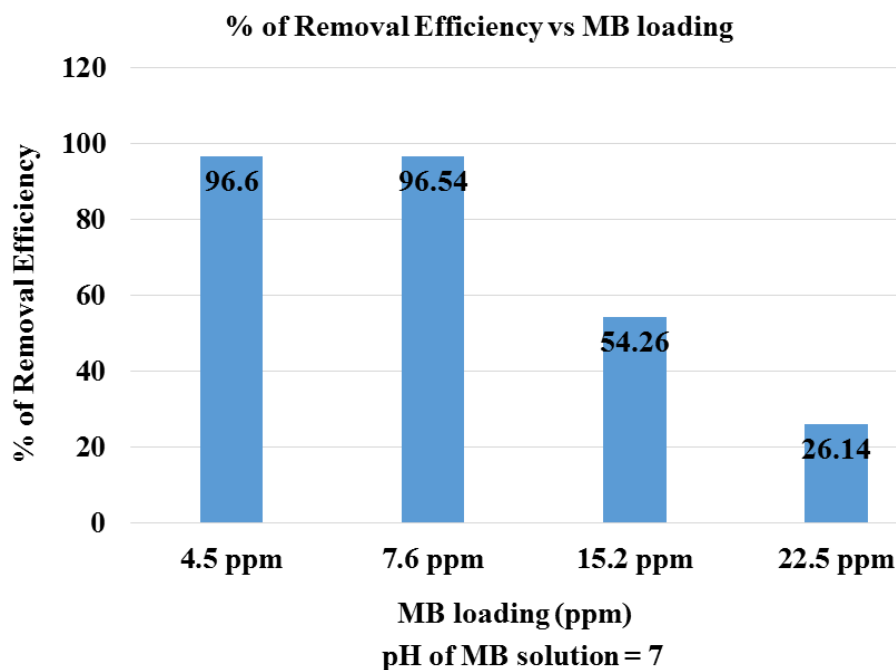


**Figure 6.11.** Graph represents that the higher dye loading (in 100 mL volume) decreases the adsorption by DMS-B5 (150 mg).

### 6.5.3 Effect of pH

The 7.5 ppm MB adsorption has been examined at different pH values. The pH of the solution alters the surface charge of adsorbent, ionized the pollutants in their aqueous solution media, can dissociate functional groups, and also have the ability to change the structure of the pollutants [28]. The influence of pH on the removal of MB from its aqueous solution by DMS-B5 nanoparticles has been investigated for further adsorption process. The adsorption and removal efficiency of MB by DMS-B5 nanoparticles have exaggerated in Figure 6.12a over the pH range 1 to 14. The pH of the system exerts a deep influence on the uptake of adsorbate perhaps due to its impact on the surface properties of the adsorbate and adsorbent molecules. The absorbance data have repeated and here two times data named Run-1 and Run-2 are shown in Figure 6.12a.

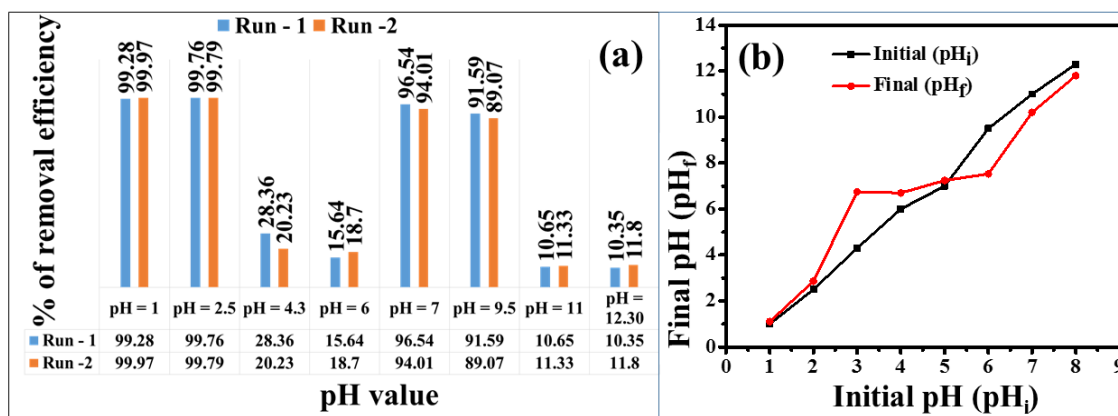


**Figure 6.12. (a) Percentage of removal efficiency at different pH values, and (b) pH of MB aqueous solution before adsorption (pH<sub>i</sub>) and after adsorption (pH<sub>f</sub>) treatment.**

Nearly 100% dye removes at pH-1 and pH-2 as represented in Figure 6.12a. It is noticed that the MB degradation efficiencies rapidly reduce to around 28.36% and 15.64% at pH-4.3 and pH-6 respectively. Surprisingly, the degradation efficiencies jumped abruptly till 96.54% at natural pH-7 and slightly decreases to 91.59% at pH-9.5. Further in a highly basic medium, again the degradation efficiencies abruptly decreased to 11% as illustrated. Thus, the dye uptake is found to be pH-dependent. Table 6.4 summarizes the initial pH before adsorption and final pH values after adsorption of the MB aqueous solution.

**Table 6.4. The pH of MB aqueous solution before and after adsorption process.**

|                       |       |       |       |       |       |      |       |       |
|-----------------------|-------|-------|-------|-------|-------|------|-------|-------|
| <b>pH<sub>i</sub></b> | 1     | 2.50  | 4.3   | 6     | 7     | 9.5  | 11    | 12.30 |
| <b>pH<sub>f</sub></b> | 1.10  | 2.86  | 6.75  | 6.70  | 7.24  | 7.53 | 10.20 | 11.80 |
| <b>ΔpH</b>            | -0.10 | -0.36 | -2.45 | -0.70 | -0.24 | 1.97 | +0.80 | +0.50 |

The value of the zero point charge ( $pH_{zpc}$ ) is calculated to be 5.10 from the intersection of the point between the initial pH curve and the final pH curve as shown in Figure 6.12b. At solution  $pH < pH_{zpc}$ , the BFO surface may acquire a positive charge while at solution

pH > pH<sub>zpc</sub>, the BFO surface may get a negative charge [312]. The MB is a cationic dye and we found maximum adsorption in a highly acidic medium (pH-1 to pH-3). This is doubtful to us why the cationic MB gets highly adsorbed in the acidic medium where the surface charge of BFO may be positive from the zero point charge calculation. So the possibility of electrostatic attraction may be omitted here. But, the high adsorption can suggest the involvement of the other factors such as hydrogen bonding and perhaps coordination bonding effect because nitrogen in MB has a high tendency to make coordination bonding with iron. While in the range of pH 4 to 6 nearby the pH<sub>zpc</sub> value, the adsorption decreases sharply to 20% and 15% approximately respectively. This can be attributed to the repulsion between the positive charge of the BFO surface and the cationic nature of MB. However, low adsorption may be due to physical attraction such as hydrogen bonding and coordination bonding. It is interesting to observe the dramatic improvement of MB adsorption around 95% and 90% approximately at pH 7 and pH 9.5 respectively. This can be explained as at pH greater than pH<sub>zpc</sub> (5.10), the BFO surface acquires a negative charge and MB is cationic therefore electrostatic interaction is dominant here and leading to the higher adsorption. But, negligible MB adsorption results in a highly basic medium (pH-11 to pH-12.30). A high basic medium leads to the enhancement of –OH ions in solution which further competing with the MB molecules thereby adsorption will be dramatically decreased.

#### **6.5.4 Adsorption Kinetics**

The adsorption ( $Q_t$ ) of dye at the time ( $t$ ) is calculated by Equation (5-1). The calculated adsorption ( $Q_t$ ) values for the different concentrations are shown in Figure 6.13 and the corresponding equilibrium adsorption ( $Q_e$ ) is also calculated for each concentration. The  $Q_e$  is defined at the equilibrium concentration where no more dye molecules are left for the adsorption or system reaches equilibrium adsorption. The  $Q_e$  for 4.5 ppm and 7.5 ppm

dye concentration can be calculated directly from Figure 6.13. However,  $Q_e$  is difficult to find for higher concentrations due to the slow adsorption process and limited adsorption data. But  $Q_e$  can be calculated by a modified pseudo-first-order rate Equation (6-2).

$$Q_t = Q_e \left[ 1 - \exp\left(\frac{-k_1 t}{2.303}\right) \right] \quad (6-2)$$

Where,  $k_1$  represents the pseudo-first-order rate constant in  $\text{sec}^{-1}$ . The obtained values of  $Q_e$  and  $k_1$  are listed in Table 6.5 [312].

**Table 6.5. Adsorption parameters are calculated from the pseudo-first-order equation.**

| <b>Initial Concentration</b> | <b><math>Q_e</math> (mol/kg)</b> | <b><math>k_1</math> (1/sec)</b> | <b><math>R^2</math></b> |
|------------------------------|----------------------------------|---------------------------------|-------------------------|
| 4.5 ppm                      | 0.00446                          | 0.00462                         | 0.999                   |
| 7.6 ppm                      | 0.00685                          | 0.00184                         | 0.994                   |
| 15.2 ppm                     | 0.00776                          | 0.000789                        | 0.993                   |
| 22.8 ppm                     | 0.00965                          | 0.000211                        | 0.997                   |

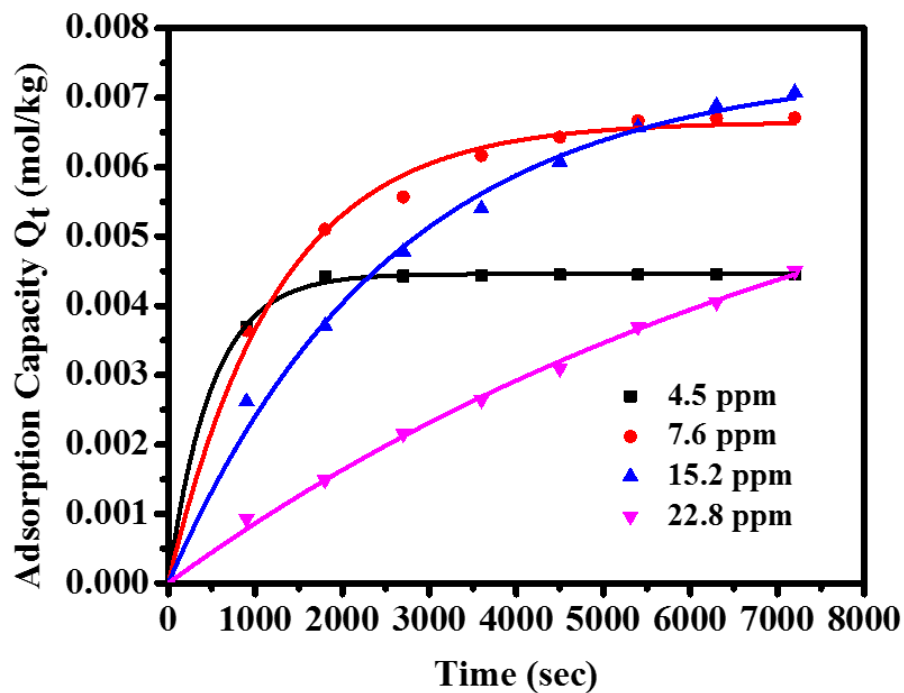


**Figure 6.13. Fitting of pseudo-first-order equation for MB adsorption at different dye concentrations.**

The kinetic of the MB adsorption onto BFO is important which is derived by using the pseudo-second-order model as represented in Equation (5-2). The linear fitting of the data in a plot of  $Q_t$  vs.  $t$  in Figure 6.14 gives the values of  $k_2$  and  $Q_e$ . The value of  $Q_e$  and  $k_2$  are summarized in Table 6.6.

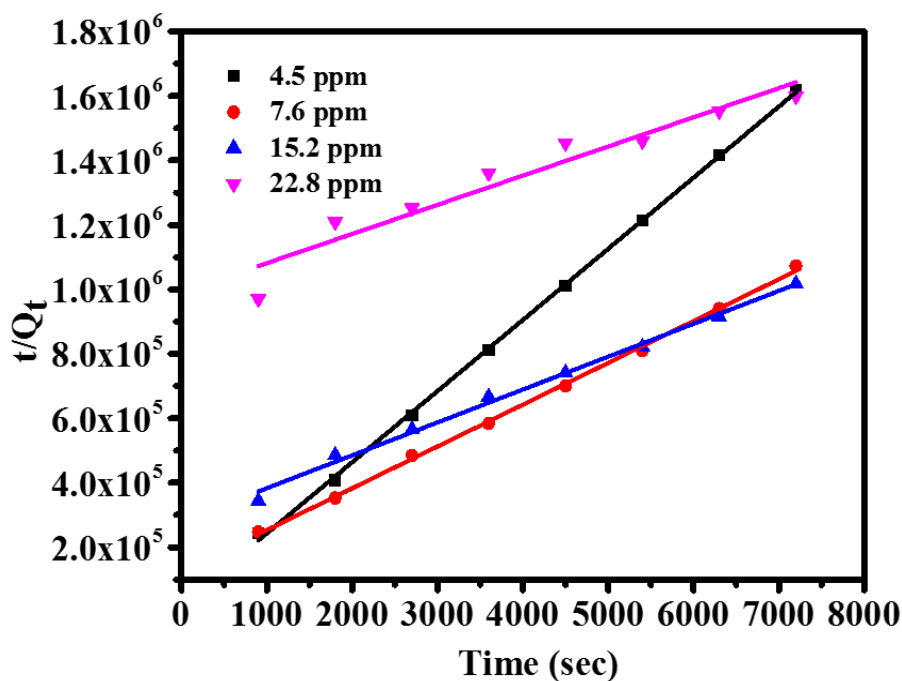


Figure 6.14: Pseudo second-order plots of  $t/Q_t$  versus time  $t$ .

Table 6.6. Adsorption parameters obtained from the modified pseudo-second-order equation.

| Initial Concentration ( $C_0$ ) | $Q_e$ (mol/kg) | $k_2$ (1/sec) | $R^2$ |
|---------------------------------|----------------|---------------|-------|
| 4.5 ppm                         | 0.004531       | 2.15662       | 0.999 |
| 7.6 ppm                         | 0.007708       | 0.136183      | 0.998 |
| 15.2 ppm                        | 0.009801       | 0.037018      | 0.993 |
| 22.8 ppm                        | 0.011052       | 0.008259      | 0.917 |

It is interesting to notice that the pseudo-second-order rate constant  $k_2$  is gradually decreased with the increase in concentration. The decreases in  $k_2$  values suggest that the adsorption is being slowed down at a higher concentration may be due to steric hindrance of the dye molecules.

Weber-Morris intra-particle diffusion model in Equation (5-3) has been used to describe the adsorption mechanics of MB onto BFO nanoparticles. The three linear regions have

been identified in this model at lower concentrations after fitting to the adsorption data.

The notion of these regions is well explained in **section 5.5.2**.

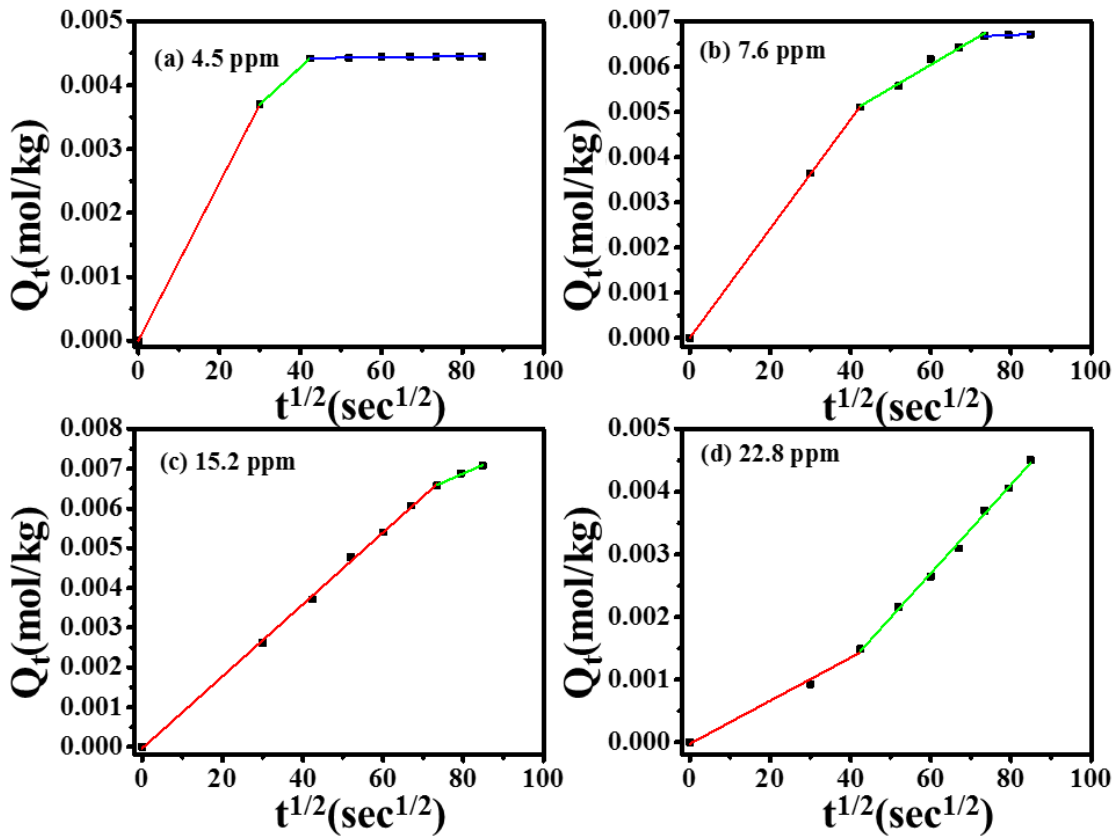


**Figure 6.15. Intra-particle diffusion model (plots between adsorption capacity  $Q_t$  vs  $t^{1/2}$ ) suggests film diffusion as rate controlling diffusion.**

Till now the Weber-Morris equation suggests that the adsorption rate is controlled by the film diffusion and intra-particle diffusion simultaneously. But to determine, the actual rate-controlling step involved in the adsorption is identified by Boyd kinetic model. The model is described as Equation (6-3) [388].

$$F = 1 - \frac{6}{\pi^2} \exp(-B_t) \quad (6-3)$$

Where,  $F$  is the fraction of solute adsorbed at a different time ( $t$ ) and  $B_t$  is the function of  $F$ , called Boyd parameter which is given as Equation (6-4).

$$B_t = -0.4977 - \ln(1 - F) \quad (6-4)$$

The distinction between the intra-particle diffusion and external diffusion (film diffusion) transport controlled rate can be defined based on the linearity of the curve passes through the origin of the  $B_t$  versus time ( $t$ ) plot as shown in Figure 6.16a.

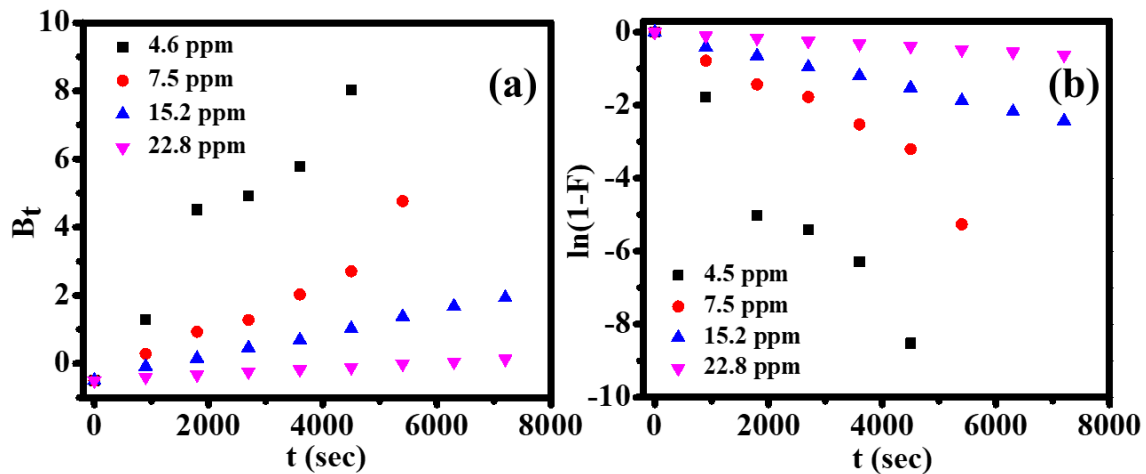


**Figure 6.16. (a) Boyd parameter  $B_t$  versus time ( $t$ ) and (b) film diffusion model for the adsorption of MB on BFO.**

The Boyd model equation suggests that if the straight line passes through the origin then the adsorption process is governed by the intra-particle diffusion mechanism otherwise by film diffusion or external mass diffusion transport mechanism [389]. From Figure 6.16a, the plots are almost linear but do not pass through the origin which means that the adsorption process fails to be intra-particle diffusion process solely, therefore, another mechanism (external mass transfer) is also involved in the rate-limiting steps in the MB adsorption onto BFO. To see the involvement of film diffusion in the adsorption process, the film diffusion model in Equation (6-4) has been used. Where the graphs are passing through the origin suggests the film diffusion mechanism. Thus, now it is confirmed that the two steps as described above are involved in the rate-limiting step [390].

### 6.5.5 Adsorption Isotherms

The nature of the adsorption and the adsorption isotherms has been analyzed by using the Langmuir isotherms model as given in Equation (5-4). The value of  $Q_m$  and  $b$

are calculated from the slope and intercept of the plot between  $C_e/Q_e$  versus  $C_e$  and the parameters are tabulated in Table 6.7. Figure 6.17a shows that the correlation coefficient ( $R^2$ ) of the isotherm is relatively high (0.998) which suggests that the Langmuir model is suitable for describing the adsorption equilibrium of MB onto BFO. The  $Q_m$  is calculated by 0.00878 mol/kg.

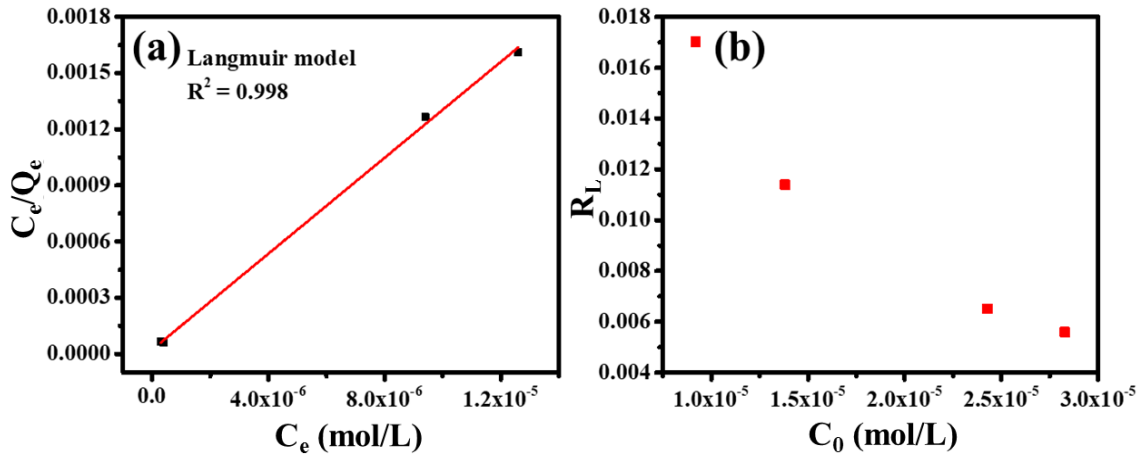


**Figure 6.17: (a). Langmuir isotherm model suggests monolayer adsorption and (b). Separation factor  $R_L$  versus initial concentration  $C_0$  for the adsorption of MB represents minimum values of  $R_L$  which suggests stronger interaction.**

The separation factor ( $R_L$ ) is the essential characteristics of the Langmuir isotherms which describes the nature of the isotherms to be either unfavorable ( $R_L > 1$ ), linear ( $R_L = 1$ ), favorable ( $0 < R_L < 1$ ) and reversible ( $R_L = 0$ ). The  $R_L$  is given by the following Equation (6-5) [342].

$$R_L = \frac{1}{1 + bC_0} \quad (6-5)$$

Where,  $C_0$  is the initial concentration and  $b$  is calculated from the Langmuir model. The value of  $R_L$  is calculated at different initial concentrations and has shown in Figure 6.17b. The value of  $R_L$  is in the range of 0 and 1 which indicates that the adsorption of MB onto BFO is a favorable process. In the present study, the  $R_L$  value is very low ( $0.004 < R_L <$

0.02) which might be because of the strong adsorption of MB onto BFO [391]. The adsorption data has been fitted also in the Freundlich model where it fails as its  $R^2$  is 0.237 but this model favors the adsorption as the value of  $n$  is 10.

**Table 6.7. Parameters obtained from the isotherms models.**

| Model                           | Parameters   | Values                  |
|---------------------------------|--|-------------------------|
| Langmuir model                  | $b$ (kg/mol)   | $6.282 \times 10^6$     |
|                                 | $Q_m$ (mol/kg)   | 0.00878                 |
|                                 | $R^2$  | 0.962                   |
| Freundlich model                | $n$  | 10                      |
|                                 | $K_f$ (mol/kg)   | 0.0266                  |
|                                 | $R^2$  | 0.237                   |
| Dubinin -<br>Radushkevich model | $B$ (mol <sup>2</sup> /k <sup>2</sup> J <sup>2</sup> ) | $0.4721 \times 10^{-2}$ |
|                                 | $Q_m$ (mol/kg)   | 0.008443                |
|                                 | $E$ (kJ/mol)   | 10.29                   |
|                                 | $R^2$  | 0.856                   |

So far in the present study, the adsorption mechanism has been understood but still, it is unclear whether the adsorption is physical or chemical. To distinguish between the physical and chemical adsorption, the Dubinin-Radushkevich model has been studied, which applies to both the homogeneous and heterogeneous surface of the adsorbent. The D-R model is given in Equation (5-6), (5-7), and (5-8). The value of  $E$  is calculated to be 10.29 kJ/mol. Based on this value, physisorption and chemisorption can be distinguished. The physisorption is corresponding to the mean free energy of the adsorption below 50 kJ/mol and above this value is indicative of chemisorption [392]. So, the present  $E$  value is strongly in favor of physisorption. The D-R model is depicted in Figure 6.18a. The  $Q_m$

is calculated by 0.00878 mol/kg by this model which is in good agreement with the Langmuir model ( $Q_m = 0.00844$  mol/kg).

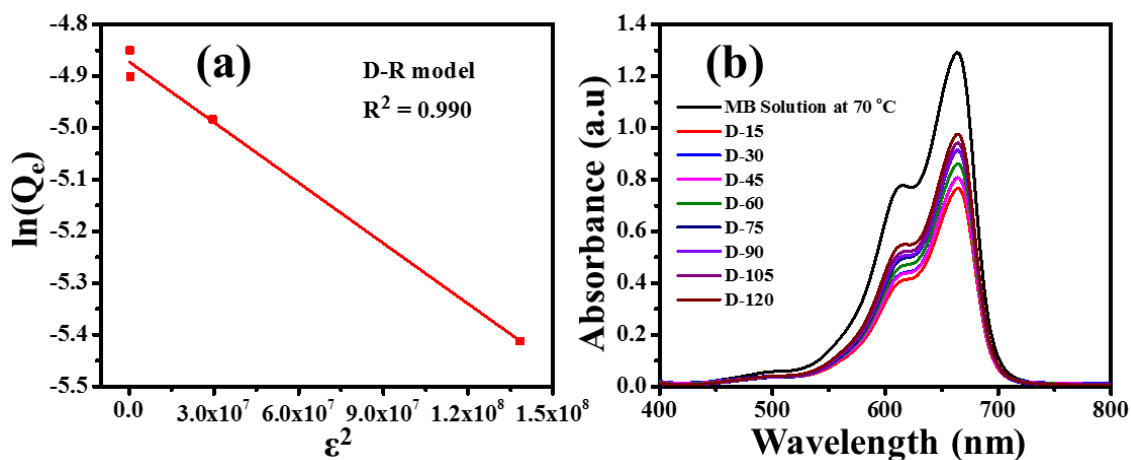


**Figure 6.18. (a) Dubinin-Radushkevich (D-R) model infers physisorption and (b). UV-Vis adsorption data of MB adsorption at 70 °C.**

### 6.5.6 Thermodynamics of adsorption

Next, we calculate the Gibbs free energy change ( $\Delta G^\circ$ ) for each concentration at room temperature, and the values are given in Table 6.8. The Gibbs free energy ( $\Delta G^\circ$ ) provides information about inherent energy changes during adsorption. The  $\Delta G^\circ$  is given by Equation (5-10). The negative values of the Gibbs free energy indicate that the adsorption process is favorable and spontaneous corresponds to the physisorption of MB onto BFO [343]. However, negative values are decreasing for higher concentrations which indicates that the adsorption is less favorable at higher concentrations.

**Table 6.8. Thermodynamic parameter for the adsorption of MB onto BFO.**

| Initial Concentration | $\Delta G^\circ$ (kJ/mol) |
|-----------------------|---------------------------|
| 4.6 ppm               | -8.57                     |
| 7.5 ppm               | -8.80                     |
| 15.2 ppm              | -3.67                     |
| 22.8 ppm              | -2.96                     |

Further, we have examined MB adsorption at higher temperatures. Where it has been investigated that the MB gets desorbed at a higher temperature. This has been shown in Figure 6.18b at 70 °C. Initially, little adsorption occurs, and then subsequently desorption starts.

## **Chapter 7: Rapid adsorption of congo-red dye by polyaniline-bismuth ferrite nanocomposite**

### **7.1 Abstract**

In the present study, the polyaniline/bismuth ferrite nanocomposite (PANI/BFO) has been synthesized by a chemical polymerization method and its adsorption capacity is investigated towards the adsorption of congo red (CR) dye. The PANI/BFO nanocomposite has been characterized by X-ray Diffraction (XRD), Fourier Transform Infrared (FTIR) Spectroscopy, Field Emission Scanning Electron Microscopy (FESEM), X-ray Photoelectron Spectroscopy (XPS), and Dynamic Light Scattering (DLS). The characterization results indicate that both chemical bonding and physical bonding involve in the composite formation of PANI and BFO. The interpretation of the kinetics, isotherms, and thermodynamics has been carried out of the adsorption of CR onto PANI/BFO nanocomposite. The results demonstrate that about 95% of adsorption completes within 5 minutes of contact. Adsorption data follows the pseudo-second-order rate kinetic equation. The adsorption kinetics is chiefly controlled by the film diffusion. The isotherms study has been investigated by the Langmuir model suggesting the monolayer adsorption where the maximum adsorption is calculated 81.16 mg/g. Thermodynamic parameters such as standard Gibbs free energy change, standard enthalpy change, and standard entropy change were calculated. The negative value of standard Gibbs energy change favors the physisorption of CR onto PANI/BFO, which is also confirmed by the Dubinin–Radushkevich model. The adsorption is exothermic as revealed by the negative value of standard enthalpy change. Quantitative analysis infers 7 monomers in a polyaniline chain. Results show that the PANI/BFO played a key role in the adsorption of CR.

## 7.2 Introduction

Industrialization is increasing globally in the current scenario. Therefore, the by-products of the industries are a matter of concern because whenever the by-products discharged untreated, causing environmental pollution. Water pollution is one of the major issues among environmental pollutions. Water is being contaminated with chemicals such as organic dyes, pesticides, heavy metals, domestic waste, and industrial waste. The industries are the major sources of water contamination as their effluent contains chemicals and other hazardous materials. Among the industries, textile industries are the bigger water polluters because a huge amount of water is required to color the fabric, simultaneously remnant water is being discharged as wastewater into natural sources of water. The uses of organic dyes are major sources of environmental contamination as dyes are highly toxic and non-biodegradable which whenever discharged, damage the aquatic system and produced a carcinogenic effect on a human being. Therefore, the removal of contamination from industrial wastewater is a prodigious concern and equally important before releasing it into the environment [25]. To overcome this problem, efforts have been made to develop new methods and technologies to remove the contaminants from waste, post to release in the environment. Up to date, several techniques such as membrane treatment [305], ozone treatment [307], biological and chemical oxidation [310], coagulation/flocculation [306], photocatalysis [309], and adsorptions [311], *etc.* are well known. Adsorption is one of the techniques which is extensively useful and acceptable due to its advantage over other methods as simplicity of the process, flexibility, rapid operational, economically feasible, easy to operate, re-usability of adsorbent after simple desorption of dyes, and wide suitability for various dyes [341,393].

Recently, research pursuing over to design the new materials of high adsorption capacity for the removal of dyes from aqueous solution is still under development to make it economically feasible and resolve the disposal problem effectively. In this regard, the conducting polymers such as polyaniline, polypyrrole, polythiophene, polyindole, and its derivatives have attracted much attention due to their wide range of applications in sensors, photocatalysis, photovoltaic cell, and microelectronics [394]. Among all of these conducting polymers, polyaniline has been more recognized due to its unique properties like electrochemical stability, electrically conductive, charge separation capability, better stability in the environment, low toxicity, low cost, and simple synthesis [395]. The properties of polyaniline can be tuned by simple doping with protonic acid and de-doping. Some of its unique properties such as better stability and, adsorption and desorption reversibility make it a suitable material for pollutant adsorption. But, polyaniline is a low mass density material that inhibits its use as an adsorbent [318,319,396].

In order to overcome this drawback, polyaniline-metal oxides nanocomposite has been prepared. BFO is a perovskite material having the rhombohedral structure of space group R3c [358]. It is a multiferroic material having electric and magnetic ordering that exists simultaneously at room temperature. BFO shows outstanding performance due to its high Curie temperature ( $T_c = 1100^\circ\text{C}$ ) and G-type ferromagnetic ordering below the Neel temperature ( $T_N = 643^\circ\text{C}$ ) [359]. BFO has its potential applications in many areas such as spintronics, memory devices, information storage, sensors and magnetoelectronics, *etc* [360,361]. In addition to its multiferroic properties, the BFO shows fascinating physio-chemical properties such as photocatalysis due to its narrow bandgap (2.18 eV) and chemical stability [146].

In the present study, the PANI/BFO nanocomposite was prepared by in situ chemical oxidation of aniline in the presence of BFO nanoparticles, where BFO

nanoparticles were synthesized by the sol-gel method. The PANI/BFO nanocomposite was well characterized by XRD, FTIR, FESEM, XPS, and DLS techniques. The applicability of PANI/BFO nanocomposite was examined towards the adsorption of congo red from its aqueous solution of different concentrations. The kinetic, isotherm, and thermodynamic studies were elicited of the adsorption in detail.

### **7.3 Experimental section**

#### **7.3.1 Synthesis of PANI.**

The synthesis of the polyaniline (PANI) is described in section 5.3.2. The scheme for polyaniline preparation is shown in Figure 5.1.

#### **7.3.2 Synthesis of BFO.**

The synthesis of BFO with DMSO as solvent is described in section 6.3.1. The experimental process of synthesis is well represented in Figure 6.1.

#### **7.3.3 Synthesis of PANI/BFO nanocomposite.**

The PANI/BFO was synthesized by the chemical polymerization process as represented in Figure 7.1. First of all, BFO powder was mixed in solution 1 for 10 minutes at room temperature. Afterward, solution 2 and solution 3 (as defined in section 2.2.1) were added respectively following continuous stirring for 12 hours at room temperature. Then, the resultant solution was filtered and the collected residue was washed several times with ethanol and water respectively. The residue was dried at 90 °C for 5 hours in the oven. In this method of preparation, it is proposed that the polyaniline has been polymerized over the surface of BFO i.e the polyaniline has been coated over the BFO surface.

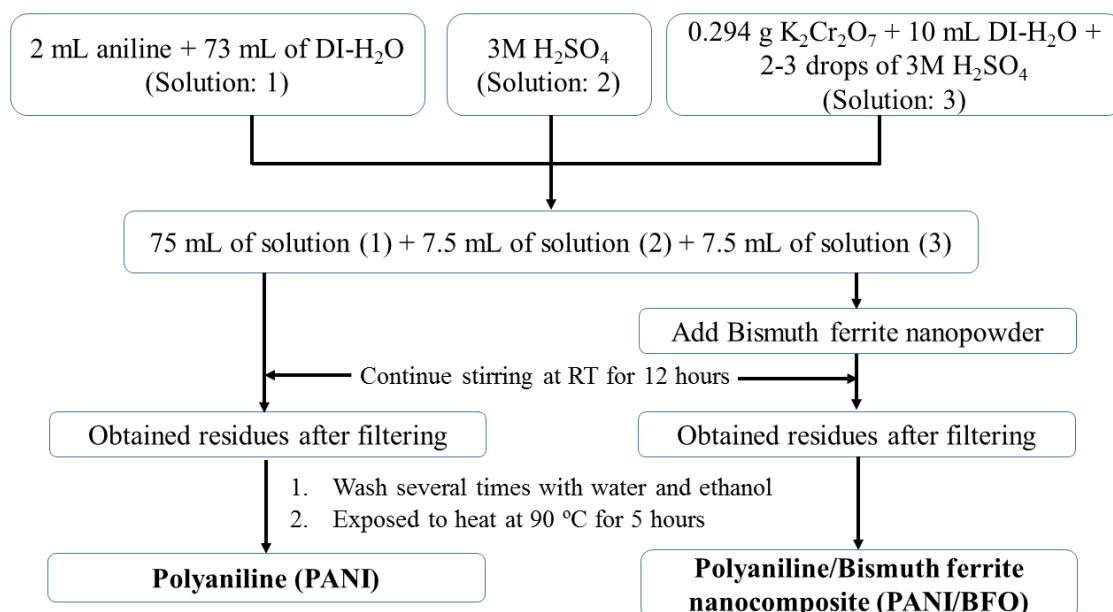


**Figure 7.1. Pathway of synthesis of polyaniline/bismuth ferrite nanocomposite.**

### 7.3.4 Batch Adsorption Experiments.

The batch adsorption experiments were performed in a beaker of 250 ml capacity. The beaker contained a 100 ml aqueous solution of congo red dye. Adsorption studies were conducted for different concentrations (50 ppm, 75 ppm, 100 ppm, and 125 ppm) of congo red dye while keeping the adsorbent amount fixed at 100 mg. PANI/BFO was added to the CR aqueous solution during stirring at 600 rpm. A 2 ml suspension was collected after a fixed interval (5, 10, 15, 30, 45, 60, 75, and 90 minutes) and centrifuged to settle down the adsorbent. Later, the supernatant was used to record the adsorption data of the remnant concentration of CR in aqueous media. Congo red is characterized by its two peaks at 344 nm and 498 nm. Both the peaks were monitored and recorded during adsorption. However, the adsorption data is presented for a peak at 498 nm only. Temperature is an important factor in the adsorption therefore, the adsorption was examined at the higher temperatures 303, 313, 323, and 333 K. The adsorption ( $Q_t$ ) is defined as the amount of adsorbate adhere to the adsorbent and the equilibrium adsorption ( $Q_e$ ) is corresponding to

the equilibrium in adsorption. The adsorption ( $Q_t$ ) and the dye removal efficiency ( $\%R$ ) can be calculated by Equation (5-1) and Equation (6-1) respectively.

## 7.4 Result and discussion

### 7.4.1 X-Ray Diffractogram analysis

The XRD patterns of PANI, BFO, and PANI/BFO nanocomposite are depicted in Figure 7.2. Figure 7.2a represents the XRD pattern of PANI which is well explained in section 5.4.1. Figure 7.2b represents the XRD pattern of bismuth ferrite (BFO) which is well explained in section 6.4.1.

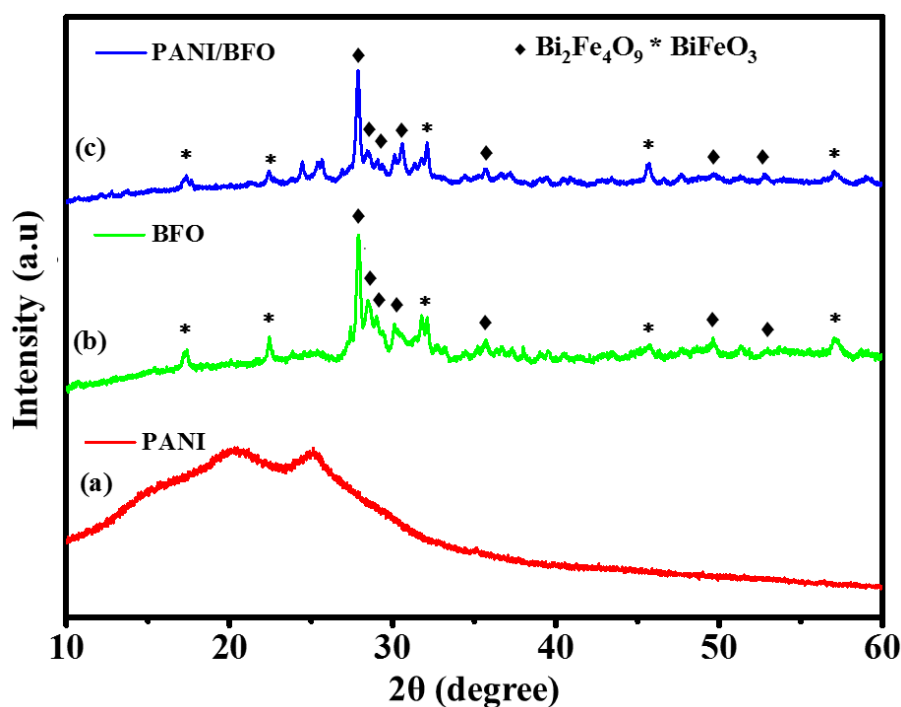


**Figure 7.2. XRD pattern of (a) PANI, (b) BFO, and (c) PANI/BFO nanocomposite.**

The XRD pattern of PANI/BFO nanocomposite has been represented in Figure 7.2c. All peaks of BFO are presented in XRD of composite nanoparticles but comparatively, their intensities have changed. This indicates that the crystallinity of BFO does not disturb PANI/BFO formation however, a change in intensities can be due to a change in the mass fraction of samples for performing XRD. We have also noticed changes in the XRD

pattern of the nanocomposite. The broad peaks at  $20.42^\circ$  and  $25.13^\circ$  of PANI correspond to its amorphous and semi-crystalline nature has been disappeared in the XRD pattern of PANI/BFO nanocomposite. This infers that the PANI has lost its semicrystalline nature after adding BFO nanoparticles during the polymerization process. Thus, the addition of BFO nanoparticles leads to an increase in the amorphous nature of PANI. Meanwhile, the two sharp peaks at  $24.46^\circ$  and  $25.65^\circ$  have appeared in the XRD of the nanocomposite. These peaks can be assigned to the orthorhombic crystal structure of  $\text{Bi}_2\text{Fe}_4\text{O}_9$  matched with JCPDS files as stated above. The emergence of these peaks may be the result of enhancement of the broad hump present in the range of  $24^\circ$ - $26^\circ$  in BFO. The peak at  $25.65^\circ$  in PANI/BFO is associated with one more band at  $25.38^\circ$ . Thus, the XRD data suggests that the addition of BFO hamper the polymerization process resulting in the enhancement of the amorphous nature of PANI. The FWHM values of the most intense bands have been calculated at  $0.2677^\circ$  and  $0.2539^\circ$  for BFO and PANI/BFO nanocomposite respectively. As the FWHM of the PANI/BFO band is lesser than the BFO, this indicates that the PANI has been polymerized over the nanocomposite surface. The crystallite size of BFO and PANI/BFO nanocomposite is calculated by the Debye-Scherrer formula in Equation (3-1). The most intense peak at  $27.90^\circ$  is chosen to calculate the crystallite size of BFO and PANI/BFO nanocomposite. The crystallite size of BFO and PANI/BFO is calculated at 30.50 nm and 32.23 nm respectively. Thus, the crystallite size is higher in the case of PANI/BFO by 1.73 nm which reveals that the BFO nanoparticles have been encapsulated into the PANI matrix.

#### **7.4.2 Fourier Transform Infrared Spectroscopy (FTIR).**

Figure 7.3 shows the FTIR spectra of PANI, BFO, and PANI/BFO nanocomposite. The common bands appear around  $3660\text{ cm}^{-1}$ ,  $2980\text{ cm}^{-1}$ , and  $2887\text{ cm}^{-1}$  in all samples. The bands at around  $3660\text{ cm}^{-1}$  can be assigned to the O-H stretching of

hydroxyl ions [369]. The C-H stretching vibration can be identified at  $2980\text{ cm}^{-1}$  to  $2887\text{ cm}^{-1}$ , which are common to all the samples [370]. A detailed explanation of FT-IR of BFO is given in section 6.4.2.

In the FTIR spectrum of PANI, sharp bands at  $2980\text{ cm}^{-1}$ , and  $2887\text{ cm}^{-1}$  are also assigned to  $-\text{NH}_2^+$ - and N-H stretching of aromatic amine [398]. The other characteristic bands occur at  $1560\text{ cm}^{-1}$  and  $1369\text{ cm}^{-1}$  are ascribed to the C=C stretching vibration of the benzenoid unit and quinoid unit respectively [399]. While the C=N stretching vibration of the quinoid ring and C-N<sup>+</sup> (or C=N<sup>+</sup>) stretching vibration emerge at  $1481\text{ cm}^{-1}$  and  $1236\text{ cm}^{-1}$  respectively. FTIR band at  $1293\text{ cm}^{-1}$  can be assigned to C-N stretching vibration of secondary aromatic amines owing to the  $\pi$ -electrons delocalization induced by protonation of PANI, this may be due to the synthesis of PANI in the acidic medium [329].

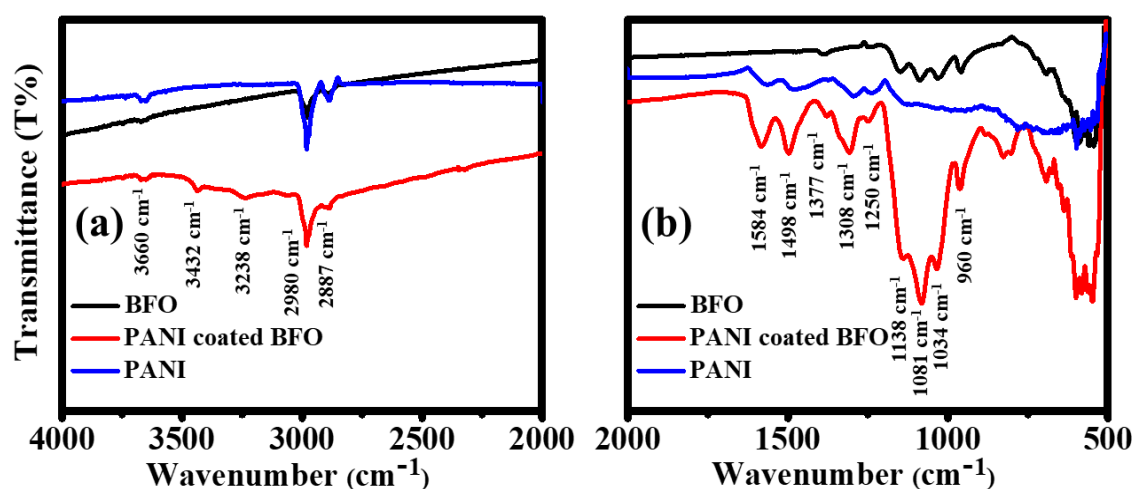


**Figure 7.3. FTIR spectra of PANI, BFO, and PANI coated BFO.**

On the inspection of FTIR bands of PANI/BFO nanocomposite, it is observed that the PANI/BFO comprises the FTIR peaks of PANI and BFO both. It is interesting to notice two major phenomena that few of the bands in FTIR of PANI/BFO nanocomposite have been shifted with respect to their FTIR spectra of pure form and also their intensities

changed. The FTIR bands in the range of  $4000\text{ cm}^{-1}$  to  $2000\text{ cm}^{-1}$  are located in the same position as PANI while the intensities of the peaks have been changed as depicted in Figure 7.3a. The intensity of the band at  $3660\text{ cm}^{-1}$  corresponds to free -OH stretching is diminished comparatively with PANI which indicates the interaction of PANI with BFO. In addition, the two bands associated with N-H vibration are noticed at  $3432\text{ cm}^{-1}$  and  $3238\text{ cm}^{-1}$  corresponds to free -NH- stretching vibration and hydrogen-bonded -NH- vibration between amine and imine sites [400]. The FTIR bands of PANI contributing to FTIR spectra of PANI/BFO are observed to be shifted towards higher wavenumbers at  $1250\text{ cm}^{-1}$ ,  $1308\text{ cm}^{-1}$ ,  $1377\text{ cm}^{-1}$ ,  $1498\text{ cm}^{-1}$ , and  $1584\text{ cm}^{-1}$ . Meanwhile, the FTIR band of BFO contributing to the FTIR spectra of PANI/BFO is found to shift towards lower wavenumber sides  $1081\text{ cm}^{-1}$  and  $1138\text{ cm}^{-1}$ . The shifting of the peaks indicates the physical interaction of PANI with BFO nanoparticles. Interestingly, the intensity and sharpness of the FTIR peaks related to PANI in nanocomposites have been improved and the FWHM values have been reduced comparatively. These observations suggest that that the crystalline nature of PANI increases over the BFO surface during polymerization as also confirmed by XRD data [325]. It is found that the band's intensity of F=S, F-S, and S-S changes but their position is fixed in PANI/BFO composite. Thus, these observations clearly demonstrate the surface modification of BFO by polymerization of PANI over the BFO nanoparticles constitute PANI/BFO nanocomposite by hydrogen bonding or coordination effect [401]. Besides, three bands at  $882\text{ cm}^{-1}$ ,  $826\text{ cm}^{-1}$ , and  $805\text{ cm}^{-1}$  have been observed in FTIR of PANI/BFO nanocomposite while these are absent in PANI and BFO both. So, the attachment of the polyaniline with bismuth ferrite can be described by these bands. These bands can be attributed to the Fe-N stretching vibrations [402,403]. Therefore, it can be demonstrated here that the PANI has a dual approach to interact with BFO through chemical bonding in the form of Fe-N bonds and physical bonding. The

chemical bonding causes new bands and physical bonding shifts the peaks as observed in FTIR of PANI/BFO nanocomposite concerning their neat compounds. It is interesting here to notice that only iron participates in the composite formation while bismuth is unreactive. XPS also supports this statement. This is because of the nature of the bismuth as it is least reactive as compared to iron.

### **7.4.3 DLS analysis**

To confirm the presence of PANI over BFO, we further analyzed the samples by the DLS. Figure 7.4a-c represents the particle's size of the PANI, BFO, and PANI/BFO nanocomposite respectively. The average particle's size has been calculated at 611.0 nm, 250.7 nm, and 385.6 nm from Figure 7.4. As the particle size of the nanocomposite is higher than the particle size of BFO which indicates the presence of PANI over BFO. Also, the BFO particle size suggests that the BFO tether the polyaniline in nanocomposite formation. The zeta potential of the PANI, BFO, and PANI/BFO nanocomposite are found -22.3 mV, -10.9 eV, and -3.43 mV respectively. The zeta potential of the nanocomposite suggests the aggregation of the nanoparticles in the nanocomposite.

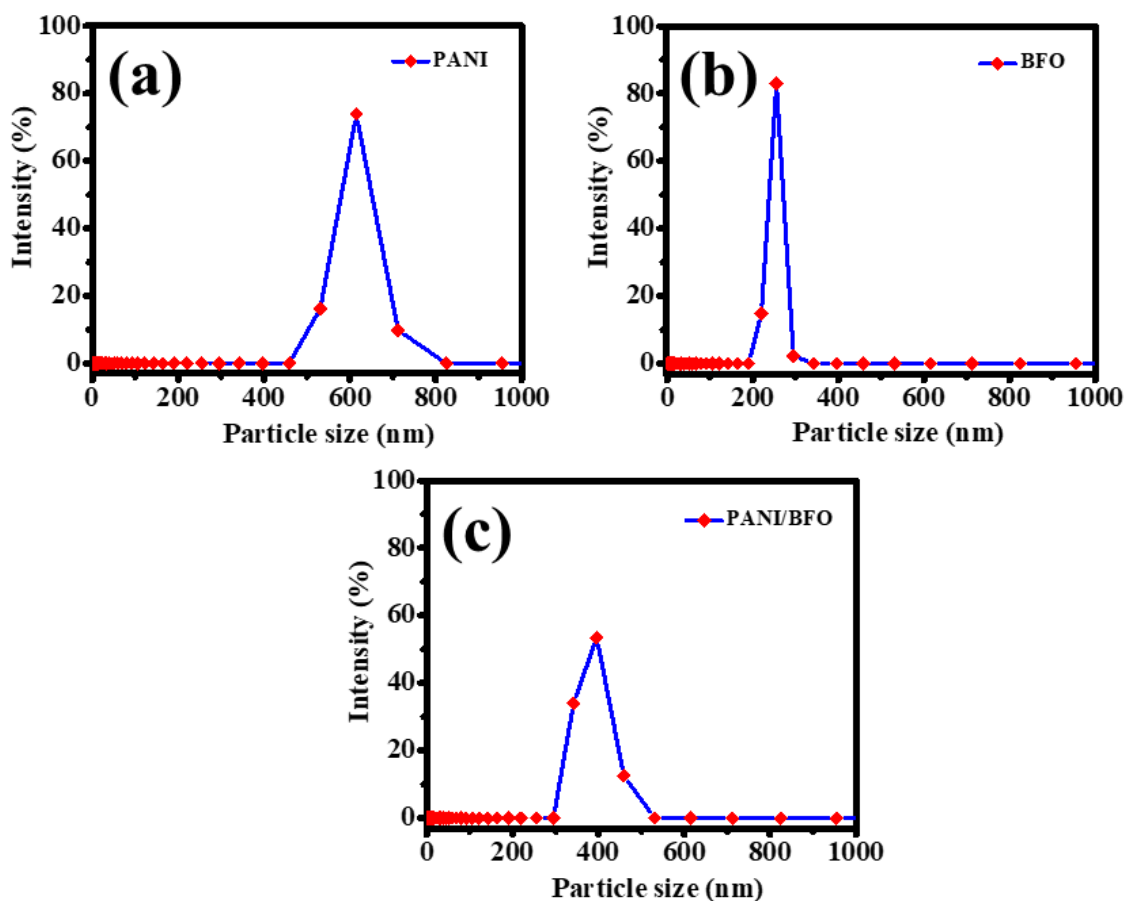


**Figure 7.4. DLS study of (a) PANI, (b) BFO, and (c) PANI/BFO. The larger particle size of PANI/BFO than BFO confirms the coating of PANI over BFO.**

#### 7.4.4 XPS analysis

The elemental analysis of PANI, BFO, and PANI/BFO nanocomposite has been studied with the help of XPS. Table 7.1 represents the peak positions and % area of all peaks. Figure 7.5a represents the C 1s peak of PANI which is deconvoluted into three XPS peaks at 284.75 eV, 286.04 eV, and 287.86 eV correspond to C-C, C-H, and C-N or C=N respectively while the C 1s peaks of PANI/BFO shows a remarkable shift centered at 284.84 eV, 285.92 eV, and 287.64 eV which might be due to the interaction between PANI and BFO. The XPS spectra of N 1s in PANI have been deconvoluted into four different peaks corresponds to three different nitrogen species depending on nitrogen position in PANI: imine nitrogen (=N-), amine nitrogen (-NH-), positively charged nitrogen (-N<sup>+</sup>-) [332,404]. As represents in Figure 7.5c, N 1s signals can be found at

398.23 eV and 399.11 eV corresponds to imine nitrogen (=N-) of the quinoid ring and amine nitrogen (-NH-) of the benzenoid ring respectively meanwhile the signals at 400.10 eV and 401.97 corresponds to positively charged nitrogen (N<sup>+</sup>). The XPS results indicate that the number of benzenoid units (-NH-) is higher than the number of quinonoid units (=N-). The ratio of the XPS peak area of -NH- (49.17%) is higher than the XPS peak area of =N- (24.67%). The XPS peak area of positive nitrogen (-N<sup>+</sup>) is found at 26.14 eV. This difference can be attributed to the fact that quinonoid units get protonated when doped with H<sub>2</sub>SO<sub>4</sub>. However, in the nanocomposite formation, the peaks related to various nitrogen species were found to be shifted at 398.40 eV, 399.27 eV, 400.26 eV, and 401.30 eV respectively. XPS peaks area calculation helps to determine the doping level in samples. The doping levels can be calculated by the XPS peak ratio (-N<sup>+</sup>/N). It is noticed that the doping level in the nanocomposite (0.473) increases as compare to the PANI (0.260). From these observations, it can be concluded that PANI anchor over the BFO exposed more -NH- units to be protonated therefore the units of benzenoids units decrease and simultaneously increases positively charged nitrogen species while imine nitrogen is constant. These observations suggest the physical interaction between PANI and BFO.

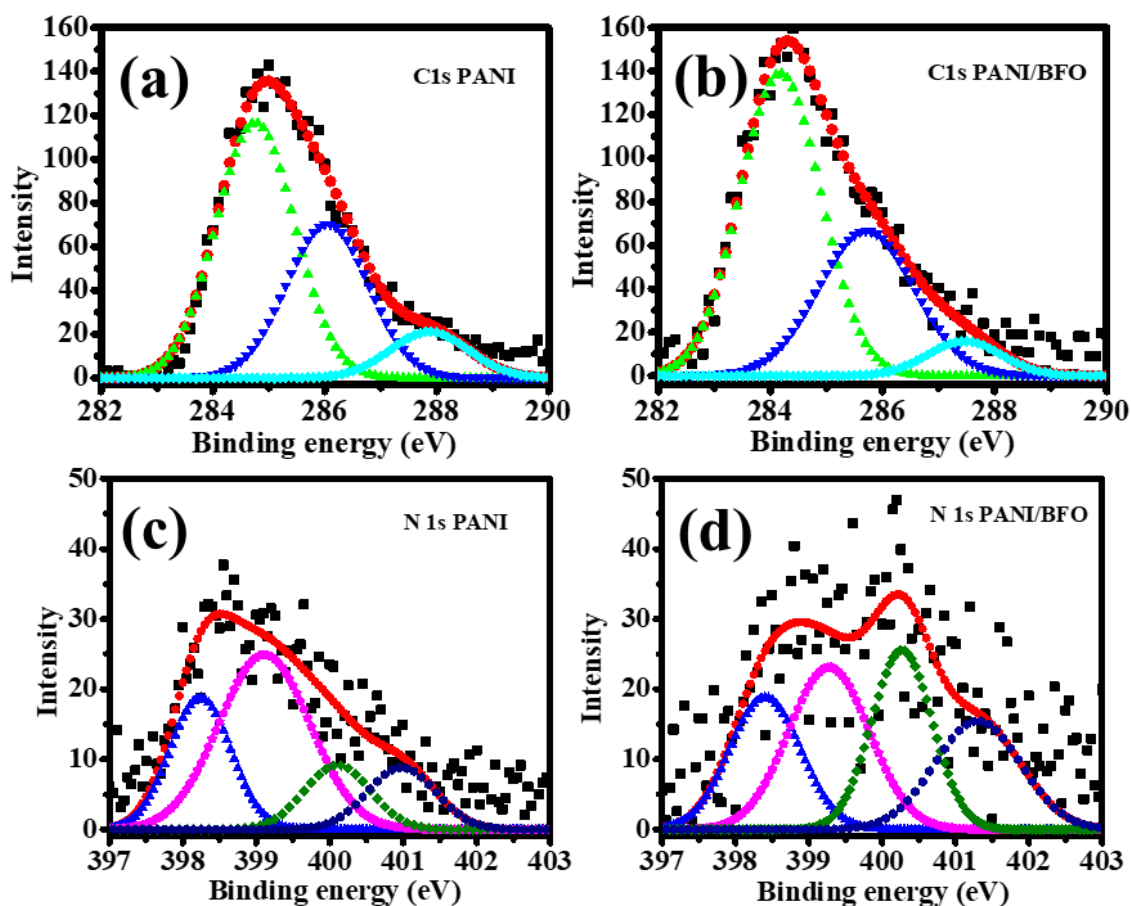


**Figure 7.5.** XPS deconvolution spectra of (a) C 1s PANI, (b) C 1s PANI/BFO, (c) N 1s PANI, and (d) N 1s PANI/BFO.

The Fe of BFO sample is displayed two signals Fe  $2p_{3/2}$  and Fe  $2p_{1/2}$  at 711.12 eV and 724.22 eV in Figure 7.6b indicating +3 oxidation state of Fe [405]. Additionally, a peak at 717.50 eV is detected corresponds to the satellite peak of Fe  $2p_{3/2}$ . The respective Fe signals of PANI/BFO nanocomposite show a remarkable shift and appeared at 710.30 eV and 724.05 eV respectively in Figure 7.6d. The intensity of Fe<sup>3+</sup> peaks in PANI/BFO nanocomposite decreases which may be due to less exposure of Fe to X-ray because polyaniline is present over the BFO surface in the nanocomposite.

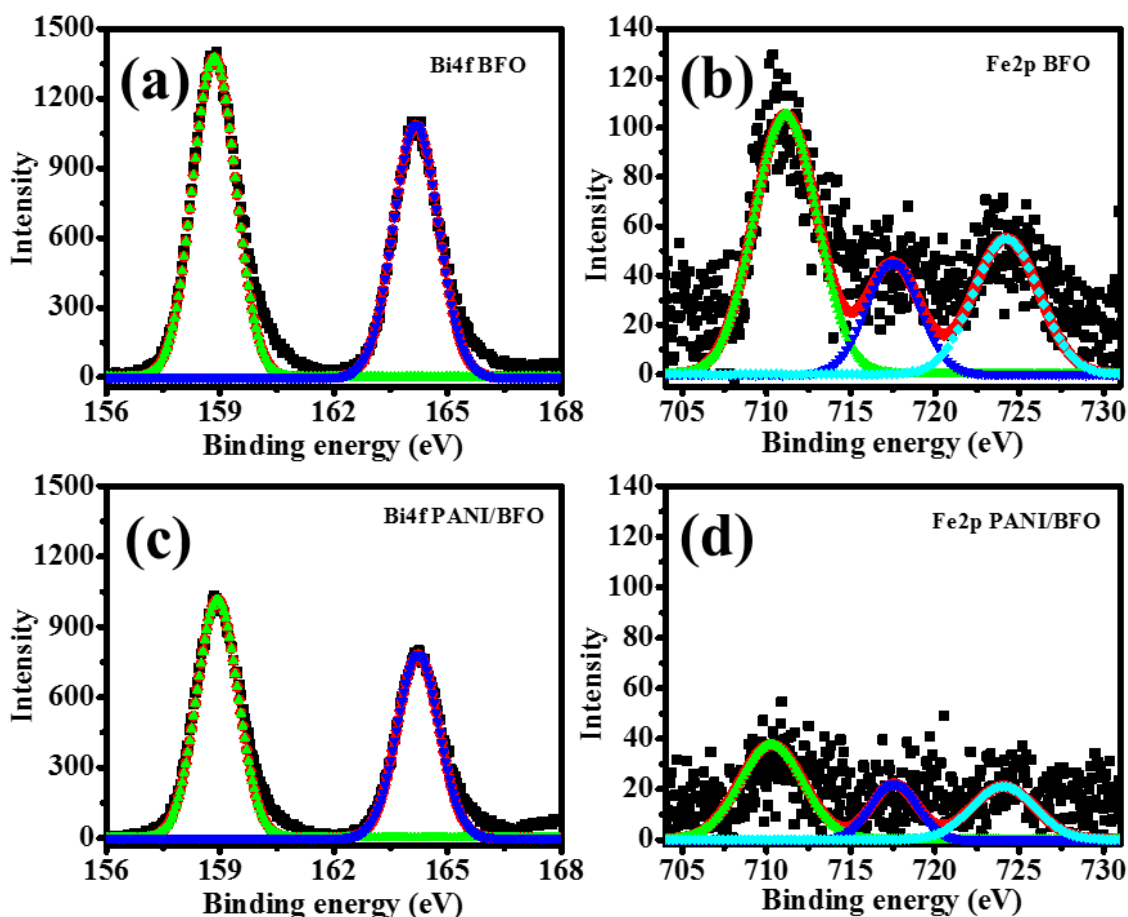


**Figure 7.6.** XPS spectrum of (a) Fe 2p of BFO, (b) Fe 2p of PANI/BFO, (c) Bi 4f of BFO, (d) Bi 4f of PANI/BFO.

The obtained XPS spectra for Bi 4f are shown in Figure 7.6a and Figure 7.6c for both BFO and PANI/BFO nanocomposite. The characteristic signals can be deconvoluted into two bands at 158.84 eV and 164.16 eV corresponds to Bi 4f<sub>7/2</sub> and Bi 4f<sub>5/2</sub> respectively, indicating that the Bi exists in the form of Bi<sup>3+</sup> in both the samples [406]. Trivial change has been noticed in the binding energy of Bi after decorated with PANI in the nanocomposite. The Bi signals can be deconvoluted into two peaks at 158.93 eV and 164.22 eV in PANI/BFO nanocomposite. These observations suggest that the polymerization of PANI onto BFO is mediated by the interaction of –NH– of PANI with BFO through coordination bonding. Also, an increasing number of positive nitrogen in the composite may attract towards the –OH ions present over the BFO surface thereby electrostatic interaction may take involve. Quantitative analysis demonstrates that the

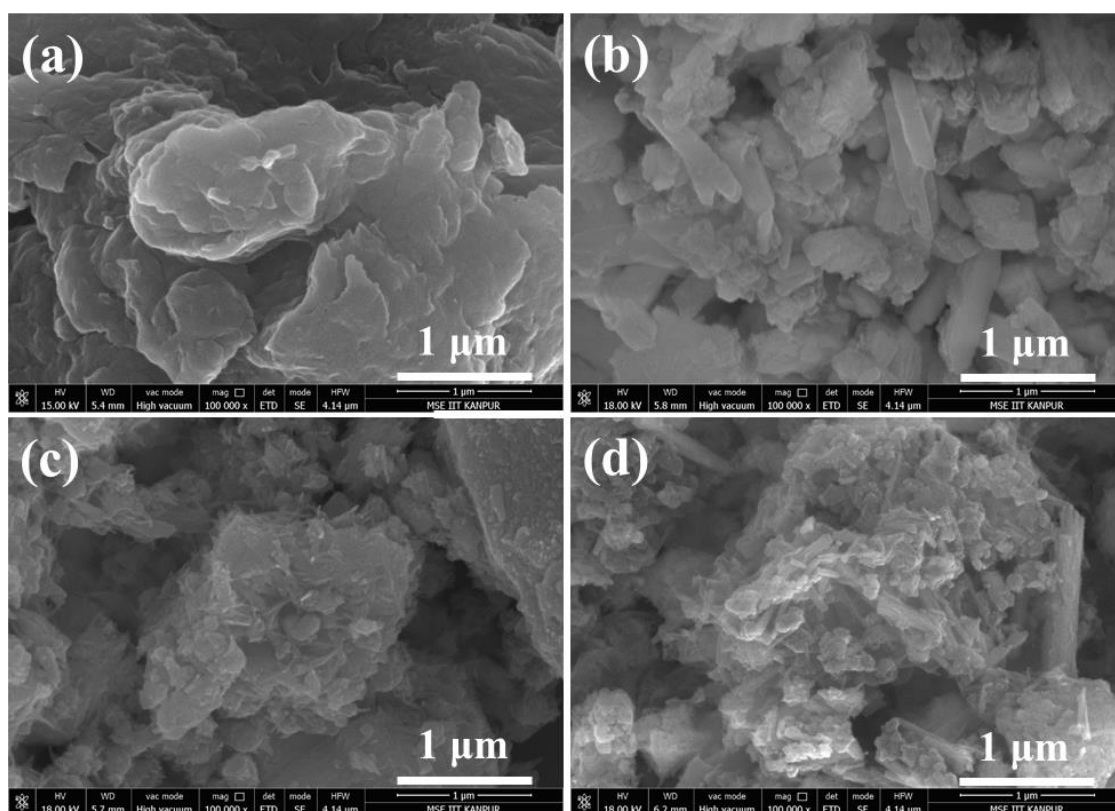
**Table 7.1. Summary of binding energy and area% of the XPS peaks for PANI, BFO, and PANI/BFO nanocomposite.**

| Element      | PANI  |        | ZTO  |        | PANI/ZTO |        |
|--------------|---|--------|--|--------|----------|--------|
|              | B.E (eV)  | % Area | B.E (eV)                                     | % Area | B.E (eV) | % Area |
| <b>C 1s</b>  | 284.75<br>(C-C or C-H)                            | 46.29  |  |        | 284.84   | 39.66  |
|              | 286.04<br>(C-N or C=N)                            | 44.72  |  |        | 285.92   | 43.99  |
|              | 287.86<br>(C-N <sup>+</sup> or C=N <sup>+</sup> ) | 8.97   |  |        | 287.64   | 16.34  |
| <b>N 1s</b>  | 398.23<br>(=N-)                                   | 24.67  |  |        | 398.40   | 21.90  |
|              | 399.11<br>(-NH-)                                  | 49.17  |  |        | 399.27   | 30.76  |
|              | 400.10<br>(-N <sup>+</sup> -)                     | 13.07  |  |        | 400.26   | 25.46  |
|              | 401.97 (-N <sup>+</sup> -)                        | 13.07  |  |        | 401.30   | 21.85  |
| <b>Fe 2p</b> |   |        | 711.12 (Fe <sup>+3</sup> 2p <sub>3/2</sub> ) | 52.65  | 710.30   | 50.86  |
|              |   |        | 717.50                                       | 18.97  | 717.57   | 21.04  |
|              |   |        | 724.22 (Fe <sup>+3</sup> 2p <sub>1/2</sub> ) | 28.37  | 724.05   | 28.08  |
| <b>Bi 4f</b> |   |        | 158.84 (Bi <sup>+3</sup> 2p <sub>1/2</sub> ) | 54.90  | 158.93   | 56.21  |
|              |   |        | 164.16 (Bi <sup>+3</sup> 2p <sub>1/2</sub> ) | 45.09  | 164.22   | 43.78  |

change in B.E of Fe is much higher (~92%) than the change in B.E of bismuth (~8%) in the composite signifying that the polymerization of polyaniline is chiefly mediated by the iron. This supports the FTIR spectra.

#### 7.4.5 FESEM Imaging

The morphologies of the synthesized samples PANI, BFO, and PANI/BFO nanocomposite has been investigated by the FESEM technique at magnification (100000 X) and scale (1  $\mu\text{m}$ ) as represented in Figure 7.7. Figure 7.7a represents the surface morphology of PANI which infers that the PANI synthesized in the layered form whose planes are closely packed with each other.



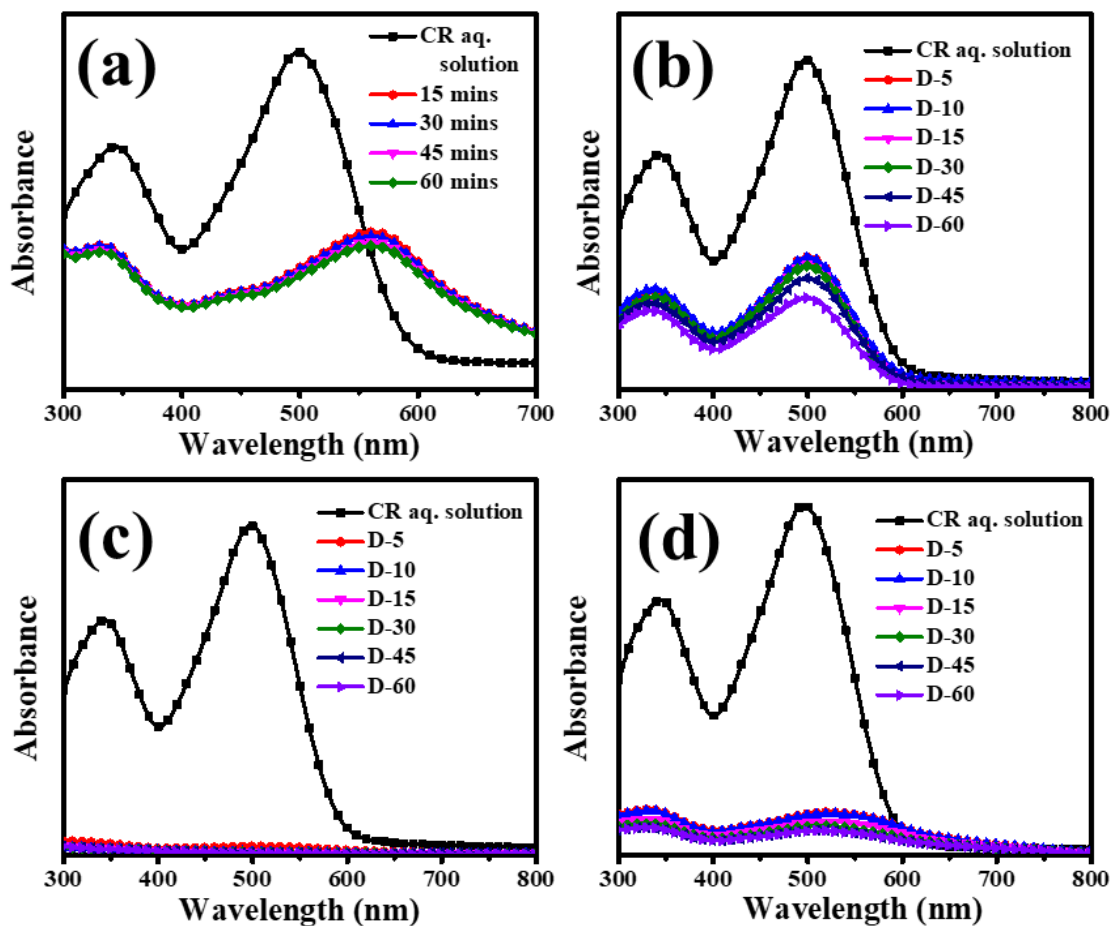
**Figure 7.7. FESEM images of (a) PANI, (b) BFO, (c) PANI/BFO nanocomposite, and (d) CR-PANI/BFO.**

Figure 7.7b shows that the BFO surface is being embedded by nanorods which are anisotropically distributed. The typical lengths of the nanorods are found to be 0.2  $\mu\text{m}$  to 1  $\mu\text{m}$ . It is revealed in Figure 7.7c that the BFO nanorods are uniformly dispersed in the PANI matrix, resulting in the coating of PANI onto BFO. Thus, it has been proposed that the PANI has been synthesized over the surface of BFO during the synthesis of PANI/BFO nanocomposite. The surface morphology changes after the adsorption of CR onto nanocomposite is displayed in Figure 7.7d, where a bunch of small particles present on the surface can easily identify which are CR molecules.

## **7.5 Adsorption Study**

### **7.5.1 Adsorption kinetics**

The CR adsorption by the PANI, BFO, and PANI/BFO nanocomposite has been evaluated and compared. Figure 7.8 compares the adsorption of congo red by PANI, BFO, and PANI/BFO nanocomposite. Rapid adsorption is noticed by PANI/BFO as compared to PANI and BFO separately. Adsorption is still faster for the higher concentration (125 ppm) of CR as represented in Figure 7.8d. The CR adsorption and CR removal efficiency for the PANI, BFO, and PANI/BFO nanocomposite has been evaluated by using Equation (5-1) and Equation . Adsorption of CR is higher by PANI/BFO as represented in Figure 7.9a. Quantitatively, the CR removal efficiencies of the PANI, BFO, and PANI/BFO nanocomposite are calculated 59.84 %, 62.52 %, and 99.35 % respectively for 5 minutes as depicted in Figure 7.9b. Two major happenings are noticed during the adsorption of CR by PANI that (I) the red color of CR dye solution changed to green and (II) the characteristic peak at 498 nm has been shifted to higher wavelength 562 nm as displayed in Figure 7.8a. This is well explained in section 5.5.2.



**Figure 7.8. Time-dependent adsorption of 50 ppm CR dye (a) by PANI, (b) BFO, (c) 50 ppm CR solution by PANI/BFO; and (d) 125 ppm CR solution by PANI/BFO.**

Be motivated by the quick and complete adsorption of 50 ppm CR by PANI/BFO, the research proceeded further for highly concentrated CR solutions of 75 ppm, 100 ppm, and 125 ppm while keeping the mass of adsorbent (100 mg) and other conditions fixed (Temperature and Stirring).

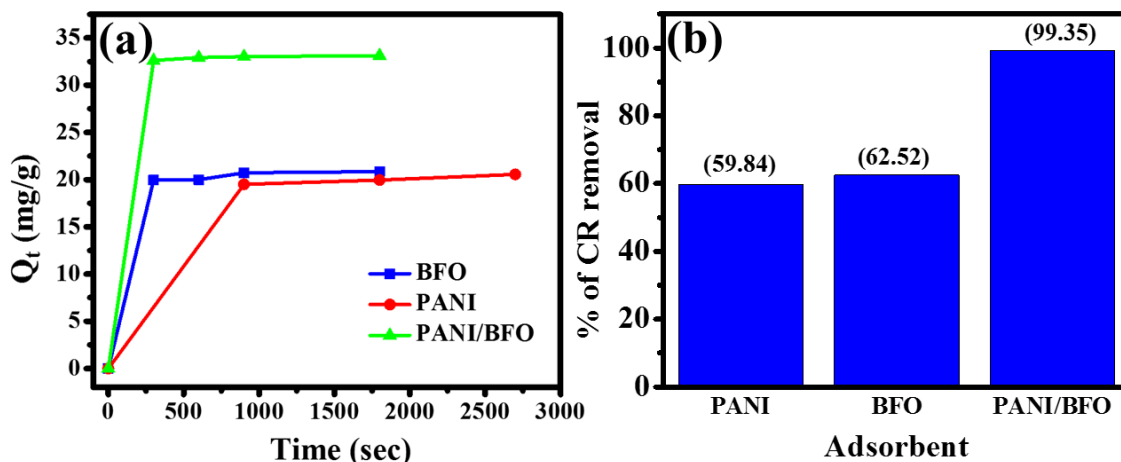


Figure 7.9. (a) Adsorption capacity vs. time (s), and (b) percentage of 50 ppm CR (from 100 mL aqueous solution) removal by PANI, BFO, and PANI/BFO nanocomposite (150 mg of each adsorbent).

Figure 7.10a-b represents the dramatic change in concentration ( $C_t$ ) and adsorption ( $Q_t$ ) with time for higher CR loading. We have noticed that nearly 95% of adsorption completed within 5 mins which indicates the high adsorption capability of the PANI/BFO nanocomposite. In Figure 7.10b, the adsorption increases with dye concentration may be due to a driving force provided by initial dye concentration that dominates over the mass transfer resistance of the dye molecules between the liquid and solid phase [312].

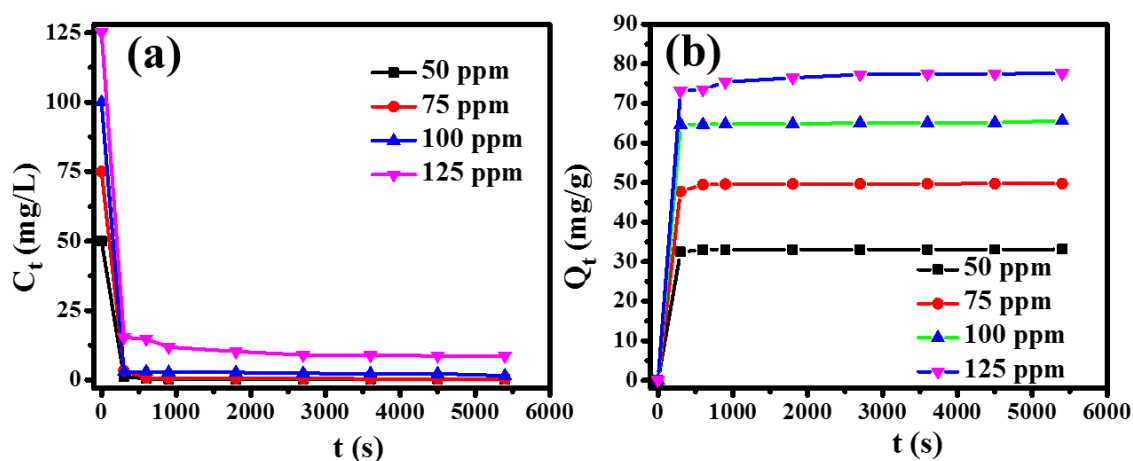
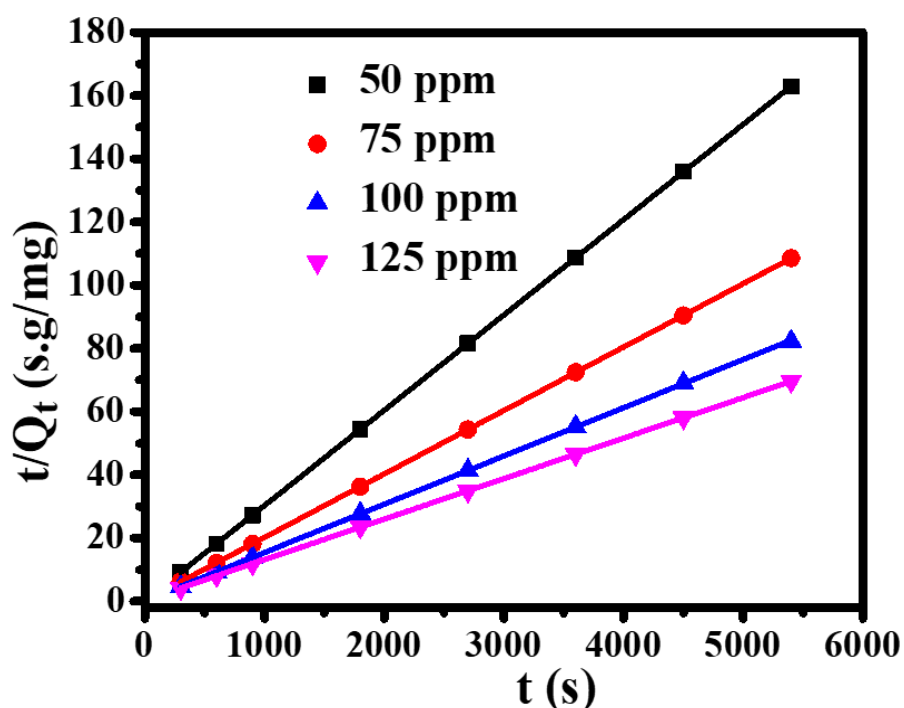


Figure 7.10. (a) Instantaneous concentration ( $C_t$ ) versus time ( $t$ ), and (b) Adsorption capacity  $Q_t$  versus time  $t$ ; for the adsorption of CR onto the PANI/BFO nanocomposites at a different initial concentration of 50 ppm, 75 ppm, 100 ppm, and 125 ppm.

In order to study the adsorption mechanism of CR onto PANI/BFO, the Lagergren second-order-kinetic model has been applied which is expressed in Equation (5-2). The values of  $k_2$  and  $Q_e$  are calculated from the slope and intercept of the linear plot between  $t/Q_t$  and  $t$  as displayed in Figure 7.11 and corresponding values are given in Table 7.2. The  $Q_e$  (cal) from this model is also compared with the  $Q_e$  (exp) calculated from Equation (5-1).



**Figure 7.11.** The adsorption data fits pseudo-second order equation for the adsorption of the CR onto PANI/BFO nanocomposite.

Table 7.2 suggests that the  $Q_e$  (cal) and  $Q_e$  (exp) are nearly equal and correlation coefficients ( $R^2$ ) are equal to 1 indicating the best fitting of the adsorption data by this model. Pseudo-second-order adsorption rate constant ( $k_2$ ) gradually decreases with an increase in the initial concentration of CR due to steric hindrance of higher concentration of CR [339].

**Table 7.2. Kinetic parameters of the pseudo-second-order adsorption kinetic model.**

| S.No | C <sub>0</sub> (ppm) | Q <sub>e</sub> (exp) | k <sub>2</sub> | Q <sub>e</sub> (cal) | R <sup>2</sup> |
|------|----------------------|----------------------|----------------|----------------------|----------------|
| 1    | 50                   | 33.09468             | 0.007025       | 33.1565              | 1              |
| 2    | 75                   | 49.65449             | 0.002695       | 49.82561             | 1              |
| 3    | 100                  | 65.06806             | 0.001284       | 65.5308              | 1              |
| 4    | 125                  | 77.33271             | 0.000439       | 78.00312             | 1              |

The adsorption mechanism of dyes is given in section 5.5.2. Further, we are interested to identify the actual rate-controlling steps in the adsorption of CR onto PANI/BFO nanocomposite, the intraparticle diffusion model proposed by Weber-Morris can be employed, which is described in Equation (5-3). The values of  $k_i$  and  $C$  are calculated from the slope and intercept of the plot between  $Q_t$  and  $t^{1/2}$  as abbreviating in Table 7.3. As represented in Figure 7.12, two linear regions are observed. The first linear region (red line) can be assigned to film diffusion or external mass transfer followed by the second linear region belongs to intra-particle diffusion. The external mass transfer completes within 5 minutes of the adsorption process irrespective of CR concentrations. The external mass transfer rates increase with the dye concentration signifying higher adsorption capability of the PANI/BFO nanocomposite. The intra-particle diffusion is linked to the diffusion into the pores onto the adsorbent [340]. It is characterized by diffusion in macropores, transitional pores, and micropores. Therefore, the observance of one linear region in the intra-particle equation fitting in 50 ppm, 75 ppm, 100 ppm, and 125 ppm dye concentrations can be attributed to the macropore's intra-particles diffusion however the transitional diffusion can be also seen in the intra-particle fitting of 125 ppm CR adsorption system. The intra-particles diffusion constant is determined from the slope of the second and third linear region and is given in Table 7.3. It is noticed that the intra-

particle diffusion rate constant increases with increasing initial dye concentration. This is because increasing initial dye concentration in bulk solution will increase the driving force of adsorption. In Figure 7.12d for higher dye concentration, the third linear region is obtained in the intra-particle diffusion equation is assigned to the transitional pores intra-particle diffusion. The slope and intercept for this region are calculated at  $0.010 \text{ mg.g}^{-1}.\text{sec}^{-1/2}$  and  $76.82 \text{ mg/g}$  respectively. It is noticeable here that the rate constant for transitional pores diffusion ( $0.010 \text{ mg.g}^{-1}.\text{sec}^{-1/2}$ ) is much lower than macropores diffusion rate constant ( $0.128 \text{ mg.g}^{-1}.\text{sec}^{-1/2}$ ). This is because the relative availability of the free path for transition pores diffusion is much lower than macropores diffusion hence the diffusion rate has been decreased. However, the researcher also showed that the second linear region (green line) represents the adsorption over active sites which corresponds to the equilibrium state of the adsorption due to the extremely low adsorbate left in the aqueous solution and decrease of active sites [407]. Therefore, it is found here that the external mass transfer and intra-particle diffusion both are involving in the adsorption of CR by PANI/BFO nanocomposite. Also from the above results, it seems that the intra-particle diffusion is the rate-determining step. Further, the rate-controlling step is confirmed by the Boyd model in equation (6-4).

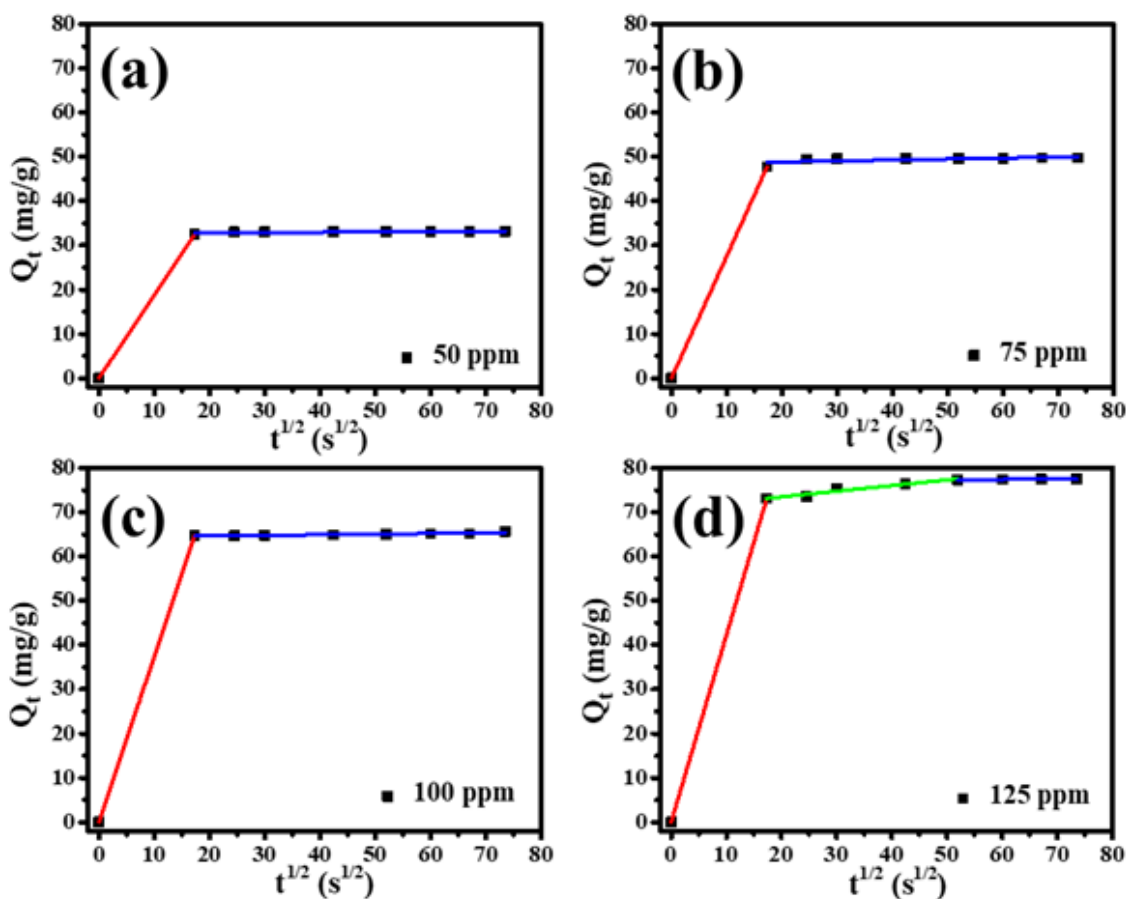
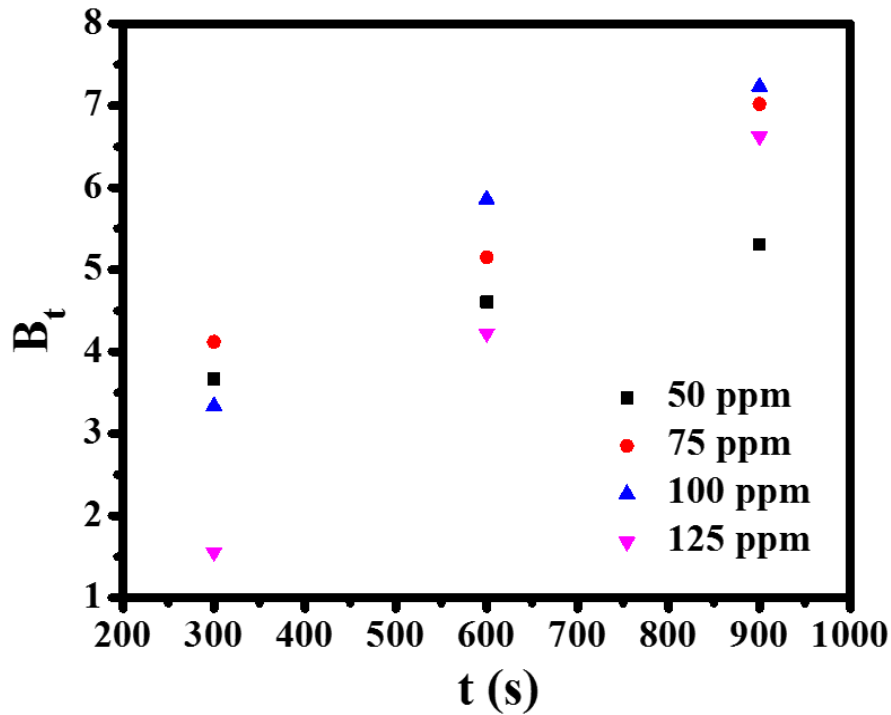


Figure 7.12. Intra-particle diffusion model ( $Q_t$  versus  $t^{1/2}$ ) suggests film diffusion as rate-limiting process for the adsorption of CR onto PANI/BFO for different concentrations (a) 50 ppm, (b) 75 ppm, (c) 100 ppm, and (d) 125 ppm.

Table 7.3. Intra-particles diffusion model parameters for the adsorption of CR onto PANI/BFO nanocomposites.

| S.No. | Conc/parameter                                  | 50 ppm  | 75 ppm  | 100 ppm | 125 ppm |
|-------|---|---------|---------|---------|---------|
| 1     | $k_{i1}$ ( $mg \cdot g^{-1} \cdot sec^{-1/2}$ ) | 1.87421 | 2.75674 | 3.73495 | 4.22072 |
| 2     | $C_1$ ( $mg \cdot g^{-1}$ )                     | 0       | 0       | 0       | 0       |
| 3     | $R^2_1$   | -       | -       | -       | -       |
| 4     | $k_{i2}$ ( $mg \cdot g^{-1} \cdot sec^{-1/2}$ ) | 0.00196 | 0.00487 | 0.01388 | 0.128   |
| 5     | $C_2$ ( $mg \cdot g^{-1}$ )                     | 32.99   | 49.40   | 64.36   | 70.91   |
| 6     | $R^2_2$   | 0.820   | 0.930   | 0.803   | 0.838   |

Figure 7.13 suggests that the plots are linear but these do not pass through the origin therefore, the possibility of intra-particle diffusion as a rate-controlling step is omitted. Therefore, film diffusion plays a key role in the rate-controlling step in the adsorption process.



**Figure 7.13.** Plots of Boyd model parameter  $B_t$  versus time  $t$  for adsorption of CR onto PANI/BFO nanocomposite.

### 7.5.2 Adsorption Isotherms

To find the distribution of CR onto PANI/BFO in the liquid-solid phase and to understand the interaction between CR and PANI/BFO nanocomposite, Langmuir, and Dubinin-Radushkevich (D-R) models have been applied to the equilibrium adsorption data. The Langmuir isotherms model is expressed in Equation (5-4). The  $Q_m$  and  $b$  are calculated from the slope and intercept of the linear plot between  $C_e/Q_e$  versus  $C_e$  as shown in Figure 7.14a and the corresponding values are given in Table 7.4.

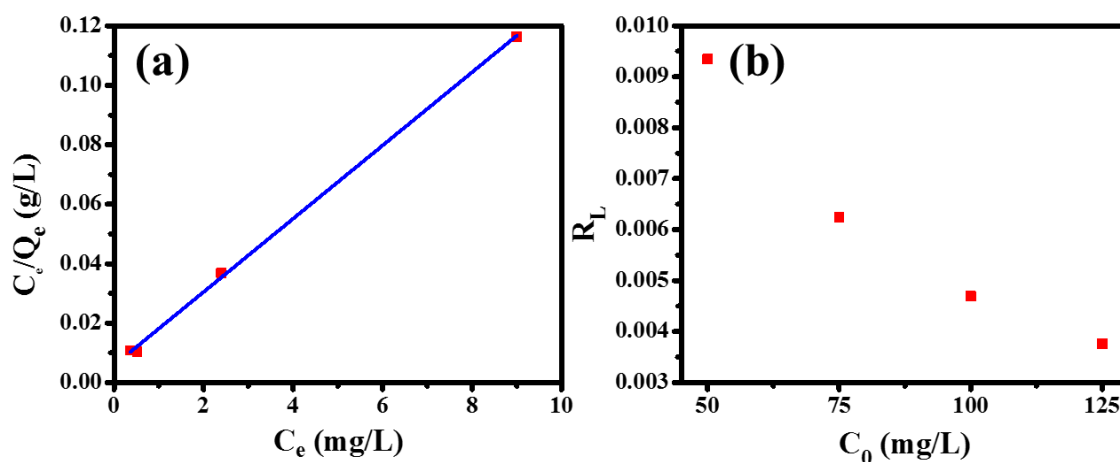


**Figure 7.14. Plots of (a) Langmuir model infers monolayer adsorption, and (b) Separation factor  $R_L$  versus initial concentration  $C_0$ .**

The values of  $Q_m$  and  $b$  are calculated to be 81.16 mg/g and 2.11 L/mg respectively whereas the correlation coefficient ( $R^2$ ) was found to be quite high at 0.998 which shows the better applicability of the Langmuir model to best describe the adsorption equilibrium of CR onto PANI/BFO nanocomposite. The essential characteristics of the Langmuir model can be described by a dimensionless constant separation factor  $R_L$  which is given by Equation (6-5). In Figure 7.14b, the value of  $R_L$  estimates in the range of 0.003 to 0.01 in the current study, which indicates the isotherm is favorable and since the  $R_L$  values are too low that shows the interaction of CR molecules onto PANI/BFO nanocomposite is relatively strong.

The maximum adsorption value  $Q_m$  obtained from the Langmuir model is useful in calculating the maximum surface coverage ( $S_c$ ) of the PANI/BFO surface by the CR molecules. The  $S_c$  can be calculated by Equation (5-5). The value of  $Q_m$  is obtained to be 81.16 mg/g (Table 7.4) and the size of the CR molecule is about 2.3 nm whereby the surface area is estimated to be around 6 nm<sup>2</sup>. The surface coverage  $S_c$  is calculated at 421.00 m<sup>2</sup>/g. Thus, the  $S_c$  of CR on PANI/BFO is quite large revealing the large surface area exposes for CR adsorption. This is the conclusion of why the adsorption of CR onto PANI/BFO is enhanced dramatically.

We have also used the Freundlich model to describe the isotherms of adsorption as represents in Figure 7.15a. The results indicate that the adsorption data is not well fit for this model. The Freundlich model generally describes the chemisorption of adsorbate onto the adsorbent. Therefore the failure of this model omitted the possibility of chemisorption in the adsorption process. Besides, it indirectly signifying the physisorption of CR onto PANI/BFO nanocomposite.

Thus, the Langmuir model indicates the physisorption nevertheless to further confirm, D-R model in Equation (5-6), (5-7), and (5-8) has been applied.

**Table 7.4. Isotherms parameters for the Langmuir model, and Dubinin-Radushkevich model.**

| Model                             | Parameters   | Values |
|-----------------------------------|--|--------|
| <b>Langmuir model</b>             | b (L/g)  | 2.12   |
|                                   | Q <sub>m</sub> (mg/g)                                | 81.16  |
|                                   | R <sup>2</sup>                                       | 0.998  |
| <b>Dubinin Radushkevich model</b> | B (mol <sup>2</sup> /k <sup>2</sup> J <sup>2</sup> ) | 0.067  |
|                                   | Q <sub>m</sub> (mg/g)                                | 74.30  |
|                                   | E (kJ/mol)   | 2.72   |
|                                   | R <sup>2</sup>                                       | 0.929  |

Therefore, in the present case under all studies CR concentration, the obtained value is given in Table 7.4 which reveals that the value of *E* is 2.72 kJ/mol that strongly in favor of the physisorption of CR onto PANI/BFO.

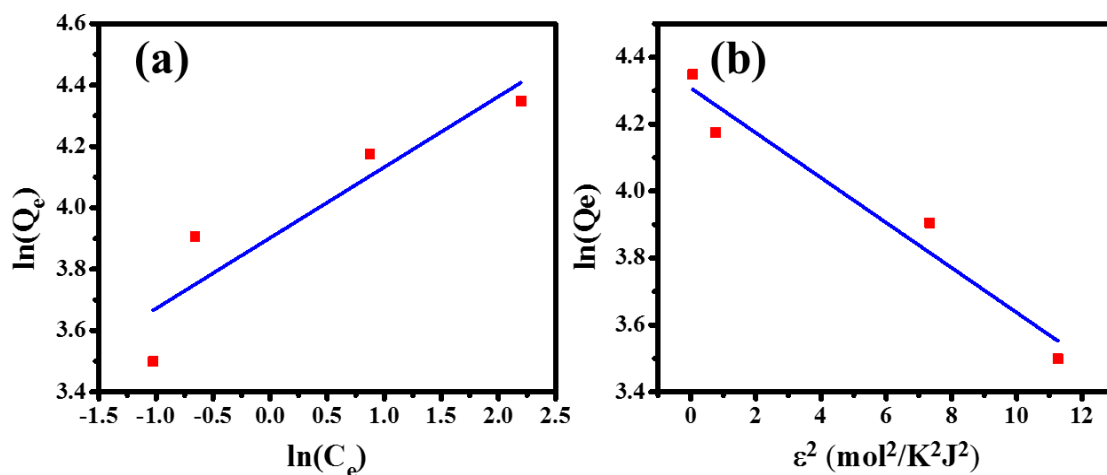


**Figure 7.15. Linear fitting of (a) Freundlich model, and (b) D-R model.**

### 7.5.3 Thermodynamics of adsorption

The thermodynamic parameters of the adsorption of CR onto PANI/BFO can provide in-depth information about the change in the inherent energy of adsorption. The free energy of adsorption ( $\Delta G^\circ$ ) can be calculated by the thermodynamic equilibrium constant ( $K_d$ ) obtained from the equilibrium adsorption data of 50 ppm CR dye adsorption at the temperature range 30 °C to 60 °C. The thermodynamic equilibrium constant ( $K_d$ ), Gibbs energy change ( $\Delta G^\circ$ ), enthalpy change ( $\Delta H^\circ$ ), and entropy change ( $\Delta S^\circ$ ) are determined by using the Equations (5-9), (5-10), and (5-11) respectively.  $\Delta H^\circ$  and  $\Delta S^\circ$  are calculated from the slope and intercept of the van't Hoff plot as represented in Figure 7.16a. The calculated values of the  $\Delta H^\circ$  and  $\Delta S^\circ$  are given in Table 7.5. It is demonstrated from the Table 7.5 that the Gibbs free energy is negative which increases from -11.4 to -13.8 kJ/mol for 50 ppm at 303 and 313 K thereafter it is almost constant for the higher temperature at 323 K and 333 K. The negative values of Gibbs free energy suggested that the adsorption of CR onto PANI/BFO is feasible, spontaneous and more favorable at a higher temperature. Therefore, the obtained value of  $\Delta G^\circ$  in the current research is between -11 to -14 kJ/mol which strongly in the favor of physisorption of CR onto PANI/BFO nanocomposite surface which is in the confirmation of the Langmuir model

and D-R model. The negative value of the  $\Delta S^\circ$  which is  $-53.83 \text{ J}\cdot\text{mol}^{-1}\cdot\text{K}^{-1}$  indicates the decrease of randomness at the solid-liquid interfaces during the adsorption process. The decrease of randomness at a solid-liquid interface might be due to the rapid selectivity of CR molecules from its aqueous solution by PANI/BFO adsorbent. During the adsorption process, the CR molecules strongly attracted by the PANI/BFO adsorbent through various forces from the CR aqueous solution instantaneously and repel water from the adsorbent surface which decreases the randomness at the interface.

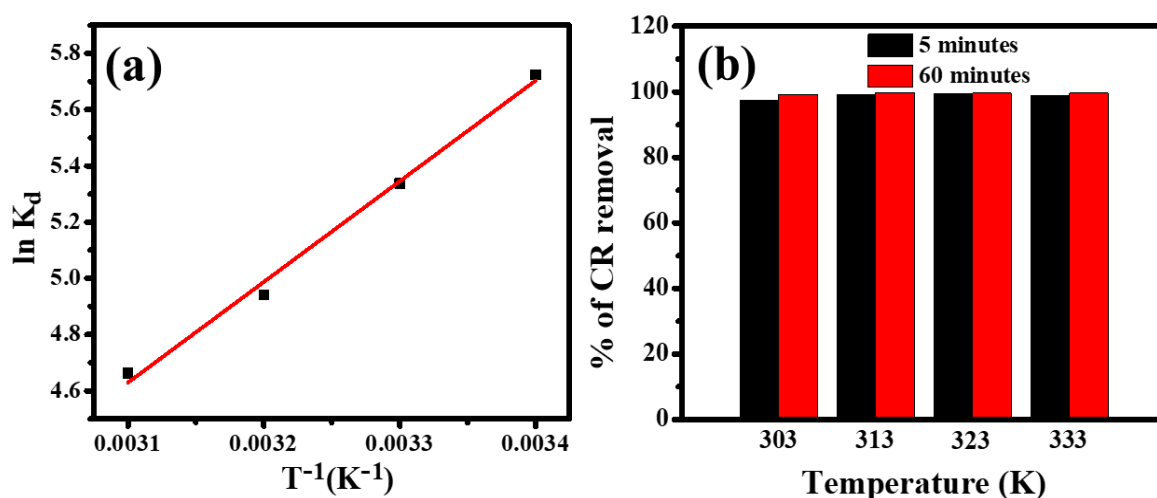


**Figure 7.16. (a) van't Hoff plot used to calculate thermodynamics parameters, and (b) Graph shows the CR (50 ppm) equally adsorbed at higher temperature by PANI/BFO.**

Since the adsorption of CR onto PANI/BFO is too fast as it can adsorb almost 100% dye from aqueous solution even within 5 minutes as shown in Figure 7.16b, once all the CR molecules attached to the PANI/BFO surface then the randomness at the solid-liquid decreases. This might be the cause of negative values of  $\Delta S^\circ$  and  $\Delta H^\circ$ . The value of enthalpy change ( $\Delta H^\circ$ ) has been calculated  $-29.34 \text{ kJ/mol}$  which indicates the adsorption is exothermic.

**Table 7.5. Thermodynamic parameters for the adsorption of CR onto PANI/BFO nanocomposites.**

| S.No. | T (K) | $\Delta G$ (kJ/mol) | $\Delta H$ (kJ/mol) | $\Delta S$ (J/mol.K) |
|-------|-------|---------------------|---------------------|----------------------|
| 1     | 293   | -11.4               | -29.34              | -53.83               |
| 2     | 303   | -13.8               |                     |                      |
| 3     | 313   | -13.5               |                     |                      |
| 4     | 323   | -13.4               |                     |                      |

It has been also noticed that the % removal of CR by PANI/BFO nanocomposite is almost constant with respect to time as shown in Figure 7.16b at two different times 5 minutes and 60 minutes. The typical number of the polyaniline monomers can be calculated from the striking entropy value  $53.83 \text{ J}\cdot\text{mol}^{-1}\cdot\text{K}^{-1}$ . The total change in entropy can be expressed in terms of monomer numbers as  $\Delta S = N_{av} \times k \times N$ . Where  $N_{av}$  is the Avogadro number ( $6.023 \times 10^{23} / \text{mol}$ ),  $k$  is Boltzmann constant ( $1.38 \times 10^{-23} \text{ J/K}$ ) and  $N$  represents the number of polyaniline monomers. The above equation turns out to be as  $\Delta S = R \times N$  where  $R (=kN)$  denotes gas constant. This equation gives a total number of  $N \sim 7$  monomers in a polyaniline chain. This is also in agreement with the previously reported data [349]. This number can also be justified from XRD data as the XRD peaks in PANI/BFO nanocomposite related to PANI have been disappeared which suggested that the addition of BFO hinders the polymerization of PANI over its surface. This might be in result of short polymeric chains of less number of monomers.

## 7.6 Reusability of adsorbent PANI/BFO

The reusability of the adsorbent is a substantial factor for its economic and practical applications. The reusability of the PANI/BFO has been tested four times the adsorption cycle one by one without performing the desorption experiment as represented in Figure 7.17. In this context, the adsorbent was fed to the next adsorption cycle in its original form after collecting from the previous experiment followed by filtration and drying. The adsorption efficiency of the PANI/BFO decreases slightly (8.42 %) after the four times of re-use. Thus, the results show that the PANI/BFO can be re-used many times as an effective and economical adsorbent towards CR removal.

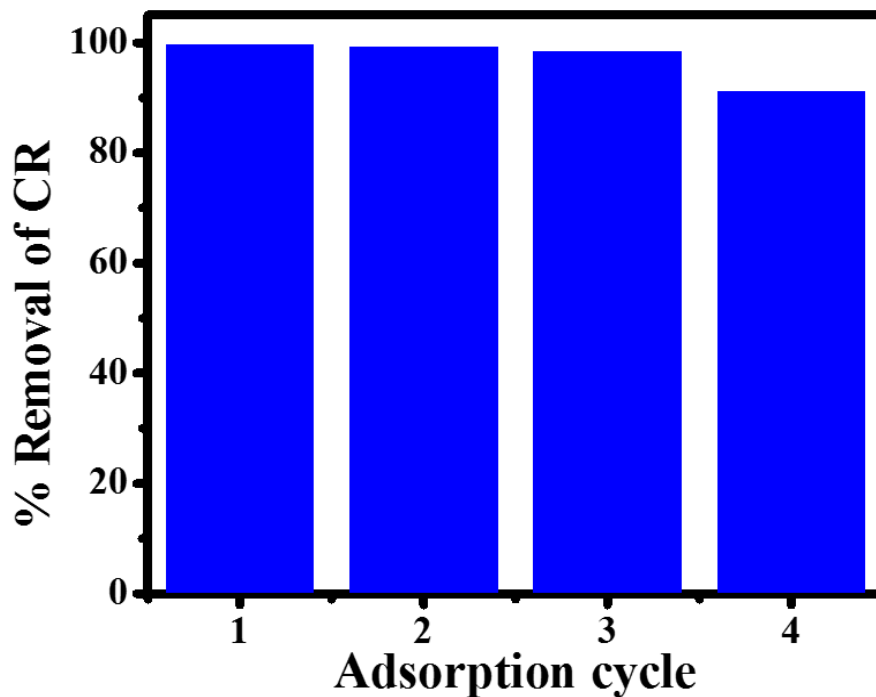


**Figure 7.17.** The re-usability shows the higher capacity of the adsorbent towards CR removal.

## **Chapter: 8 Conclusions and future work**

### **8.1 Conclusions**

#### **8.1.1 Chapter 3**

- Zinc titanate nanorods are successfully prepared by the sol-electrospinning method by using PVP as guiding polymer.
- The characterization reveals that the surface states increases in EZT nanorods.
- The surface states are acceptor levels and lie below the conduction band minimum.
- The effective bandgap of EZT nanorods decreases.
- EZT nanorods are more efficient for visible light photocatalytic degradation of the phenol than the BZT nanoparticles.
- The higher efficiency of EZT nanorods is ascribed to the synergic effect from the presence of surface states and charge transport to the surface of the nanorods.

#### **8.1.2 Chapter 4**

- ZTO has been prepared by the sol-electrospinning technique successfully.
- Nitrogen has been doped into the ZTO lattice successfully.
- XRD, FTIR, XPS, and Raman spectroscopy confirms the nitrogen doping.
- Nitrogen-doped at both interstitial and substitutional positions confirm by FTIR and XPS data.
- The shift in the XRD pattern shows induced compressive microstrain in N-ZTO.
- A compressive microstrain is calculated by the Williamson-Hall model.
- The ZTO lattice parameters are in good agreement with the previous study.

- Nitrogen doping led to the reduction of bandgap energy, the generation of more surface states, and increase the charge carrier's lifetime.
- The N-ZTO has enhanced phenol degradation under visible light.

### 8.1.3 Chapter 5

- The successful synthesis of PANI/ZTO nanocomposite by the polymerization process.
- The XRD, FTIR, and XPS confirm the formation of PANI/ZTO nanocomposite.
- XRD infers the amorphous phase of PANI when polymerized over the ZTO surface.
- Experimental data suggest the formation of the PANI layer onto ZTO nanoparticles.
- PANI/ZTO shows excellent adsorption for CR dye.
- The CR adsorption is jointly controlled by *film diffusion* and *intra-particles* diffusion.
- Langmuir model suggests the physisorption of CR onto the adsorbent.
- Physisorption is confirmed by the D-R model.
- The thermodynamics of adsorption reveals the spontaneity and endothermic reaction.
- The proposed scheme relates to the enhancement of adsorption.

### 8.1.4 Chapter 6

- BFO has been synthesized by a non-aqueous sol-gel route in three different solvents.
- DMSO, THF, and DMF have been used three solvents separately.
- Two-phase has recognized in BFO namely  $\text{BiFeO}_3$  and  $\text{Bi}_2\text{Fe}_4\text{O}_9$ .

- $\text{Bi}_2\text{Fe}_4\text{O}_9$  dominant in BFO when prepared with DMSO.
- $\text{BiFeO}_3$  dominant in BFO if prepared in THF and DMF.
- XRD, FTIR, and Raman confirm the crystal structure of BFO.
- BFO prepared in DMSO shows ample adsorption of MB.
- Adsorption kinetics has been determined by the pseudo-second-order model.
- The Langmuir model suggested the physisorption of MB onto BFO.
- Weber-morris equation reveals the multilinearity of the graphs to describe adsorption.
- Gibbs free energy tells the unfavorability of adsorption at a higher temperature.
- Desorption takes place at a higher temperature.

### 8.1.5 Chapter 7

- The synthesis of PANI/BFO nanocomposite has been achieved by the polymerization route successfully.
- The XRD, FTIR, and XPS confirm the PANI/BFO preparation through physical forces.
- XRD infers the crystalline phase of PANI when adsorbed over BFO.
- The dramatic increment has been observed in CR adsorption by PANI/BFO.
- Data fitting to the Langmuir model suggests physical adsorption of CR on PANI/BFO.
- Physical adsorption confirms by the D-R model.
- The *film diffusion* is identified as the rate-controlling step by Weber-morris equation.
- The thermodynamics of adsorption reveals the exothermic adsorption.
- The reusability test suggests the high uptake capacity of PANI/BFO.

## 8.2 Future work

- The bandgap engineering of zinc titanate ( $\text{ZnTiO}_3$ ) by vanadium doping and its application into wastewater treatment.
- The spin coating assisted fabrication of ZnO and  $\text{TiO}_2$  sol to prepare zinc titanate thin film for visible light photocatalysis and water splitting.
- EPR study of nitrogen-doped  $\text{ZnTiO}_3$  nanopowders.
- Quantitative determination of reactive species generated in N-ZTO during phenol degradation under visible light.
- Visible light photocatalytic degradation of various pollutants by PANI/ZTO and PANI/BFO nanocomposites.
- Preparation of nanocomposites with ZTO as one entity for various catalytic applications.



Contents lists available at ScienceDirect

Journal of Physics and Chemistry of Solids

journal homepage: [www.elsevier.com/locate/jpcs](http://www.elsevier.com/locate/jpcs)



## Enhancing the visible light induced photocatalytic activity in sol-electrospun zinc titanate nanopowders by nitrogen doping

Somendra Singh, Shama Perween, Amit Ranjan <sup>\*</sup>

Department of Chemical Engineering, Rajiv Gandhi Institute of Petroleum Technology, Jaiz, Amethi, Uttar Pradesh, 229304, India

### ARTICLE INFO

*Keywords:*

Sol electrospinning  
Nitrogen doping  
Zinc titanate  
Visible light photocatalysis

### ABSTRACT

Hexagonal phase of Zinc titanate (ZTO) powder obtained by calcining the electrospun sol in the temperature range of 700–800 °C has shown bandgap in the visible region (Perween and Ranjan, 2017) [1]. Owing to this, ZTO can be considered as a candidate material for visible light induced photocatalysis applications, and therefore can serve as a suitable alternative for solar radiation aided treatment of environmental pollutants. Doping ZTO with a suitable dopant atom such as nitrogen can further reduce its bandgap and thereby enhance the efficacy of its catalytic response to solar light. Here we report successful incorporation of nitrogen in zinc titanate with varying fraction of nitrogen using urea as a nitrogen source. Nitrogen incorporation leads to reduction in the bandgap, and thereby improvement in its visible light induced catalytic performance of ZTO towards the degradation of phenol. Presence of nitrogen also promotes the formation of the high-temperature phase of cubic  $Zn_2TiO_4$ . Nitrogen incorporated ZTO (N-ZTO) nanoparticles lead to a reduction in the bandgap from 2.83 eV in



Contents lists available at [ScienceDirect](#)

## Journal of Environmental Chemical Engineering

journal homepage: [www.elsevier.com/locate/jece](http://www.elsevier.com/locate/jece)



### Dramatic enhancement in adsorption of congo red dye in polymer-nanoparticle composite of polyaniline-zinc titanate

Somendra Singh, Shama Perween, Amit Ranjan\*

Department of Chemical Engineering, Rajiv Gandhi Institute of Petroleum Technology, Jais, Uttar Pradesh 229304, India

#### ARTICLE INFO

Editor: Dr. Zhang Xiwang

#### Keywords:

Polymer/oxides nanoparticles  
Polyaniline/zinc titanate nanocomposite  
Congo red adsorption  
Physisorption

#### ABSTRACT

In this paper, we report a dramatic enhancement in the adsorptive removal of Congo Red (CR) dye by polyaniline-zinc titanate (PANI/ZTO) nanocomposite as compared with that when PANI or ZTO are used separately. The dye exhibited little adsorption in the presence of lab-synthesized pristine ZnTiO<sub>3</sub> (ZTO) powder as adsorbent and somewhat moderate adsorption in the presence of neat polyaniline whereas excellent and much faster adsorption was exhibited in the presence of PANI/ZTO nanocomposite. The composite was prepared by carrying out the polymerization of aniline in the presence of ZTO suspensions. The composite samples were characterized using X-Ray diffraction, FT-IR Spectroscopy, Field emission scanning electron microscopy, X-ray photoelectron spectroscopy, and Dynamic light spectroscopy, and the adsorption kinetics were studied using UV-Vis spectroscopy. The characterization data suggest that the adsorption of the CR dye gets enhanced because PANI chain molecules which are chiefly responsible for adsorption through hydrogen bonding and  $\pi$ - $\pi$  in-

OPEN

## PVA-PDMS-Stearic acid composite nanofibrous mats with improved mechanical behavior for selective filtering applications

Received: 22 June 2018

Accepted: 12 October 2018

Published online: 30 October 2018

Shama Perween<sup>1</sup>, Ziyauddin Khan<sup>2,3</sup>, Somendra Singh<sup>1</sup> & Amit Ranjan<sup>1</sup>

In this work, we report a facile way to fabricate composite nanofibrous mats of polyvinyl alcohol (PVA), polydimethylsiloxane (PDMS), and stearic acid (SA) by employing the electrospinning-technique, with PDMS fraction ranging from 40w% to nearly 80w%. The results show that for a predetermined fraction of PVA and SA, incorporation of an optimal amount of PDMS is necessary for which the mats exhibit the best mechanical behavior. Beyond this optimal PDMS fraction, the mechanical properties of the composite mats deteriorate. This result has been attributed to the ability of the SA molecules to mediate binding between the PVA and PDMS long-chain molecules via van-der-Waals bonding. The morphological, structural, mechanical, and thermal characterizations respectively using SEM, XRD, DMA/tensile test, and DSC lend support to this explanation. By this method, it is possible to control the hydrophilicity/oleophilicity of the mats, and the mats show an excellent selective permeability to oil as compared to water and successfully filter water from a water-in-oil emulsion. Incorporation of SA not only serves to aid in electrospinning of a PDMS-rich nanofibrous mat with good mechanical

### **Polyacryloyl Hydrazide Incorporation in Ionic Hydrogels Improves Toughness, Elasticity, Self-Healability, Adhesive & Strain Sensing Properties**

Subhankar Mandal<sup>1†</sup>, Niharika Pandey<sup>1†</sup>, Somendra Singh<sup>2</sup>, Amit Ranjan<sup>2</sup>, Umapasana Ojha<sup>\*,1</sup>

<sup>1</sup>Department of Chemistry, <sup>2</sup>Department of Chemical Engineering, Rajiv Gandhi Institute of Petroleum Technology, Jais, UP, India-229304

**Keywords:** Tough hydrogel, Self-healing, Strain sensor, Adhesive, Ionic interaction, Polyacryloyl hydrazide.

#### **Abstract**

---

## Dr. SOMENDRA SINGH

Ph.D. (Materials Science) (2015-2020)

Thesis Supervisor: Dr. Amit Ranjan (Associate Professor)

Department of Chemical Engineering and Engineering Sciences

Address: Rajiv Gandhi Institute of Petroleum Technology

Jais, Amethi, U.P, India-229304

Contact No: +91-9839737597

Email: [pms15001@rgipt.ac.in](mailto:pms15001@rgipt.ac.in), [somendra9286@gmail.com](mailto:somendra9286@gmail.com)



### EDUCATION

---

|  |   |
|--|---|
| 28 <sup>th</sup> AUGUST, 2020<br>-Till now | <b>Research Associate</b> at RGIPT, Jais, Amethi, UP<br>Advisor: Dr. Amit Ranjan  |
| 4 <sup>th</sup> AUGUST, 2021               | <b>Successfully defended Ph.D oral presentation</b>   |
| 25 <sup>th</sup> AUGUST 2020               | <b>Submitted Ph.D. thesis in Materials Science</b>   Thesis topic “ <i>Novel oxide nanoparticles and their polymer composites for visible light photocatalysis and adsorption applications</i> ”.<br>RGIPT, Jais, Amethi   Thesis advisor: <b>Dr. Amit Ranjan</b> |
| DECEMBER 2015<br>- APRIL 2016              | Ph.D. Course Work at <b>IIT, Kanpur</b>   |
| SEPTEMBER 2014<br>UP.                      | <b>Master of Science in Physics</b> , CCS University Meerut,<br>First Class, 73.45%   Specialization: Electronics   |
| JULY 2012                                  | <b>Bachelor of Science</b> , CCS University Meerut, UP.<br>First Class, 69.54%   Major in Physics, Chemistry, and Maths   |
| AUGUST 2008                                | <b>Intermediate</b> , UP Board, Allahabad, UP.<br>First Class, 65.60%   Major in Physics, Chemistry, and Maths  |
| JULY 2006                                  | <b>SSC</b> , UP Board, Allahabad, UP.<br>First Class, 73.00%   Major in Science, Maths, Hindi, English, Social Science, Art.  |

## PUBLICATIONS

---

- [Shama Perween, Ziyauddin Khan, Somendra Singh, \\*Amit Ranjan. PVA-PDMS-Stearic acid composite nanofibrous mats with improved mechanical behavior for selective filtering application. \*Scientific Reports\*. \(2018\) 8: 16038.](#)
- [Subhankar Mandal, Niharika Pandey, Somendra Singh, Amit Ranjan, \\*Umamprasad Ojha. Polyacryloyl hydrazide incorporation into ionic hydrogels improved toughness, elasticity, self-healability, adhesive & strain sensing properties. \*Mater. Chem. Front.\*, 2019, 3, 690-701.](#)
- **Somendra Singh**, Shama Perween, \*Amit Ranjan. Dramatic enhancement in adsorption of congo red dye in polymer-nanoparticle composite of polyaniline-zinc titanate. *Journal of Environmental Chemical Engineering*, **2021**, **9** (3), 105149.
- **Somendra Singh**, Shama Perween, \*Amit Ranjan. *Enhancing the visible light induced photocatalytic activity in sol-electrospun zinc titanate nanopowders by nitrogen doping. *Journal of Physics and Chemistry of Solids*. 158 (2021), 110221.*
- Zinc titanate nanorods through the sol-electrospinning route for visible light photocatalysis applications. **(Under review)**
- Polyaniline coated bismuth ferrite nanoparticles exhibiting fast adsorption of congo red dye. **(Manuscript submitted)**
- Induced adsorption of methylene blue dye in bismuth ferrite nanorods prepared in different solvents. **(Manuscript submitted)**
- Higher adsorption of congo red dye by nanocomposite of vanadium trioxide-zinc titanate nanoparticles. **(Manuscript under preparation)**
- Photocatalytic activity of spin coated zinc titanate nanorods over glass and quartz substrate for methylene blue degradation **(Manuscript under preparation)**

## CONFERENCES and SEMINARS

---

- Abstract has been accepted for ORAL presentation at the “**International Conference on Advances in Functional Materials**” (AFM-2017) at the University of California, Los Angeles, USA.
- ORAL and poster presentation at the “**Think Nano Conference**” (Think Nano-2017) in IISc, Bangalore, India.
- Poster presentation at **JNCASR-I2CAM (2017)** school on "Clean and Renewable Energy Technologies via Chemical Route" in JNCASR, Bangalore, India.
- Oral presentation at “**International Conference on Nanotechnology: Ideas, Innovations, and Initiatives (ICN: 3I-2017)**” in IIT-Roorkee, India.

- Abstract has been accepted for the poster presentation at “**MRS Fall Meeting & Exhibit-2018**” in Boston, Massachusetts, USA.
- Presented a research paper at “**2<sup>nd</sup> International Conference on Nanoscience and Nanotechnology (ICNAN’19)**” organized by “Centre for Nanotechnology Research” in Vellore Institute of Technology, Vellore, India-2019.

#### **ACHIEVEMENTS**

---

|                  |  |
|------------------|--|
| <b>GATE 2016</b> | Qualified Graduate Aptitude Test Engineering Exam in Physics<br>Score 481   AIR 657  |
| <b>GATE 2015</b> | Qualified Graduate Aptitude Test Engineering Exam in Physics<br>Score 359   AIR 1184 |

#### **RESEARCH INTEREST**

---

- Development of electrospun nanofibers for Energy and Environment applications.
- Engineering metal oxide materials for hydrogen evolution.
- Conducting polymer/metal oxides nanocomposite as electrodes for supercapacitor and battery applications.
- Dielectric, Magnetic, and Ferromagnetic Materials.
- Adsorption of industrial waste and radioactive waste materials.
- Electrospun nanofibrous mats for oil-in-water filtration, thermal energy storage, and wound healing applications.
- Metal oxides and their polymer composite thin-film deposition by spin coating technique.

#### **TEACHING EXPERIENCES**

---

- Teaching Assistant (TA) to Dr. Amit Ranjan at RGIPT for “**Materials Science course and Materials Science Lab**” (Undergraduate level).
- Teaching Assistant to Dr. Arshad Aijaz at RGIPT for “**Materials Science Lab and Lab experiments teaching**” (Undergraduate level).
- Teaching Assistant to Dr. Gunjan Agrahari at RGIPT for the course entitled “**Thermodynamics of Hydrocarbons**” (Undergraduate level).
- Teaching Assistant to Dr. K.G Biswas at RGIPT for “**Chemical Engineering Unit Operation Processing Lab**” (Undergraduate level).
- Teaching Assistant to Dr. U.D Dwivedi at RGIPT for “**MATLAB Course**”.

## **TECHNICAL KNOWLEDGE**

---

### **Equipment Handle**

- UV-Vis Spectrometer (UV-Vis), Differential Scanning Calorimetry (DSC) Universal Tensile Machine (UTM), Fourier Transform Infrared Spectroscopy (FTIR), Fluorescence Spectrometer, and Dynamic Light Scattering (DLS), Electrospinning Unit, and Spin Coater.

### **Equipment can handle**

- X-Ray Photoelectron Spectroscopy (XPS), Thermal Gravimetric Analysis (TGA), Nuclear Magnetic Resonance (NMR) Spectroscopy, Electrochemical Analyzer (CH Instruments), Time-Correlated Single Photon Counting System (TCSPC), X-Ray diffractometer (XRD), Field Emission Scanning Electron Microscopy (FESEM), Gas Chromatography, and Raman Spectroscopy.

### **Software Skills**

- Origin, Microsoft Excel, PowerPoint, Microsoft Word, and Peak fit.

### **Laboratory handling experience**

- Materials Science Lab (Two Probe method, Four Probe method, Hall Effect, Dielectric Constant measurement, Magnetoresistance experiment, etc.) undergraduate level.

## **EXTRA ACTIVITIES**

---

- **Student Coordinator for Annual Research Symposium Parishti'18 (Dated: 17<sup>th</sup> and 18<sup>th</sup> March 2018 )** organized at RGIPT.
- Member of Unfair Means Committee (UFM) at RGIPT (Academic session 2018-2019).
- **HOD of Physics** in Social Club “Project Amethi” conduct by RGIPT for 9<sup>th</sup> to 12<sup>th</sup> standard students of District Amethi, UP (Academic session 2019-2020).
- **Faculty of Science** in Social Club “Gyan Arpan” at RGIPT.
- The organizer of many programs at RGIPT during the visit of dignitaries.

## **PERSONAL DATA**

---

- Parents Name: Mr. Mahodar Singh & Mrs. Kamla Devi
- Nationality: Indian
- Date of Birth: 10<sup>th</sup> July 1991
- Gender: Male
- Marital Status: Unmarried
- Languages: Hindi & English
- Permanent Address: Village- Ranethi, Post- Raja Rijola, Distt- Kasganj, U.P

- Current Address: Pin code- 207243  
Rajiv Gandhi Institute of Petroleum Technology  
Jais, Amethi, Uttar Pradesh, Pin code-229304

## REFERENCES

---

| S.No | Referee's Name                      | Faculty   | Institution           | Email/Contact   |
|------|-------------------------------------|---|-----------------------|---|
| 1    | Dr. Amit Ranjan<br>(Thesis Advisor) | Associate Professor,<br>(Chemical Engineering)<br>Department of Chemical<br>Engineering and<br>Engineering Sciences | RGIPT,<br>Jais, India | <a href="mailto:aranjan@rgipt.ac.in">aranjan@rgipt.ac.in</a><br>+91-535-2704503 |
| 2    | Dr. Umapasana Ojha                  | Associate Professor,<br>(Chemistry)<br>Department of Basic<br>Science and Humanities                                | RGIPT,<br>Jais, India | <a href="mailto:uojha@rgipt.ac.in">uojha@rgipt.ac.in</a><br>+91-535-2704510     |
| 3    | Dr. Arshad Aijaz                    | Assistant Professor,<br>(Chemistry)<br>Department of Basic<br>Science and Humanities                                | RGIPT,<br>Jais, India | <a href="mailto:aaijaz@rgipt.ac.in">aaijaz@rgipt.ac.in</a><br>+91-535-2704517   |

## DECLARATION

---

I hereby declare that all the information mentioned above is true to the best of my knowledge.

Thanking You

**Place: Ranethi, Kasganj, UP**

**Date: 07-08-2021**

**Dr. Somendra Singh**



## References:

- [1] A. Abel, The history of dyes and pigments, in: *Colour Des.*, Second Edi, Elsevier Ltd., United Kindom, 2012: pp. 557–587. <https://doi.org/10.1016/b978-0-08-101270-3.00024-2>.
- [2] S.K. Sharma, *Green Chemistry for Dyes Removal from Waste Water*, 1st ed., Scrivener Publishing LLC, Wiley, Beverly, MA, 2015.
- [3] A. Gürses, M. Açıkyıldız, K. Güneş, M.S. Gürses, “Dyes and Pigments: Their Structure and Properties” in *SpringerBriefs in Green Chemistry for Sustainability*, A. Gürses Al., Dye. Pigment. SpringerBriefs Green Chem. Sustain. (2016) 13–29. <https://doi.org/10.1007/978-3-319-33892-7>.
- [4] F. Fu, Q. Wang, Removal of heavy metal ions from wastewaters: A review, *J. Environ. Manage.* 92 (2011) 407–418. <https://doi.org/10.1016/j.jenvman.2010.11.011>.
- [5] K.S. Egorova, V.P. Ananikov, Toxicity of Metal Compounds: Knowledge and Myths, *Organometallics.* 36 (2017) 4071–4090. <https://doi.org/10.1021/acs.organomet.7b00605>.
- [6] D.A. Scholz, M. Yaseen, Textile dye wastewater characteristics and constituents of synthetic effluents : a critical review, *Int. J. Environ. Sci. Technol.* 16 (2019) 1193–1226. <https://doi.org/10.1007/s13762-018-2130-z>.
- [7] Q. Sun, L. Yang, The adsorption of basic dyes from aqueous solution on modified peat – resin particle, *Water Res.* 37 (2003) 1535–1544.
- [8] S. Maria, A. Guelli, U. De Souza, E. Forgiarini, U. De Souza, Toxicity of textile dyes and their degradation by the enzyme horseradish peroxidase ( HRP ), *J. Hazard. Mater.* 147 (2007) 1073–1078. <https://doi.org/10.1016/j.jhazmat.2007.06.003>.
- [9] L. Susskind, R. Chittaranjan, R. Jain, *Strategies for Sustainability Series*, USA, 2011. <https://doi.org/https://dx.doi.org/10.1007/s40256-015-0131-6>.
- [10] A. Ajmal, I. Majeed, N. Malik, Principles and mechanisms of photocatalytic dye degradation on TiO<sub>2</sub> based photocatalysts : a comparative review, *RSC Adv.* (2014) 37003–37026. <https://doi.org/10.1039/C4RA06658H>.
- [11] P. V Nidheesh, M. Zhou, M.A. Oturan, An overview on the removal of synthetic dyes from water by electrochemical advanced oxidation processes, *Chemosphere.* 197 (2018) 210–227. <https://doi.org/10.1016/j.chemosphere.2017.12.195>.
- [12] V.J.P. Poots, G. McKay, J.J. Healy, The removal of acid dye from effluent using natural adsorbents-I peat, *Water Res.* 10 (1976) 1061–1066. [https://doi.org/10.1016/0043-1354\(76\)90036-1](https://doi.org/10.1016/0043-1354(76)90036-1).
- [13] M.A. Hassaan, A. El Nemr, Health and Environmental Impacts of Dyes : Mini Review, *Am. J. Environ. Sci. Eng.* 1 (2017) 64–67. <https://doi.org/10.11648/j.ajese.20170103.11>.
- [14] S. Khan, A. Malik, Environmental and Health Effects of Textile Industry Wastewater, in: *Environ. Deterior. Hum. Heal.*, 2014: pp. 55–71.

<https://doi.org/10.1007/978-94-007-7890-0>.

- [15] M. Ismail, K. Akhtar, M.I. Khan, T. Kamal, M.A. Khan, A. M. Asiri, J. Seo, S.B. Khan, Pollution, Toxicity and Carcinogenicity of Organic Dyes and their Catalytic Bio-Remediation, *Curr. Pharm. Des.* 25 (2019) 3645–3663. <https://doi.org/10.2174/1381612825666191021142026>.
- [16] D. Ghosh, K.G. Bhattacharyya, Adsorption of methylene blue on kaolinite, *Appl. Clay Sci.* 20 (2002) 295–300.
- [17] Public Health Statement for Benzidine, Atlanta, GA 30333, 2001.
- [18] R.S. De Farias, H. Leonardo, D.B. Buarque, M. Ribeiro, L. Meg, F. Cardoso, T.D.A. Gondim, V.R. De Paulo, Adsorption of congo red dye from aqueous solution onto amino-functionalized silica gel, *Eng. Sanit. Ambient.* 23 (2018) 1053–1060. <https://doi.org/10.1590/S1413-41522018172982>.
- [19] M. Hernández-zamora, F. Martínez-jerónimo, E.C.R.O. Cañizares-villanueva, Congo red dye affects survival and reproduction in the cladoceran *Ceriodaphnia dubia*. Effects of direct and dietary exposure, *Ecotoxicology*. (2016) 0–1. <https://doi.org/10.1007/s10646-016-1731-x>.
- [20] I.C. McCall, A. Betanzos, D.A. Weber, G.W. Miller, C.A. Parkos, Effects of phenol on barrier function of a human intestinal epithelial cell line correlate with altered tight junction protein localization, *Toxicol. Appl. Pharmacol.* 241 (2009) 61–70. <https://doi.org/10.1016/j.taap.2009.08.002>.
- [21] M. Ali, T.R. Sreekrishnan, Aquatic toxicity from pulp and paper mill effluents: A review, *Adv. Environ. Res.* 5 (2001) 175–196. [https://doi.org/10.1016/S1093-0191\(00\)00055-1](https://doi.org/10.1016/S1093-0191(00)00055-1).
- [22] C.R. Holkar, A.J. Jadhav, D. V. Pinjari, N.M. Mahamuni, A.B. Pandit, A critical review on textile wastewater treatments: Possible approaches, *J. Environ. Manage.* 182 (2016) 351–366. <https://doi.org/10.1016/j.jenvman.2016.07.090>.
- [23] S. Benkhaya, S. M'rabet, A. El Harfi, A review on classifications, recent synthesis and applications of textile dyes, *Inorg. Chem. Commun.* 115 (2020) 107891. <https://doi.org/10.1016/j.inoche.2020.107891>.
- [24] J.R. Aspland, Anionic Dyes and Their Application to Ionic Fibers : Dyeing Nylon with Acid Dyes, in: *A Ser. Dying*, School of Textiles, Clemson University, Clemson, S. C, 1993: pp. 19–23.
- [25] S.K. Sharma, *Green Chemistry for Dyes Removal from Waste Water: Research Trends and Applications*, Wiley, 2015. <https://doi.org/10.1002/9781118721001>.
- [26] Y. Artioli, The Chemistry of Adsorption, in: *Encycl. Ecol.*, Elsevier B.V, Netherlands, 2008: pp. 60–65.
- [27] R. Kecili, C.M. Hussain, Mechanism of Adsorption on Nanomaterials, in: *Nanomater. Chromatogr.*, Elsevier Inc., 2018: pp. 89–115. <https://doi.org/10.1016/B978-0-12-812792-6/00004-2>.
- [28] J. Ma, F. Yu, L. Zhou, L. Jin, M. Yang, J. Luan, Y. Tang, H. Fan, Z. Yuan, J. Chen, Enhanced adsorptive removal of methyl orange and methylene blue from aqueous solution by alkali-activated multiwalled carbon nanotubes, *ACS Appl. Mater.*

- Interfaces. 4 (2012) 5749–5760. <https://doi.org/10.1021/am301053m>.
- [29] T.J. Cerofolini, G. F; Meda, L; Bandoz, Adsorption with soft adsorbents or adsorbates. Theory and practice, in: A. Dabrowski (Ed.), *Adsorpt. Its Appl. Ind. Environ. Prot.*, Elsevier Science B.V, 1998: pp. 227–272. [https://doi.org/10.1016/S0167-2991\(99\)80554-0](https://doi.org/10.1016/S0167-2991(99)80554-0).
- [30] B.D. Zdravkov, J.J. Čermák, M. Šefara, J. Janků, Pore classification in the characterization of porous materials: A perspective, *Cent. Eur. J. Chem.* 5 (2007) 385–395. <https://doi.org/10.2478/s11532-007-0017-9>.
- [31] P. Pizarro, C. Guillard, N. Perol, J. Herrmann, Photocatalytic degradation of imazapyr in water: Comparison of activities of different supported and unsupported TiO<sub>2</sub>-based catalysts, *Catal. Today.* 101 (2005) 211–218. <https://doi.org/10.1016/j.cattod.2005.03.008>.
- [32] H.M. Yates, M.G. Nolan, D.W. Sheel, M.E. Pemble, The role of nitrogen doping on the development of visible light-induced photocatalytic activity in thin TiO<sub>2</sub> films grown on glass by chemical vapour deposition, *J. Photochem. Photobiol. A Chem.* 179 (2006) 213–223. <https://doi.org/10.1016/j.jphotochem.2005.08.018>.
- [33] S. Zhu, D. Wang, Photocatalysis: Basic Principles, Diverse Forms of Implementations and Emerging Scientific Opportunities, *Adv. Energy Mater.* 1700841 (2017) 1–24. <https://doi.org/10.1002/aenm.201700841>.
- [34] A. Fujishima, K. Honda, Electrochemical Photolysis of Water, *Nature.* 238 (1972) 37–38.
- [35] H. Kisch, *Semiconductor Photocatalysis: Principles and Applications*, WILEY-VCH Verlag GmbH & Co, Weinheim, 2015. <https://doi.org/10.1002/9783527673315>.
- [36] N. Armaroli, V. Balzani, Solar Electricity and Solar Fuels: Status and Perspectives in the Context of the Energy Transition, *Chem. - A Eur. J. Rev.* 22 (2016) 32–57. <https://doi.org/10.1002/chem.201503580>.
- [37] S. Perween, Electrospinning assisted fabrication of metal oxides/polymer composite nanomaterials for energy and environmental applications, Rajiv Gandhi Institute of Petroleum Technology, Jais, India, 2018.
- [38] M. Zayat, P. Garcia-parejo, D. Levy, Preventing UV-light damage of light sensitive materials using a highly protective UV-absorbing coating, *Chem. Soc. Rev.* 36 (2007) 1270–1281. <https://doi.org/10.1039/b608888k>.
- [39] J. Li, N. Wu, Semiconductor-Based Photocatalyst and Photoelectrochemical Cells for Solar Fuel Generation: A Review, *Catal. Sci. Technol.* (2014). <https://doi.org/10.1039/C4CY00974F>.
- [40] T. Gershon, B. Shin, N. Bojarczuk, M. Hopstaken, D.B. Mitzi, S. Guha, The role of sodium as a surfactant and suppressor of non-radiative recombination at internal surfaces in Cu<sub>2</sub>ZnSnS<sub>4</sub>, *Adv. Energy Mater.* 5 (2015) 1–8. <https://doi.org/10.1002/aenm.201400849>.
- [41] T. Simon, M.T. Carlson, J.K. Stolarczyk, J. Feldmann, Electron Transfer Rate vs Recombination Losses in Photocatalytic H<sub>2</sub> Generation on Pt-Decorated CdS Nanorods, *ACS Energy Lett.* 1 (2016) 1137–1142.

<https://doi.org/10.1021/acsenergylett.6b00468>.

- [42] W.K. Jo, R.J. Tayade, Recent developments in photocatalytic dye degradation upon irradiation with energy-efficient light emitting diodes, *Cuihua Xuebao/Chinese J. Catal.* 35 (2014) 1781–1792. [https://doi.org/10.1016/S1872-2067\(14\)60205-9](https://doi.org/10.1016/S1872-2067(14)60205-9).
- [43] A. Hernández-Ramírez, I. Medina-Ramírez, *Photocatalytic Semiconductors: Synthesis, Characterization, and Environmental Applications*, Springer London, London, 2015. <https://doi.org/10.1007/978-3-319-10999-2>.
- [44] R. Ameta, S.C. Ameta, *Photocatalysis : principles and applications*, CRC Press, Taylor & Francis Group, London, 2017.
- [45] X. Chen, S.S. Mao, Titanium dioxide nanomaterials: Synthesis, properties, modifications and applications, *Chem. Rev.* 107 (2007) 2891–2959. <https://doi.org/10.1021/cr0500535>.
- [46] J. Schneider, M. Matsuoka, M. Takeuchi, J. Zhang, Y. Horiuchi, M. Anpo, D.W. Bahnemann, Understanding TiO<sub>2</sub> photocatalysis: Mechanisms and materials, *Chem. Rev.* 114 (2014) 9919–9986. <https://doi.org/10.1021/cr5001892>.
- [47] M.A. Mohd Adnan, N.M. Julkapli, S.B. Abd Hamid, Review on ZnO hybrid photocatalyst: Impact on photocatalytic activities of water pollutant degradation, *Rev. Inorg. Chem.* 36 (2016) 77–104. <https://doi.org/10.1515/revic-2015-0015>.
- [48] Y.T. Asahi, R., T. Morikawa, T. Ohwaki, K. Aoki, Visible-Light Photocatalysis in Nitrogen-Doped Titanium Oxides, *Science* (80). 293 (2001) 269–271. <https://doi.org/10.1126/science.1061051>.
- [49] V. Lachom, P. Poolchauansin, P. Laokul, Preparation, Characterizations and Photocatalytic Activity of a ZnO/TiO<sub>2</sub> Nanocomposite, *Mater. Res. Express.* 4 (2017) 035006. <https://doi.org/10.1088/2053-1591/aa60d1>.
- [50] Z. Nanofiber, N. Synthesized, T. Electrospinning, T. Photocatalytic, A. Under, V. Light, ZnO Nanofiber and Nanoparticle Synthesized Through Electrospinning and Their Photocatalytic Activity Under Visible Light, *J. Am. Ceram. Soc.* 91 (2008) 1287–1291. <https://doi.org/10.1111/j.1551-2916.2008.02299.x>.
- [51] K. Mun, C. Wei, K. Sing, J. Ching, Recent developments of zinc oxide based photocatalyst in water treatment technology : A review, *Water Res.* 88 (2016) 428–448. <https://doi.org/10.1016/j.watres.2015.09.045>.
- [52] M. Anpo, H. Nakaya, S. Kodama, Y. Kubokawa, Photocatalysis over binary metal oxides. Enhancement of the photocatalytic activity of TiO<sub>2</sub> in titanium-silicon oxides, *J. Phys. Chem.* 90 (1986) 1633–1636. <https://doi.org/10.1021/j100399a036>.
- [53] K. Domen, S. Naito, T. Onishi, K. Tamaru, Study of the photocatalytic decomposition of water vapor over a NiO-SrTiO<sub>3</sub> catalyst, *J. Phys. Chem.* 86 (1982) 3657–3661. <https://doi.org/10.1021/j100215a032>.
- [54] N. Kakuta, K.H. Park, M.F. Finlayson, A. Ueno, A.J. Bard, A. Campion, M.A. Fox, S.E. Webber, J.M. White, Photoassisted hydrogen production using visible light and coprecipitated ZnS·CdS without a noble metal, *J. Phys. Chem.* 89 (1985) 732–734. <https://doi.org/10.1021/j100251a002>.

- [55] S. Prabhu, T. Viswanathan, K. Jothivenkatachalam, K. Jeganathan, Visible Light Photocatalytic Activity of CeO<sub>2</sub>-ZnO-TiO<sub>2</sub> Composites for the Degradation of Rhodamine B, *Indian J. Mater. Sci.* 2014 (2014) 1–10. <https://doi.org/10.1155/2014/536123>.
- [56] M.A. Habib, M.T. Shahadat, N.M. Bahadur, I.M.I. Ismail, A.J. Mahmood, Synthesis and characterization of ZnO-TiO<sub>2</sub> nanocomposites and their application as photocatalysts, *Int. Nano Lett.* 3 (2013) 1–8. <https://doi.org/10.1186/2228-5326-3-5>.
- [57] D. Ramírez-Ortega, A.M. Meléndez, P. Acevedo-Peña, I. González, R. Arroyo, Semiconducting properties of ZnO/TiO<sub>2</sub> composites by electrochemical measurements and their relationship with photocatalytic activity, *Electrochim. Acta.* 140 (2014) 541–549. <https://doi.org/10.1016/j.electacta.2014.06.060>.
- [58] C. Wang, B.Q. Xu, X. Wang, J. Zhao, Preparation and photocatalytic activity of ZnO/TiO<sub>2</sub>/SnO<sub>2</sub> mixture, *J. Solid State Chem.* 178 (2005) 3500–3506. <https://doi.org/10.1016/j.jssc.2005.09.005>.
- [59] H. Tanaka, M. Misono, Advances in designing perovskite catalysts, *Curr. Opin. Solid State Mater. Sci.* 5 (2001) 381–387. [https://doi.org/10.1016/S1359-0286\(01\)00035-3](https://doi.org/10.1016/S1359-0286(01)00035-3).
- [60] B. Chamberland, The major ternary structural families, *Int. J. Miner. Process.* 2 (1975) 368. [https://doi.org/10.1016/0301-7516\(75\)90030-7](https://doi.org/10.1016/0301-7516(75)90030-7).
- [61] C. Li, K.C.K. Soh, P. Wu, Formability of ABO<sub>3</sub> perovskites, *J. Alloys Compd.* 372 (2004) 40–48. <https://doi.org/10.1016/j.jallcom.2003.10.017>.
- [62] L.M. Feng, L.Q. Jiang, M. Zhu, H.B. Liu, X. Zhou, C.H. Li, Formability of ABO<sub>3</sub> cubic perovskites, *J. Phys. Chem. Solids.* 69 (2008) 967–974. <https://doi.org/10.1016/j.jpcs.2007.11.007>.
- [63] E.A. Wood, Polymorphism in Potassium Niobate, Sodium Niobate, and other ABO<sub>3</sub> Compounds, *Acta Cryst.* 4 (1951) 358–362. <https://doi.org/10.1107/S0365110X51001112>.
- [64] J.L. Wang, Z.C. Kang, *Functional and Smart Materials*, Springer, Boston, MA, Boston, 1998. <https://doi.org/10.1007/978-1-4615-5367-0>.
- [65] M.W. Lufaso, P.M. Woodward, Prediction of the crystal structures of perovskites using the software program SPuDS, *Acta Crystallogr. Sect. B Struct. Sci.* 57 (2001) 725–738. <https://doi.org/10.1107/S0108768101015282>.
- [66] W.. Mosser, E; Pearson, On The Crystal Chemistry of The Normal Valence Compounds, *Acta Cryst.* 12 (1959) 1015. <https://doi.org/10.1107/S0365110X59002857>.
- [67] F.H. Dulin, D.E. Rase, Phase Equilibria in the System ZnO-TiO<sub>2</sub>, *J. Am. Ceram. Soc.* 43 (1960) 125–131. <https://doi.org/10.1111/j.1151-2916.1960.tb14326.x>.
- [68] O. Park, P.E.E. Poer, G.T. Mccoy, J.H. Beumer, Synthesis of Zinc titanate pigment and coating containing the same, 1971.
- [69] B.C. Yadav, A. Yadav, S. Singh, K. Singh, Nanocrystalline zinc titanate synthesized via physicochemical route and its application as liquefied petroleum

- gas sensor, *Sensors Actuators, B Chem.* 177 (2013) 605–611. <https://doi.org/10.1016/j.snb.2012.11.045>.
- [70] M. Salavati-Niasari, F. Soofivand, A. Sobhani-Nasab, M. Shakouri-Arani, A. Yeganeh Faal, S. Bagheri, Synthesis, characterization, and morphological control of ZnTiO<sub>3</sub> nanoparticles through sol-gel processes and its photocatalyst application, *Adv. Powder Technol.* 27 (2016) 2066–2075. <https://doi.org/10.1016/j.appt.2016.07.018>.
- [71] S. Perween, A. Ranjan, Improved visible-light photocatalytic activity in ZnTiO<sub>3</sub> nanopowder prepared by sol-electrospinning, *Sol. Energy Mater. Sol. Cells.* 163 (2017) 148–156. <https://doi.org/10.1016/j.solmat.2017.01.020>.
- [72] W. Mojtahedi, K. Salo, J. Abbasian, Desulfurization of hot coal gas in fluidized bed with regenerable zinc titanate sorbents, *Fuel Process. Technol.* 37 (1994) 53–65. [https://doi.org/10.1016/0378-3820\(94\)90005-1](https://doi.org/10.1016/0378-3820(94)90005-1).
- [73] S. Ozdemir, T. Bardakci, Hydrogen sulfide removal from coal gas by zinc titanate sorbent, *Sep. Purif. Technol.* 16 (1999) 225–234. [https://doi.org/10.1016/S1383-5866\(99\)00013-1](https://doi.org/10.1016/S1383-5866(99)00013-1).
- [74] J.T. Konttinen, C.A.P. Zevenhoven, M.M. Hupa, Hot gas desulfurization with zinc titanate sorbents in a fluidized bed. 2. Reactor model, *Ind. Eng. Chem. Res.* 36 (1997) 2340–2345. <https://doi.org/10.1021/ie960687p>.
- [75] K. Jothimurugesan, S.K. Gangwal, Regeneration of Zinc Titanate H<sub>2</sub>S Sorbents, *Ind. Eng. Chem. Res.* 37 (1998) 1929–1933. <https://doi.org/10.1021/ie970857d>.
- [76] V. Ageh, H. Mohseni, T.W. Scharf, Lubricious Zinc Titanate Coatings for High Temperature Applications *Surface & Coatings Technology* Lubricious zinc titanate coatings for high temperature applications, *Surf. Coat. Technol.* (2017). <https://doi.org/10.1016/j.surfcoat.2013.06.082>.
- [77] A.R. Phani, M. Passacantando, S. Santucci, Synthesis of nanocrystalline ZnTiO<sub>3</sub> perovskite thin films by sol-gel process assisted by microwave irradiation, *J. Phys. Chem. Solids.* 68 (2007) 317–323. <https://doi.org/10.1016/j.jpcs.2006.09.010>.
- [78] C. Ye, Y. Wang, Y. Ye, J. Zhang, G.H. Li, C. Ye, Y. Wang, Y. Ye, J. Zhang, G.H. Li, Preparation and photoluminescence of undoped ZnTiO<sub>3</sub> thin films, *033520* (2012) 1–5. <https://doi.org/10.1063/1.3190820>.
- [79] H.T. Kim, S.H. Kim, S. Nahm, J.D. Byun, Y. Kim, Low-temperature sintering and microwave dielectric properties of zinc metatitanate-rutile mixtures using boron, *J. Am. Ceram. Soc.* 82 (1999) 3043–3048. <https://doi.org/10.1111/j.1151-2916.1999.tb02200.x>.
- [80] H.T. Kim, S. Nahm, J.D. Byun, Low-Fired (Zn,Mg)TiO<sub>3</sub> Microwave Dielectrics, *J. Am. Ceram. Soc.* 82 (1999) 3476–3480.
- [81] Y.S. Chang, Y.H. Chang, I.G. Chen, G.J. Chen, Y.L. Chai, Synthesis and characterization of zinc titanate nano-crystal powders by sol-gel technique, *J. Cryst. Growth.* 243 (2002) 319–326. [https://doi.org/10.1016/S0022-0248\(02\)01490-2](https://doi.org/10.1016/S0022-0248(02)01490-2).
- [82] J. Arin, S. Thongtem, A. Phuruangrat, T. Thongtem, Characterization of ZnO–TiO<sub>2</sub> and zinc titanate nanoparticles synthesized by hydrothermal process, *Res.*

- Chem. Intermed. 43 (2017) 3183–3195. <https://doi.org/10.1007/s11164-016-2818-y>.
- [83] L. Budigi, M.R. Nasina, K. Shaik, S. Amaravadi, Structural and optical properties of zinc titanates synthesized by precipitation method, *J. Chem. Sci.* 127 (2015) 509–518. <https://doi.org/10.1007/s12039-015-0802-5>.
- [84] B. Lokesh, S. Kaleemulla, N.M. Rao, Synthesis and Characterization of Zinc titanates by Solid state reaction, *Int. J. ChemTech Res.* 6 (2014) 1929–1932.
- [85] Y.L. Chai, Y.S. Chang, G.J. Chen, Y.J. Hsiao, The effects of heat-treatment on the structure evolution and crystallinity of ZnTiO<sub>3</sub> nano-crystals prepared by Pechini process, *Mater. Res. Bull.* 43 (2008) 1066–1073. <https://doi.org/10.1016/j.materresbull.2007.06.002>.
- [86] Y.C. Lee, Y.L. Huang, W.H. Lee, F.S. Shieu, Formation and transformation of ZnTiO<sub>3</sub> prepared by sputtering process, in: *Thin Solid Films*, 2010: pp. 7366–7371. <https://doi.org/10.1016/j.tsf.2010.05.005>.
- [87] K.H. Reddy, S. Martha, K.M. Parida, Fabrication of novel p-BiOI/n-ZnTiO<sub>3</sub> heterojunction for degradation of rhodamine 6G under visible light irradiation, *Inorg. Chem.* 52 (2013) 6390–6401. <https://doi.org/10.1021/ic400159m>.
- [88] P. Fischer, M. Polomska, I. Sosnowska, M. Szymanski, Temperature dependence of the crystal and magnetic structures of BiFeO<sub>3</sub>, *J. Phys. C Solid State Phys.* 13 (1980) 1931–1940. <https://doi.org/10.1088/0022-3719/13/10/012>.
- [89] I.G. Ismailzade, X-Ray Diffractometric Determination of the Curie Temperature and Temperature Dependence of Spontaneous Polarization of Hexagonal (Rhombohedral) Ferroelectrics, *Phys. Status Solidi.* 46 (1971) K39–K41. <https://doi.org/10.1002/pssb.2220460156>.
- [90] C. Tab Ares-Muñoz, J.P. Rivera, A. Bezinges, A. Monnier, H. Schmid, Measurement of the quadratic magnetoelectric effect on single crystalline BiFeO<sub>3</sub>, *Jpn. J. Appl. Phys.* 24 (1985) 1051–1053. <https://doi.org/10.7567/JJAPS.24S2.1051>.
- [91] M.M. Rashad, Effect of synthesis conditions on the preparation of BiFeO<sub>3</sub> nanopowders using two different methods, *J. Mater. Sci. Mater. Electron.* 23 (2012) 882–888. <https://doi.org/10.1007/s10854-011-0513-8>.
- [92] S.K. Singh, Y.K. Kim, H. Funakubo, H. Ishiwara, Epitaxial BiFeO<sub>3</sub> thin films fabricated by chemical solution deposition, *Appl. Phys. Lett.* 88 (2006) 3–6. <https://doi.org/10.1063/1.2196477>.
- [93] C.J. Tsai, C.Y. Yang, Y.C. Liao, Y.L. Chueh, Hydrothermally grown bismuth ferrites: Controllable phases and morphologies in a mixed KOH/NaOH mineralizer, *J. Mater. Chem.* 22 (2012) 17432–17436. <https://doi.org/10.1039/c2jm33859a>.
- [94] D.C. Jia, J.H. Xu, H. Ke, W. Wang, Y. Zhou, Structure and multiferroic properties of BiFeO<sub>3</sub> powders, *J. Eur. Ceram. Soc.* 29 (2009) 3099–3103. <https://doi.org/10.1016/j.jeurceramsoc.2009.04.023>.
- [95] Y.P. Wang, L. Zhou, M.F. Zhang, X.Y. Chen, J.M. Liu, Z.G. Liu, Room-temperature saturated ferroelectric polarization in BiFeO<sub>3</sub> ceramics synthesized by

- rapid liquid phase sintering, *Appl. Phys. Lett.* 84 (2004) 1731–1733. <https://doi.org/10.1063/1.1667612>.
- [96] M. Mahesh Kumar, V.R. Palkar, K. Srinivas, S. V Suryanarayana, Ferroelectricity in a pure BiFeO<sub>3</sub> ceramic, *Appl. Phys. Lett.* 76 (2000) 2764–2766. <https://doi.org/10.1063/1.126468>.
- [97] S.H. Xie, J.Y. Li, R. Proksch, Y.M. Liu, Y.C. Zhou, Y.Y. Liu, Y. Ou, L.N. Lan, Y. Qiao, Nanocrystalline multiferroic BiFeO<sub>3</sub> ultrafine fibers by sol-gel based electrospinning, *Appl. Phys. Lett.* 93 (2008) 24–27. <https://doi.org/10.1063/1.3040010>.
- [98] L. Zhai, Y.G. Shi, J.L. Gao, S.L. Tang, Y.W. Du, Ferroelectric and magnetic properties in high-pressure synthesized BiFeO<sub>3</sub> compound, *J. Alloys Compd.* 509 (2011) 7591–7594. <https://doi.org/10.1016/j.jallcom.2011.04.046>.
- [99] H.D. Megaw, C.N.W. Darlington, Geometrical and structural relations in the rhombohedral perovskites, *Acta Crystallogr. Sect. A.* 31 (1975) 161–173. <https://doi.org/10.1107/S0567739475000332>.
- [100] T. Zhao, A. Scholl, F. Zavaliche, K. Lee, M. Barry, A. Doran, M.P. Cruz, Y.H. Chu, C. Ederer, N.A. Spaldin, R.R. Das, D.M. Kim, S.H. Baek, C.B. Eom, R. Ramesh, Electrical control of antiferromagnetic domains in multiferroic BiFeO<sub>3</sub> films at room temperature, *Nat. Mater.* 5 (2006) 823–829. <https://doi.org/10.1038/nmat1731>.
- [101] L.I. Dan, J. Huang, R.B. Kaner, Polyaniline nanofibers: a unique polymer nanostructure for versatile applications, *Acc. Chem. Res.* 42 (2009) 135–145. <https://doi.org/10.1021/ar800080n>.
- [102] P. Chandrasekhar, *Conducting polymers, fundamentals and applications: A practical approach*, 1st ed., Springer US, 1991. <https://doi.org/10.1007/978-1-4615-5245-1>.
- [103] A.G. MacDiarmid, J.C. Chiang, A.F. Richter, A.J. Epstein, Polyaniline: a new concept in conducting polymers, *Synth. Met.* 18 (1987) 285–290. [https://doi.org/10.1016/0379-6779\(87\)90893-9](https://doi.org/10.1016/0379-6779(87)90893-9).
- [104] E.M. Geniès, A. Boyle, M. Lapkowski, C. Tsintavis, Polyaniline: A historical survey, *Synth. Met.* 36 (1990) 139–182. [https://doi.org/10.1016/0379-6779\(90\)90050-U](https://doi.org/10.1016/0379-6779(90)90050-U).
- [105] N. Gospodinova, L. Terlemezyan, Conducting polymers prepared by oxidative polymerization: Polyaniline, *Prog. Polym. Sci.* 23 (1998) 1443–1484. [https://doi.org/10.1016/S0079-6700\(98\)00008-2](https://doi.org/10.1016/S0079-6700(98)00008-2).
- [106] S.K. Dhawan, D. Kumar, M.K. Ram, S. Chandra, D.C. Trivedi, Application of conducting polyaniline as sensor material for ammonia, *Sensors Actuators, B Chem.* 40 (1997) 99–103. [https://doi.org/10.1016/S0925-4005\(97\)80247-X](https://doi.org/10.1016/S0925-4005(97)80247-X).
- [107] A.G. MacDiarmid, L.S. Yang, W.S. Huang, B.D. Humphrey, Polyaniline: Electrochemistry and application to rechargeable batteries, *Synth. Met.* 18 (1987) 393–398. [https://doi.org/10.1016/0379-6779\(87\)90911-8](https://doi.org/10.1016/0379-6779(87)90911-8).
- [108] C.Y. Chen, J.I. Garnica-Rodriguez, M.C. Duke, R.F.D. Costa, A.L. Dicks, J.C.D. da Costa, Nafion/polyaniline/silica composite membranes for direct methanol fuel

- cell application, *J. Power Sources*. 166 (2007) 324–330. <https://doi.org/10.1016/j.jpowsour.2006.12.102>.
- [109] M.M. Ayad, A.A. El-Nasr, Adsorption of cationic dye (methylene blue) from water using polyaniline nanotubes base, *J. Phys. Chem. C*. 114 (2010) 14377–14383. <https://doi.org/10.1021/jp103780w>.
- [110] Y. Bu, Z. Chen, Role of polyaniline on the photocatalytic degradation and stability performance of the polyaniline/silver/silver phosphate composite under visible light, *ACS Appl. Mater. Interfaces*. 6 (2014) 17589–17598. <https://doi.org/10.1021/am503578s>.
- [111] A. Watanabe, K. Mori, Y. Iwasaki, Y. Nakamura, A. Chemistry, S. Niizuma, Electrochromism of Polyaniline Film Prepared, *Macromolecules*. 20 (1987) 1793–1796.
- [112] T. Sen, S. Mishra, N.G. Shimpi, Synthesis and sensing applications of polyaniline nanocomposites: A review, *RSC Adv*. 6 (2016) 42196–42222. <https://doi.org/10.1039/c6ra03049a>.
- [113] P. V. Kamat, Native and Surface Modified Semiconductor Nanoclusters, in: *Mol. Lev. Artif. Photosynth. Mater.*, 2007: pp. 273–343. <https://doi.org/10.1002/9780470166451.ch6>.
- [114] M. Dahl, Y. Liu, Y. Yin, Composite titanium dioxide nanomaterials, *Chem. Rev*. 114 (2014) 9853–9889. <https://doi.org/10.1021/cr400634p>.
- [115] S. Saha, P. Samanta, N.C. Murmu, T. Kuila, A review on the heterostructure nanomaterials for supercapacitor application, *J. Energy Storage*. 17 (2018) 181–202. <https://doi.org/10.1016/j.est.2018.03.006>.
- [116] D. Beydoun, R. Amal, G. Low, S. McEvoy, Role of nanoparticles in photocatalysis, *J. Nanoparticle Res*. 1 (1999) 439–458. <https://doi.org/10.1023/A:1010044830871>.
- [117] S. Ramakrishna, K. Fujihara, W.-E. Teo, T.-C. Lim, Z. Ma, *An Introduction to Electrospinning and Nanofibers*, World Scientific Publication Co. Pte. Ltd, 2005.
- [118] S.S. Ray, S. Chen, C. Li, C. Nguyen, A comprehensive review : electrospinning technique for fabrication and surface modification, *RSC Adv*. 6 (2016) 85495–85514. <https://doi.org/10.1039/C6RA14952A>.
- [119] N. Bhardwaj, S.C. Kundu, Electrospinning : A fascinating fiber fabrication technique, *Biotechnol. Adv*. 28 (2010) 325–347. <https://doi.org/10.1016/j.biotechadv.2010.01.004>.
- [120] Y. Liao, T. Fukuda, S. Wang, Electrospun Metal Oxide Nanofibers and Their Energy Applications, *Nanofiber Res. - Reach. New Height*. (2016) 169–190. <https://doi.org/10.5772/63414>.
- [121] Q.N. Pham, U. Sharma, Electrospinning of Polymeric Nanofibers for Tissue Engineering Applications : A Review, *Tissue Eng*. 12 (2006) 1197–1211. <https://doi.org/10.1089/ten.2006.12.1197>.
- [122] V. Pillay, C. Dott, Y.E. Choonara, C. Tyagi, L. Tomar, P. Kumar, L.C. Toit, V.M.K. Ndesendo, A Review of the Effect of Processing Variables on the

- Fabrication of Electrospun Nanofibers for Drug Delivery Applications, *J. Nan.* 2013 (2012) 1–22.
- [123] I. Alghoraibi, S. Alomari, Different methods for nanofibers design and fabrication, in: *Handb. Nanofibres*, Springer, 2019: pp. 1–47. <https://doi.org/10.1007/978-3-319-42789-8>.
- [124] R. Ashraf, H.S. Sofi, A. Malik, M.A. Beigh, Recent Trends in the Fabrication of Starch Nanofibers : Electrospinning and Non-electrospinning Routes and Their Applications in Biotechnology, Springer. (2018) 1–28.
- [125] G. Jeong, J.-G. Kim, M.-S. Park, M. Seo, S.M. Hwang, Y.-U. Kim, Y.-J. Kim, J.H. Kim, S.X. Dou, Core- Shell Structured Silicon Nanoparticles@TiO<sub>2-x</sub>/Carbon Mesoporous Microfiber Composite as a Safe and High-Performance Lithium-Ion Battery Anode, *ACS Nano.* 8 (2014) 2977–2985. <https://doi.org/10.1021/nn500278q>.
- [126] A.K. Moghe, B.S. Gupta, Co-axial electrospinning for nanofiber structures: Preparation and applications, *Polym. Rev.* 48 (2008) 353–377. <https://doi.org/10.1080/15583720802022257>.
- [127] E. Prabakaran, K. Pillay, Synthesis of N-doped ZnO nanoparticles with cabbage morphology as a catalyst for the efficient photocatalytic degradation of methylene blue under UV and visible light, *RSC Adv.* 9 (2019) 7509–7535. <https://doi.org/10.1039/C8RA09962F>.
- [128] A. Zulfi, D.A. Hapidin, M.M. Munir, F. Iskandar, K. Khairurrijal, The synthesis of nanofiber membranes from acrylonitrile butadiene styrene ( ABS ) waste using electrospinning for use as air filtration media, *RSC.* (2019) 30741–30751. <https://doi.org/10.1039/c9ra04877d>.
- [129] Q. Huang, Y. Huang, C. Xiao, Y. You, C. Zhang, Electrospun ultrafine fibrous PTFE-supported ZnO porous membrane with self-cleaning function for vacuum membrane distillation, *J. Memb. Sci.* 534 (2017) 73–82.
- [130] C. Liu, P. Hsu, H. Lee, M. Ye, G. Zheng, N. Liu, W. Li, Y. Cui, Transparent air filter for high-efficiency PM<sub>2.5</sub> capture, *Nat. Commun.* 6 (2015) 1–9. <https://doi.org/10.1038/ncomms7205>.
- [131] K. Vocetkova, M. Buzgo, V. Sovkova, M. Rampichova, A comparison of high throughput core–shell 2D electrospinning and 3D centrifugal spinning techniques to produce platelet lyophilisate-loaded fibrous scaffolds and their effects on skin cells, *RSC Adv.* (2017) 53706–53719. <https://doi.org/10.1039/C7RA08728D>.
- [132] Z. Duan, Y. Huang, D. Zhang, S. Chen, Electrospinning Fabricating Au/TiO<sub>2</sub> Network-like Nanofibers as Visible Light Activated Photocatalyst, *Scientia.* (2019) 1–8. <https://doi.org/10.1038/s41598-019-44422-w>.
- [133] S. Gautam, H. Agrawal, M. Thakur, A. Akbari, H. Sharda, R. Kaur, M. Amini, Metal oxides and metal organic frameworks for the photocatalytic degradation: A review, *J. Environ. Chem. Eng.* 8 (2020) 103726. <https://doi.org/10.1016/j.jece.2020.103726>.
- [134] K. Mondal, A. Sharma, Recent advances in the synthesis and application of photocatalytic metal-metal oxide core-shell nanoparticles for environmental

- remediation and their recycling process, *RSC Adv.* 6 (2016) 83589–83612. <https://doi.org/10.1039/c6ra18102c>.
- [135] R. Asahi, T. Morikawa, H. Irie, T. Ohwaki, Nitrogen-doped titanium dioxide as visible-light-sensitive photocatalyst: Designs, developments, and prospects, *Chem. Rev.* 114 (2014) 9824–9852. <https://doi.org/10.1021/cr5000738>.
- [136] O. Morton, Silicon valley sunrise, a new day dawning, *Nature.* 443 (2006) 19–22.
- [137] M. Gao, L. Zhu, C.K. Peh, G.W. Ho, Solar absorber material and system designs for photothermal water vaporization towards clean water and energy production, *Energy Environ. Sci.* 12 (2019) 841–864. <https://doi.org/10.1039/c8ee01146j>.
- [138] W. Choi, A. Termin, M.R. Hoffmann, The role of metal ion dopants in quantum-sized TiO<sub>2</sub>: Correlation between photoreactivity and charge carrier recombination dynamics, *J. Phys. Chem.* 98 (1994) 13669–13679. <https://doi.org/10.1021/j100102a038>.
- [139] D.M. Smyth, Effects of dopants on the properties of metal oxides, *Solid State Ionics.* 129 (2000) 5–12. [https://doi.org/10.1016/S0167-2738\(99\)00312-4](https://doi.org/10.1016/S0167-2738(99)00312-4).
- [140] Y. Liu, W. Wang, X. Xu, J.P. Marcel Veder, Z. Shao, Recent advances in anion-doped metal oxides for catalytic applications, *J. Mater. Chem. A.* 7 (2019) 7280–7300. <https://doi.org/10.1039/C8TA09913H>.
- [141] R. Kumari, A. Sahai, N. Goswami, Effect of nitrogen doping on structural and optical properties of ZnO nanoparticles, *Prog. Nat. Sci. Mater. Int.* 25 (2015) 300–309. <https://doi.org/10.1016/j.pnsc.2015.08.003>.
- [142] K.O. Obodo, L.L. Noto, S.J. Mofokeng, C.N.M. Ouma, M. Braun, M.S. Dhlamini, Influence of Tm, Ho and Er dopants on the properties of Yb activated ZnTiO<sub>3</sub> perovskite: A density functional theory insight, *Mater. Res. Express.* 5 (2018) 106202. <https://doi.org/10.1088/2053-1591/aadaf2>.
- [143] R. Asahi, T. Morikawa, T. Ohwaki, K. Aoki, Y. Taga, Visible-light photocatalysis in nitrogen-doped titanium oxides, *Science* (80-. ). 293 (2001) 269–271.
- [144] S. Singh, S. Perween, A. Ranjan, Enhancing the visible light induced photocatalytic activity in sol-electrospun zinc titanate nanopowders by nitrogen doping, *J. Phys. Chem. Solids.* (2021) 110221. <https://doi.org/10.1016/j.jpcs.2021.110221>.
- [145] T. Gao, Z. Chen, Y. Zhu, F. Niu, Q. Huang, L. Qin, X. Sun, Y. Huang, Synthesis of BiFeO<sub>3</sub> nanoparticles for the visible-light induced photocatalytic property, *Mater. Res. Bull.* 59 (2014) 6–12. <https://doi.org/10.1016/j.materresbull.2014.06.022>.
- [146] S. Li, Y. Lin, B. Zhang, Y. Wang, C. Nan, Controlled Fabrication of BiFeO<sub>3</sub> Uniform Microcrystals and Their Magnetic and Photocatalytic Behaviors, *J. Phys. Chem. C.* 114 (2010) 2903–2908. <https://doi.org/10.1021/jp910401u>.
- [147] S. Sakka, Sol-Gel Process and Applications, in: *Handb. Adv. Ceramics*, 2013: pp. 883–910. <https://doi.org/10.1016/B978-0-12-385469-8.00048-4>.
- [148] B.G. Rao, D. Mukherjee, B.M. Reddy, Novel approaches for preparation of nanoparticles, in: *Nanostructures Nov. Ther.*, Elsevier Inc., 2017: pp. 1–36.

<https://doi.org/10.1016/B978-0-323-46142-9/00001-3>.

- [149] C.J. Brinker, G.W. Scherer, *Sol-Gel Science: The Physics and Chemistry of Sol-Gel Processing*, 1st ed., Academic Press Limited, New York, 1990.
- [150] J. Yuh, L. Perez, W.M. Sigmund, J.C. Nino, Sol-gel based synthesis of complex oxide nanofibers, *J. Sol-Gel Sci. Technol.* 42 (2007) 323–329. <https://doi.org/10.1007/s10971-007-0736-6>.
- [151] A.R. Phani, S. Santucci, Structural characterization of iron titanium oxide synthesized by sol – gel spin-coating technique, *Mater. Lett.* 50 (2001) 240–245.
- [152] A.E. Danks, S.R. Hall, Z. Schnepf, The evolution of “sol-gel” chemistry as a technique for materials synthesis, *Mater. Horizons.* 3 (2016) 91–112. <https://doi.org/10.1039/c5mh00260e>.
- [153] J. Livage, D. Ganguli, Sol-gel electrochromic coatings and devices : A review, *Sol. Energy Mater. Sol. Cells.* 68 (2001) 365–381.
- [154] L.L. Hench, J.O.N.K. West, The Sol-Gel Process, *Chem. Rev.* 90 (1990) 33–72. <https://doi.org/10.1021/cr00099a003>.
- [155] I. Hayati, A.I. Bailey, T.H.F. Tadros, Investigations into the Mechanisms of Electrohydrodynamic Spraying of Liquids., *J. Colloid Interface Sci.* 117 (1987) 205–221.
- [156] S. Chew, Y. Wen, Y. Dzenis, K. Leong, The Role of Electrospinning in the Emerging field of Nanomedicine, *Curr Pharm Des.* 12 (2008) 4751–4770.
- [157] G. Taylor, P.R.S.L. A, Electrically driven jets, *Proc. R. Soc. London. A. Math. Phys. Sci.* 313 (1969) 453–475. <https://doi.org/10.1098/rspa.1969.0205>.
- [158] W.K. Son, J.H. Youk, T.S. Lee, W.H. Park, The effects of solution properties and polyelectrolyte on electrospinning of ultrafine poly (ethylene oxide) fibers, *Polymer (Guildf).* 45 (2004) 2959–2966. <https://doi.org/10.1016/j.polymer.2004.03.006>.
- [159] H. Bagheri, A. Aghakhani, M. Baghernejad, A. Akbarinejad, Novel polyamide-based nanofibers prepared by electrospinning technique for headspace solid-phase microextraction of phenol and chlorophenols from environmental samples, *Anal. Chim. Acta.* 716 (2012) 34–39. <https://doi.org/10.1016/j.aca.2011.03.016>.
- [160] P. Shankar, J.B.B. Payappan, Room Temperature Ethanol Sensing Properties of ZnO Nanorods Prepared usin Electrospinning Technique, *J. Mater. Chem. C.* 5 (2017) 10869–10880. <https://doi.org/10.1039/C7TC03771F>.
- [161] Z. Li, Y. Fan, J. Zhan, In<sub>2</sub>O<sub>3</sub> Nanofibers and Nanoribbons : Preparation by Electrospinning and Their Formaldehyde Gas-Sensing Properties, *Eur. J. Inorg. Chem.* (2010) 3348–3353. <https://doi.org/10.1002/ejic.201000313>.
- [162] B.K. Woan, G. Pyrgiotakis, W. Sigmund, Photocatalytic Carbon-Nanotube – TiO<sub>2</sub> Composites, *Adv. Mater.* 21 (2009) 2233–2239. <https://doi.org/10.1002/adma.200802738>.
- [163] Z.X. Huang, J.W. Wu, S.C. Wong, J.P. Qu, T.S. Srivatsan, The technique of electrospinning for manufacturing core-shell nanofibers, *Mater. Manuf. Process.* 33 (2018) 202–219. <https://doi.org/10.1080/10426914.2017.1303144>.

- [164] J. Zhao, Y. Cheng, X. Yan, D. Sun, Q. Xue, Magnetic and electrochemical properties of CuFe<sub>2</sub>O<sub>4</sub> hollow fibers fabricated by simple electrospinning and direct annealing, *CrystEngComm*. 14 (2012) 5879–5885. <https://doi.org/10.1039/c2ce25684c>.
- [165] E. Maccaferri, L. Mazzocchetti, T. Benelli, T.M. Brugo, A. Zucchelli, L. Giorgini, Rubbery Nanofibers by co-Electrospinning of Almost Immiscible NBR and PCL blend, *Mater. Des.* (2019) 108210. <https://doi.org/10.1016/j.matdes.2019.108210>.
- [166] Y.B. Kim, D. Cho, W.H. Park, Electrospinning of Poly (Dimethyl Siloxane) by Sol – Gel Method, *J. Appl. Polym. Sci.* 114 (2009) 3870–3874. <https://doi.org/10.1002/app>.
- [167] S. Jiang, H. Hou, S. Agarwal, A. Greiner, Polyimide Nanofibers by “Green” Electrospinning via Aqueous Solution for Filtration Applications, *ACS Sustainable Chem. Eng.* 4 (2016) 4797–4804. <https://doi.org/10.1021/acssuschemeng.6b01031>.
- [168] D. Weiss, D. Skrybeck, H. Misslitz, D. Nardini, A. Kern, K. Kreger, H. Schmidt, Tailoring Supramolecular Nanofibers for Air Filtration Applications, *ACS Appl. Mater. Interfaces*. 8 (2016) 14885–14892. <https://doi.org/10.1021/acsaami.6b04720>.
- [169] J. Venugopal, S. Ramakrishna, Applications of Polymer Nanofibers in Biomedicine and Biotechnology, *Appl. Biochem. Biotechnol.* 125 (2005) 147–157.
- [170] A.L. Yarin, B. Pourdeyhimi, S. Ramakrishna, Military applications of micro- and nanofibers, in: *Fundam. Appl. Micro- Nanofibers*, Cambridge University Press, 2014: pp. 359–379.
- [171] S. Perween, Z. Khan, S. Singh, A. Ranjan, PVA-PDMS-Stearic acid composite nanofibrous mats with improved mechanical behavior for selective filtering applications, *Science (80-. )*. 8 (2018) 1–14. <https://doi.org/10.1038/s41598-018-34440-5>.
- [172] R. Dersch, M. Steinhart, U. Boudriot, A. Greiner, J.H. Wendorff, Nanoprocessing of polymers: Applications in medicine, sensors, catalysis, photonics, *Polym. Adv. Technol.* 16 (2005) 276–282. <https://doi.org/10.1002/pat.568>.
- [173] I.G. Loscertales, A. Barrero, I. Guerrero, R. Cortijo, M. Marquez, A.M. Gañán-Calvo, Micro/nano encapsulation via electrified coaxial liquid jets, *Science (80-. )*. 295 (2002) 1695–1698. <https://doi.org/10.1126/science.1067595>.
- [174] H. Higashimura, S. Kobayashi, Oxidative polymerization, in: *Encycl. Polym. Sci. Technol.*, John Wiley & Sons, Inc, 2004: pp. 740–764.
- [175] N.Y. Abu-thabit, Chemical Oxidative Polymerization of Polyaniline: A Practical Approach for Preparation of Smart Conductive Textiles, *J. Chem. Educ.* 93 (2016) 1606–1611. <https://doi.org/10.1021/acs.jchemed.6b00060>.
- [176] I.Y. Sapurina, M.A. Shishov, Oxidative Polymerization of Aniline : Molecular Synthesis of Polyaniline and the Formation of Supramolecular Structures, in: *New Polym. Spec. Appl. PANI*, Licensee IntechOpen, 2012: pp. 251–312.
- [177] Y. Ding, A.B. Radias, H.K. Hall, Chemical trapping experiments support a cation-

- radical mechanism for the oxidative polymerization of aniline, *J. Polym. Sci. Part A Polym. Chem.* 37 (1999) 2569–2579. [https://doi.org/10.1002/\(SICI\)1099-0518\(19990715\)37:14<2569::AID-POLA30>3.0.CO;2-N](https://doi.org/10.1002/(SICI)1099-0518(19990715)37:14<2569::AID-POLA30>3.0.CO;2-N).
- [178] C. Suryanarayana, M. Grant Norton, *X-Ray Diffraction: A Practical Approach*, 1st ed., Springer Science+Business Media New York, Pullman, WA, 1998. <https://doi.org/10.1201/9781315364445>.
- [179] W.L. Bragg, The diffraction of X-rays by crystals, *Scientia*. 23 (1922) 153.
- [180] A.L. Patterson, The scherrer formula for X-ray particle size determination, *Phys. Rev.* 56 (1939) 978–982. <https://doi.org/10.1103/PhysRev.56.978>.
- [181] J.-Z. Kong, A.-D. Li, H.-F. Zhai, H. Li, Q.-Y. Yan, J. Ma, D. Wu, Preparation, characterization and photocatalytic properties of ZnTiO<sub>3</sub> powders, *J. Hazard. Mater.* 171 (2009) 918–923. <https://doi.org/10.1016/j.jhazmat.2009.06.092>.
- [182] P. Bindu, S. Thomas, Estimation of lattice strain in ZnO nanoparticles: X-ray peak profile analysis, *J. Theor. Appl. Phys.* 8 (2014) 123–134. <https://doi.org/10.1007/s40094-014-0141-9>.
- [183] V. Mote, Y. Purushotham, B. Dole, Williamson-Hall analysis in estimation of lattice strain in nanometer-sized ZnO particles, *J. Theor. Appl. Phys.* 6 (2012) 2–9. <https://doi.org/10.1186/2251-7235-6-6>.
- [184] A. Sahai, Y. Kumar, V. Agarwal, S.F. Olive-Méndez, N. Goswami, Doping concentration driven morphological evolution of Fe doped ZnO nanostructures, *J. Appl. Phys.* 116 (2014). <https://doi.org/10.1063/1.4900721>.
- [185] J. Luo, Y. Xu, D. Gao, Synthesis, characterization and microwave absorption properties of polyaniline/Sm-doped strontium ferrite nanocomposite, *Solid State Sci.* 37 (2014) 40–46. <https://doi.org/10.1016/j.solidstatesciences.2014.08.007>.
- [186] G.K. Williamsom, W.H. Hall, X-Ray Line Broadening from Field Aluminium and Wolfram, *Acta Metall.* 1 (1953) 22–31.
- [187] P.R. Griffiths, J.A. d. Haseth, *Fourier transform infrared spectrometry*, 2007. [https://doi.org/10.1007/978-1-4614-3909-7\\_6](https://doi.org/10.1007/978-1-4614-3909-7_6).
- [188] M.A. Mohamed, J. Jaafar, A.F. Ismail, M.H.D. Othman, M.A. Rahman, *Fourier Transform Infrared (FTIR) Spectroscopy*, in: *Membr. Charact.*, Elsevier B.V., 2017: pp. 3–29. <https://doi.org/10.1016/B978-0-444-63776-5.00001-2>.
- [189] W. Zhou, R. Apkarian, Z.L. Wang, D. Joy, *Fundamentals of scanning electron microscopy (SEM)*, in: Z. W, W. Z.L (Eds.), *Scanning Microsc. Nanotechnol.*, Springer, New York, NY, 2006: pp. 1–40. [https://doi.org/10.1007/978-0-387-39620-0\\_1](https://doi.org/10.1007/978-0-387-39620-0_1).
- [190] N. Brodusch, H. Demers, R. Gauvin, *Field Emission Scanning Electron Microscopy*, Spinger Nature, Canada, 2018. <https://doi.org/10.1007/978-981-10-4433-5>.
- [191] Sina Ebnesajjad, *Surface Treatment of Materials for Adhesive Bonding*, Second, Elsevier Inc., 2014. <https://doi.org/10.1016/B978-0-323-26435-8.00012-5>.
- [192] Y. Leng, *Scanning electron microscopy*, in: *Mater. Charact. Introd. to Microsc. Spectrosc. Methods*, John Wiley & Sons (Asia) Pte Ltd, 2018: pp. 121–144.

[https://doi.org/10.1007/978-981-13-0454-5\\_2](https://doi.org/10.1007/978-981-13-0454-5_2).

- [193] H.-H. Perkampus, *UV-VIS Spectroscopy and Its Applications*, Springer Berlin Heidelberg, 1992.
- [194] J.M. Hollas, *Modern Spectroscopy*, Forth, 2004.
- [195] S. Mourdikoudis, R.M. Pallares, N.T.K. Thanh, Characterization techniques for nanoparticles: Comparison and complementarity upon studying nanoparticle properties, *Nanoscale*. 10 (2018) 12871–12934. <https://doi.org/10.1039/c8nr02278j>.
- [196] J.F. Watts, J. Wolstenholme, *An Introduction to Surface Analysis by XPS and AES*, John Wiley & Sons, Ltd, 2003.
- [197] R. Pecora, *Dynamic Light Scattering - Applications of Photo Correlation Spectroscopy*, Springer US, 1985.
- [198] J. Lim, S.P. Yeap, H.X. Che, S.C. Low, Characterization of magnetic nanoparticle by dynamic light scattering, *Nanoscale Res. Lett.* 8 (2013) 1–14. <https://doi.org/10.1186/1556-276X-8-381>.
- [199] J. Lim, C. Lanni, E.R. Evarts, F. Lanni, R.D. Tilton, S.A. Majetich, Magnetophoresis of nanoparticles, *ACS Nano*. 5 (2011) 217–226. <https://doi.org/10.1021/nn102383s>.
- [200] F. Baldassarre, M. Cacciola, G. Ciccarella, A predictive model of iron oxide nanoparticles flocculation tuning Z-potential in aqueous environment for biological application, *J. Nanoparticle Res.* 17 (2015). <https://doi.org/10.1007/s11051-015-3163-6>.
- [201] W. Groenewoud, *Characterisation of Polymers by Thermal Analysis*, Elsevier B.V., 2001. <https://doi.org/10.1016/b978-0-444-50604-7.x5000-6>.
- [202] P. Dolez, O. Vermeersch, V. Izquierdo, *Advanced Characterization and Testing of Textiles*, Elsevier Ltd., 2018.
- [203] S. Loganathan, R.B. Valapa, R. Mishra, G. Pugazhenthii, Thermogravimetry Analysis for Characterization of Nanomaterials, in: S. Thomas, R. Thomas, A. Zachariah, R. Misra (Eds.), *Therm. Rheol. Meas. Tech. Nanomater. Charact.*, Elsevier, 2017: pp. 1–47. <https://doi.org/10.1016/b978-0-323-46139-9.12001-8>.
- [204] C. V. Raman, K.S. Krishnan, A new type of secondary radiation, *Nature*. 121 (1928) 501–502. <https://doi.org/10.1038/121501c0>.
- [205] J.R. Ferraro, K. Nakamoto, C.W. Brown, *Introductory Raman Spectroscopy*, 2nd ed., Elsevier, USA, 2003. <https://doi.org/10.1016/B978-0-12-254105-6.X5000-8>.
- [206] E. Smith, G. Dent, *Modern Raman Spectroscopy: A Practical Approach*, John Wiley & Sons, Ltd, England, 2005. <https://doi.org/10.1002/9781119440598>.
- [207] Y. Si, X. Tang, J. Yu, B. Ding, *Electrospun nanofibers for energy and environmental applications*, Springer-Verlag Berlin Heidelberg, 2011.
- [208] H. Qi, P. Hu, J. Xu, A. Wang, Encapsulation of drug reservoirs in fibers by emulsion electrospinning: Morphology characterization and preliminary release assessment, *Biomacromolecules*. 7 (2006) 2327–2330.

<https://doi.org/10.1021/bm060264z>.

- [209] R. Gopal, S. Kaur, Z. Ma, C. Chan, S. Ramakrishna, T. Matsuura, Electrospun nanofibrous filtration membrane, *J. Memb. Sci.* 281 (2006) 581–586. <https://doi.org/10.1016/j.memsci.2006.04.026>.
- [210] Y. Wu, Z. Dong, S. Wilson, R.L. Clark, Template-assisted assembly of electrospun fibers, *Polymer (Guildf)*. 51 (2010) 3244–3248. <https://doi.org/10.1016/j.polymer.2010.04.039>.
- [211] Y. Yang, X. Fan, Y. Long, K. Su, D. Zou, N. Li, J. Zhou, K. Li, F. Liu, A simple fabrication of electrospun nanofiber sensing materials based on fluorophore-doped polymer, *J. Mater. Chem.* 19 (2009) 7290–7295. <https://doi.org/10.1039/b908154b>.
- [212] S. Chen, J. V. John, A. McCarthy, J. Xie, New forms of electrospun nanofiber materials for biomedical applications, *J. Mater. Chem. B*. 8 (2020) 3733–3746. <https://doi.org/10.1039/d0tb00271b>.
- [213] T. Pirzada, S.A. Arvidson, C.D. Saquing, S.S. Shah, S.A. Khan, Hybrid silica-PVA nanofibers via sol-gel electrospinning, *Langmuir*. 28 (2012) 5834–5844. <https://doi.org/10.1021/la300049j>.
- [214] T. Ochiai, A. Fujishima, Photoelectrochemical properties of TiO<sub>2</sub> photocatalyst and its applications for environmental purification, *J. Photochem. Photobiol. C Photochem. Rev.* 13 (2012) 247–262. <https://doi.org/10.1016/j.jphotochemrev.2012.07.001>.
- [215] M.M. Khan, S.F. Adil, A. Al-Mayouf, Metal oxides as photocatalysts, *J. Saudi Chem. Soc.* 19 (2015) 462–464. <https://doi.org/10.1016/j.jscs.2015.04.003>.
- [216] K.S. Ranjith, T. Uyar, Conscientious Design of Zn-S/Ti-N Layer by Transformation of ZnTiO<sub>3</sub> on Electrospun ZnTiO<sub>3</sub>@TiO<sub>2</sub> Nanofibers: Stability and Reusable Photocatalytic Performance under Visible Irradiation, *ACS Sustain. Chem. Eng.* 6 (2018) 12980–12992. <https://doi.org/10.1021/acssuschemeng.8b02455>.
- [217] A. Ali, X. Li, J. Song, S. Yang, W. Zhang, Z. Zhang, R. Xia, L. Zhu, X. Xu, Nature-mimic ZnO nanoflowers architecture: Chalcogenide quantum dots coupling with ZnO/ZnTiO<sub>3</sub> Nanoheterostructures for efficient photoelectrochemical water splitting, *J. Phys. Chem. C*. 121 (2017) 21096–21104. <https://doi.org/10.1021/acs.jpcc.7b04701>.
- [218] J. Zhao, C. Jia, H. Duan, H. Li, E. Xie, Structural properties and photoluminescence of TiO<sub>2</sub> nanofibers were fabricated by electrospinning, *J. Alloys Compd.* 461 (2008) 447–450. <https://doi.org/10.1016/j.jallcom.2007.07.018>.
- [219] X. Zhang, J. Qin, Y. Xue, P. Yu, B. Zhang, L. Wang, R. Liu, Effect of aspect ratio and surface defects on the photocatalytic activity of ZnO nanorods, *Sci. Rep.* 4 (2014) 4–11. <https://doi.org/10.1038/srep04596>.
- [220] E.. Baran, I. Botto, The Raman spectra of ZnTiO<sub>3</sub> and CdTiO<sub>3</sub>, *J. Inorg. General Chem.* 448 (1979) 188–192. <https://doi.org/10.1017/CBO9781107415324.004>.
- [221] S. Lei, H. Fan, X. Ren, J. Fang, L. Ma, Z. Liu, Novel sintering and band gap

- engineering of ZnTiO<sub>3</sub> ceramics with excellent microwave dielectric properties, *J. Mater. Chem. C*. 5 (2017) 4040–4047. <https://doi.org/10.1039/c7tc00815e>.
- [222] K.R. Zhu, M.S. Zhang, Q. Chen, Z. Yin, Size and phonon-confinement effects on low-frequency Raman mode of anatase TiO<sub>2</sub> nanocrystal, *Phys. Lett. A*. 340 (2005) 220–227. <https://doi.org/10.1016/j.physleta.2005.04.008>.
- [223] L. Li, S. Gao, T. Cui, B. Li, Q. Zhou, H. Yuan, D. Xu, Temperature-dependent optical phonon behaviour of a spinel Zn<sub>2</sub>TiO<sub>4</sub> single crystal grown by the optical floating zone method in argon atmosphere, *RSC Adv.* 7 (2017) 35477–35481. <https://doi.org/10.1039/c7ra05267g>.
- [224] A. Sarkar, G.G. Khan, The formation and detection techniques of oxygen vacancies in titanium oxide-based nanostructures, *Nanoscale*. 11 (2019) 3414–3444. <https://doi.org/10.1039/c8nr09666j>.
- [225] X.Q. Zhang, J.B. Chen, C.W. Wang, A.Z. Liao, X.F. Su, Low-temperature liquid phase reduced TiO<sub>2</sub> nanotube arrays: Synergy of morphology manipulation and oxygen vacancy doping for enhancement of field emission, *Nanotechnology*. 26 (2015) 1–12. <https://doi.org/10.1088/0957-4484/26/17/175705>.
- [226] A.C. Chaves, S.J.G. Lima, R.C.M.U. Araújo, M.A.M.A. Maurera, E. Longo, P.S. Pizani, L.G.P. Simões, L.E.B. Soledade, A.G. Souza, I.M.G. Dos Santos, Photoluminescence in disordered Zn<sub>2</sub>TiO<sub>4</sub>, *J. Solid State Chem.* 179 (2006) 985–992. <https://doi.org/10.1016/j.jssc.2005.12.018>.
- [227] N.T. McDevitt, W.L. Baun, Infrared absorption study of metal oxides in the low frequency region (700-240 cm<sup>-1</sup>), *Spectrochim. Acta*. 20 (1964) 799–808. [https://doi.org/10.1016/0371-1951\(64\)80079-5](https://doi.org/10.1016/0371-1951(64)80079-5).
- [228] L. Hou, Y.D. Hou, M.K. Zhu, J. Tang, J.B. Liu, H. Wang, H. Yan, Formation and transformation of ZnTiO<sub>3</sub> prepared by sol-gel process, *Mater. Lett.* 59 (2005) 197–200. <https://doi.org/10.1016/j.matlet.2004.07.046>.
- [229] M.R. Mohammadi, D.J. Fray, Low temperature nanostructured zinc titanate by an aqueous particulate sol-gel route: Optimisation of heat treatment condition based on Zn:Ti molar ratio, *J. Eur. Ceram. Soc.* 30 (2010) 947–961. <https://doi.org/10.1016/j.jeurceramsoc.2009.09.031>.
- [230] P.A. Connor, K.D. Dobson, A. James McQuillan, Infrared spectroscopy of the TiO<sub>2</sub>/aqueous solution interface, *Langmuir*. 15 (1999) 2402–2408. <https://doi.org/10.1021/la980855d>.
- [231] R. Al-Gaashani, S. Radiman, A.R. Daud, N. Tabet, Y. Al-Douri, XPS and optical studies of different morphologies of ZnO nanostructures prepared by microwave methods, *Ceram. Int.* 39 (2013) 2283–2292. <https://doi.org/10.1016/j.ceramint.2012.08.075>.
- [232] H. Zhou, Z. Li, Synthesis of nanowires, nanorods and nanoparticles of ZnO through modulating the ratio of water to methanol by using a mild and simple solution method, *Mater. Chem. Phys.* 89 (2005) 326–331. <https://doi.org/10.1016/j.matchemphys.2004.09.006>.
- [233] H. Wagata, K. Sakakibara, K. Kawashima, M. Hojamberdiev, K. Yubuta, K. Teshima, Alkali Metal Chloride Flux Growth of Ilmenite-Type ZnTiO<sub>3</sub> and

- Subsequent Nitrogen Doping for Visible-Light-Driven Water Oxidation Catalysis, *ACS Appl. Energy Mater.* 2 (2019) 7762–7771. <https://doi.org/10.1021/acsaem.9b00815>.
- [234] C. Chuaicham, S. Karthikeyan, J.T. Song, T. Ishihara, B. Ohtani, K. Sasaki, Importance of ZnTiO<sub>3</sub> Phase in ZnTi-Mixed Metal Oxide Photocatalysts Derived from Layered Double Hydroxide, *ACS Appl. Mater. Interfaces.* 12 (2020) 9169–9180. <https://doi.org/10.1021/acsaem.9b18785>.
- [235] O. Secundino-Sánchez, J. Díaz-Reyes, J.F. Sánchez-Ramírez, J. Martínez-Juárez, Stimulation of the photoluminescent properties of electrospinning TiO<sub>2</sub> nanofibres induced by structural modifications resulting from annealing at high temperatures, *J. Lumin.* 215 (2019). <https://doi.org/10.1016/j.jlumin.2019.116700>.
- [236] A.A. Mosquera, D. Horwat, A. Rashkovskiy, A. Kovalev, P. Miska, D. Wainstein, J.M. Albella, J.L. Endrino, Exciton and core-level electron confinement effects in transparent ZnO thin films, *Sci. Rep.* 3 (2013) 1–6. <https://doi.org/10.1038/srep01714>.
- [237] B. Bharti, S. Kumar, H.N. Lee, R. Kumar, Formation of oxygen vacancies and Ti<sup>3+</sup> state in TiO<sub>2</sub> thin film and enhanced optical properties by air plasma treatment, *Sci. Rep.* 6 (2016) 1–12. <https://doi.org/10.1038/srep32355>.
- [238] R. López, R. Gómez, Band-gap energy estimation from diffuse reflectance measurements on sol-gel and commercial TiO<sub>2</sub>: A comparative study, *J. Sol-Gel Sci. Technol.* 61 (2012) 1–7. <https://doi.org/10.1007/s10971-011-2582-9>.
- [239] P. Kubelka, New Contributions to the Optics of Intensely Light-Scattering Materials Part II: Nonhomogeneous Layers, *J. Opt. Soc. Am.* 44 (1954) 330. <https://doi.org/10.1364/JOSA.44.000330>.
- [240] Z.X. Li, F.B. Shi, Y. Ding, T. Zhang, C.H. Yan, Facile synthesis of highly ordered mesoporous ZnTiO<sub>3</sub> with crystalline walls by self-adjusting method, *Langmuir.* 27 (2011) 14589–14593. <https://doi.org/10.1021/la2034615>.
- [241] C. Zhang, X. Li, T. Zheng, Y. Yang, Y. Li, Y. Li, C. Wang, L. Li, Beaded ZnTiO<sub>3</sub> Fibers Prepared by Electrospinning and Their Photocatalytic Properties, *Desalin. Water Treat.* 45 (2012) 324–330. <https://doi.org/10.1080/19443994.2012.692030>.
- [242] M. Salavati-niasari, F. Soofivand, A. Sobhani-nasab, M. Shakouri-arani, Synthesis, characterization, and morphological control of ZnTiO<sub>3</sub> nanoparticles through sol-gel processes and its photocatalyst application, (2016) 1–10. <https://doi.org/10.1016/j.appt.2016.07.018>.
- [243] J.A. Mcleod, A.F. Zatsepin, E. Kurmaev, A. Wypych, Predicting the band gap of ternary oxides containing 3d<sup>10</sup> and 3d<sup>0</sup> metals, *Phys. Rev. B.* 86 (2012) 195207. <https://doi.org/10.1103/PhysRevB.86.195207>.
- [244] W.F. Zhang, Z. Yin, M.S. Zhang, Z.L. Du, W.C. Chen, Roles of Defects and Grain Sizes in Photoluminescence of Nanocrystalline SrTiO<sub>3</sub>, *J. Phys. Condens. Matter.* 11 (1999) 5655–5660.
- [245] Y. Cong, J. Zhang, F. Chen, M. Anpo, Synthesis and characterization of nitrogen-doped TiO<sub>2</sub> nanophotocatalyst with high visible light activity, *J. Phys. Chem. C.* 111 (2007) 6976–6982. <https://doi.org/10.1021/jp0685030>.

- [246] L. Nikam, R. Panmand, S. Kadam, S. Naik, B. Kale, Enhanced hydrogen production under visible light source and dye degradation under natural sunlight using nanostructured doped zinc orthotitanates, *New J. Chem.* 39 (2015) 3821–3834. <https://doi.org/10.1039/b000000x>.
- [247] B. Liu, L. Wen, X. Zhao, The photoluminescence spectroscopic study of anatase TiO<sub>2</sub> prepared by magnetron sputtering, *Mater. Chem. Phys.* 106 (2007) 350–353. <https://doi.org/10.1016/j.matchemphys.2007.06.012>.
- [248] D. Damberg, R. Viter, V. Fedorenko, I. Iatsunskyi, E. Coy, O. Graniel, S. Balme, P. Miele, M. Bechelany, Photoluminescence Study of Defects in ZnO-Coated Polyacrylonitrile Nanofibers, *J. Phys. Chem. C.* 124 (2020) 9434–9441. <https://doi.org/10.1021/acs.jpcc.0c00326>.
- [249] S.K. Choi, S. Kim, S.K. Lim, H. Park, Photocatalytic comparison of TiO<sub>2</sub> nanoparticles and electrospun TiO<sub>2</sub> nanofibers: Effects of mesoporosity and interparticle charge transfer, *J. Phys. Chem. C.* 114 (2010) 16475–16480. <https://doi.org/10.1021/jp104317x>.
- [250] M.C. Wu, C.H. Chen, W.K. Huang, K.C. Hsiao, T.H. Lin, S.H. Chan, P.Y. Wu, C.F. Lu, Y.H. Chang, T.F. Lin, K.H. Hsu, J.F. Hsu, K.M. Lee, J.J. Shyue, K. Kordás, W.F. Su, Improved Solar-Driven Photocatalytic Performance of Highly Crystalline Hydrogenated TiO<sub>2</sub> Nanofibers with Core-Shell Structure, *Sci. Rep.* 7 (2017) 1–12. <https://doi.org/10.1038/srep40896>.
- [251] A. Ghobadi, T.G. Ulusoy, R. Garifullin, M.O. Guler, A.K. Okyay, A Heterojunction Design of Single Layer Hole Tunneling ZnO Passivation Wrapping around TiO<sub>2</sub> Nanowires for Superior Photocatalytic Performance, *Sci. Rep.* 6 (2016) 1–15. <https://doi.org/10.1038/srep30587>.
- [252] H.S. Kushwaha, N.A. Madhar, B. Ilahi, P. Thomas, A. Halder, R. Vaish, Efficient Solar Energy Conversion Using CaCu<sub>3</sub>Ti<sub>4</sub>O<sub>12</sub> Photoanode for Photocatalysis and Photoelectrocatalysis, *Sci. Rep.* 6 (2016) 18557. <https://doi.org/10.1038/srep18557>.
- [253] S. Chen, T. Takata, K. Domen, Particulate photocatalysts for overall water splitting, *Nat. Rev. Mater.* 2 (2017) 1–17. <https://doi.org/10.1038/natrevmats.2017.50>.
- [254] S. Ghosh, N.A. Kouame, S. Remita, L. Ramos, F. Goubard, P.H. Aubert, A. Dazzi, A. Deniset-Besseau, H. Remita, Visible-light active conducting polymer nanostructures with superior photocatalytic activity, *Sci. Rep.* 5 (2015) 18002. <https://doi.org/10.1038/srep18002>.
- [255] S. Ghosh, N.A. Kouamé, L. Ramos, S. Remita, A. Dazzi, A. Deniset-Besseau, P. Beaunier, F. Goubard, P.H. Aubert, H. Remita, Conducting polymer nanostructures for photocatalysis under visible light, *Nat. Mater.* 14 (2015) 505–511. <https://doi.org/10.1038/nmat4220>.
- [256] V.S. Vyas, F. Haase, L. Stegbauer, G. Savasci, F. Podjaski, C. Ochsenfeld, B. V. Lotsch, A tunable azine covalent organic framework platform for visible light-induced hydrogen generation, *Nat. Commun.* 6 (2015) 1–9. <https://doi.org/10.1038/ncomms9508>.
- [257] V.J. Babu, M.K. Kumar, A.S. Nair, T.L. Kheng, S.I. Allakhverdiev, S.

- Ramakrishna, Visible Light Photocatalytic Water Splitting for Hydrogen Production from N-TiO<sub>2</sub> Rice Grain Shaped Electrospun Nanostructures, *Int. J. Hydrogen Energy*. 37 (2012) 8897–8904. <https://doi.org/10.1016/j.ijhydene.2011.12.015>.
- [258] D. Wu, X. Zhang, Y. Jing, X. Zhao, Z. Zhou, Towards visible-light water splitting Photocatalysts: Band engineering of two-dimensional A<sub>5</sub>B<sub>4</sub>O<sub>15</sub> perovskites, *Nano Energy*. 28 (2016) 390–396. <https://doi.org/10.1016/j.nanoen.2016.08.064>.
- [259] R.M. Navarro, F. del Valle, J.A. Villoria de la Mano, M.C. Álvarez-Galván, J.L.G. Fierro, Photocatalytic Water Splitting Under Visible Light. Concept and Catalysts Development, *Adv. Chem. Eng.* 36 (2009) 111–143. [https://doi.org/10.1016/S0065-2377\(09\)00404-9](https://doi.org/10.1016/S0065-2377(09)00404-9).
- [260] R. Abe, Recent progress on photocatalytic and photoelectrochemical water splitting under visible light irradiation, *J. Photochem. Photobiol. C Photochem. Rev.* 11 (2010) 179–209. <https://doi.org/10.1016/j.jphotochemrev.2011.02.003>.
- [261] R.K. Kotnala, R. Gupta, A. Shukla, S. Jain, A. Gaur, J. Shah, Metal Oxide Based Hydroelectric Cell for Electricity Generation by Water Molecule Dissociation without Electrolyte/Acid, *J. Phys. Chem. C*. 122 (2018) 18841–18849. <https://doi.org/10.1021/acs.jpcc.8b04999>.
- [262] V.M. Aroutiounian, V.M. Arakelyan, G.E. Shahnazaryan, Metal oxide photoelectrodes for hydrogen generation using solar radiation-driven water splitting, *Sol. Energy*. 78 (2005) 581–592. <https://doi.org/10.1016/j.solener.2004.02.002>.
- [263] S.A. Ansari, M.M. Khan, M.O. Ansari, M.H. Cho, Nitrogen-doped titanium dioxide (N-dopedTiO<sub>2</sub>) for visible light photocatalysis, *New J. Chem.* 40 (2016) 3000–3009. <https://doi.org/10.1039/C5NJ03478G>.
- [264] H. Ling, K. Kim, Z. Liu, J. Shi, X. Zhu, J. Huang, Photocatalytic degradation of phenol in water on as-prepared and surface modified TiO<sub>2</sub> nanoparticles, *Catal. Today*. 258 (2015) 96–102. <https://doi.org/10.1016/j.cattod.2015.03.048>.
- [265] H. Xu, W. Liu, L. Cao, G. Su, R. Duan, Preparation of porous TiO<sub>2</sub>/ZnO composite film and its photocathodic protection properties for 304 stainless steel, *Appl. Surf. Sci.* 301 (2014) 508–514. <https://doi.org/10.1016/j.apsusc.2014.02.114>.
- [266] S.H. Ko, D. Lee, H.W. Kang, K.H. Nam, J.Y. Yeo, S.J. Hong, C.P. Grigoropoulos, H.J. Sung, Nanoforest of hydrothermally grown hierarchical ZnO nanowires for a high efficiency dye-sensitized solar cell, *Nano Lett.* 11 (2011) 666–671. <https://doi.org/10.1021/nl1037962>.
- [267] Z. Ali, S. Ali, I. Ahmad, I. Khan, H.A. Rahnamaye Aliabad, Structural and optoelectronic properties of the zinc titanate perovskite and spinel by modified Becke-Johnson potential, *Phys. B Condens. Matter*. 420 (2013) 54–57. <https://doi.org/10.1016/j.physb.2013.03.042>.
- [268] S.C. Das, R.J. Green, J. Podder, T.Z. Regier, G.S. Chang, A. Moewes, Band gap tuning in ZnO through ni doping via spray pyrolysis, *J. Phys. Chem. C*. 117 (2013) 12745–12753. <https://doi.org/10.1021/jp3126329>.
- [269] K. Sarkar, E. V. Braden, T. Fröschl, N. Hüsing, P. Müller-Buschbaum, Spray-

- deposited zinc titanate films obtained *via* sol–gel synthesis for application in dye-sensitized solar cells, *J. Mater. Chem. A.* 2 (2014) 15008–15014. <https://doi.org/10.1039/C4TA02031F>.
- [270] Y.S. Chang, Y.H. Chang, I.G. Chen, G.J. Chen, Y.L. Chai, T.H. Fang, S. Wu, Synthesis, Formation and Characterization of ZnTiO<sub>3</sub> Ceramics, *Ceram. Int.* 30 (2004) 2183–2189. <https://doi.org/10.1016/j.ceramint.2004.01.002>.
- [271] C.L. Wang, W.S. Hwang, H.L. Chu, H.H. Ko, C.S. Hsi, W.L. Li, K.M. Chang, M.C. Wang, Phase Formation of Zinc Titanate Precursor Powders Prepared by A Hydrothermal Process in Various pH Environments, *Metall. Mater. Trans. A Phys. Metall. Mater. Sci.* 45 (2014) 2689–2698. <https://doi.org/10.1007/s11661-014-2282-5>.
- [272] V.J. Babu, R.P. Rao, A.S. Nair, S. Ramakrishna, Nitrogen-doped rice grain-shaped titanium dioxide nanostructures by electrospinning: Frequency and temperature dependent conductivity, *J. Appl. Phys.* 110 (2011) 0–7. <https://doi.org/10.1063/1.3642979>.
- [273] L.K. Preethi, R.P. Antony, T. Mathews, L. Walczak, C.S. Gopinath, A Study on Doped Heterojunctions in TiO<sub>2</sub> Nanotubes: An Efficient Photocatalyst for Solar Water Splitting, *Sci. Rep.* 7 (2017) 1–15. <https://doi.org/10.1038/s41598-017-14463-0>.
- [274] P. Muhammed Shafi, A. Chandra Bose, Impact of Crystalline Defects and Size on X-Ray Line Broadening: A Phenomenological Approach for Tetragonal SnO<sub>2</sub> Nanocrystals, *AIP Adv.* 5 (2015). <https://doi.org/10.1063/1.4921452>.
- [275] Q.J. Liu, N.C. Zhang, F.S. Liu, H.Y. Wang, Z.T. Liu, Theoretical study of structural, elastic, electronic properties, and dispersion of optical functions of hexagonal ZnTiO<sub>3</sub>, *Phys. Status Solidi Basic Res.* 1–6 (2013) 1810–1815. <https://doi.org/10.1002/pssb.201349093>.
- [276] S. Lei, H. Fan, X. Ren, J. Fang, L. Ma, Z. Liu, Novel sintering and band gap engineering of ZnTiO<sub>3</sub> ceramics with excellent microwave dielectric properties, *J. Mater. Chem. C.* 5 (2017) 4040–4047. <https://doi.org/10.1039/c7tc00815e>.
- [277] S. Gayathri, P. Jayabal, M. Kottaisamy, V. Ramakrishnan, Synthesis of the Graphene-ZnTiO<sub>3</sub> Nanocomposite for Solar Light Assisted Photodegradation of Methylene Blue, *J. Phys. D. Appl. Phys.* 48 (2015) 415305. <https://doi.org/10.1088/0022-3727/48/41/415305>.
- [278] L. Li, S. Gao, T. Cui, B. Li, Q. Zhou, H. Yuan, D. Xu, Temperature-dependent optical phonon behaviour of a spinel Zn<sub>2</sub>TiO<sub>4</sub> single crystal grown by the optical floating zone method in argon atmosphere, *RSC Adv.* 7 (2017) 35477–35481. <https://doi.org/10.1039/c7ra05267g>.
- [279] W. Spengler, R. Kaiser, A.N. Christensen, G. Müller-Vogt, Raman scattering, superconductivity, and phonon density of states of stoichiometric and nonstoichiometric TiN, *Phys. Rev. B.* 17 (1978) 1095–1101. <https://doi.org/10.1103/PhysRevB.17.1095>.
- [280] D. Nassoko, Y.F. Li, H. Wang, J.L. Li, Y.Z. Li, Y. Yu, Nitrogen-Doped TiO<sub>2</sub> Nanoparticles by Using EDTA as Nitrogen Source and Soft Template: Simple Preparation, Mesoporous Structure, and Photocatalytic Activity under Visible

- Light, J. Alloys Compd. 540 (2012) 228–235. <https://doi.org/10.1016/j.jallcom.2012.06.085>.
- [281] W. Junwei, Z. Wei, Z. Yinqing, L. Shuangxi, An efficient two-step technique for nitrogen-doped titanium dioxide synthesizing: Visible-light-induced photodecomposition of methylene blue, *J. Phys. Chem. C.* 111 (2007) 1010–1014. <https://doi.org/10.1021/jp066156o>.
- [282] G. Yang, Z. Jiang, H. Shi, T. Xiao, Z. Yan, Preparation of highly visible-light active N-doped TiO<sub>2</sub> photocatalyst, *J. Mater. Chem.* 20 (2010) 5301–5309. <https://doi.org/10.1039/c0jm00376j>.
- [283] T. Surendar, S. Kumar, V. Shanker, Influence of La-doping on phase transformation and photocatalytic properties of ZnTiO<sub>3</sub> nanoparticles synthesized via modified sol-gel method, *Phys. Chem. Chem. Phys.* 16 (2014) 728–735. <https://doi.org/10.1039/c3cp53855a>.
- [284] Y. Huo, Z. Bian, X. Zhang, Y. Jin, J. Zhu, H. Li, Highly active TiO<sub>2-x</sub>N<sub>x</sub> visible photocatalyst prepared by N-doping in Et<sub>3</sub>N/EtOH fluid under supercritical conditions, *J. Phys. Chem. C.* 112 (2008) 6546–6550. <https://doi.org/10.1021/jp711966c>.
- [285] S. Sakthivel, M. Janczarek, H. Kisch, Visible light activity and photoelectrochemical properties of nitrogen-doped TiO<sub>2</sub>, *J. Phys. Chem. B.* 108 (2004) 19384–19387. <https://doi.org/10.1021/jp046857q>.
- [286] Y. Huo, Y. Jin, J. Zhu, H. Li, Highly active TiO<sub>2-x-y</sub>N<sub>x</sub>F<sub>y</sub> visible photocatalyst prepared under supercritical conditions in NH<sub>4</sub>F/EtOH fluid, *Appl. Catal. B Environ.* 89 (2009) 543–550. <https://doi.org/10.1016/j.apcatb.2009.01.019>.
- [287] Z. Cai, J. Li, Y. Wang, Fabrication of zinc titanate nanofibers by electrospinning technique, *J. Alloys Compd.* 489 (2010) 167–169. <https://doi.org/10.1016/j.jallcom.2009.09.044>.
- [288] F. Peng, L. Cai, H. Yu, H. Wang, J. Yang, Synthesis and characterization of substitutional and interstitial nitrogen-doped titanium dioxides with visible light photocatalytic activity, *J. Solid State Chem.* 181 (2008) 130–136. <https://doi.org/10.1016/j.jssc.2007.11.012>.
- [289] J. Lynch, C. Giannini, J.K. Cooper, A. Loiudice, I.D. Sharp, R. Buonsanti, Substitutional or interstitial site selective nitrogen doping in TiO<sub>2</sub> nanostructures, *J. Phys. Chem. C.* 119 (2015) 7443–7452. <https://doi.org/10.1021/jp512775s>.
- [290] R.G. Palgrave, D.J. Payne, R.G. Egdell, Nitrogen diffusion in doped TiO<sub>2</sub> (110) single crystals: A combined XPS and SIMS study, *J. Mater. Chem.* 19 (2009) 8418–8425. <https://doi.org/10.1039/b913267h>.
- [291] C. Di Valentin, G. Pacchioni, A. Selloni, S. Livraghi, E. Giamello, Characterization of paramagnetic species in N-doped TiO<sub>2</sub> powders by EPR spectroscopy and DFT calculations, *J. Phys. Chem. B.* 109 (2005) 11414–11419. <https://doi.org/10.1021/jp051756t>.
- [292] L. Mi, P. Xu, P.N. Wang, Experimental study on the bandgap narrowings of TiO<sub>2</sub> films calcined under N<sub>2</sub> or NH<sub>3</sub> atmosphere, *Appl. Surf. Sci.* 255 (2008) 2574–2580. <https://doi.org/10.1016/j.apsusc.2008.07.150>.

- [293] D. Koch, S. Manzhos, On the charge state of titanium in titanium dioxide, *J. Phys. Chem. Lett.* 8 (2017) 1593–1598. <https://doi.org/10.1021/acs.jpcclett.7b01886>.
- [294] C.T. Wang, J.C. Lin, Surface nature of nanoparticle zinc-titanium oxide aerogel catalysts, *Appl. Surf. Sci.* 254 (2008) 4500–4507. <https://doi.org/10.1016/j.apsusc.2008.01.024>.
- [295] K.H. Reddy, S. Martha, K.M. Parida, Erratic charge transfer dynamics of Au/ZnTiO<sub>3</sub> nanocomposites under UV and visible light irradiation and their related photocatalytic activities, *Nanoscale*. 10 (2018) 18540–18554. <https://doi.org/10.1039/c8nr06158k>.
- [296] T.C. Jagadale, S.P. Takale, R.S. Sonawane, H.M. Joshi, S.I. Patil, B.B. Kale, S.B. Ogale, N-doped TiO<sub>2</sub> nanoparticle based visible light photocatalyst by modified peroxide sol-gel method, *J. Phys. Chem. C*. 112 (2008) 14595–14602. <https://doi.org/10.1021/jp803567f>.
- [297] N. Lu, Y. Wang, S. Ning, W. Zhao, M. Qian, Y. Ma, J. Wang, L. Fan, J. Guan, X. Yuan, Design of plasmonic Ag-TiO<sub>2</sub>/H<sub>3</sub>PW<sub>12</sub>O<sub>40</sub> composite film with enhanced sunlight photocatalytic activity towards o-chlorophenol degradation, *Sci. Rep.* 7 (2017) 17298. <https://doi.org/10.1038/s41598-017-17221-4>.
- [298] J. Zhao, C. Chen, W. Ma, Photocatalytic Degradation of Organic Pollutants Under Visible Light Irradiation, *Top. Catal.* 35 (2005) 269–278. <https://doi.org/10.1007/s11244-005-3834-0>.
- [299] C. Dai, B. Liu, Conjugated polymers for visible-light-driven photocatalysis, *Energy Environ. Sci.* 13 (2020) 24–52. <https://doi.org/10.1039/c9ee01935a>.
- [300] X. Huang, P. Jiang, Core-shell structured high-k polymer nanocomposites for energy storage and dielectric applications, *Adv. Mater.* 27 (2014) 546–554. <https://doi.org/10.1002/adma.201401310>.
- [301] Q. Wang, L. Zhu, Polymer nanocomposites for electrical energy storage, *J. Polym. Sci. Part B Polym. Phys.* 49 (2011) 1421–1429. <https://doi.org/10.1002/polb.22337>.
- [302] I. Ali, New generation adsorbents for water treatment, *Chem. Rev.* 112 (2012) 5073–5091. <https://doi.org/10.1021/cr300133d>.
- [303] T. Hanemann, D.V. Szabó, Polymer-nanoparticle composites: From synthesis to modern applications, *Materials (Basel)*. 3 (2010) 3468–3517. <https://doi.org/10.3390/ma3063468>.
- [304] G. Zhao, X. Huang, Z. Tang, Q. Huang, F. Niu, X. Wang, Polymer-based nanocomposites for heavy metal ions removal from aqueous solution: A review, *Polym. Chem.* 9 (2018) 3562–3582. <https://doi.org/10.1039/c8py00484f>.
- [305] M.G. Buonomenna, A. Gordano, G. Golemme, E. Drioli, Preparation, characterization and use of PEEKWC nanofiltration membranes for removal of Azur B dye from aqueous media, *React. Funct. Polym.* 69 (2009) 259–263. <https://doi.org/10.1016/j.reactfunctpolym.2009.01.004>.
- [306] J.W. Lee, S.P. Choi, R. Thiruvengkatachari, W.G. Shim, H. Moon, Submerged microfiltration membrane coupled with alum coagulation/powdered activated carbon adsorption for complete decolorization of reactive dyes, *Water Res.* 40

- (2006) 435–444. <https://doi.org/10.1016/j.watres.2005.11.034>.
- [307] H. Selcuk, Decolorization and detoxification of textile wastewater by ozonation and coagulation processes, *Dye. Pigment.* 64 (2005) 217–222. <https://doi.org/10.1016/j.dyepig.2004.03.020>.
- [308] C.H. Liu, J.S. Wu, H.C. Chiu, S.Y. Suen, K.H. Chu, Removal of anionic reactive dyes from water using anion exchange membranes as adsorbers, *Water Res.* 41 (2007) 1491–1500. <https://doi.org/10.1016/j.watres.2007.01.023>.
- [309] C.H. Wu, J.M. Chern, Kinetics of photocatalytic decomposition of methylene blue, *Ind. Eng. Chem. Res.* 45 (2006) 6450–6457. <https://doi.org/10.1021/ie0602759>.
- [310] K. Dutta, S. Mukhopadhyay, S. Bhattacharjee, B. Chaudhuri, Chemical oxidation of methylene blue using a Fenton-like reaction, *J. Hazard. Mater.* 84 (2001) 57–71. [https://doi.org/10.1016/S0304-3894\(01\)00202-3](https://doi.org/10.1016/S0304-3894(01)00202-3).
- [311] M. Arami, N.Y. Limaee, N.M. Mahmoodi, N.S. Tabrizi, Equilibrium and kinetics studies for the adsorption of direct and acid dyes from aqueous solution by soy meal hull, *J. Hazard. Mater.* 135 (2006) 171–179. <https://doi.org/10.1016/j.jhazmat.2005.11.044>.
- [312] L. Ai, M. Li, L. Li, Adsorption of methylene blue from aqueous solution with activated carbon/cobalt ferrite/alginate composite beads: Kinetics, isotherms, and thermodynamics, *J. Chem. Eng. Data.* 56 (2011) 3475–3483. <https://doi.org/10.1021/je200536h>.
- [313] K.S. Bharathi, S.T. Ramesh, Removal of dyes using agricultural waste as low-cost adsorbents: a review, *Appl. Water Sci.* 3 (2013) 773–790. <https://doi.org/10.1007/s13201-013-0117-y>.
- [314] M.Y. Chong, Y.J. Tam, Bioremediation of dyes using coconut parts via adsorption: a review, *SN Appl. Sci.* 2 (2020) 1–16. <https://doi.org/10.1007/s42452-020-1978-y>.
- [315] N. Wang, J. Li, W. Lv, J. Feng, W. Yan, Synthesis of polyaniline/TiO<sub>2</sub> composite with excellent adsorption performance on acid red G, *RSC Adv.* 5 (2015) 21132–21141. <https://doi.org/10.1039/c4ra16910g>.
- [316] R. Kumar, S.A. Ansari, M.A. Barakat, A. Aljaafari, M.H. Cho, A polyaniline@MoS<sub>2</sub>-based organic-inorganic nanohybrid for the removal of Congo red: Adsorption kinetic, thermodynamic and isotherm studies, *New J. Chem.* 42 (2018) 18802–18809. <https://doi.org/10.1039/c8nj02803f>.
- [317] D. Zhou, B. Che, X. Lu, Rapid one-pot electrodeposition of polyaniline/manganese dioxide hybrids: a facile approach to stable high-performance anodic electrochromic materials, *J. Mater. Chem. C.* 5 (2017) 1758–1766. <https://doi.org/10.1039/c6tc05216a>.
- [318] M. Laabd, H. Ait Ahsaine, A. El Jaouhari, B. Bakiz, M. Bazzaoui, M. Ezahri, A. Albourine, A. Benlhachemi, Congo red removal by PANi/Bi<sub>2</sub>WO<sub>6</sub> nanocomposites: Kinetic, equilibrium and thermodynamic studies, *J. Environ. Chem. Eng.* 4 (2016) 3096–3105. <https://doi.org/10.1016/j.jece.2016.06.024>.
- [319] S. Dhanavel, E.A.K. Nivethaa, K. Dhanapal, V.K. Gupta, V. Narayanan, A. Stephen,  $\alpha$ -MoO<sub>3</sub>/polyaniline composite for effective scavenging of Rhodamine B,

- Congo red and textile dye effluent, *RSC Adv.* 6 (2016) 28871–28886. <https://doi.org/10.1039/c6ra02576e>.
- [320] H. Chafai, M. Laabd, S. Elbariji, M. Bazzaoui, A. Albourine, Study of congo red adsorption on the polyaniline and polypyrrole, *J. Dispers. Sci. Technol.* 38 (2017) 832–836. <https://doi.org/10.1080/01932691.2016.1207185>.
- [321] M.O. Ansari, R. Kumar, S.A. Ansari, S.P. Ansari, M.A. Barakat, A. Alshahrie, M.H. Cho, Anion selective pTSA doped polyaniline@graphene oxide-multiwalled carbon nanotube composite for Cr(VI) and Congo red adsorption, *J. Colloid Interface Sci.* 496 (2017) 407–415. <https://doi.org/10.1016/j.jcis.2017.02.034>.
- [322] S. Yang, L. Wang, X. Zhang, W. Yang, G. Song, Enhanced adsorption of Congo red dye by functionalized carbon nanotube/mixed metal oxides nanocomposites derived from layered double hydroxide precursor, *Chem. Eng. J.* 275 (2015) 315–321. <https://doi.org/10.1016/j.cej.2015.04.049>.
- [323] R.L. BURWELL, Manual of Symbols and Terminology for Physicochemical Quantities and Units, in: *IUPAC Compend. Chem. Terminol.*, Elsevier, Washington DC, USA, 1976: pp. 579–638.
- [324] J.P. Pouget, M.E. Józefowicz, A.J. Epstein, X. Tang, A.G. MacDiarmid, X-ray Structure of Polyaniline, *Macromolecules.* 24 (1991) 779–789. <https://doi.org/10.1021/ma00003a022>.
- [325] L. Zhang, P. Liu, Z. Su, Preparation of PANI-TiO<sub>2</sub> nanocomposites and their solid-phase photocatalytic degradation, *Polym. Degrad. Stab.* 91 (2006) 2213–2219. <https://doi.org/10.1016/j.polymdegradstab.2006.01.002>.
- [326] J. Stejskal, M. Trchová, P. Bober, P. Humpolíček, V. Kašpárková, I. Sapurina, M.A. Shishov, M. Varga, Conducting Polymers: Polyaniline, in: *Encycl. Polym. Sci. Technol.*, 4th ed., John Wiley & Sons, Inc, 2015: pp. 1–44. <https://doi.org/10.1002/0471440264.pst640>.
- [327] D.L. Liao, G.S. Wu, B.Q. Liao, Zeta potential of shape-controlled TiO<sub>2</sub> nanoparticles with surfactants, *Colloids Surfaces A Physicochem. Eng. Asp.* 348 (2009) 270–275. <https://doi.org/10.1016/j.colsurfa.2009.07.036>.
- [328] A. Drury, S. Chaure, M. Kröll, V. Nicolosi, N. Chaure, W.J. Blau, Fabrication and characterization of silver/polyaniline composite nanowires in porous anodic alumina, *Chem. Mater.* 19 (2007) 4252–4258. <https://doi.org/10.1021/cm071102s>.
- [329] B. Mu, J. Tang, L. Zhang, A. Wang, Facile fabrication of superparamagnetic graphene/polyaniline/Fe<sub>3</sub>O<sub>4</sub> nanocomposites for fast magnetic separation and efficient removal of dye, *Sci. Rep.* 7 (2017) 1–12. <https://doi.org/10.1038/s41598-017-05755-6>.
- [330] T. Ohsaka, Y. Ohnuki, N. Oyama, G. Katagiri, K. Kamisako, IR absorption spectroscopic identification of electroactive and electroinactive polyaniline films prepared by the electrochemical polymerization of aniline, *J. Electroanal. Chem.* 161 (1984) 399–405. [https://doi.org/10.1016/S0022-0728\(84\)80198-9](https://doi.org/10.1016/S0022-0728(84)80198-9).
- [331] S.N. Kumar, G. Bouyssoux, F. Gaillard, Electronic and structural characterization of electrochemically synthesized conducting polyaniline from XPS studies, *Surf. Interface Anal.* 15 (1990) 531–536. <https://doi.org/10.1002/sia.740150906>.

- [332] G. Qiu, Q. Wang, M. Nie, Polyaniline/Fe<sub>3</sub>O<sub>4</sub> magnetic nanocomposite prepared by ultrasonic irradiation, *J. Appl. Polym. Sci.* 102 (2006) 2107–2111. <https://doi.org/10.1002/app.24100>.
- [333] Y. Li, Y. Yu, L. Wu, J. Zhi, Processable polyaniline/titania nanocomposites with good photocatalytic and conductivity properties prepared via peroxo-titanium complex catalyzed emulsion polymerization approach, *Appl. Surf. Sci.* 273 (2013) 135–143. <https://doi.org/10.1016/j.apsusc.2013.01.213>.
- [334] Y. Kim, K. Kook, S.K. Hwang, C. Park, J. Cho, Polymer/perovskite - type nanoparticle multilayers with multi electric properties prepared from ligand addition-induced layer - by - layer assembly, *ACS Nano.* 8 (2014) 2419–2430. <https://doi.org/10.1021/nn405988d>.
- [335] S.S.M. Bhat, N.G. Sundaram, Efficient visible light photocatalysis of Bi<sub>4</sub>TaO<sub>8</sub>Cl nanoparticles synthesized by solution combustion technique, *RSC Adv.* 3 (2013) 14371–14378. <https://doi.org/10.1039/c3ra40240a>.
- [336] Q. Zhou, C. Xie, W. Gong, N. Xu, W. Zhou, Comments on the method of using maximum absorption wavelength to calculate Congo Red solution concentration, *J. Hazard. Mater.* 198 (2011) 381–382. <https://doi.org/10.1016/j.jhazmat.2011.08.015>.
- [337] D. Mahanta, G. Madras, S. Radhakrishnan, S. Patil, Adsorption of sulfonated dyes by polyaniline emeraldine salt and its kinetics, *J. Phys. Chem. B.* 112 (2008) 10153–10157. <https://doi.org/10.1021/jp803903x>.
- [338] Y.S. Ho, G. McKay, Sorption of copper(II) from aqueous solution by Peat, *Water. Air. Soil Pollut.* 158 (2004) 77–97. <https://doi.org/10.1023/B:WATE.0000044830.63767.a3>.
- [339] H.M.H. Gad, A.A. El-Sayed, Activated carbon from agricultural by-products for the removal of Rhodamine-B from aqueous solution, *J. Hazard. Mater.* 168 (2009) 1070–1081. <https://doi.org/10.1016/j.jhazmat.2009.02.155>.
- [340] S.J. Allen, G. McKay, K.Y.H. Khader, Intraparticle diffusion of a basic dye during adsorption onto sphagnum peat, *Environ. Pollut.* 56 (1989) 39–50. [https://doi.org/10.1016/0269-7491\(89\)90120-6](https://doi.org/10.1016/0269-7491(89)90120-6).
- [341] R. Kumar, M.O. Ansari, M.A. Barakat, Adsorption of brilliant green by surfactant doped polyaniline/MWCNTs composite: Evaluation of the kinetic, thermodynamic, and isotherm, *Ind. Eng. Chem. Res.* 53 (2014) 7167–7175. <https://doi.org/10.1021/ie500100d>.
- [342] G. McKay, Adsorption of Dyestuffs From Aqueous Solutions With Activated Carbon - 1. Equilibrium and Batch Contact-Time Studies., *J. Chem. Technol. Biotechnol.* 32 (1982) 759–772. <https://doi.org/10.1002/jctb.5030320712>.
- [343] Y. Bulut, H. Aydin, A kinetics and thermodynamics study of methylene blue adsorption on wheat shells, *Desalination.* 194 (2006) 259–267. <https://doi.org/10.1016/j.desal.2005.10.032>.
- [344] M. Manes, L.J.E. Hofer, Application of the polanyi adsorption potential theory to adsorption from solution on activated carbon, *J. Phys. Chem.* 73 (1969) 584–590. <https://doi.org/10.1021/j100723a018>.

- [345] M. Horsfall, A.I. Spiff, Adsorption of transition metals in aqueous solutions by fluted pumpkin (*Telfairia occidentalis* Hook f) waste, *Chem. Biodivers.* 2 (2005) 1266–1276. <https://doi.org/10.1002/cbdv.200590097>.
- [346] S.S. Tahir, N. Rauf, Removal of a cationic dye from aqueous solutions by adsorption onto bentonite clay, *Chemosphere.* 63 (2006) 1842–1848. <https://doi.org/10.1016/j.chemosphere.2005.10.033>.
- [347] C.N. and K. Ranganathan, Waste Fe(III)/Cr(III) Hydroxide as Adsorbent for the Removal of Cr(VI) From Aqueous Solution and Chromium Plating Industry Wastewater, *Environ. Pollut.* 82 (1993) 255–261.
- [348] W. Konicki, K. Cendrowski, X. Chen, E. Mijowska, Application of hollow mesoporous carbon nanospheres as an high effective adsorbent for the fast removal of acid dyes from aqueous solutions, *Chem. Eng. J.* 228 (2013) 824–833. <https://doi.org/10.1016/j.cej.2013.05.067>.
- [349] C.H. Hsu, P.M. Peacock, R.B. Flippen, S.K. Manohar, A.G. MacDiarmid, The molecular weight of polyaniline by light scattering and gel permeation chromatography, *Synth. Met.* 60 (1993) 233–237. [https://doi.org/10.1016/0379-6779\(93\)91285-A](https://doi.org/10.1016/0379-6779(93)91285-A).
- [350] J.M. Thomas, The existence of endothermic adsorption, *J. Chem. Educ.* 38 (1961) 138. <https://doi.org/10.1021/ed038p138>.
- [351] E. Ozkazanc, S. Zor, H. Ozkazanc, H.Y. Guney, U. Abaci, Synthesis, characterization and dielectric behavior of (ES)-form polyaniline/cerium(III)-nitrate-hexahydrate composites, *Mater. Chem. Phys.* 133 (2012) 356–362. <https://doi.org/10.1016/j.matchemphys.2012.01.037>.
- [352] W.F. Alves, E.C. Venancio, F.L. Leite, D.H.F. Kanda, L.F. Malmonge, J.A. Malmonge, L.H.C. Mattoso, Thermo-analyses of polyaniline and its derivatives, *Thermochim. Acta.* 502 (2010) 43–46. <https://doi.org/10.1016/j.tca.2010.02.003>.
- [353] S. Bhadra, D. Khastgir, Glass-rubber transition temperature of polyaniline: Experimental and molecular dynamic simulation, *Synth. Met.* 159 (2009) 1141–1146. <https://doi.org/10.1016/j.synthmet.2009.01.052>.
- [354] J.L. Keddie, R.A.L. Jones, R.A. Cory, Size-dependent depression of the glass transition temperature in polymer films, *Epl.* 27 (1994) 59–64. <https://doi.org/10.1209/0295-5075/27/1/011>.
- [355] F.M. MacHado, C.P. Bergmann, E.C. Lima, B. Royer, F.E. De Souza, I.M. Jauris, T. Calvete, S.B. Fagan, Adsorption of Reactive Blue 4 dye from water solutions by carbon nanotubes: Experiment and theory, *Phys. Chem. Chem. Phys.* 14 (2012) 11139–11153. <https://doi.org/10.1039/c2cp41475a>.
- [356] M. Niederberger, Nonaqueous sol-gel routes to metal oxide nanoparticles, *Acc. Chem. Res.* 40 (2007) 793–800. <https://doi.org/10.1021/ar600035e>.
- [357] M. Niederberger, N. Pinna, *Metal oxides nanoparticles in organic solvents*, Springer London, London New York, 2006. <https://doi.org/10.1007/978-1-84882-671-7>.
- [358] S.M. Selbach, M.-A. Einarsrud, T. Grande, On the Thermodynamic Stability of BiFeO<sub>3</sub>, *Chem. Mater.* 21 (2009) 169–173. <https://doi.org/10.1021/cm802607p>.

- [359] N. Zhang, D. Chen, F. Niu, S. Wang, L. Qin, Y. Huang, Enhanced visible light photocatalytic activity of Gd-doped BiFeO<sub>3</sub> nanoparticles and mechanism insight, *Nat. Publ. Gr.* (2016) 1–11. <https://doi.org/10.1038/srep26467>.
- [360] G. Catalan, J.F. Scott, Physics and applications of bismuth ferrite, *Adv. Mater.* 21 (2009) 2463–2485. <https://doi.org/10.1007/s10973-018-7261-4>.
- [361] H. Search, C. Journals, A. Contact, M. Iopscience, I.P. Address, Spintronics with multiferroics, 434221 (2008). <https://doi.org/10.1088/0953-8984/20/43/434221>.
- [362] M. Bibes, A. Barthélémy, Multiferroics: Towards a magnetoelectric memory, *Nat. Mater.* 7 (2008) 425–426. <https://doi.org/10.1038/nmat2189>.
- [363] B.F. Gao, X. Chen, K. Yin, S. Dong, Z. Ren, F. Yuan, T. Yu, Z. Zou, Visible-Light Photocatalytic Properties of Weak Magnetic BiFeO<sub>3</sub> Nanoparticles, (2007) 2889–2892. <https://doi.org/10.1002/adma.200602377>.
- [364] X. Wang, M. Zhang, P. Tian, W.S. Chin, C.M. Zhang, A facile approach to pure-phase Bi<sub>2</sub>Fe<sub>4</sub>O<sub>9</sub> nanoparticles sensitive to visible light, *Appl. Surf. Sci.* 321 (2014) 144–149. <https://doi.org/10.1016/j.apsusc.2014.09.166>.
- [365] T. Zhang, Y. Shen, Y. Qiu, Y. Liu, R. Xiong, J. Shi, J. Wei, Facial Synthesis and Photoreaction Mechanism of BiFeO<sub>3</sub>/Bi<sub>2</sub>Fe<sub>4</sub>O<sub>9</sub> Heterojunction Nanofibers, *ACS Sustain. Chem. Eng.* 5 (2017) 4630–4636. <https://doi.org/10.1021/acssuschemeng.6b03138>.
- [366] Y. Feng, Y. Li, M. Xu, S. Liu, J. Yao, Fast adsorption of methyl blue on zeolitic imidazolate framework-8 and its adsorption mechanism, *RSC Adv.* 6 (2016) 109608–109612. <https://doi.org/10.1039/c6ra23870j>.
- [367] G. Crini, Non-conventional low-cost adsorbents for dye removal: A review, *Bioresour. Technol.* 97 (2006) 1061–1085. <https://doi.org/10.1016/j.biortech.2005.05.001>.
- [368] S.K. Henninger, H.A. Habib, C. Janiak, MOFs as adsorbents for low temperature heating and cooling applications, *J. Am. Chem. Soc.* 131 (2009) 2776–2777. <https://doi.org/10.1021/ja808444z>.
- [369] H. Wu, P. Xue, Y. Lu, X. Zhu, Microstructural, optical and magnetic characterizations of BiFeO<sub>3</sub> multiferroic nanoparticles synthesized via a sol-gel process, *J. Alloys Compd.* 731 (2018) 471–477. <https://doi.org/10.1016/j.jallcom.2017.10.087>.
- [370] M.A. Basith, R. Ahsan, I. Zarin, M.A. Jalil, Enhanced photocatalytic dye degradation and hydrogen production ability of Bi<sub>25</sub>FeO<sub>40</sub>-rGO nanocomposite and mechanism insight, *Sci. Rep.* 8 (2018) 1–11. <https://doi.org/10.1038/s41598-018-29402-w>.
- [371] G.S. Lotey, N.K. Verma, Synthesis and characterization of BiFeO<sub>3</sub> nanowires and their applications in dye-sensitized solar cells, *Mater. Sci. Semicond. Process.* 21 (2014) 206–211. <https://doi.org/10.1016/j.mssp.2013.11.029>.
- [372] J. Zhao, T. Liu, Y. Xu, Y. He, W. Chen, Synthesis and characterization of Bi<sub>2</sub>Fe<sub>4</sub>O<sub>9</sub> powders, *Mater. Chem. Phys.* 128 (2011) 388–391. <https://doi.org/10.1016/j.matchemphys.2011.03.011>.

- [373] D. Voll, A. Beran, H. Schneider, Variation of infrared absorption spectra in the system  $\text{Bi}_2\text{Al}_{4-x}\text{Fe}_x\text{O}_9$  ( $x=0-4$ ), structurally related to mullite, *Phys. Chem. Miner.* 33 (2006) 623–628. <https://doi.org/10.1007/s00269-006-0108-8>.
- [374] T. Liu, Y. Xu, J. Zhao, Low-temperature synthesis of  $\text{BiFeO}_3$  via PVA Sol-Gel route, *J. Am. Ceram. Soc.* 93 (2010) 3637–3641. <https://doi.org/10.1111/j.1551-2916.2010.03945.x>.
- [375] F.A. Miller, C.H. Wilkins, Infrared spectra and characteristic frequencies of inorganic ions, *Anal. Chem.* 24 (1952) 1253–1294. <https://doi.org/10.7498/aps.58.3665>.
- [376] X. Qiao, F. Zhang, F. Sha, J. Zhao, H. Shi, J. Zhang, Controllable synthesis of nanostructured  $\text{BaSO}_4$  and  $\text{BaSO}_3$  crystals on the basis of DMSO oxidation chemistry, *CrystEngComm.* 20 (2018) 173–180. <https://doi.org/10.1039/c7ce01937h>.
- [377] A. Kirsch, M.M. Murshed, P. Gaczynski, K.D. Becker, T.M. Gesing,  $\text{Bi}_2\text{Fe}_4\text{O}_9$ : Structural changes from nano-to micro-crystalline state, *Zeitschrift Fur Naturforsch. B.* 71 (2016) 447–455. <https://doi.org/10.1515/znb-2015-0227>.
- [378] A.A. Porporati, K. Tsuji, M. Valant, A.K. Axelsson, G. Pezzotti, Raman tensor elements for multiferroic  $\text{BiFeO}_3$  with rhombohedral  $R3c$  symmetry, *J. Raman Spectrosc.* 41 (2010) 84–87. <https://doi.org/10.1002/jrs.2394>.
- [379] B. Safizade, S.M. Masoudpanah, M. Hasheminasari, A. Ghasemi, Photocatalytic activity of  $\text{BiFeO}_3/\text{ZnFe}_2\text{O}_4$  nanocomposites under visible light irradiation, *RSC Adv.* 8 (2018) 6988–6995. <https://doi.org/10.1039/c7ra13380d>.
- [380] T. Wu, L. Liu, M. Pi, D. Zhang, S. Chen, Enhanced magnetic and photocatalytic properties of  $\text{Bi}_2\text{Fe}_4\text{O}_9$  semiconductor with large exposed (001) surface, *Appl. Surf. Sci.* 377 (2016) 253–261. <https://doi.org/10.1016/j.apsusc.2016.03.140>.
- [381] S.J.A. Moniz, D. Pugh, C.S. Blackman, J. Tang, C.J. Carmalt, Photocatalytic Oxygen Evolution from Cobalt-Modified Nanocrystalline  $\text{BiFeO}_3$  Films Grown via Low-Pressure Chemical Vapor Deposition from  $\beta$ -Diketonate Precursors, *Cryst. Growth Des.* 16 (2016) 3818–3825. <https://doi.org/10.1021/acs.cgd.6b00370>.
- [382] M.N. Iliev, A.P. Litvinchuk, V.G. Hadjiev, M.M. Gospodinov, V. Skumryev, E. Ressouche, Phonon and magnon scattering of antiferromagnetic  $\text{Bi}_2\text{Fe}_4\text{O}_9$ , *Phys. Rev. B - Condens. Matter Mater. Phys.* 81 (2010) 1–8. <https://doi.org/10.1103/PhysRevB.81.024302>.
- [383] R. Palai, H. Schmid, J.F. Scott, R.S. Katiyar, Raman spectroscopy of single-domain multiferroic  $\text{BiFeO}_3$ , (2010) 1–7. <https://doi.org/10.1103/PhysRevB.81.064110>.
- [384] M. Cazayous, D. Malka, D. Lebeugle, D. Colson, Electric field effect on  $\text{BiFeO}_3$  single crystal investigated by Raman spectroscopy Electric field effect on  $\text{BiFeO}_3$  single crystal investigated by Raman spectroscopy, 071910 (2007) 1–4. <https://doi.org/10.1063/1.2771380>.
- [385] P. Hermet, M. Goffinet, J. Kreisel, P. Ghosez, Raman and infrared spectra of multiferroic bismuth ferrite from first principles, (2007) 3–6.

<https://doi.org/10.1103/PhysRevB.75.220102>.

- [386] R. Guo, L. Fang, W. Dong, F. Zheng, M. Shen, Enhanced Photocatalytic Activity and Ferromagnetism in Gd Doped BiFeO<sub>3</sub> Nanoparticles, (2010) 21390–21396.
- [387] M. Thommes, K. Kaneko, A. V. Neimark, J.P. Olivier, F. Rodriguez-Reinoso, J. Rouquerol, K.S.W. Sing, Physisorption of gases, with special reference to the evaluation of surface area and pore size distribution (IUPAC Technical Report), *Pure Appl. Chem.* 87 (2015) 1051–1069. <https://doi.org/10.1515/pac-2014-1117>.
- [388] G.E. Boyd, J. Schubert, A.W. Adamson, The Exchange Adsorption of Ions from Aqueous Solutions by Organic Zeolites. Ion-exchange Equilibria, *J. Am. Chem. Soc.* 69 (1947) 2818–2829. <https://doi.org/10.1021/ja01203a064>.
- [389] A.M. El-Kamash, A.A. Zaki, M.A. El Geleel, Modeling batch kinetics and thermodynamics of zinc and cadmium ions removal from waste solutions using synthetic zeolite A, *J. Hazard. Mater.* 127 (2005) 211–220. <https://doi.org/10.1016/j.jhazmat.2005.07.021>.
- [390] E.O. Oyelude, J.A.M. Awudza, S.K. Twumasi, Equilibrium , Kinetic and Thermodynamic Study of Removal of Eosin Yellow from Aqueous Solution Using Teak Leaf Litter Powder, *Sci. Rep.* (2017) 1–10. <https://doi.org/10.1038/s41598-017-12424-1>.
- [391] L. Xiong, Y. Yang, J. Mai, W. Sun, C. Zhang, D. Wei, Q. Chen, J. Ni, Adsorption behavior of methylene blue onto titanate nanotubes, *Chem. Eng. J.* 156 (2010) 313–320. <https://doi.org/10.1016/j.cej.2009.10.023>.
- [392] P.F. Technology, Adsorption and Ion Exchange : Basic Principles and Their Application in Food Processing, (2011) 22–42. <https://doi.org/10.1021/jf1032203>.
- [393] M. Ghaedi, M. Ghayedi, S. Nasiri, R. Sahraei, A. Daneshfar, Journal of Industrial and Engineering Chemistry Palladium , silver , and zinc oxide nanoparticles loaded on activated carbon as adsorbent for removal of bromophenol red from aqueous solution, *J. Ind. Eng. Chem.* 19 (2013) 1209–1217. <https://doi.org/10.1016/j.jiec.2012.12.020>.
- [394] T.K. Das, S. Prusty, Review on Conducting Polymers and Their Applications, *Polym. - Plast. Technol. Eng.* 51 (2012) 1487–1500. <https://doi.org/10.1080/03602559.2012.710697>.
- [395] S. Bhadra, D. Khastgir, N.K. Singha, J.H. Lee, Progress in preparation, processing and applications of polyaniline, *Prog. Polym. Sci.* 34 (2009) 783–810. <https://doi.org/10.1016/j.progpolymsci.2009.04.003>.
- [396] Y. dong Liang, Y. jun He, Y. hang Zhang, Q. qian Zhu, Adsorption property of alizarin red S by NiFe<sub>2</sub>O<sub>4</sub>/polyaniline magnetic composite, *J. Environ. Chem. Eng.* 6 (2018) 416–425. <https://doi.org/10.1016/j.jece.2017.12.022>.
- [397] H. Gülce, V. Eskizeybek, B. Haspulat, F. Sari, A. Gülce, A. Avci, Preparation of a new polyaniline/CdO nanocomposite and investigation of its photocatalytic activity: Comparative study under UV light and natural sunlight irradiation, *Ind. Eng. Chem. Res.* 52 (2013) 10924–10934. <https://doi.org/10.1021/ie401389e>.
- [398] S. Nasirian, H. Milani Moghaddam, Effect of different titania phases on the hydrogen gas sensing features of polyaniline/TiO<sub>2</sub> nanocomposite, *Polymer*

- (Guildf). 55 (2014) 1866–1874. <https://doi.org/10.1016/j.polymer.2014.02.030>.
- [399] E.T. Kang, K.G. Neoh, K.L. Tan, Polyaniline: A polymer with many interesting intrinsic redox states, *Prog. Polym. Sci.* 23 (1998) 277–324. [https://doi.org/10.1016/S0079-6700\(97\)00030-0](https://doi.org/10.1016/S0079-6700(97)00030-0).
- [400] W. Zheng, M. Angelopoulos, A.J. Epstein, A.G. MacDiarmid, Experimental evidence for hydrogen bonding in polyaniline: Mechanism of aggregate formation and dependency on oxidation state, *Macromolecules*. 30 (1997) 2953–2955. <https://doi.org/10.1021/ma9700136>.
- [401] A. Mehdinia, F. Roohi, A. Jabbari, Rapid magnetic solid phase extraction with in situ derivatization of methylmercury in seawater by Fe<sub>3</sub>O<sub>4</sub>/polyaniline nanoparticle, *J. Chromatogr. A*. 1218 (2011) 4269–4274. <https://doi.org/10.1016/j.chroma.2011.04.070>.
- [402] E. Andris, R. Navrátil, J. Jašík, G. Sabenya, M. Costas, M. Srnec, J. Roithová, Detection of Indistinct Fe–N Stretching Bands in Iron(V) Nitrides by Photodissociation Spectroscopy, *Chem. - A Eur. J.* 24 (2018) 5078–5081. <https://doi.org/10.1002/chem.201705307>.
- [403] G. V. Chertihin, L. Andrews, M. Neurock, Reactions of laser-ablated iron atoms with nitrogen atoms and molecules. Matrix infrared spectra and density functional calculations of novel iron nitride molecules, *J. Phys. Chem.* 100 (1996) 14609–14617. <https://doi.org/10.1021/jp961423j>.
- [404] B. Sreedhar, M. Sairam, D.K. Chattopadhyay, P.P. Mitra, D. V. Mohan Rao, Thermal and XPS studies on polyaniline salts prepared by inverted emulsion polymerization, *J. Appl. Polym. Sci.* 101 (2006) 499–508. <https://doi.org/10.1002/app.23301>.
- [405] Z.T. Hu, S.K. Lua, T.T. Lim, Cuboid-like Bi<sub>2</sub>Fe<sub>4</sub>O<sub>9</sub>/Ag with Graphene-Wrapping Tribid Composite with Superior Capability for Environmental Decontamination: Nanoscaled Material Design and Visible-Light-Driven Multifunctional Catalyst, *ACS Sustain. Chem. Eng.* 3 (2015) 2726–2736. <https://doi.org/10.1021/acssuschemeng.5b00571>.
- [406] L. Zhang, X. Zhang, Y. Zou, Y.H. Xu, C.L. Pan, J.S. Hu, C.M. Hou, Hydrothermal synthesis, influencing factors and excellent photocatalytic performance of novel nanoparticle-assembled Bi<sub>25</sub>FeO<sub>40</sub> tetrahedrons, *CrystEngComm*. 17 (2015) 6527–6537. <https://doi.org/10.1039/c5ce00743g>.
- [407] X. Wang, J. Pan, W. Guan, J. Dai, X. Zou, Y. Yan, C. Li, Selective Removal of 3-Chlorophenol from Aqueous Solution Using Surface Molecularly Imprinted Microspheres, (2011) 2793–2801. <https://doi.org/10.1021/je101275e>.